

AD-A275 678



3



Boundary Layers Induced by Three-Dimensional Vortex Loops

A. T. Conlisk, H. Affes, O. R. Burggraf, and Z. Xiao
Department of Mechanical Engineering

DTIC
ELECTE
FEB 09 1994
S E D

U.S. Army Research Office
Research Triangle Park, North Carolina 27709-2211

Contract No. DAAL03-89-K-0095
Final Report

December 1993

Approved for public release; distribution unlimited.

94 2 08 15 6

27828 94-04456

REPORT DOCUMENTATION PAGE

Form Approved
OMB No. 0704-0188

Public reporting burden for this collection of information is estimated to average 1 hour per response, including the time for reviewing instructions, searching existing data sources, gathering and maintaining the data needed, and completing and reviewing the collection of information. Send comments regarding this burden estimate or any other aspect of this collection of information, including suggestions for reducing this burden, to Washington Headquarters Services, Directorate for Information Operations and Reports, 1215 Jefferson Davis Highway, Suite 1204, Arlington, VA 22202-4302, and to the Office of Management and Budget, Paperwork Reduction Project (0704-0188), Washington, DC 20503.

1. AGENCY USE ONLY (Leave blank)		2. REPORT DATE <i>Dec 93</i>	3. REPORT TYPE AND DATES COVERED <i>Final 1 May 89-31 Aug 93</i>	
4. TITLE AND SUBTITLE Boundary Layers Induced by Three-Dimensional Vortex Loops			5. FUNDING NUMBERS DAAL03-89-K-0095	
6. AUTHOR(S) Terrence Conlisk				
7. PERFORMING ORGANIZATION NAME(S) AND ADDRESS(ES) Ohio State University Research Foundation 1960 Kenny Rd. Columbus, Ohio 43210			8. PERFORMING ORGANIZATION REPORT NUMBER RF 767440/722045	
9. SPONSORING/MONITORING AGENCY NAME(S) AND ADDRESS(ES) U. S. Army Research Office P. O. Box 12211 Research Triangle Park, NC 27709-2211			10. SPONSORING/MONITORING AGENCY REPORT NUMBER <i>ARO 26595.7-EG</i>	
11. SUPPLEMENTARY NOTES The view, opinions and/or findings contained in this report are those of the author(s) and should not be construed as an official Department of the Army position, policy, or decision, unless so designated by other documentation.				
12a. DISTRIBUTION/AVAILABILITY STATEMENT Approved for public release; distribution unlimited.			12b. DISTRIBUTION CODE	
13. ABSTRACT (Maximum 200 words) The flow field generated by a helicopter in flight is extremely complex and it has been recognized that interactions between different components can significantly affect helicopter performance. In particular, the effects of the interaction between the rotor wake and the helicopter fuselage are extremely difficult to predict and pose a challenging problem for researchers and designers in the rotorcraft area. In the present work, a model for the interaction of a rotor-tip-vortex with the airframe of a helicopter is developed. The present report describes the calculation of the motion of the tip-vortex toward the airframe, the calculation of the induced pressure on the airframe, and the calculation of the boundary-layer flow under the vortex during the time period prior to the time when a portion of the tip-vortex collides with the airframe.				
14. SUBJECT TERMS			15. NUMBER OF PAGES 310	
			16. PRICE CODE	
17. SECURITY CLASSIFICATION OF REPORT UNCLASSIFIED	18. SECURITY CLASSIFICATION UNCLASSIFIED	19. SECURITY CLASSIFICATION OF ABSTRACT UNCLASSIFIED	20. LIMITATION OF ABSTRACT UL	



Boundary Layers Induced by Three-Dimensional Vortex Loops

A. T. Conlisk, H. Affes, O. R. Burggraf, and Z. Xiao
Department of Mechanical Engineering

U.S. Army Research Office
Research Triangle Park, North Carolina 27709-2211

Contract No. DAAL03-89-K-0095
Final Report
RF Project No. 767440/722045

December 1993

Approved for public release; distribution unlimited.

DTIC QUALITY INSPECTED 8

Accession For	
NTIS	CRA&I <input checked="" type="checkbox"/>
DTIC	IAS <input type="checkbox"/>
Unannounced	<input type="checkbox"/>
Justification	
By	
Distribution /	
Availability Codes	
Dist	Avail and/or Special
A-1	

The views, opinions, and/or findings contained in this report are those of the author(s) and should not be construed as an official Department of the Army position, policy, or decision, unless so designated by other documentation.

Acknowledgments

The authors wish to express their appreciation to the contract monitor Dr. Thomas L. Doligalski for his support and guidance during the course of the research. The authors appreciate the support of The Ohio Supercomputer Center through a grant of computer time to perform the intensive calculations in this work. Professor Narayanan Komerath of the Georgia Institute of Technology provided the experimental data with which some of the numerical results have been compared. Frequent discussions with Professor Komerath and his students have been extremely valuable during the course of this work. The material presented in Chapters 7 and 8 is largely the work of Zhenhua Xiao and Professor O. R. Burggraf. The authors appreciate the assistance of Julian Soell in preparing some of the three-dimensional streamline patterns.

Table of Contents

ACKNOWLEDGMENTS	iii
LIST OF FIGURES	xvii
LIST OF TABLES	xviii
 CHAPTER	 PAGE
I Introduction	1
1.1 Background	1
1.2 Description of the Problem	2
1.3 Review of Generalized Theories to Model the Rotor Wake	3
1.4 Rotor Wake-Airframe Interaction	12
1.5 Boundary-Layers Induced by a Moving Vortex Filament	14
1.6 Unsteady Boundary Layer Separation	15
1.7 Outline of the Present Work	17
 II Motion of a Vortex Filament Above a Cylinder	 21
2.1 Introduction	21
2.2 A Procedure to Compute the Vortex Image System . . .	22
2.3 Vortex Core Flow	25
2.4 The Self-Induced Motion of the Vortex Filament	27
2.5 The Image-Induced Velocity Field on the Vortex	29
2.6 Filament Motion	31
2.7 The Pressure Field	31
2.8 Numerical Methods	34
2.9 Results	36
2.10 Vortex Structure	59
2.11 Summary	64
 III Comparison with Experiments	 65
3.1 Introduction	65
3.2 Experimental Methods used by Komerath et al.	69
3.3 Modelling of the Experiments	70

3.4	Experimental Conditions	75
3.5	Results	77
3.6	Summary	84
IV The Impulsively Started Two-Dimensional Boundary-Layer Flow Past a Circular Cylinder		90
4.1	Introduction	90
4.2	The Inviscid Flow	91
4.3	Boundary-Layer Formulation	93
4.4	Numerical Methods	96
4.5	Results and Discussion	99
4.6	Summary	107
V The Boundary Layer Induced by a Vortex Impinging on an Air- frame		113
5.1	Introduction	113
5.2	The Inviscid Flow	114
5.3	Boundary Layer Formulation	129
5.4	Numerical Methods	142
5.5	Results	150
5.6	Discussion	214
VI The Vortex-Body Collision Problem		218
6.1	Introduction	218
6.2	Phase 2.1: Initial Deformation of the Vortex Core . . .	219
6.3	Phase 2.2: Vortex Core Jet Development	224
6.4	Phase 2.3: Final Merger With the Boundary Layer . . .	226
6.5	Phase 3: Convection of the Vortex Along the Airframe .	227
6.6	Summary	227
VII A Model for the Deformation of the Vortex Core		228
7.1	Introduction	228
7.2	The Two Dimensional Point-Vortex Model	228
7.3	The Three Dimensional Multiple Vortex Model	234
7.4	Summary	246
VIII The Three-Dimensional Interacting Boundary Layer		253
8.1	Introduction	253
8.2	Numerical Methods	256
8.3	Inviscid Flow Solution	257
8.4	Viscous-Inviscid Flow Interaction	257

8.5	Numerical Results and Discussion	259
8.6	Summary	264
IX	Summary and Conclusions	268
9.1	Summary	268
9.2	Future Work	273
APPENDICES		PAGE
A	The Calculation of the Self-Induced Velocity Field	275
A.1	Evaluation of $\int \vec{Q}_{V\infty} ds'$	275
A.2	Evaluation of the integral $\int_{-l}^l P ds'$	276
A.3	Approximation of \vec{R}_V	277
A.4	Evaluation of the integral \vec{I}_V	277
B	Evaluation of the integrals H and G	279
C	Calculation of the Pressure Gradients on the Cylinder	281
D	Papers and Presentations and Degrees Awarded	282
BIBLIOGRAPHY		284

List of Figures

1.1	Geometry of the present work and the coordinate systems employed. An expanded view of the expected vortex induced boundary-layer flow which is characterized by the appearance of a secondary eddy is also shown. The initial vortex configuration is arbitrary.	4
1.2	Rotor wake in hover as described by Seddon (1990) using momentum theory.	6
1.3	Rotor wake in hover as described by Gray (1956).	10
2.1	Filament positions for the case of no mean flow. (a) End view, (b) top view, (c) side view. The positions are plotted every 10 time steps starting from $t = 0$. Here $\Delta t = 0.01$ and the vortex core radius $a_v = 0.1$. Arrow denotes increasing time.	38
2.2	Results for the axial pressure gradient and pressure at $\theta = \pi/2$ for the parameters of Figure 2.1. (a) Pressure gradient, (b) pressure. Here results are plotted every ten time steps ($\Delta t = 0.01$) up to $t = 0.9$ including the results at $t = 0.96$. The circles denote the positions of the vortex center.	40
2.3	Results for surface pressure for the parameters of Figure 2.1. Pressure contours are plotted at different levels given on the side of the figure. Here results are plotted at time $t = 0.95$	41
2.4	Filament positions for the mean flow case where $\alpha = 1.0$, $\beta = 3.0$. (a) End view, (b) top view, (c) side view. Here $\Delta t = 0.01$ and the vortex core radius $a_v = 0.1$. Arrow denotes increasing time. Here positions are plotted every 5 time steps ($\Delta t = 0.01$) up to $t = 0.4$	43
2.5	Filament positions for the mean flow case where $\alpha = 2.0$, $\beta = 3.0$. (a) End view, (b) top view, (c) side view. Here $\Delta t = 0.01$ and the vortex core radius $a_v = 0.1$. Arrow denotes increasing time. Here positions are plotted every 5 time steps ($\Delta t = 0.01$) up to $t = 0.4$	45
2.6	Filament positions for the mean flow case where $\alpha = 2.0$, $\beta = 3.0$. (a) End view, (b) top view, (c) side view. Here $\Delta t = 0.01$ and the vortex core radius $a_v = 0.05$. Arrow denotes increasing time. Here positions are plotted every 5 time steps ($\Delta t = 0.01$) up to $t = 0.4$	47

2.7	Filament positions for the case of Bi and Leishman where $\alpha = 1.72$, $\beta = 2.4$. (a) End view, (b) top view, (c) side view. Here $\text{sgn}(\Gamma) = -1$, $\Delta t = 0.01$ and the vortex core radius $a_v = 0.1$. Arrow denotes increasing time. Here positions are plotted every 5 time steps ($\Delta t = 0.01$) up to $t = 0.45$	49
2.8	Results for the axial pressure gradient and pressure at $\theta = \pi/2$ for the parameters of Figure 2.4 where $\alpha = 1$ and $\beta = 3$. (a) Pressure gradient, (b) pressure. Here results are plotted every 5 time steps ($\Delta t = 0.01$) starting from $t = 0.05$ and ending at $t = 0.4$. The circles denote the positions of the vortex center.	52
2.9	Results for surface pressure for the parameters of Figure 2.4 where $\alpha = 1$ and $\beta = 3$. Pressure contours are plotted at different levels given on the side of the figure. Here results are plotted at time $t = 0.4$	53
2.10	Results for the axial pressure gradient and pressure at $\theta = \pi/2$ for the parameters of Figure 2.5 where $\alpha = 2$ and $\beta = 3$. (a) Pressure gradient, (b) pressure. Here results are plotted every 5 time steps ($\Delta t = 0.01$) starting from $t = 0.05$ and ending at $t = 0.4$. The circles denote the positions of the vortex center.	54
2.11	Results for surface pressure for the parameters of Figure 2.5 where $\alpha = 2$ and $\beta = 3$. Pressure contours are plotted at different levels given on the side of the figure. Here results are plotted at time $t = 0.4$	55
2.12	Results for the axial pressure gradient and pressure at $\theta = \pi/2$ for the parameters of Figure 2.6 where $\alpha = 2$, $\beta = 3$ and $a_v = 0.05$. (a) Pressure gradient, (b) pressure. Here results are plotted every 5 time steps ($\Delta t = 0.01$) starting from $t = 0.05$ with the exception that the last time step corresponds to $t = 0.37$ instead of $t = 0.4$. The circles denote the positions of the vortex center.	56
2.13	Results for the axial pressure gradient and pressure at $\theta = \pi/2$ for the parameters of Figure 2.7 where $\alpha = 1.72$ and $\beta = 2.4$. (a) Pressure gradient, (b) pressure. Here results are plotted every 5 time steps ($\Delta t = 0.01$) starting from $t = 0.05$ and ending at $t = 0.45$. The circles denote the positions of the vortex center.	57
2.14	Results for surface pressure for the parameters of Figure 2.7 where $\alpha = 1.72$ and $\beta = 2.4$. Pressure contours are plotted at different levels given on the side of the figure. Here results are plotted at time $t = 0.45$	58

2.15	Azimuthal and radial velocity relative to the vortex core at the assumed vortex core radius $\bar{r} = a_v$ around the vortex as a function of local polar angle. The curves are plotted at $t=0$ (straight line) and at latter times, $t=.35, .36, .37, .38, .39$ and $.4$. These results are for $s = 0$. Here $\alpha = 2$, $\beta = 3$ and $a_v = .1$	60
2.16	(a) Flattening of the vortex core as it approaches the cylinder (Komerath 1992). The vortex core is denoted by the dark region at the end of the arrow. (b) A close-up view of the vortex core.	61
2.17	Stretching of the vortex as illustrated by the plots of (a) the arc length τ v.s. s , (b) the tangential velocity U_τ v.s. s , (c) $\frac{\partial U_\tau}{\partial s}$ v.s. s . The results correspond to the mean flow case where $\alpha=2$ and $\beta=3$, and they are shown at various times $t=0, .1, .2, .3$ and $.4$	63
3.1	(a) The wake of a single-bladed rotor in low-speed forward flight. (b) Experimental configuration and coordinate system.	66
3.2	Three-dimensional perspective view of the experimental unsteady pressure variation along the airframe surface (Komerath 1992). The advance ratio is $\mu = .1$. Note the blade passage effect near $\psi = 0^\circ, 180^\circ, 360^\circ$. The regime of interest in the present modeling effort is indicated by the additional tick marks.	68
3.3	Sketch of the mean flow viewed from upstream and top of the cylinder. Note the linear profiles of the downwash $v(x)$ and the the axial flow $w(x)$	72
3.4	The vortex trajectory for advance ratio $\mu = .1$. (a) Upstream end view; (b) top view. The circles denote the experimental results (not to scale for the vortex core); the times shown are for $\psi = 0$ (the initial condition), $\psi = 30^\circ$, and $\psi = 60^\circ$. The error bar in the experiments is also shown. The arrows indicate the sense of vortex circulation ($\Gamma > 0$).	78
3.5	Pressure gradient $\frac{\partial p}{\partial x}$ for $\mu = .1$ along the top of the airframe for several values of $\psi = 18^\circ, 24^\circ, 30^\circ, 36^\circ, 42^\circ, 48^\circ$ and 54° . The amplitude of the pressure gradient spike increases as ψ increases. The open circles are side views of the computed vortex center ($s = 0$) position.	79
3.6	Pressure distribution along the top of the airframe for several values of ψ for $\mu = .1$. The circle is the side view of the computed vortex center ($s = 0$) position. (a) $\psi = 18^\circ$, (b) $\psi = 24^\circ$, (c) $\psi = 30^\circ$, (d) $\psi = 36^\circ$, (e) $\psi = 42^\circ$, (f) $\psi = 48^\circ$, (g) $\psi = 54^\circ$	80
3.7	Pressure gradient $\frac{\partial p}{\partial z}$ for $\mu = .075$ along the top of the airframe for several values of $\psi = 18^\circ, 24^\circ, 30^\circ, 36^\circ$ and 42° . The amplitude of the pressure gradient spike increases as ψ increases. The open circles are side views of the computed vortex center ($s = 0$) position.	85

3.8	Pressure distribution along the top of the airframe for several values of ψ for $\mu = .075$. The circle is the side view of the computed vortex center ($s = 0$) position. (a) $\psi = 18^\circ$, (b) $\psi = 24^\circ$, (c) $\psi = 30^\circ$, (d) $\psi = 36^\circ$, and (e) $\psi = 42^\circ$	86
4.1	Geometry and coordinate system employed for the two-dimensional impulsively-started cylinder.	92
4.2	Temporal development of the displacement thickness. (a) From van Dommelen (1981) using the Lagrangian method, (b) from Xiao et al. (1990) using a non-iterative method with upwind differencing. Note that the time scale in (b) is half of that in (a).	103
4.3	Temporal development of wall shear. (a) From van Dommelen (1981) using the Lagrangian method, (b) from Xiao et al. (1990) using a non-iterative method with upwind differencing. Note that the time scale in (b) is half of that in (a).	104
4.4	Temporal development of the displacement thickness computed in the present work.	105
4.5	Temporal development of the wall shear computed in the present work.	106
4.6	Instantaneous streamline patterns for the boundary-layer flow past an impulsively started circular cylinder. The results are shown for the times (a) $t=0.2$, (b) $t=0.4$, (c) $t=0.6$, (d) $t=0.8$, (e) $t=1.0$, (f) $t=1.2$, (g) $t=1.4$, (h) $t=1.45$. The boundary-layer and the recirculating regions are greatly expanded in the normal direction, and not to scale.	108
5.1	Filament positions for the case of no mean flow. (a) End view, (b) top view and (c) side view. The results shown here are slightly different from those shown on Figure 2.1 in that a different initial configuration of the vortex ($x_s=s$, $y_s=1.3$ and $z_s=0$) and a different time scale are employed. Here $\Delta t=0.05$ and the vortex core radius $a_v=0.11$. The filament positions are plotted every 10 time steps starting from $t=0$. The arrow denotes the direction of increasing time; the last time step corresponds to $t=3.0$	117
5.2	Temporal development of the inviscid flow field and the pressure at the top of the cylinder ($r=1$ and $\theta = \pi/2$). (a) The velocity component U_z , (b) the pressure and (c) the pressure gradient $\frac{\partial p}{\partial z}$. Here, the results are for the stagnant medium case and they are plotted at times $t=0.1, 0.2, 0.3, \dots, 0.8$	119
5.3	Lines of constant azimuthal inviscid velocity U_θ computed around the cylinder at the surface. Here the results are for the stagnant medium case and are plotted at time $t=0.6$	121

5.4	Lines of constant axial inviscid velocity U_z computed around the cylinder at the surface. Here the results are for the stagnant medium case and are plotted at time $t=0.6$	122
5.5	Lines of constant pressure p computed around the cylinder at the surface. Here the results are for the stagnant medium case and are plotted at time $t=0.6$	123
5.6	Lines of constant pressure gradient $\frac{\partial p}{\partial \theta}$ computed around the cylinder at the surface. Here the results are for the stagnant medium case and are plotted at time $t=0.6$	124
5.7	Lines of constant pressure gradient $\frac{\partial p}{\partial z}$ computed around the cylinder at the surface. Here the results are for the stagnant medium case and are plotted at time $t=0.6$	125
5.8	Filament positions for the symmetric mean flow case. (a) End view, (b) top view and (c) side view. The initial configuration of the vortex corresponds to $x_s=s$, $y_s=1.5$ and $z_s=0$. Here $\Delta t=0.01$ and the vortex core radius $a_v=0.11$. The filament positions are plotted every 10 time steps starting from $t=0$. The arrow denotes the direction of increasing time; the last time step corresponds to $t=0.6$	126
5.9	Temporal development of the inviscid flow field and the pressure at the top of the cylinder ($r=1$ and $\theta = \pi/2$). (a) The velocity component U_z , (b) the pressure and (c) the pressure gradient $\frac{\partial p}{\partial z}$. Here, the results are for the symmetric mean flow case and are plotted at times $t=0.05, 0.1, 0.15, \dots, 0.4$	128
5.10	Lines of constant azimuthal inviscid velocity U_θ computed around the cylinder at the surface. Here the results are for the symmetric mean flow case and are plotted at time $t=0.3$	130
5.11	Lines of constant axial inviscid velocity U_z computed around the cylinder at the surface. Here the results are for the symmetric mean flow case and are plotted at time $t=0.3$	131
5.12	Lines of constant pressure p computed around the cylinder at the surface. Here the results are for the symmetric mean flow case and are plotted at time $t=0.3$	132
5.13	Lines of constant pressure gradient $\frac{\partial p}{\partial \theta}$ computed around the cylinder at the surface. Here the results are for the symmetric mean flow case and are plotted at time $t=0.3$	133
5.14	Lines of constant pressure gradient $\frac{\partial p}{\partial z}$ computed around the cylinder at the surface. Here the results are for the symmetric mean flow case and are plotted at time $t=0.3$	134

5.15	Lines of constant azimuthal inviscid velocity U_θ computed around the cylinder at the surface. Here the results are for the asymmetric mean flow case and are plotted at time $t=0.3554$ ($\psi = 30^\circ$). Here $z=Z - Z_{V_c}(t=0)$	135
5.16	Lines of constant axial inviscid velocity U_z computed around the cylinder at the surface. Here the results are for the asymmetric mean flow case and are plotted at time $t=0.3554$ ($\psi = 30^\circ$).	136
5.17	Lines of constant pressure gradient $\partial p/\partial z$ computed around the cylinder at the surface. Here the results are for the asymmetric mean flow case and are plotted at time $t=0.3554$ ($\psi = 30^\circ$).	137
5.18	Streamline patterns for the stagnant medium at $\theta=\pi/2$ plotted at various times. In the symmetry plane at (a) $t=0.3$, (o) $t=0.6$, (c) $t=0.8$; and a fully three-dimensional view at (d) $t=0.3$, (e) $t=0.6$, (f) $t=0.8$	152
5.19	Lines of constant total azimuthal vorticity ω_θ at $t=0.6$ for several azimuthal locations around the cylinder: (a) $\theta=\pi/2$, (b) $\theta=3\pi/8$, (c) $\theta=\pi/4$, (d) $\theta=0$, (e) $\theta=-\pi/4$, (f) $\theta=-\pi/2$. The results are for the stagnant medium case where the boundary-layer flow is symmetric about $\theta = \pi/2$. The line of $\omega_\theta=0$ is marked by an arrow.	155
5.20	Temporal development of the azimuthal vorticity ω_θ in the symmetry plane $\theta = \pi/2$. Here the results are for the stagnant medium case and they are shown as lines of constant ω_θ which are plotted at various times: (a) $t=0.2$, (b) $t=0.4$, (c) $t=0.5$, (d) $t=0.6$, (e) $t=0.7$, (f) $t=0.8$. The line of $\omega_\theta=0$ is marked by an arrow.	157
5.21	The effect of the grid size Δz on the computed azimuthal vorticity component which is plotted as contour lines in the symmetry plane $\theta = \pi/2$. Here the results are for the stagnant medium case and are plotted at time $t=0.8$ for 3 grid sizes: (a) $\Delta z=0.025$, (b) $\Delta z=0.0125$, (c) $\Delta z=0.00625$	160
5.22	Temporal development of the radial velocity at the edge of the boundary-layer evaluated in the symmetry plane $\theta = \pi/2$. Here the results are for the stagnant medium case and they are plotted at several times $t=0.1, 0.2, 0.3, \dots, 0.8$	162
5.23	Lines of constant radial velocity u_r at the edge of the boundary-layer plotted around the cylinder for various times. (a) $t = 0.2$, (b) $t = 0.4$, (c) $t = 0.6$, (d) $t = 0.8$. Here the results are for the stagnant medium case where the flow is symmetric about $\theta=\pi/2$ (or 90°). The values of u_r are shown.	163

5.24	Surface streamlines for the stagnant medium at various times showing the development of a nodal point of attachment(N) and a saddle point of separation(S). (a) $t = 0.3$, (b) $t = 0.6$, (c) $t = 0.8$. (d) expanded view of the surface streamline labelled L.	167
5.25	Lines of constant azimuthal vorticity ω_θ evaluated at the wall of the cylinder and plotted around the cylinder for the time $t=0.6$. Here the results are for the stagnant flow case where the flow is symmetric about $\theta=\pi/2$ (or 90°). The values of ω_θ are shown.	168
5.26	Temporal development of the velocity profiles of u_z plotted across the boundary-layer for the stagnant medium ($0 \leq \eta \leq 6$) at various times: (a) $t=0.2$, (b) $t=0.3$, (c) $t=0.4$, (d) $t=0.5$, (e) $t=0.6$. The profiles are shown at 9 equally spaced locations which are centered around $z = Z - Z_{Vc} = -0.25$ and separated by $\Delta z = 0.025$	169
5.27	Contours of constant enstrophy which are shown by: (a) $\eta=0$, (b) $\eta=.268$, (c) surface of the constant value equal to .27. Here the results are for the stagnant medium case and are plotted at $t=.7$	171
5.28	Streamline patterns for the symmetric mean flow plotted at various times. On the symmetry plane at (a) $t=0.1$, (b) $t=0.2$, (c) $t=0.3$, (d) $t=0.4$; and a fully three-dimensional view at (e) $t=0.1$, (f) $t=0.2$, (g) $t=0.3$, (h) $t=0.4$	173
5.29	Vector plots of the velocity field at various locations in $Z - Z_{Vc}$ at $t = 0.4$ across the boundary layer. The upper edge on the Figure is at $\eta = 2$; the edge of the boundary layer is at $\eta = 6$. (a) $Z - Z_{Vc} = -0.3$, $Z - Z_{Vc} = -0.125$, (c) $Z - Z_{Vc} = 0$	176
5.30	Lines of constant azimuthal vorticity ω_θ at $t=0.3$ for several azimuthal locations around the cylinder: (a) $\theta=\pi/2$, (b) $\theta=3\pi/8$, (c) $\theta=\pi/4$, (d) $\theta=0$, (e) $\theta=-\pi/4$, (f) $\theta=-\pi/2$. The zero lines are marked by an arrow.	177
5.31	Temporal development of the azimuthal vorticity ω_θ in the symmetry plane $\theta = \pi/2$. Here the results are for the symmetric mean flow case and they are shown as lines of constant azimuthal vorticity which are plotted at various times: (a) $t=0.1$, (b) $t=0.3$, (c) $t=0.4$. The zero lines are marked by an arrow.	179
5.32	Evolution of the zero azimuthal vorticity line in the symmetry plane $\theta = \pi/2$. Here the results correspond exactly to the those shown in previous figure except for the fact that negative vorticity lines are not plotted. The zero lines are marked by an arrow and are shown for times (a) $t=0.1$, (b) $t=0.3$, (c) $t=0.4$	180

5.33	Lines of constant velocity u_x plotted across the boundary-layer in the symmetry plane $\theta = \pi/2$. Here the results are for the symmetric mean flow case and are shown at various times: (a) $t=0.1$, (b) $t=0.3$, (c) $t=0.4$. The zero velocity line is marked by an arrow.	181
5.34	Temporal development of the radial velocity at the edge of the boundary-layer evaluated in the symmetry plane $\theta = \pi/2$. Here the results are for the symmetric mean flow case and they are plotted at several times $t=0.05, 0.1, 0.15, \dots, 0.4$	182
5.35	Lines of constant radial velocity u_r at the edge of the boundary-layer for the symmetric mean flow case plotted around the cylinder for various times. (a) $t = 0.1$, (b) $t = 0.2$, (c) $t = 0.3$, (d) $t = 0.4$. The values of u_r are shown.	184
5.36	Surface streamlines for the symmetric mean flow at various times showing the development of a saddle point of attachment(S) and a nodal point of separation(N). (a) $t = 0.1$, (b) $t = 0.2$, (c) $t = 0.3$, (d) $t = 0.4$	188
5.37	Lines of constant azimuthal vorticity ω_θ evaluated at the wall of the cylinder and plotted around the cylinder for various times. (a) $t = 0.1$, (b) $t = 0.2$, (c) $t = 0.3$, (d) $t = 0.4$. Here the results are for the symmetric mean flow case where the flow is symmetric about $\theta=\pi/2$ (or 90°). The values of ω_θ are shown.	190
5.38	Lines of constant axial vorticity ω_z evaluated at the wall of the cylinder and plotted around the cylinder for various times. (a) $t = 0.1$, (b) $t = 0.2$, (c) $t = 0.3$, (d) $t = 0.4$. Here the results are for the symmetric mean flow case where the flow is symmetric about $\theta=\pi/2$ (or 90°). The values of ω_z are shown.	194
5.39	Lines of constant axial vorticity ω_z plotted across the boundary-layer around the cylinder in the z plane $z = -0.2$. Here the results are for the symmetric mean flow case and are shown at various times: (a) $t=0.1$, (b) $t=0.3$, (c) $t=0.4$. The zero axial vorticity line is marked by an arrow.	198
5.40	Lines of constant axial vorticity ω_z plotted across the boundary-layer around the cylinder at a fixed time $t=0.35$. Here the results are for the symmetric mean flow case and are shown at various z locations: (a) $z=-0.4$, (b) $z=-0.1$, (c) $z= 0.3$. The zero axial vorticity line is marked by an arrow.	199

5.41	Temporal development of the velocity profiles of u_z plotted across the boundary-layer ($0 \leq \eta \leq 6$) at various times: (a) $t=0.1$, (b) $t=0.15$, (c) $t=0.2$, (d) $t=0.25$, (e) $t=0.3$. The profiles are shown at 9 equally spaced locations which are centered around $z = Z - Z_{Vc} = 0.375$ and separated by $\Delta z = 0.025$. The results are for the symmetric mean flow case.	200
5.42	Contours of constant enstrophy plotted in the planes (a) $\eta=0$, (b) $\eta=.268$ and (c) along the surface of the constant value equal to 1.47. Here the results are for the symmetric mean flow case at $t=.3$. . .	201
5.43	Three dimensional streamline patterns for several times in a frame of reference moving with a point on the vortex. (a) $t = .2843(\psi = 24^\circ)$; (b) $t = .3554(\psi = 30^\circ)$; (c) $t = .3953(\psi = 33.3^\circ)$; (d) another view at $t = .3953$ indicating azimuthal extent of the secondary eddy. . . .	204
5.44	Three dimensional streamline patterns at $\psi = 30^\circ$ in the fixed frame of reference with origin in z directly under the vortex at time $\psi = 0$.	205
5.45	Azimuthal component of vorticity at time $t = .3554$ at several locations around the cylinder. (a) $\theta = 90^\circ$; (b) $\theta = 101.25^\circ$; (c) $\theta = 112.5^\circ$.	207
5.46	Three-dimensional plot of the radial velocity around the cylinder at $\psi = 30^\circ$. Note the large spike around where the tip vortex will eventually impact the airframe.	208
5.47	(a) Vortex cross-section image at $\psi = 72^\circ$ in the plane 30° from the vertical on the retreating side of the rotor($\theta = 120^\circ$). (b) In the vertical plane of symmetry.	210
5.48	Pressure distribution along the airframe under the tip vortex on the wall at rotor phase angle $\psi = 72^\circ$. (a) In the plane 30° from the vertical; (b) on the top of the airframe. The second spike is believed to be due to the development of the reversed flow eddy in the boundary layer.	211
5.49	Temporal development of the velocity profiles of u_z plotted across the boundary-layer $0 \leq \eta \leq 6$ at various times: (a) $t=0.0711$ ($\psi = 6^\circ$), (b) $t=0.1421$ ($\psi = 12^\circ$), (c) $t=0.2133$ ($\psi = 18^\circ$), (d) $t=0.2843$ ($\psi = 24^\circ$), (e) $t=0.3554$ ($\psi = 30^\circ$). The profiles are shows at 9 equally spaced locations which are centered around $z=0.75$ and separated by $\Delta z=0.025$. The results are for the asymmetric mean flow case.	213
5.50	Different stages of the interaction of the tip-vortex with the airframe as observed experimentally by Liou, Komerath and McMahon (1990). The coordinate system on this figure is in the notation of the LKM paper.	215
5.51	End view of necklace vortex legs and induced surface eruptions (from Smith et al. 1991).	217

6.1	The local coordinate system around the vortex which is used in the present chapter. (a) View of the vortex core boundary; this is from a side view of the airframe. (b) End view showing airframe.	221
6.2	The physical picture of a three-dimensional erupting boundary layer flow under a rotor tip vortex during Phase 2.1. (a) Side view of the vortex and fluid erupting from the boundary layer. (b) Perspective view showing approximate spanwise extent of secondary separation.	225
7.1	Two-dimensional point vortex model for the vortex core deformation.	230
7.2	Pressure on the wall for the indicated times. (a) four vortices; (b) single vortex.	232
7.3	The position of four point vortices at several times.	233
7.4	Three-dimensional oblique view of a typical set of cylinder panels and vortex segments for each being of constant size.	236
7.5	A single source panel and local panel coordinates.	237
7.6	Vortex line segment AB and field point C.	239
7.7	Three dimensional view of the four-vortex bundle showing local nature of the core deformation at two different times. The results are computed with a variable panel geometry even though a constant panel grid is shown. (a) $t = 0.0$, (b) $t = 0.6$	242
7.8	Top view of the position of the four-vortex bundle at $t = 0.5$ showing the variable panel distribution.	243
7.9	View of the four-vortex bundle motion on the symmetry plane for three times. (a) $t = 0.0$, (b) $t = 0.25$. (c) $t = 0.5$	244
7.10	View of the four-vortex bundle motion on the symmetry plane at three different times showing the rotation of the vortices about themselves. (a) $t = 0.50$, (b) $t = 0.52$, (c) $t = 0.54$	245
7.11	View of the nine-vortex bundle motion on the symmetry plane for three times. (a) $t = 0.0$, (b) $t = 0.25$. (c) $t = 0.5$	247
7.12	View of the nine-vortex bundle motion on the symmetry plane at three different times showing the rotation of the vortices about themselves. (a) $t = 0.50$, (b) $t = 0.52$, (c) $t = 0.54$	248
7.13	Pressure gradient on the top of the cylinder for the four-vortex bundle. (a) Vortex bundle; (b) single vortex.	249
7.14	Pressure on the top of the cylinder for the four-vortex bundle. (a) Vortex bundle; (b) single vortex.	250
7.15	Pressure gradient on the top of the cylinder for the nine-vortex bundle. (a) Vortex bundle; (b) single vortex.	251
7.16	Pressure on the top of the cylinder for the nine-vortex bundle. (a) Vortex bundle; (b) single vortex.	252

8.1	Pressure gradient and streamlines for the two-dimensional boundary layer induced by a vortex. ξ is the streamwise variable and the results are for $t = 0.88$	255
8.2	Streamwise pressure gradient on the symmetry plane for $Re = 10^6$; (a) $t = 0.4$, (b) $t = 0.5$, (c) $t = 0.6$, (d) $t = 0.7$	260
8.3	Three dimensional streamline patterns for $Re = 10^6$; (a) $t = 0.4$, (b) $t = 0.5$, (c) $t = 0.6$, (d) $t = 0.7$	261
8.4	Pressure on the symmetry plane for $Re = 10^6$; (a) $t = 0.4$, (b) $t = 0.5$, (c) $t = 0.6$, (d) $t = 0.7$	262
8.5	Axial shear stress τ_{rz} on the symmetry plane for $Re = 10^6$; (a) $t = 0.4$, (b) $t = 0.5$, (c) $t = 0.6$, (d) $t = 0.7$	263
8.6	Surface streamlines for $Re = 10^6$; (a) $t=0.1$, (b) $t=0.3$, (c) $t=0.5$, (d) $t=0.7$	265
8.7	Edge velocity on the symmetry plane for $Re = 10^6$ at several times. (a) $t = 0.4$, (b) $t = 0.5$, (c) $t = 0.6$, (d) $t = 0.7$	266

List of Tables

4.1	Effect of $\Delta\eta$ on the azimuthal velocity at $t=1.4$	100
4.2	Effect of $\Delta\theta$ on the azimuthal velocity at $t=1.4$	101
4.3	Effect of Δt on the azimuthal velocity $t=1.4$	102
5.1	Effect of $\Delta\xi$ on the axial velocity u_z at $t=0.6$	146
5.2	Effect of $\Delta\theta$ on the axial velocity u_z at $t=0.6$	147
5.3	Effect of Δz on the axial velocity u_z at $t=0.6$	148
5.4	Effect of Δt on the axial velocity u_z at $t=0.6$	149

Summary

The flow field generated by a helicopter in flight is extremely complex and it has been recognized that interactions between different components can significantly affect helicopter performance. In particular, the effects of the interaction between the rotor wake and the helicopter fuselage are extremely difficult to predict and pose a challenging problem for researchers and designers in the rotorcraft area. In the present work, a model for the interaction of a rotor-tip-vortex with the airframe of a helicopter is developed. The present report describes the calculation of the motion of the tip-vortex toward the airframe, the calculation of the induced pressure on the airframe, and the calculation of the boundary-layer flow under the vortex during the time period prior to the time when a portion of the tip-vortex collides with the airframe.

First, a simplified model for the interaction of a rotor tip-vortex with a fuselage or airframe is developed using three-dimensional potential flow analysis. The tip-vortex is idealized as a single three-dimensional vortex filament and the fuselage is modeled by an infinitely long circular cylinder. The Biot-Savart law is employed to describe the flow induced by the vortex and the flow is assumed to be inviscid and irrotational outside the core of the vortex. The present analytical/numerical results for both the vortex trajectory and the pressure distribution on the airframe are in substantial agreement with experimental results prior to impact of the vortex with the airframe. The numerical calculations indicate that a large adverse pressure gradient develops under the vortex on the fuselage causing a rapid drop in the pressure there.

Next the problem of the unsteady classical three-dimensional boundary-layer flow induced by the vortex filament moving above the fuselage is considered. Three

types of external flow in which the vortex is embedded are considered. These flows are respectively a stagnant medium, a symmetric mean flow and an asymmetric mean flow, the latter of which corresponds to the experimental conditions. In each case, the computed results show the development of a variety of complex three-dimensional boundary-layer separation phenomena. In all cases, the boundary-layer solutions show the formation of a secondary eddy which grows in time; this situation is expected to lead to an eruption of boundary-layer fluid into the free stream. The nature of this complicated secondary flow is elucidated by the analysis of three-dimensional streamline patterns.

In the calculations described above, the vortex core flow is assumed to be independent of time. This assumption is valid during the time period when the vortex is more than about one core radius from the airframe. However, experimental studies conducted at Georgia Institute of Technology indicate that just prior to impact, the vortex core flow seems to undergo significant change. After this initial collision, the end of the vortex and the boundary layer coincide. Based on these experimental results, a preliminary view of the entire collision process has been formulated and the calculations extended into the regime where the tip-vortex is modified locally by the presence of the airframe. The entire collision process is divided nominally into three phases: a pre-collision phase, the collision phase, and the post-collision phase. In the pre-collision phase the vortex core flow is unaffected by the presence of the airframe while in the collision phase, the vortex core is locally destroyed. The post-collision phase in the present scenario corresponds to the situation where the end of the vortex coincides with the boundary layer on the airframe.

Motivated by the picture of the collision process described above, a simple model for the initial stages of the deformation of the vortex core flow has been developed using a multiple vortex model. Finally, the three-dimensional interacting boundary layer problem has also been formulated and solved; this problem describes the initial response of the boundary layer flow to the vortex at finite

Reynolds numbers.

The major conclusions of this study may be identified as follows:

(1) The motion of the tip vortex and the pressure distribution on the top of the airframe may be adequately predicted using a three-dimensional potential flow analysis in the time regime when the vortex is nominally more than one core radius from the airframe. This time regime corresponds to Phase 1 identified earlier. During this period, the results are independent of the size of the vortex core and a large adverse axial pressure gradient develops. When compared with experimental data, this period extends to perhaps sometime just prior to $\psi = 54^\circ$.

(2) As the vortex approaches the airframe, the strong adverse pressure gradient induced by the vortex initiates a reversed flow leading to the development of a complicated three-dimensional secondary flow. The existence of the secondary flow is confirmed by experiments which indicate the presence of a high vorticity region subsequent to the time frame covered by the computations.

(3) Experiments show that just prior to impact of the vortex with the airframe, the vortex core begins to deform and initiate a pressure modulation (i.e. a decrease in the pressure spike amplitude). This effect has been modelled using several vortices to describe the tip-vortex. The computational results do show a modulation of the pressure suction peak seen in experiments although additional computations are required to delineate the influence of the number of vortices required to model the vortex core. Additional results to confirm the actual time of initiation of the vortex core deformation and computations for the parameters of the experiments are also required.

(4) Evidence exists to support the view that the secondary spike in the pressure distribution seen in experiments may be modelled by incorporating interaction between the inviscid and viscous flows near the airframe. Additional calculations

for the experimental flow conditions are required.

CHAPTER I

Introduction

1.1 Background

The flow field generated by a helicopter in flight is extremely complex consisting of a highly three-dimensional inboard vortex sheet as well as a high-strength tip-vortex. Moreover, it has been recognized that aerodynamic interactions between different components may adversely affect helicopter performance, dynamics, handling qualities, and noise. In recent years, the focus of rotorcraft research has been on developing a more complete understanding of the interactional aerodynamic phenomena observed on a helicopter. As indicated by Sheridan and Smith (1980), among the general characteristics of interactional aerodynamics (based on experience with Boeing Vertol UTTAS development program) are flow unsteadiness, flow redirection, flow field distortion, vortex surface impact and wake impingement. The term Interactional Aerodynamics (I/A) was introduced to describe the complex interaction mechanisms that occur when the helicopter is operating in different flight conditions. According to Sheridan and Smith (1980): "*Interactional Aerodynamics* is by definition the study of the various interrelated aerodynamic processes that result from elements being brought together in close proximity. I/A deals specifically with the underlying physical processes of the fluid mechanics and the associated body forces that arise from the combined flow fields and flow influences." A detailed classification of a variety of aerodynamic interactions between major components of the helicopter is also given by Sheridan and Smith (1980). The intensity of these interactions, however, depends on the relative proximity of individual components, their size, their shape and the type of wake produced. Flight conditions in which the helicopter operates may also complicate the interactional mechanisms.

Modern design requirements for the new generation Army helicopter often result in higher disc loading with smaller clearances between the main rotor and the fuselage. Therefore, it is desirable to understand the consequences of various

complex interaction mechanisms in order to meet the challenging new design specifications. The most important type of aerodynamic interaction is that between the rotor wake and the fuselage. In particular, it has been observed in experiments (Brand 1989) that the effects of the rotor tip-vortex interaction with the airframe are associated with an extremely unsteady high-amplitude, short-scale suction peak on the airframe. These effects are difficult to predict theoretically and pose a challenging problem to designers and researchers in the rotorcraft area. Much of the computational work dealing with the interaction of the rotor wake with the body of a helicopter focuses on either using large-scale computer codes which, in general, can only model the gross aspects of the flow (Lorber and Egolf 1988 and others) or using simple image systems inside simple geometries such as a plane wall or a sphere to represent the complex three-dimensional vortex (Mavris et al. 1989 and others). Although these methods have been successful in predicting the unsteady pressure distribution on the fuselage when the tip-vortex is far from the body, they show limited predictive capability when the wake vortex comes in close proximity to the body surface.

The purpose of the present work is to develop the capacity to better understand the unsteady effects resulting from the close interaction of a rotor-wake tip-vortex with an airframe. The main objectives of this work are to develop the capability to predict the unsteady airloads associated with the rotor tip-vortex and to investigate the character of the viscous flow generated on the airframe, both in the time frame prior to the actual collision of the tip-vortex with the airframe. However, during the course of this work a framework within which a comprehensive model of the vortex-airframe impingement including the collision and subsequent convection of the vortex down the sides of the airframe has been developed.

A description of the vortex/airframe interaction problem considered in this work is discussed next, followed by a review of the various methods and theories which have been employed to analyze the performance of isolated rotors as well as the interaction between the rotor wake and the airframe. Prior work on the viscous flow induced by a moving vortex is also reviewed; this aspect of the work leads naturally into the discussion of unsteady boundary-layer separation phenomena.

1.2 Description of the Problem

In the present work a simplified model for the interaction of a tip-vortex with an airframe is developed. The airframe is modeled as an infinite circular cylinder and the tip-vortex is idealized as an infinitely long single vortex filament of arbitrary shape. We use the term filament here to denote both an infinitesimally thin line of fluid having locally large values of vorticity and a vortex tube of finite thickness. The vortex-filament geometry depicted in Figure 1.1 is an idealization of the actual case where the tip-vortex is a continuous helical line of concentrated vorticity. The

radius of curvature of the helix is approximately constant and very nearly the radius of the rotor; if the fuselage or airframe radius is much smaller than the radius of the rotor, then as the filament approaches, it appears as a nearly straight filament oriented at approximately 90° to the generators of the cylinder. Thus the motion of a single vortex filament, of mild curvature above the cylinder should be an adequate model for the actual physical situation during the interaction period of interest.

The objectives of the present work are to predict the vortex trajectory above the cylindrical airframe, to predict the unsteady pressure distribution on the surface of the cylinder, and to calculate the unsteady boundary-layer flow induced by the vortex filament during the time period prior to collision of the vortex with the airframe. In particular, classical three-dimensional potential flow methods are employed to describe the motion of the vortex toward the airframe; a combination of finite difference and Fourier Transform techniques are employed to describe the initial development of the boundary layer on the airframe.

1.3 Review of Generalized Theories to Model the Rotor Wake

Momentum Theory

The most attractive feature of a helicopter is probably the distinguished ability to climb vertically and to hover. For both of these regimes of flight, the study of propellers provides useful concepts and theories which can be applied directly to rotorcraft. In the mid 19th century, theories were developed to meet the steady growth of the ship propeller industry. Rankine (1865) developed a simple model of a propeller flow field by applying linear momentum theory derived from the basic relationships of Newtonian mechanics. The actuator disc concept was then introduced by Froude (1878,1889) to provide a better model to simulate an open airscrew in an inviscid, incompressible medium. In this model the rotor may be conceived as having an infinite number of blades. Subsequently, this early theory was applied to rotorcraft.

During hover, which is the simplest helicopter flight regime, the rotor produces an upward thrust by pushing a column of air downwards through the rotor plane. By applying the laws of conservation of mass, momentum and energy to the overall process, a relationship between the thrust generated and the resulting velocity field is obtained. This approach which provides the simplest model of a rotor flow field is commonly referred to as the momentum theory for helicopters. It corresponds essentially to the theory developed by Glauert (1922) for aircraft propellers, based on earlier work by Rankine and Froude for marine propellers. In this approach, the

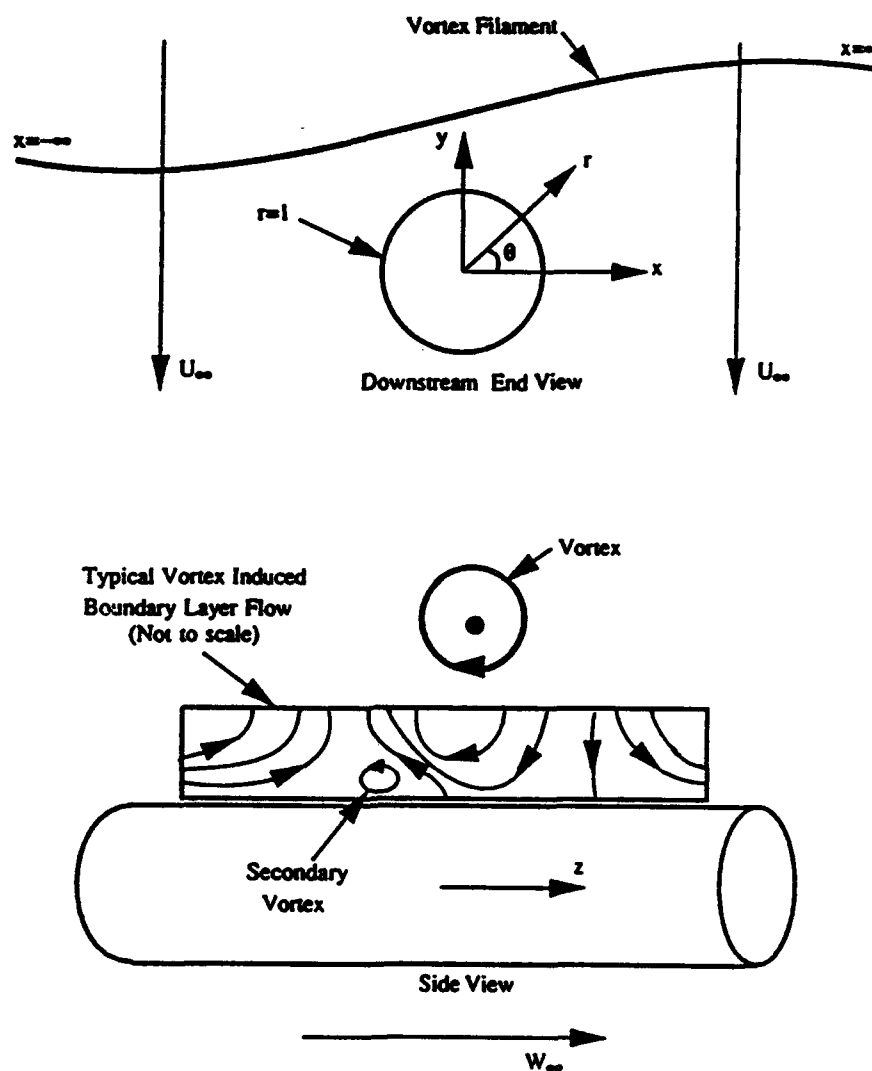


Figure 1.1: Geometry of the present work and the coordinate systems employed. An expanded view of the expected vortex induced boundary-layer flow which is characterized by the appearance of a secondary eddy is also shown. The initial vortex configuration is arbitrary.

rotor is viewed as an actuator disc, across which the fluid is energized by means of a static pressure jump equal to the disc loading which is defined as thrust per unit area. In hover, the rotor wake is regarded as a clearly defined streamtube consisting of a column of air passing across the rotor disc. Because no fluid is created by the actuator disc and the fluid is assumed incompressible, the mass flow rate through any cross-section of the tube is constant and equal to that through the disc itself. The situation as described by Seddon (1990) is depicted in Figure 1.2. As air is sucked into the disc from above, the static pressure falls from p_∞ to p_{inflow} which is the pressure just above the disc. Across the disc, the pressure suddenly increases to $p_{outflow}$ which is the pressure just below the disc. The increase in static pressure $\Delta p = p_{outflow} - p_{inflow}$ is gradually converted into kinetic energy as the static pressure approaches p_∞ in the far downstream part of the streamtube. The velocity in the streamtube increases from zero to a value v_i at the rotor-plane and continues to increase, as the static pressure falls, to a value v_∞ far downstream. Continuity of mass flow requires that the velocity must be continuous across the rotor disc. Since the flow is inviscid and incompressible, Bernoulli's equation can be applied above and below the disc. Above the disc, we have

$$p_\infty = p_{inflow} + \frac{1}{2}\rho v_i^2. \quad (1.1)$$

Below the disc, we obtain

$$p_{outflow} + \frac{1}{2}\rho v_i^2 = p_\infty + \frac{1}{2}\rho v_\infty^2. \quad (1.2)$$

Adding both equations, we obtain the following equation

$$\Delta p = \frac{1}{2}\rho v_\infty^2, \quad (1.3)$$

which states that the increase of the static pressure is completely converted to kinetic energy at the downstream part of the tube. It should be noted that, in hover, the total increase in the velocity is effectively equal to v_∞ . Therefore, the thrust generated by the disc is $T = \dot{m}v_\infty$ where $\dot{m} = \rho\pi R^2 v_i$ is the mass flow rate through the actuator disc. The power required for this process can also be obtained by examining the difference in the rate of flow of kinetic energy through a cross-section of the streamtube far downstream in the wake (\dot{E}_u) and far upstream (\dot{E}_{up}):

$$P = \dot{E}_u - \dot{E}_{up} = \frac{1}{2}\rho v_\infty^3. \quad (1.4)$$

Since Δp is the thrust per unit area of the disc, we have

$$\Delta p = \frac{T}{A} = \rho v_i v_\infty. \quad (1.5)$$

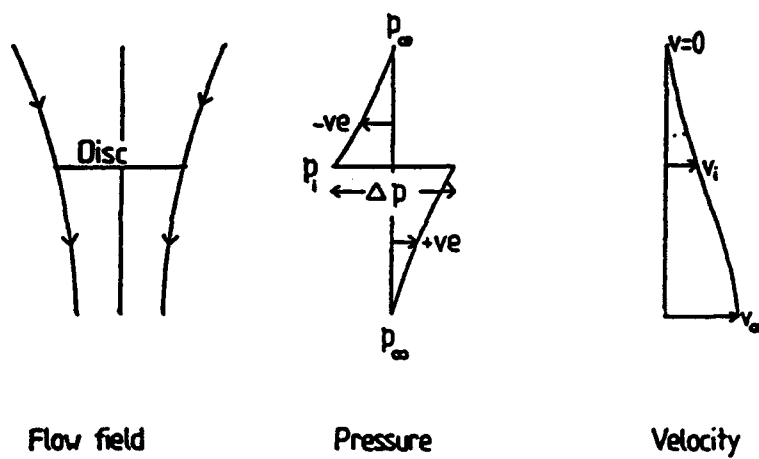


Figure 1.2: Rotor wake in hover as described by Seddon (1990) using momentum theory.

From equations (1.3) and (1.5) it follows that

$$v_{\infty} = 2v_i. \quad (1.6)$$

The above equation explains why wake contraction occurs as the fluid approaches v_{∞} at the downstream part of the tube. In hover, it is easy to show that the wake contracts in diameter by a factor of $\frac{1}{\sqrt{2}}$ which is called the *contraction ratio* and is defined by Bramwell (1976) as the ratio of the radius of the final wake to that of the disk.

Despite several refinements that have been made to improve the momentum theory, such as the inclusion of slipstream rotation by Betz (1915) and the extension of the theory to forward flight applications by Glauert (1928), the prediction of the wake velocity field still remains a challenging problem. However, the application of the momentum theory yields a broad understanding of the overall process that may not be achieved when applying more complicated methods. In particular, by applying the momentum theory, basic relationships between such important parameters as disc loading and power required per unit thrust can be obtained.

In the case where an airframe is immersed in the rotor wake, the procedure to obtain the wake velocity field using momentum theory is no longer valid because of the induced perturbation of the pressure field far upstream in the wake which is not accounted for. The major disadvantage of the momentum theory is that it does not provide a physical framework to explain the nonuniformities of downwash, flow periodicity (due to a finite number of blades) and unsteadiness and the presence of tip losses. Another deficiency of elementary momentum theory is that it does not predict the influence of such rotor design parameters as blade geometry (planform, airfoil, twist and taper), airfoil characteristics, solidity ratio (defined by $s = bc/\pi R$ where b is the number of blades, c the chord length and R is the rotor radius), and tip speed on helicopter performance. However, blade element momentum theory considered in the next section is a more refined model of the rotor wake that accounts for these blade characteristics.

Blade Element Theory

In momentum theory the relationship (1.5) for Δp implies that either the thrust or the induced velocity is known. The blade element theory, by considering the characteristics of the rotor blades and applying the standard methods of airfoil theory, provides another relationship between the thrust and the induced velocity and enables both to be evaluated. Thus, the combination of blade element and the momentum theory is the simplest method of finding time-averaged induced velocities at various points of the rotor disc as well as predicting, with sufficient accuracy, the influence of such design parameters (tip speed, rotor solidity, blade planform, twist and airfoil characteristics) on helicopter performance.

According to Bramwell (1976), the theory is attributed to Glauert (1922) who included an additional assumption to earlier theories proposed by Drzewiecki (1920) and Betz (1915). He stated that the blade should be regarded as being composed of aerodynamically independent, chordwise-oriented, narrow strips or elements. He indicated that two-dimensional airfoil characteristics could be used to determine the forces and moments experienced by the blade as a whole. The validity of this assumption was verified experimentally by Lock (1924) who investigated the elements of an airscrew blade. Klemin (1945) determined the induced velocity at the blade as a function of blade radius. The rotor disc is divided into concentric annular elements which extend the length of the slipstream. By equating the thrust produced by each elementary annulus (according to momentum theory) to the elemental thrust experienced by a number of blade elements (according to blade element theory), and integrating the resulting equation along the rotor radius, an expression for the induced velocity at any location on the disc is obtained. A detailed description of the method can be found in the texts by Gessow and Myers (1952) and Stepniewski and Keys (1984).

Although the combined blade element momentum theory provides a more realistic model than that of the simple momentum theory, the predicted velocity induced at the rotor is still somewhat idealized. This is due to the unsteady nature of the rotor wake flow field and the fact that only time averaged quantities are used to obtain the thrust. As a consequence, the combined blade element momentum theory fails to predict time-dependent aerodynamic events such as blade loading, vibrational excitations, and interaction of the rotor wake with the helicopter airframe. Vortex theory can predict the unsteady effects of the rotor wake on the blades and on the airframe and this is discussed next.

Vortex Theory

Unlike the momentum and blade element theories, vortex theory is free from the restriction of defining a streamtube outside of which the velocity field is zero. The influence of a vortex on the velocity field is extensive, even though according to the Biot-Savart law (Batchelor 1967), the strength of that influence decreases with distance from the vortex. In addition, within certain assumptions (i.e. the flow is inviscid and irrotational), the vortex approach has proven to be a viable computational tool to examine the unsteady, three-dimensional and complex flow field of the rotor wake, a capability that is missing in the theories discussed previously.

The idea of modeling both fixed and rotary wings through vortices was initiated by Joukowski and Kutta in the beginning of this century (Baskin 1975); they showed that lift generation is related to the presence of a vortex placed in a flow field having a velocity component perpendicular to the vortex filament. Since physical observations indicate that the rotor wake consists of highly concentrated

regions of vorticity (tip vortices and a vortex sheet), it is not surprising that vortex theory is extensively used to model the extremely complex rotor wake. Helmholtz in 1858 and Kelvin in 1869 (see Duncan et al. 1960) developed what is generally called vortex theory. However, the application of vortex theory to rotary-wing aerodynamics was begun only in the early 1900's by Joukowski in the former USSR and Goldstein (1929) in the West. Joukowski also applied the vortex concept to a hovering rotor composed of infinitely many blades. The same problem was also investigated by Knight and Hefner (1937). The application of vortex theory has continued to grow ever since, and many investigators have made important contributions to the theory. An excellent summary of the theory can be found in Landgrebe and Cheney (1972). A more elaborate discussion of the method can be found in the text by Stepniewski and Keys (1984).

Gray (1955,1956) conducted experiments that led to the characterization of the wake as being composed of high strength tip-vortices and an inboard vortex sheet. Figure 1.3 shows the vortex wake structure of a one-bladed rotor in hover as described by Gray (1956). The vortex sheet shed by the blade quickly breaks into an inboard vortex sheet and a high-strength rolled-up tip-vortex. The inboard vortex sheet is roughly helical and is made up of trailing vortices which emanate from the blade trailing edge. In modeling the rotor wake by systems of vortices, three approaches have generally been used:

1. Rigid wake models
2. Prescribed wake models
3. Free wake models

The objective of the wake models has been, in most applications, to predict the performance of isolated rotors in hover and forward flight, although it has been shown by Landgrebe et al. (1977) that the presence of the fuselage distorts the airflow and wake causing harmonic excitation at the rotor.

The rigid wake (i.e. classical wake) model in hover has a geometry described by a cylindrical surface of vorticity for the limiting case of a rotor with an infinite number of blades (Knight and Hefner 1937). In forward flight, the undisturbed wake geometry is represented by a skewed cylindrical surface of vorticity. For a rotor with a finite number of blades, the wake is represented by discrete helical sheets whose geometry is determined by the advance ratio of the rotor and the mean inflow velocity through the rotor disc. The rigid wake concept was first applied to aerodynamics of propellers using vortex theory. Betz (1958) showed that an isolated optimum propeller generates a vortex sheet structure which moves as though it is a rigid screw of constant pitch. Goldstein (1929), Lock (1931) and Theodorsen (1948) were able to utilize the rigid wake model by calculating the radial distribution of vorticity in the helical vortex sheets.

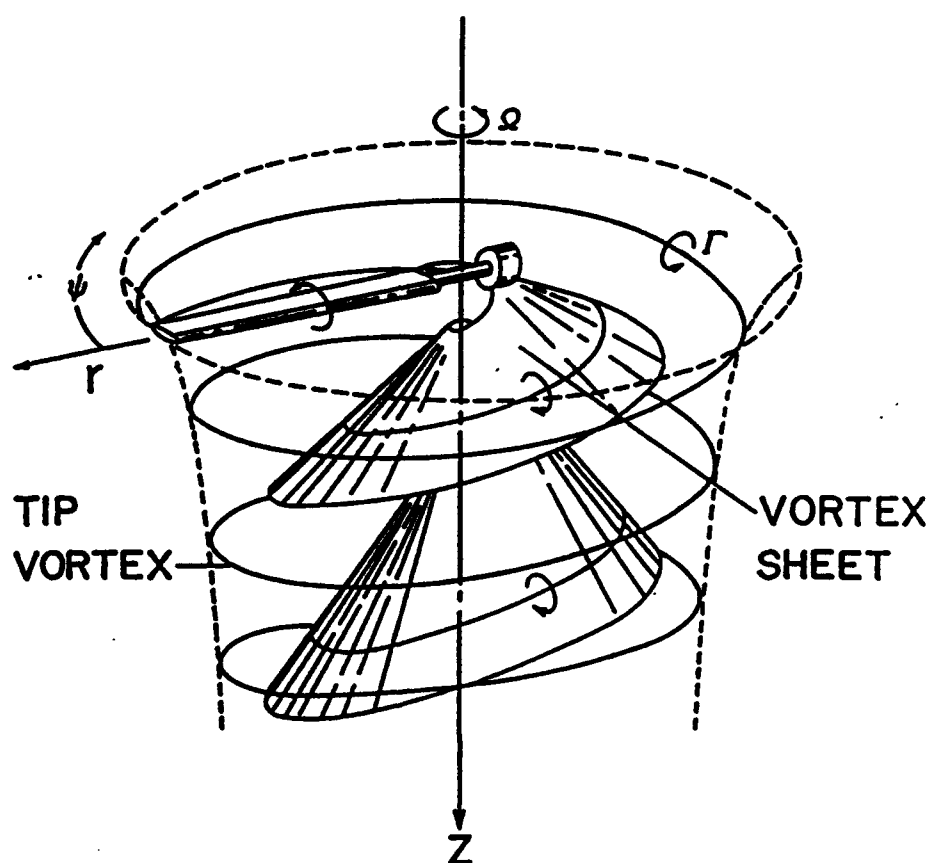


Figure 1.3: Rotor wake in hover as described by Gray (1956).

Since the rigid wake model is developed with the assumption that the total inflow through the propeller is large compared with the velocity induced by the vortex wake system and wake contraction occurs at a considerable distance from the propeller disc, fairly good predictions of the performance of a conventional propeller can be obtained. This assumption is valid when applied to the analysis of a rotor in forward flight; however, it is no longer true if the wake model is applied to a hovering rotor. In hover, the mean axial velocity through the rotor disk is small and wake contraction occurs very close to the rotor. Although the amount of wake contraction (as we have seen by applying momentum theory) is easy to obtain, it is very difficult to calculate the rate of contraction in the neighborhood of the rotor. In addition, despite the computational simplicity of the application of the undisturbed rotor wake geometry concept, the sensitivity of blade inflow and associated airloading to wake distortion can be very significant (Landgrebe and Cheney 1972). Thus, a more advanced wake model that can describe accurately the geometry of the rotor wake should be developed.

The prescribed wake model whose geometry is obtained in terms of experimental data or from some analytical results provides a better method to account for wake contraction. The prescribed wake geometry is defined by a set of equations in terms of a few parameters, such as thrust coefficient, twist rate, rotor solidity, number of blades etc. The equations, generated by interpolation of an experimental data base produced by Landgrebe (1971), are frequently used as an initial guess for the wake geometry in the free-wake analysis which will be discussed next. This model is the most widely used method in the helicopter industry because it predicts rotor performance such as lift, drag and torque with considerable accuracy. However, it requires an extensive and expensive experimental data base. For more detail, the work of Egolf and Landgrebe (1983) provides a complete discussion of the prescribed wake method.

Unlike the prescribed wake model, the free-wake has a geometry that is either generated automatically as an integral part of the solution or obtained after iterating around an initial guess usually provided by the prescribed wake method. Chen (1987), by applying free wake analysis to a helicopter rotor in hover, has used an initial geometry described by Landgrebe's prescribed wake equations (Landgrebe 1971). On the other hand, automatic generation of the wake using potential flow methods which will be discussed next has been considered for instance by Scully (1971), Summa (1976), Summa and Clark (1979), and Morino, Kaprielian, and Sipcic (1985).

Potential Theory

Unlike the vortex theory which is based on the application of the Biot-Savart law to compute the mutual interactions of wake vortices, potential theory consists

of solving the Laplace equation for the velocity potential in the form of an integral equation over the surface of the body and its wake. The solution may be obtained numerically by properly distributing various singularities (sources and doublets and vortices) on the body surface and in the wake. Mangler and Squire (1950) applied potential flow methods to rotary-wing aerodynamics. The early work by Hess (1962) can be cited as one of the first attempts to develop engineering applications of these analytical techniques. They use constant strength source-elements to solve the problem of steady subsonic flow around nonlifting bodies. Hess and Smith (1972) have extended this method to lifting bodies by adding vortex, doublet and lifting-surface panels. Since the numerical solutions to the surface integral equations are obtained by subdividing the body surface into surface elements or panels, most numerical methods are referred to in the literature as panel methods. A review of panel methods existing through about 1976 can be found in the work of Kraus (1978). In general, the panel method (also called the boundary element method) consists of the finite-element solution (over the surface body and its wake) of integral equations for potential aerodynamics. Typically, the surface of the aircraft is covered with source-panels (vortex, doublet and pressure panels are also used on the surface of the body and its wake). The intensity of the source distribution is obtained by satisfying the the boundary conditions on the surface of the body. The methodology has also been applied to aerodynamics of helicopters. The work of Dvorak et al. (1977) presents a method for calculating the pressure distribution on a helicopter fuselage. The work of Morino et al. (1985), using the Green's function formulation, also discusses the application of panel methods to the analysis of the helicopter rotor wake.

1.4 Rotor Wake-Airframe Interaction

Over the years, the primary objective of studying the behavior of the wake shed from isolated rotors has been to understand and predict the unsteady blade load due to the presence of the rotor wake. However, in the early 1970's, design requirements such as higher disc loading and smaller clearance between the rotor and the fuselage for new generation Army helicopters have induced interactions between the rotor and the airframe so intense that the vehicle may exhibit poor dynamic characteristics. The resulting vibration levels are often very high and only by increasing the separation distance between the rotor and the airframe can the vibration be reduced (Schrage and Peskar 1977). Unfortunately, the wake models designed to study isolated rotors cannot accurately estimate the effects of the airframe on the wake. Thus, a more sophisticated model (which accounts for the mutual interaction between the rotor wake and the airframe) needs to be developed. Sheridan and Smith (1980) summarize the general characteristics

of interactional aerodynamics based on their experimental work with the Boeing Vertol UTTAS development program. They suggest that it is necessary to develop tractable theories and analytical methods to account for many of the interactional aerodynamic phenomena.

There have already been a number of valuable experimental and theoretical investigations into the various interactional aerodynamic problems encountered on helicopters. Johnson and Yamauchi (1984), using simplified airframe geometries, are able to predict analytically the effects of the airframe geometry on the rotor performance. In particular, their results which confirm the results of Landgrebe et al. (1977) show that wake distortions (which are caused by the presence of the fuselage) result in harmonic excitations at the rotor. Wilson and Mineck (1975) produced experimental results using a wind tunnel; they investigated the helicopter rotor wake effect on three helicopter fuselage models. They have indicated that the requirement of smaller clearance between the rotor and the fuselage would result in higher induced loads and vibration levels on the fuselage because of the violent aerodynamic interaction so generated. Freeman (1980) investigates the interaction problem between the rotor wake and the airframe by modifying a panel method code. The effect of the rotor or the airframe is accounted for by adding a disturbance velocity and varying the total pressure at a number of control points which are determined by introducing some empirical assumptions. However, the rotor is not affected by the presence of the airframe and thus the code is not fully coupled. Smith (1979) shows that the wake distortion due to the presence of the fuselage may generate enhanced rotor/wake interactions which can trigger a torsional aeroelastic response to the rotor and may lead to a premature retreating blade stall. Additional experimental investigations of the steady state mutual interaction between a rotor and an airframe have been carried out by Betzina and Smith (1983) and Smith and Betzina (1986). It is shown that the longitudinal aerodynamic characteristics of the airframe are affected by the rotor and hub.

Lorber and Egolf (1990) (see also Egolf and Lorber (1987)) develop a model for the unsteady interaction of the rotor with the fuselage in forward flight in which a lifting line and a prescribed rotor wake and a source panel airframe analysis code are combined to predict the unsteady airloads. Their results are compared with the experimental data produced by Brand et al. (1989). The overall results are encouraging; however, mean pressures on the airframe are not accurately predicted because the quasi-steady approach is used to model the rotor wake. Lorber and Egolf (1988) modified their mean pressure predictions by adding a constant value (equal to the disc loading) to account for blade passage effects which are not incorporated in the rotor wake model.

Liou, Komerath and McMahon (1990) have recently conducted experiments on the transient interaction between a cylinder and the vortex shed from a helicopter rotor (see also Brand, McMahon, and Komerath 1989 and Brand 1989). They use

laser doppler velocimetry to measure the velocity in the vicinity of the filament and obtain results for the pressure on the surface of the cylinder under the impinging vortex. They are able to map the vortex position as a function of time including the period during which a portion of the vortex impacts the cylinder. Bi and Leishman (1991) and Leishman and Bi (1990) also report on the interaction of the tip-vortex with an airframe. The vortex impinges on the aft part of the airframe in contrast to the work of Liou et al. (1990) and so the circulation of the vortex is effectively of opposite sign.

In particular, Brand (1989) performed experiments to identify and investigate the flow field features that may lead to significant interaction effects between the rotor wake and the airframe. He was able to isolate major sources of the pressure signatures produced on the airframe during the interaction period. The blade passage effects are responsible for large-amplitude positive pressure peaks occurring on the airframe. In addition, he shows that the effects of the rotor tip-vortex interaction with the airframe are associated with a large-amplitude, short-scaled, suction peak on the airframe. He observes that the pressure suction peak reaches a maximum value near the time at which the vortex collides with the surface. Moreover, the effect of the inboard vortex sheet interaction with the airframe is observed to be small compared to that of the tip-vortex. He also concludes that, in practical rotorcraft configurations where the rotor is mounted fairly high above the airframe, the tip-vortex effect may dominate the instantaneous pressure signature.

1.5 Boundary-Layers Induced by a Moving Vortex Filament

In recent years, there has been an increasing amount of attention paid to the range of problems associated with interaction of regions of concentrated vorticity with solid boundaries and the effect of these regions on the boundary-layer flow under them. Such flows occur in a wide variety of physical situations; for example, it is now commonly accepted that vortex motions play a major role in the dynamics of wall-bounded turbulent flows. Moreover, the interaction of "vortices" with solid boundaries is important in the study of impinging shear and mixing layers, in the study of the wakes of low-flying aircraft, in the flow within gas turbines, in the dynamic stall process and in the study of the induced load on the fuselage of a helicopter, among many others.

The two-dimensional boundary-layer flow induced by a vortex has been investigated by several authors. Walker (1978) was the first to calculate the boundary-layer due to a vortex in a stagnant medium. He found that the vortex induces a separated flow under the vortex in the sense that a reversed flow eddy forms early in the calculation and grows in time, eventually causing a catastrophic breakdown

of the numerical calculation. He also suggests that no physically acceptable steady solution of the boundary-layer flow exists even though the inviscid flow due to the vortex is steady in a reference frame traveling at the vortex speed. In addition, his results are suggestive of explosive boundary layer growth and he postulates that the secondary vortex which forms deep in the boundary-layer will eventually be driven away from the wall. Doligalski and Walker (1984) were the first to describe the convecting vortex-boundary interaction and their results support the conjectures of Walker (1978) for the stagnant medium. Chuang and Conlisk (1989) have computed the corresponding solution using interacting boundary-layer techniques; they show that the vortex is indeed driven from the wall under the action of the boundary-layer flow as suggested by Walker (1978). They also found that a tertiary eddy is spawned late in the calculation and they identified the development of a shear layer region above the spawned secondary vortex which may be the conduit for the ejection of the secondary vortex into the outer flow. Peridier, Smith and Walker (1991) recompute the solution of Walker (1978) for both the classical and interacting boundary layers using a Lagrangian approach and were able to continue the calculation far beyond the Eulerian fixed grid results of Walker (1978). The nature of a Lagrangian calculation permitted resolution of the van Dommelen-type singularity which forms when the eruption becomes too strong for the boundary layer approximation to hold (see just below).

In the case of three dimensions, the amount of work is very limited. Walker, Smith, Cerra, and Doligalski (1987), in a combined numerical and experimental study, have investigated the boundary-layer due to the impact of an axis-symmetric vortex ring on a wall. Here the flow is axisymmetric with respect to the axis of the ring and is thus essentially two-dimensional. Ersoy and Walker (1985, 1987), and Hon and Walker (1987) have computed the boundary-layer flow due to a loop vortex and a hairpin vortex respectively, along a symmetry plane present in each case. The vortex-boundary-layer interactions described here have been observed experimentally by Harvey and Perry (1971) and recently in the experiments described in Walker, Smith, Cerra and Doligalski (1987); in particular, they observe that the vortex induced flow is associated with an explosive boundary-layer growth and an eventual ejection of a secondary vortex ring.

Since the presence of a concentrated vortex structure above a boundary has been observed to induce boundary-layer separation in all of the work discussed just above, it is useful to review the basic concepts of unsteady boundary-layer separation.

1.6 Unsteady Boundary Layer Separation

Because the boundary-layer calculations involve reversed flow phenomena (Chapter 5) it is useful to review the concept of boundary-layer separation and, in particular,

unsteady boundary-layer separation. The definition of the term "separation" has been a matter of debate; in the early studies of unsteady boundary-layer the term "separation" usually refers to a breakaway or eruption of the boundary-layer fluid into the main stream (Sears and Telionis 1975; see also van Dommelen and Cowley 1990). In this work, separation of the boundary-layer (in two or three dimensions) will be assumed to commence in the generation of a small reversed flow eddy which eventually grows in time leading to a short-length scale, short-time scale eruption of boundary-layer fluid.

In two-dimensions, significant advances in this area have been made. In particular, it is now generally accepted that what is now known as the Moore-Rott-Sears (MRS) model for unsteady separation gives the required conditions for a boundary-layer eruption (Sears and Telionis 1975). In this model, it is argued that a singularity in the boundary-layer equations emerges at the point where the vorticity vanishes in a reference frame traveling with the local fluid velocity. These two conditions replace the condition of zero wall shear in steady flow. Moreover, the generation of a large unsteady adverse pressure gradient can hasten the eruptive process (Conlisk unpublished and Peridier, Smith and Walker 1991). In two dimensions, the eruption region consists of a wall of low streamwise velocity fluid which is turned under the action of an adverse pressure gradient and is eventually ejected vertically from the boundary-layer (see van Dommelen et al. 1990, Elliott et al. 1983, Smith 1988, van Dommelen 1981, and van Dommelen and Shen 1980 and 1982).

In three-dimensional flow, as pointed out in the review of Tobak and Peake (1982), the definition of separation and its description is difficult even when the flow is steady. This situation is due not only to the absence of a "streamfunction" in three dimensions, but also to the difficulty associated with the presence of two-components of the wall shear. Whereas, in steady flow, the definition of separation is clearly defined as the vanishing of the wall shear (Goldstein 1948), in three dimensions, the location of separation depends on the behavior of the flow in a surface immediately adjacent to the wall. Legendre (1956), suggested that separation be considered to have occurred at the location where the wall streamlines (or skin-friction lines) converge onto a particular streamline that originates from a singularity known as a saddle point. Lighthill (1963) later suggested that this phenomenon be considered a necessary condition for separation and several topological laws concerning the number and type of singularities which may occur in a steady separated flow have been deduced (Tobak and Peake 1982). Duck and Burggraf (1986) have computed the steady, separated flow past a surface protuberance or hollow illustrating, in a clear manner, the validity of the topological laws associated with three-dimensional steady separation.

However, when the flow is unsteady, since separation in general does not commence on the body surface, the steady flow definition of separation does not apply

and the surface streamlines thus have no direct connection to the presence or absence of separation. van Dommelen and Cowley (1990) have extended previous work on the Lagrangian view of two-dimensional unsteady separation (see van Dommelen 1981 and van Dommelen and Shen 1980) to three-dimensions. In particular they derive the two Moore-Rott-Sears conditions for three dimensional flow using a local analysis and find that they carry over in very similar form from the two-dimensional case. In this case, the stationary point is defined as the vanishing gradient of an oblique Lagrangian coordinate (van Dommelen and Cowley 1990). In particular, as in two dimensions, the singularity is manifest in the development of an eruptive region which narrows as the singular time is approached. The variation of the flow patterns in the cross-flow direction, however, is relatively weak and thus the flow near the eruption appears quasi-two-dimensional. In this way, the eruptive (i.e. separation in the sense of MRS) picture is similar to that proposed in two dimensions by van Dommelen and Shen (1990) with the difference that the coefficients in the scale parameters (ie. in the scales defining the separation structure) are dependent on the cross-flow variable. Physically, in an asymptotic sense the boundary-layer thickness profile has the shape of a crescent shaped ridge which is long and narrow in the cross-stream direction. The present results for the boundary-layer flow induced by a vortex filament appears to be consistent with some of the predictions of van Dommelen and Cowley (1990) and this is discussed in Chapter 5.

1.7 Outline of the Present Work

The vortex system shed by helicopter blades is very complex consisting of a fully three-dimensional vortex sheet and the associated tip-vortex and it has been recognized that interactions between different components can significantly affect helicopter performance. In particular, the prediction of the induced loads on the airframe which result from the unsteady interaction of the complex rotor wake with the airframe is of major interest to designers in the rotorcraft area. In the present work, the unsteady interaction of the rotor tip-vortex with the fuselage and the problem of the three-dimensional boundary-layer so generated on the fuselage underneath the vortex are investigated.

The approach taken here is an asymptotic one in the sense that we consider the velocity field in which the tip-vortex is imbedded to be inviscid and irrotational outside the vortex core. Moreover, we assume that significant viscous effects are confined, at most, to the vortex core and to the region immediately adjacent to the airframe. This is in distinct contrast to an approach in which the full Navier-Stokes equations are solved in the entire rotor wake-airframe domain. As will be demonstrated in Chapter 3, because of computational limitations, the latter approach cannot resolve the extremely sharp velocity and pressure gradients which

emerge as the tip-vortex approaches the airframe.

To begin, a simplified model for the interaction of a rotor tip-vortex with a fuselage or airframe is developed using three-dimensional potential flow analysis. The tip-vortex is idealized as a single three-dimensional vortex filament and the fuselage is modeled by an infinitely long circular cylinder. The Biot-Savart law is employed to describe the flow induced by the vortex and the flow is assumed to be inviscid and irrotational outside the core of the vortex. The present analytical/numerical results for both the vortex trajectory and the pressure distribution on the airframe are in substantial agreement with experimental results prior to impact of the vortex with the airframe. The numerical calculations indicate that a large adverse pressure gradient develops under the vortex on the fuselage causing a rapid drop in the pressure there. It is important to note that prior to the work of Brand (1989), there appears to be no consensus as to the quantitative effect of the tip-vortex on the pressure induced on the helicopter airframe. Moreover, the authors are aware of no computational work not involving the use of free constants, which accurately captures the effect of the tip-vortex on the pressure distribution on the airframe; the primary purpose of this phase of the work is to quantitatively calculate this effect and demonstrate substantial agreement with the experimental results of Brand (1989).

The second phase of the present work focuses on the problem of the unsteady three-dimensional boundary-layer flow induced by the vortex filament moving above the fuselage. Three types of external flow in which the vortex is embedded are considered. These flows are respectively a stagnant medium, a symmetric mean flow and an asymmetric mean flow, the latter of which corresponds to the experimental conditions described above. In each case, the computed results show the development of a variety of complex three-dimensional boundary-layer separation phenomena. In all cases, the boundary-layer solutions show the formation of a secondary eddy which grows in time; this situation is expected to lead to an eruption of boundary-layer fluid into the free stream. The purpose of investigating the vortex-induced boundary-layer is to determine the resulting wall shear on the airframe from which viscous drag may be obtained. In addition, it is desirable to determine, in general, how the boundary-layer responds to the presence of the approaching vortex filament.

Finally, as noted earlier, during the course of this work, a possible picture of the entire vortex-body collision process has been developed. In connection with this, a simple model for the initial stages of the collision process in which the vortex core may deform has also been developed. In addition, the three-dimensional interacting boundary layer problem has been solved in order to investigate the development of a secondary suction peak in the pressure profile observed in experiment (Affes et al 1993).

It is important to point out that interaction with Professor Narayanan Komerath

and his colleagues at Georgia Institute of Technology has been influential in the interpretation of the computational results. Professor Komerath has kindly provided detailed experimental data with which some of the computational results have been compared. We have had extensive discussions including visits on-site at Georgia Tech with Professor Komerath and have jointly published two papers on the present problem. The results of his experiments will be quoted throughout this document and the term experiments will refer to his work unless otherwise noted.

The plan of the present work is as follows. In Chapter 2 a simplified model for the interaction of a rotor tip-vortex is developed. The tip-vortex is idealized as a single three-dimensional vortex filament and the fuselage is modeled by an infinitely long circular cylinder. The Biot-Savart law is employed to describe the flow induced by the vortex and the flow is assumed to be inviscid and incompressible outside the core of the vortex. Transform methods are used to deduce the form of image vortex filament inside the cylinder. The numerical calculations indicate that a large adverse pressure gradient develops under the vortex on the fuselage causing a rapid drop in the pressure there; large variations in the curvature of the vortex are not observed. Numerical solutions for the vortex position and the pressure on the airframe are calculated for the situation where the surrounding medium is stagnant and for the case where the vortex is embedded in a three-dimensional steady mean flow.

In Chapter 3 experimental results produced by Professor Komerath and his colleagues at the Georgia Institute of Technology are compared with the results of the present work using the model for this interaction outlined in Chapter 2. The experimental and analytical/numerical results for both the vortex trajectory and the pressure distribution on the airframe are in substantial agreement prior to impact of the vortex with the airframe. In particular, it is shown that the position and magnitude of the suction peak induced on the airframe can be adequately predicted using a three-dimensional potential flow analysis during the time period from the onset of strong interaction with the airframe until just prior to the vortex-airframe collision.

In Chapter 4 the two-dimensional boundary-layer past an impulsively started cylinder is investigated and results are reproduced using the methodology developed in the present work. The objective of this study is to test the accuracy of the numerical techniques which will be extended to compute the three-dimensional boundary-layer flow. The results are in good agreement with previous results.

In Chapter 5, a methodology to compute the three-dimensional boundary-layer flow induced by the vortex filament moving outside a circular cylinder is developed. First, the characteristics of inviscid external flow specific to the computation of the boundary-layer flow are discussed and the three dimensional boundary-layer problem is formulated. The numerical methods employed to solve the boundary-

layer equations are described in detail. Results are obtained for three types of external flow. In the simplest case, the vortex is embedded in a stagnant medium; the induced boundary-layer results indicate that the flow separates in the sense that a closed eddy forms early in the calculation. The eddy appears bubble-like and grows in size as time increases and eventually gets stretched considerably in the vertical direction leading to an expected eruption of fluid into the inviscid external flow. In the second case, where the vortex is embedded in a symmetric mean flow, the boundary-layer flow results also show the development of a secondary eddy that grows in time; however, in contrast to the stagnant flow case, the reversed flow eddy is detached from the wall and moves vertically away from the cylinder wall as time increases. Lastly, the case of asymmetric mean flow is considered corresponding to the specific parameters employed in the experiments of Professor Komerath and his colleagues at Georgia Institute of Technology. The results for the boundary-layer flow indicate the initial stages of the formation of a secondary eddy. The work presented in Chapters 2-5 of this work describes the flow field induced by the tip-vortex near the airframe only during the time period prior to impact of the vortex with the nearest part of the airframe. Nevertheless, these results are suggestive of the behavior of the flow throughout the period of intense vortex interaction with the airframe. In Chapter 6 it is argued that three distinct phases of interaction may be identified; these are the pre-impingement phase described in Chapters 2-5; the impingement or collision phase and the post-collision phase which is characterized by the merger of the ends of the tip vortex with the boundary layer on the airframe.

In Chapter 7 the predominantly inviscid aspects of the onset of the collision phase of the motion are presented. Here a three-dimensional, multiple-vortex model is used to simulate the initial deformation of the vortex core seen in the experiments. This appears to occur just as the vortex first touches the airframe and cannot be predicted using the rigid-core model of Chapters 2 and 3. Finally, in Chapter 8, the initial response of the boundary layer is considered via consideration of the interacting boundary layer problem. Here the pressure distribution is no longer impressed on the boundary layer flow but is permitted to vary with the outer inviscid flow. The results indicate a secondary pressure suction peak in the pressure distribution on the top of the airframe, which is again a feature that is seen in the experiments of Komerath and his colleagues at Georgia Tech.

A summary of the entire project and recommendations for areas of future work follows.

CHAPTER II

Motion of a Vortex Filament Above a Cylinder

2.1 Introduction

In this chapter, a methodology to calculate the motion of a generalized vortex filament in the presence of a cylinder is developed. Although, the motion of three-dimensional vortex filaments in free space can be obtained easily by applying the Biot-Savart law, the perturbation of the vortex due to the presence of a curved solid surface is difficult to calculate. The velocity perturbation is usually determined by defining an image vortex system such that the resulting normal velocity component at the body surface vanishes. Thus the problem of deducing the image reduces to reflecting the vortex filament inside the immersed body. The situation is particularly simple in two-dimensions where the image of a potential vortex in a plane wall or a circular cylinder is easily found using standard image techniques (Milne-Thomson 1962). The form of the image of a generalized vortex filament in three-dimensions is not obvious; however, Hon and Walker (1987) have shown that the image of a generalized vortex filament in a plane wall is obtained by considering a mirror image of the actual vortex with an opposite circulation. The apparent simplicity of this procedure in three-dimensions is due to the fact that equation of the solid surface is defined by a single Cartesian coordinate. In the present case, it appears that no such simple expression for the image vortex filament exists and in the present work we use transform methods to deduce the form of the image vortex filament.

The motion of a three-dimensional vortex in free space has been documented by a number of authors and an excellent discussion of the previous work in this area is given by Hon and Walker (1987) and Sarpkaya (1989). For the case where the vortex filament interacts with a body, the amount of work is much more limited, and only simple body shapes such as a plane wall (Hon and Walker 1987) and a sphere (Lewis 1879, Larmor 1889, Lighthill 1940, Weiss 1944, and Dhanak 1981) have been considered previously. Moreover, much of this previous work is of a static

nature (Lewis 1879, Larmor 1889, Lighthill 1940, Weiss 1944); the present work is dynamic in nature and the methods employed to calculate the image distribution of the vortex in the cylinder are not trivial. These methods are considered next.

2.2 A Procedure to Compute the Vortex Image System

The unsteady interaction between a vortex filament and a bluff body was first considered by Dhanak (1981). He studied the case when a rigid sphere approaches an infinitely long straight vortex at a uniform speed. Based on the work of Lighthill (1940) who developed an image system for a vortex element in a sphere, an expression of the instantaneous velocity field due to the image of the evolving infinitely long vortex filament is obtained. The resulting image system as explained by Weiss (1944) consists of a vortex ring and a vortex sheet extending over that circle. However, in the case of a vortex filament interacting with a cylinder, no theory has been developed to obtain the form of the complex image system. Unlike the case of a sphere, there appears to be no simple expression for the image system of a vortex element of arbitrary direction in a cylinder. In the present work, this difficulty is overcome by using transform methods to deduce a suitable image system of a vortex filament convecting above a cylinder.

We first consider the inviscid flow due to a generalized vortex filament of small cross-section in a stagnant environment; the filament has dimensional strength Γ^* and outside the filament the flow is assumed to be inviscid and irrotational. A typical initial vortex position is depicted on Figure 1.1. The velocity potential due to the filament may be described by a velocity potential ϕ' which satisfies

$$\nabla^2 \phi' = 0 \quad \text{with} \quad \frac{\partial \phi'}{\partial r} \Big|_{r=1} = 0 \quad \text{and} \quad \phi' \text{ is finite as } r^2 + z^2 \rightarrow \infty, \quad (2.1)$$

where

$$\nabla^2 = \frac{\partial^2}{\partial r^2} + \frac{1}{r} \frac{\partial}{\partial r} + \frac{1}{r^2} \frac{\partial^2}{\partial \theta^2} + \frac{\partial^2}{\partial z^2},$$

is the Laplace operator in cylindrical coordinates.

Let $\phi' = \phi_I + \phi_V$ where ϕ_V is the potential due to a vortex in free space and ϕ_I is the perturbation potential due to the image of the vortex in the cylinder. (For the purpose of this discussion we omit the effect of mean flow; this will be added subsequently.) Then ϕ_I satisfies

$$\nabla^2 \phi_I = 0 \quad \text{with} \quad \frac{\partial \phi_I}{\partial r} = -\frac{\partial \phi_V}{\partial r} \quad \text{at } r = 1, \quad (2.2)$$

and ϕ_I must be bounded as $r^2 + z^2 \rightarrow \infty$. Here all lengths have been made dimensionless on the cylinder radius denoted by a and ϕ' has been made dimensionless on

$W_\infty a$ where W_∞ is the characteristic velocity ($W_\infty = \frac{\Gamma^*}{a}$ for the case of a stagnant medium.). To simplify the calculations, the cylinder is assumed to be infinite in length. To obtain the solution to the boundary value problem (2.2), we use the Fourier Transform in both the z and the θ directions (Figure 1.1); defining the double Fourier Transform of ϕ_I as

$$\hat{\phi}_I = \int_{-\infty}^{\infty} \int_{-\pi}^{\pi} \phi_I e^{-ikz - im\theta} d\theta dz, \quad (2.3)$$

the transform solution $\hat{\phi}_I$ satisfies

$$\frac{\partial^2 \hat{\phi}_I}{\partial r^2} + \frac{1}{r} \frac{\partial \hat{\phi}_I}{\partial r} - \left(\frac{m^2}{r^2} + k^2 \right) \hat{\phi}_I = 0, \quad (2.4)$$

subject to the following boundary conditions

$$\frac{\partial \hat{\phi}_I}{\partial r} = -\frac{\partial \hat{\phi}_V}{\partial r} \text{ at } r=1, \text{ and } \hat{\phi}_I \text{ is finite as } r \rightarrow \infty. \quad (2.5)$$

The apparent advantage of using the transform methods is that the partial differential equation (2.2) is reduced to an ordinary differential equation (2.4). Furthermore, the resulting ODE is a Bessel equation, and therefore an exact solution exists. After applying the appropriate boundary conditions, a final solution for $\hat{\phi}_I$ is obtained and is given by

$$\hat{\phi}_I = -\frac{\partial \hat{\phi}_V}{\partial r} \Big|_{r=1} \frac{K_m(|k|r)}{|k| K'_m(|k|)}, \quad (2.6)$$

where K_m is the modified Bessel function of order m . Note that $\frac{\partial \hat{\phi}_V}{\partial r} \Big|_{r=1}$ is the radial velocity component U_{Vr} at $r=1$. Here \vec{U}_V is the velocity field due to a vortex filament in free space and is given by the Biot-Savart law (Batchelor 1967)

$$\vec{U}_V(\vec{X}, t) = -\frac{\Gamma}{4\pi} \int_C \frac{(\vec{X} - \vec{X}') \times d\vec{X}'}{|\vec{X} - \vec{X}'|^3}, \quad (2.7)$$

where \vec{X} is a field point and \vec{X}' denotes a point on the vortex. Here Γ is the dimensionless circulation $\Gamma = \frac{\Gamma^*}{W_\infty a}$. Let s be a parametric coordinate along the space curve defining the centerline of the vortex filament, then the position of any material point on the vortex loop may be written in Cartesian coordinates as

$$\vec{X} = x(s, t)\hat{i} + y(s, t)\hat{j} + z(s, t)\hat{k}, \quad (2.8)$$

where t is the nondimensional time $t = \frac{W_m}{a} t^*$. From (2.8), equation (2.7) may be written as

$$\vec{U}_V(s, t) = -\frac{\Gamma}{4\pi} \int_C \frac{(\vec{X} - \vec{X}') \times \frac{\partial \vec{X}'}{\partial s'}}{\{|\vec{X} - \vec{X}'|^2\}^{3/2}} ds'. \quad (2.9)$$

Performing the cross-product and expanding the integrand of equation (2.9), in Cartesian coordinates, the components of the vortex induced velocity field are

$$U_{Vx}(s, t) = \frac{\Gamma}{4\pi} \int_C \frac{\left\{ \frac{\partial y'}{\partial s'}(z - z') - \frac{\partial z'}{\partial s'}(y - y') \right\} ds'}{\{(x - x')^2 + (y - y')^2 + (z - z')^2\}^{3/2}}, \quad (2.10)$$

$$U_{Vy}(s, t) = \frac{\Gamma}{4\pi} \int_C \frac{\left\{ \frac{\partial x'}{\partial s'}(x - x') - \frac{\partial z'}{\partial s'}(z - z') \right\} ds'}{\{(x - x')^2 + (y - y')^2 + (z - z')^2\}^{3/2}}, \quad (2.11)$$

$$U_{Vz}(s, t) = \frac{\Gamma}{4\pi} \int_C \frac{\left\{ \frac{\partial x'}{\partial s'}(y - y') - \frac{\partial y'}{\partial s'}(x - x') \right\} ds'}{\{(x - x')^2 + (y - y')^2 + (z - z')^2\}^{3/2}}. \quad (2.12)$$

The radial velocity can now be obtained in terms of the Cartesian velocity components and is given by

$$U_{Vr} = U_{Vx} \cos \theta + U_{Vy} \sin \theta. \quad (2.13)$$

At points on the cylinder (where $r = 1$, $x = \cos \theta$ and $y = \sin \theta$), an equation for the radial velocity can be deduced by using equations (2.10), (2.11) and (2.13) according to

$$\begin{aligned} U_{Vr}(s, t) |_{r=1} &= \frac{\Gamma}{4\pi} \int_C \frac{\left\{ \frac{\partial y'}{\partial s'}(z - z') - \frac{\partial z'}{\partial s'}(\sin \theta - y') \right\} \cos \theta ds'}{\{(\cos \theta - x')^2 + (\sin \theta - y')^2 + (z - z')^2\}^{3/2}} \\ &+ \frac{\Gamma}{4\pi} \int_C \frac{\left\{ \frac{\partial x'}{\partial s'}(\cos \theta - x') - \frac{\partial z'}{\partial s'}(z - z') \right\} \sin \theta ds'}{\{(\cos \theta - x')^2 + (\sin \theta - y')^2 + (z - z')^2\}^{3/2}}. \end{aligned} \quad (2.14)$$

As defined by equation (2.3), the Fourier Transform of the radial velocity $U_{Vr} |_{r=1}$ is given by

$$\frac{\partial \hat{\phi}_V}{\partial r} |_{r=1} = \int_{-\infty}^{\infty} \int_{-\pi}^{\pi} U_{Vr} |_{r=1} e^{-ikz - im\theta} d\theta dz. \quad (2.15)$$

Using the inversion formulas for the transforms as given in Churchill (1972, pp. 379, 471) it may easily be shown that the velocity potential due to the presence of the cylinder, henceforth termed the image field, is given by

$$\phi_I = \frac{1}{4\pi^2} \sum_{m=-\infty}^{\infty} \int_{-\infty}^{\infty} \hat{\phi}_I e^{im\theta} e^{ikz} dk. \quad (2.16)$$

The velocity potential given by equation (2.16) is expressed in polar coordinates; however, as will be evident later, it is more convenient to advance the vortex filament in the Cartesian coordinate system defined on Figure 1.1.

In a typical rotorcraft environment, the tip vortex is embedded in a downwash corresponding to the balance of the rotor wake superimposed upon a velocity component along the airframe (forward flight). In the present work we model the effect of the balance of the rotor wake by a steady downwash corresponding to two-dimensional flow past a cylinder and in the coordinate system of Figure 1.1 we have

$$\vec{U}_M = \gamma \frac{\sin 2\theta}{r^2} \hat{i} - \gamma \left(1 + \frac{\cos 2\theta}{r^2} \right) \hat{j} + \hat{k}, \quad (2.17)$$

where

$$\gamma = \frac{U_\infty}{W_\infty}$$

is the ratio of the mean velocity at infinity in the y -direction (which is the downwash mean velocity) to the characteristic velocity W_∞ . Note that the first two terms in equation (2.17) correspond to two-dimensional flow past a cylinder. For a vortex filament embedded in the mean flow given by equation (2.17) the total potential is given by

$$\phi = \phi_I + \phi_V + \phi_M, \quad (2.18)$$

where ϕ_M is the potential corresponding to \vec{U}_M ; equation (2.2) for ϕ_I is not altered since the expression (2.17) satisfies the solid wall boundary condition. The velocity field corresponding to the potential field (2.18) may be written as

$$\vec{U} = \vec{U}_I + \vec{U}_V + \vec{U}_M, \quad (2.19)$$

and the velocity \vec{U} has been nondimensionalized on W_∞ . It should be noted that a clockwise rotation of the vortex filament when looking from a side view corresponds to a circulation $\Gamma > 0$. In order to convect the filament the velocity due to the vortex itself, \vec{U}_V , and its image \vec{U}_I must be computed and the methods employed to do this are described in the next four sections.

2.3 Vortex Core Flow

The crucial difference between the motion of a two-dimensional straight vortex filament and a three-dimensional filament is the presence of a local-self-induced velocity field which, in general, imparts a finite curvature to the filament. The velocity field corresponding to a general vortex filament in free space is given by equation (2.7) provided the field point \vec{X} is not on the vortex filament. However, in order to advance the filament we must evaluate equation (2.19) on the filament

and for one value of $\vec{X} = \vec{X}'$ expression (2.7) becomes unbounded there. This is a reflection of the fact that expression (2.7) is not valid as the core of the vortex is approached; recent work by Callegari and Ting (1978) has suggested that the singularity may be removed by the incorporation of the physical effect of viscosity in the core and they show how to match this core flow solution with the inviscid solution for the case of a general, finite-length, closed filament in free space. However, the analysis is very complex and in this work a more conventional approach to remove the singularity in \vec{U}_V will be adopted.

In the present work we adopt a cut-off procedure due originally to Moore (1972) and employed recently in the work of Hon and Walker (1987) in their calculations of the flow field induced by convected hairpin vortices. The method entails inserting a parameter μ into the denominator of equation (2.7) to regularize the integrand when \vec{X} is on the filament; in this case, (2.7) becomes

$$\vec{U}_V(s, t) = -\frac{\Gamma}{4\pi} \int_C \frac{(\vec{X} - \vec{X}') \times \frac{\partial \vec{X}'}{\partial s'} ds'}{\left\{ |\vec{X} - \vec{X}'|^2 + \mu^2 \right\}^{3/2}}. \quad (2.20)$$

The value of μ is fixed by appeal to the exact solution for the vortex ring problem (Moore 1972, Ersoy and Walker 1985) and the result is

$$\ln \left(\frac{\mu^*}{a_v^*} \right) = -\frac{1}{2} - \frac{4\pi^2}{\Gamma^{*2}} \int_0^{a_v^*} v'^2 r^* dr^* + \frac{8\pi^2}{\Gamma^{*2}} \int_0^{a_v^*} w'^2 r^* dr^*, \quad (2.21)$$

where v' and w' are the velocities in the core of the vortex, a_v^* is the dimensional vortex core radius; r^* and μ^* are also dimensional. For the case of $w' = 0$ and v' corresponding to a Rankine vortex

$$v' = \begin{cases} \frac{\Gamma^*}{2\pi} \frac{r^*}{a_v^{*2}}, & \text{if } r^* \leq a_v^*, \\ \frac{\Gamma^*}{2\pi r^*}, & \text{if } r^* \geq a_v^* \end{cases} \quad (2.22)$$

then

$$\mu = a_v e^{-3/4}. \quad (2.23)$$

The parameter μ in equation (2.23) is dimensionless and is defined by $\mu = \mu^*/a$ where a is the cylindrical airframe radius. It should be noted that if, for example, the axial velocity $w' = e^{-cr^{*2}}$, where c is a constant then μ^* can also be obtained analytically using equations (2.21) and (2.22). In this case, the effect of w' on μ^* is small since c is usually chosen to be sufficiently large in order to make w' vanish at $r^* = a_v^*$ (Affes and Conlisk 1991). Therefore, in the present work we consider only the case where $w' = 0$.

2.4 The Self-Induced Motion of the Vortex Filament

The present calculation of the self-induced motion of the vortex filament is essentially that due to Hon and Walker (1987) and in what follows, we outline their procedure. The evaluation of successive positions of the vortex filament position is a Lagrangian calculation, therefore the parameter s introduced in equation (2.8) can be regarded as a Lagrangian variable in the one-dimensional domain given by the space curve defining the centerline of the vortex (see Figure 1.1).

As pointed out by Hon and Walker (1987), μ is often small for small-core vortices and consequently numerical evaluation of (2.20) is still difficult; Hon and Walker (1987) following Moore (1972) suggest using a Taylor series expansion of the integrand about the local filament point and the form of (2.20) obtained by Moore using this procedure is

$$\begin{aligned} \vec{U}_V(s, t) = \frac{\Gamma}{4\pi} \int_C \left[\frac{\frac{\partial \vec{X}'}{\partial s'} \times (\vec{X} - \vec{X}')}{\left\{ |\vec{X} - \vec{X}'|^2 + \mu^2 \right\}^{3/2}} - \left(\frac{\partial \vec{X}}{\partial s} \times \frac{\partial^2 \vec{X}}{\partial s^2} \right) P(s') \right] ds' \\ + \frac{\Gamma}{4\pi} \left(\frac{\partial \vec{X}}{\partial s} \times \frac{\partial^2 \vec{X}}{\partial s^2} \right) \int_C P(s') ds', \end{aligned} \quad (2.24)$$

where

$$P(s') = \frac{\frac{1}{2}(s' - s)^2}{\left\{ (s' - s)^2 \left(\frac{\partial \vec{X}}{\partial s} \right)_s^2 + \mu^2 \right\}^{3/2}}. \quad (2.25)$$

The second integral in equation (2.24) may be calculated analytically while the first integral can be evaluated numerically using a standard integration scheme. The deformation of the vortex filament will be local in character and occurring between say, $x = -l$ and $x = +l$ where l is a parameter. Assume that the parametric variable s' ranges from $s' = -\infty$ to $s' = +\infty$. Then the infinite integral in (2.24) can be evaluated as follows. The filament ends from $(-\infty, -l)$ and from (l, ∞) are assumed to be straight and the associated integrals may be computed analytically. Therefore equation (2.24) can be rewritten as

$$\begin{aligned} \vec{U}_V(s, t) = \frac{\Gamma}{4\pi} \left[\int_{-l}^l \vec{Q}_V(s, s', t) ds' + \int_{-\infty}^{-l} \vec{Q}_{V\infty}(s, s', t) ds' + \int_l^{\infty} \vec{Q}_{V\infty}(s, s', t) ds' \right] \\ + \frac{\Gamma}{4\pi} \left(\frac{\partial \vec{X}}{\partial s} \times \frac{\partial^2 \vec{X}}{\partial s^2} \right) \int_{-l}^l P(s') ds', \end{aligned} \quad (2.26)$$

where

$$\vec{Q}_V = \frac{\frac{\partial \vec{X}'}{\partial s'} \times (\vec{X} - \vec{X}')}{\{|\vec{X} - \vec{X}'|^2 + \mu^2\}^{3/2}} - \left(\frac{\partial \vec{X}}{\partial s} \times \frac{\partial^2 \vec{X}}{\partial s^2} \right) P(s'), \quad (2.27)$$

and

$$\vec{Q}_{V\infty} = \frac{\frac{\partial \vec{X}'}{\partial s'} \times (\vec{X} - \vec{X}')}{\{|\vec{X} - \vec{X}'|^2 + \mu^2\}^{3/2}}. \quad (2.28)$$

The accuracy of the numerical calculations of the first integral in equation (2.26) may be significantly improved if further terms in the Taylor series are included and Hon and Walker (1987) suggest that this is necessary to compute accurate solutions for filaments with small vortex cores moving near solid boundaries. For each value of s on the filament the remaining portion of the vortex filament is broken into three segments; in this case, the first term of equation (2.26) becomes

$$\int_{-l}^l \vec{Q}_V ds' = \int_{-l}^{s-\Delta s} \vec{Q}_V ds' + \int_{s-\Delta s}^{s+\Delta s} \vec{R}_V ds' + \int_{s+\Delta s}^l \vec{Q}_V ds', \quad (2.29)$$

where \vec{R}_V is an approximation to the integrand \vec{Q}_V when the field point approaches a filament point, and is given by

$$\vec{R}_V(s', s) = \vec{D}(s' - s)^3 + \vec{E}(s' - s)^4 + \dots \quad (2.30)$$

for $s' \sim s$, where \vec{D} and \vec{E} are complicated vector functions given in Appendix A. Consequently, when the field point approaches a filament point, the integrand of \vec{Q}_V given by equation (2.27) is approximately equal to \vec{R}_V and the integral around $s = s'$ defined by

$$\vec{I}_V = \int_{s-\Delta s}^{s+\Delta s} \vec{R}_V(s, s', t) ds' \quad (2.31)$$

may be performed analytically. A detailed analytical solution for \vec{I}_V due to Hon and Walker (1987) is given in Appendix A. The limits of the integral \vec{I}_V are somewhat a matter of choice; however the choice of the interval $(-\Delta s, \Delta s)$ gives excellent results when the numerical mesh on the filament is refined. Only those integrals from $-l$ to $-\Delta s$ and Δs to l need to be computed numerically. The parameter l must be determined by numerical experimentation and in all cases considered $l = 5$ is sufficient to insure that the straight portions of the filament are not affected by the deformation of the filament near the cylinder.

Having described the calculation of the self-induced portion of the velocity field, we now discuss calculation of the image field.

2.5 The Image-Induced Velocity Field on the Vortex

In Section 2.2, we have described the general procedure to obtain the image velocity field at any field point outside the cylinder. However, the transform of the radial velocity $\frac{\partial \phi}{\partial r} |_{r=1}$ given by equation (2.15) must be computed first. To evaluate ϕ_I on the vortex filament, it is more convenient to integrate equation (2.15) directly rather than using Fast Fourier Transform (FFT) techniques which are efficient only when the points of evaluation correspond exactly to the nodes of the discretized physical domain (θ, z) . Fortunately, the integral in the z direction appearing in the expression for $\hat{U}_{Vr} |_{r=1}$ defined by equation (2.15) can be obtained analytically. The procedure to obtain this analytical solution is given as follows. Let

$$\chi = z - z'$$

and

$$c = \sqrt{(\cos \theta - x')^2 + (\sin \theta - y')^2},$$

then using equations (2.14) and (2.15) we obtain

$$\hat{U}_{Vr} |_{r=1} = \frac{\Gamma}{4\pi} \int_{-\pi}^{\pi} \int_C (H + G) e^{-im\theta} e^{-ikz'} ds' d\theta, \quad (2.32)$$

where

$$H = \int_{-\infty}^{\infty} \frac{\left\{ \frac{\partial y'}{\partial s'} \chi - \frac{\partial z'}{\partial s'} (\sin \theta - y') \right\} \cos \theta e^{-ik\chi} d\chi}{\{c^2 + \chi^2\}^{3/2}}, \quad (2.33)$$

$$G = \int_{-\infty}^{\infty} \frac{\left\{ \frac{\partial z'}{\partial s'} (\cos \theta - x') - \frac{\partial x'}{\partial s'} \chi \right\} \sin \theta e^{-ik\chi} d\chi}{\{c^2 + \chi^2\}^{3/2}}. \quad (2.34)$$

Note that H and G can be obtained analytically (see Appendix B) and are given by

$$H = -2 \left\{ \frac{\partial z'}{\partial s'} (\sin \theta - y') \frac{|k|}{c} K_1(c|k|) + ik \frac{\partial y'}{\partial s'} K_0(c|k|) \right\} \cos \theta, \quad (2.35)$$

$$G = 2 \left\{ \frac{\partial z'}{\partial s'} (\cos \theta - x') \frac{|k|}{c} K_1(c|k|) + ik \frac{\partial x'}{\partial s'} K_0(c|k|) \right\} \sin \theta. \quad (2.36)$$

Therefore the transform of the radial velocity becomes

$$\hat{U}_{Vr} |_{r=1} = \frac{\Gamma}{4\pi} \int_{-\pi}^{\pi} e^{-im\theta} \int_C [ikBK_0(c|k|) + A|k|K_1(c|k|)] e^{-ikz'} ds' d\theta, \quad (2.37)$$

where

$$A = \frac{2}{c} \{ (\cos \theta - x') \sin \theta - (\sin \theta - y') \cos \theta \} \frac{\partial z'}{\partial s'}, \quad (2.38)$$

$$B = 2 \left\{ \frac{\partial x'}{\partial s'} \sin \theta - \frac{\partial y'}{\partial s'} \cos \theta \right\}. \quad (2.39)$$

The solution for the velocity field due to the image of the filament may be obtained by direct differentiation of equation (2.16) with the radial velocity due to a vortex filament in free space at the cylinder boundary given by equation (2.37). By substituting (2.37) into (2.16) and switching the order of the integral and sum, equation (2.16) may be written as

$$\phi_I = -\frac{\Gamma}{16\pi^3} \sum_{m=-\infty}^{\infty} \int_{-\pi}^{\pi} \int_C (I_1 + I_2) ds' \cos m(\theta - \alpha) d\alpha, \quad (2.40)$$

where

$$I_1 = 2 \int_0^{\infty} AK_1(ck) \frac{K_m(rk)}{K'_m(k)} \cos k(z - z') dk,$$

$$I_2 = -2 \int_0^{\infty} BK_0(ck) \frac{K_m(rk)}{K'_m(k)} \sin k(z - z') dk.$$

The velocity components can be obtained by differentiation under the integral and it follows that

$$U_{Ir} = -\frac{\Gamma}{16\pi^3} \sum_{m=-\infty}^{\infty} \int_{-\pi}^{\pi} \int_C (I_3 + I_4) ds' \cos m(\theta - \alpha) d\alpha, \quad (2.41)$$

$$U_{I\theta} = -\frac{\Gamma}{16\pi^3} \sum_{m=-\infty}^{\infty} \int_{-\pi}^{\pi} \int_C \frac{m}{r} (I_5 + I_6) ds' \sin m(\theta - \alpha) d\alpha, \quad (2.42)$$

$$U_{Iz} = -\frac{\Gamma}{16\pi^3} \sum_{m=-\infty}^{\infty} \int_{-\pi}^{\pi} \int_C (I_7 + I_8) ds' \cos m(\theta - \alpha) d\alpha, \quad (2.43)$$

where the specific forms of the integrals I_3 through I_8 are given in Appendix B; in these equations the subscript I denotes the image. Note that the self-induced velocity field is given in Cartesian coordinates; this is because it is simpler to advance the vortex in Cartesian space. The image velocity field may be rewritten in Cartesian coordinates as

$$\vec{U}_I = (U_{Ir} \cos \theta - U_{I\theta} \sin \theta) \hat{i} + (U_{Ir} \sin \theta + U_{I\theta} \cos \theta) \hat{j} + U_{Iz} \hat{k}, \quad (2.44)$$

and this expression will be used to convect the vortex. To evaluate the integrals along the space curve in equations (2.41)-(2.43), we employ a procedure similar to that used for the evaluation of the self-induced velocity.

2.6 Filament Motion

The velocity field induced by a general vortex filament in the presence of the cylinder and in a mean streaming motion is given by equation (2.19). To calculate the motion of the vortex, we evaluate (2.19) on the filament; each point is then advanced according to the evolution equation

$$\frac{\partial \vec{X}}{\partial t}(s, t) = \vec{U}. \quad (2.45)$$

In general, the initial position of the filament is given by

$$\vec{X}(s, t = 0) = f(s)\hat{i} + y_s\hat{j} + z_s\hat{k}. \quad (2.46)$$

The results shown in this Chapter correspond to the situation where the vortex is assumed initially straight and here we take $y_s = 1.5$ for the stagnant medium case and $y_s = 2.0$ for the mean flow case; also, $z_s = 0$ and $f(s) = s$.

2.7 The Pressure Field

To obtain the surface pressure field we begin by noting that the pressure gradients on the cylinder are obtained from Euler's equations which are given by, in dimensionless form

$$\frac{\partial \vec{U}}{\partial t} + (\vec{U} \cdot \nabla) \vec{U} = -\nabla p, \quad (2.47)$$

where $p = (p^* - p_\infty)/\rho W_\infty^2$ where p^* is dimensional and p_∞ is a constant reference pressure. Here \vec{U} denotes the total inviscid velocity distribution on the surface of the cylinder (i.e. $r=1$) and is, according to equation (2.19), given by

$$\vec{U} = (\vec{U}_I + \vec{U}_V + \vec{U}_M)|_{r=1}. \quad (2.48)$$

Using the definition of the velocity potential $\vec{U} = \nabla \phi$ and after interchange of the time derivative and gradient, we obtain

$$\nabla \left\{ \frac{\partial \phi}{\partial t} + \frac{|\vec{U}|^2}{2} + p \right\} = 0. \quad (2.49)$$

Integrating equation (2.49), we have

$$\frac{\partial \phi}{\partial t} + \frac{|\vec{U}|^2}{2} + p = f_0(t), \quad (2.50)$$

where f_0 is the Bernoulli constant obtained by evaluating the left hand side of equation (2.49) at the beginning of the integration path; if all paths begin at $z = -\infty$, $\theta = \theta_0$ then $f_0 = \frac{1}{2}U_M^2(r=1, \theta_0)$ where θ_0 is a parameter (see below).

The surface speed \bar{U} is computed in polar coordinates and its components in both the azimuthal direction and along the axis of the cylinder are given respectively by

$$U_\theta = U_{I\theta} + U_{V\theta} + U_{M\theta}, \quad (2.51)$$

and

$$U_z = U_{Iz} + U_{Vz} + U_{Mz}. \quad (2.52)$$

Note that in the above equations the components of \bar{U}_V , \bar{U}_I and \bar{U}_M are evaluated at $r=1$. The azimuthal and axial velocity components of \bar{U}_V (vortex induced velocity in free space) may be written as

$$\begin{aligned} U_{V\theta}(s, t) |_{r=1} = & \frac{\Gamma}{4\pi} \int_C \frac{\left\{ \frac{\partial x'}{\partial s'} (\sin \theta - y') - \frac{\partial y'}{\partial s'} (z - z') \right\} \sin \theta ds'}{\{(\cos \theta - x')^2 + (\sin \theta - y')^2 + (z - z')^2\}^{3/2}} \\ & + \frac{\Gamma}{4\pi} \int_C \frac{\left\{ \frac{\partial x'}{\partial s'} (\cos \theta - x') - \frac{\partial y'}{\partial s'} (z - z') \right\} \cos \theta ds'}{\{(\cos \theta - x')^2 + (\sin \theta - y')^2 + (z - z')^2\}^{3/2}}, \end{aligned} \quad (2.53)$$

and

$$U_{Vz} = \frac{\Gamma}{4\pi} \int_C \frac{\left\{ \frac{\partial x'}{\partial s'} (\sin \theta - y') - \frac{\partial y'}{\partial s'} (\cos \theta - x') \right\} ds'}{\{(\cos \theta - x')^2 + (\sin \theta - y')^2 + (z - z')^2\}^{3/2}}. \quad (2.54)$$

The calculation of the image induced velocity on the cylinder is not a trivial task, especially when results for surface quantities such as the pressure distribution on the surface of the cylinder are required. In this case, the methodology developed in Section 2.2 to find the image induced velocity field on the vortex is no longer efficient computationally and a large amount of computer time is required to generate results on a fairly coarse surface grid. For instance, it takes 4 hours of CPU time (using the Cray Y-MP 864) to obtain results on a (16x51) surface mesh. However, since the evaluation points on the cylinder surface can be chosen to correspond to a standard uniformly distributed grid, the Fast Fourier Transform (FFT) technique can be employed to efficiently calculate the image induced velocity on the cylinder. First the radial velocity $U_{Vr} |_{r=1}$ due to the vortex is computed according to equation (2.14), then its Fourier Transform given by equation (2.15) is obtained using the FFT. Equation (2.6) is then employed to obtain $\hat{\phi}_I |_{r=1}$ which is given by

$$\hat{\phi}_I |_{r=1} = \frac{\partial \hat{\phi}_V}{\partial r} |_{r=1} \times \frac{K_m(|k|)}{|k| K'_m(|k|)}. \quad (2.55)$$

The velocity potential is then computed according to equation (2.16) by using the inverse FFT. For example, to compute $U_{Iz} |_{r=1}$ which is equal to $\frac{\partial \phi_I}{\partial z} |_{r=1}$, the quantity $ik\hat{\phi}_I |_{r=1}$ in the spectral domain is inverted back to the physical domain using the inverse Fourier transform. All other image induced velocity components on the surface of the cylinder are obtained in a similar way.

The velocity potential ϕ includes the effect of the mean flow, the image, the vortex itself, and the mean flow potential which may be obtained directly by integration of (2.17). The potential due to the vortex itself is not easy to obtain and this is described now. Let \vec{X} denote a vector coordinate along any path in the fluid then

$$\phi_V = \phi_V(\vec{X}_0) + \int_{\text{path}} \vec{U}_V \cdot d\vec{X}, \quad (2.56)$$

where \vec{X}_0 is the initial point of the curve. Consider the case where the integration path lies on the cylinder surface at a fixed angular location θ_0 ; in the z -direction then

$$\phi_V(\theta_0, z) = \phi_V(\theta_0, -\infty) + \int_{-\infty}^z U_{Vz}(\theta_0, z) dz, \quad (2.57)$$

where U_{Vz} is the velocity due to the vortex filament alone in the z -direction and is given by equation (2.54); substitution of equation (2.54) into (2.57), switching the order of the integration and integrating in z yields

$$\phi_V(\theta_0, z) = \phi_V(\theta_0, -\infty) + \int_C \frac{F_1}{F_2^2} \left\{ \frac{z - z'}{\{(F_2^2 + (z - z')^2)^{1/2}} + 1 \right\} ds'. \quad (2.58)$$

In equation (2.58),

$$F_1 = \frac{\partial x'}{\partial s'}(\sin \theta_0 - y') - \frac{\partial y'}{\partial s'}(\cos \theta_0 - x'), \quad (2.59)$$

and

$$F_2 = c(\theta_0, s'). \quad (2.60)$$

The integral along the filament in equation (2.58) may be evaluated numerically. The azimuthal position θ_0 appearing in equation (2.57) is a parameter and may thus be varied until ϕ_V at all the desired azimuthal locations is determined.

Once the surface speeds and velocity potential are obtained, the pressure is then computed according to equation (2.59). To evaluate the pressure gradients, one is tempted to apply FFT techniques to the pressure field in a way similar to that described to obtain the image induced velocity field; there, the quantity $ik\hat{p}$ is inverted back to the physical domain using FFT to obtain $\partial p/\partial z$; similarly the quantity $im\hat{p}$ is inverted back to obtain $\partial p/\partial \theta$. However, using this procedure leads to oscillation of the results especially at points located away from the vortex in the

z -direction. On the other hand, when using the Euler's equations (2.47) directly, the pressure gradient results show no oscillatory behavior. Thus, throughout the present work, the Euler's equations are employed to obtain the pressure gradients and the procedure is explained as follows. First, the equations (2.53) and (2.54) for the vortex induced velocity field are used to analytically obtain the spatial derivatives. The resulting equations for the various derivatives in space are given in Appendix C. Similarly, FFT techniques employed to compute the image induced velocity field are applied to obtain its spatial derivatives in both θ and z directions. For example, the term $-k^2 \hat{\phi}_I|_{r=1}$ is calculated and then inverted back to the physical domain to yield $\partial U_{Iz}/\partial z$.

2.8 Numerical Methods

The evolution of the vortex filament is a non-trivial calculation which is made more difficult by the presence of the cylinder. The Lagrangian calculation corresponding to the solution of (2.45) subject to the initial condition (2.46) is computed by the 4th order Runge-Kutta method. The vortex is discretized using a mesh size Δs and the grid points are given parametrically by

$$s_j = (j - M/2 - 1)\Delta s, \quad (2.61)$$

where here $M = 100$, $j = 1, \dots, M + 1$ and $\Delta s = .1$; the length $2l$ over which the filament may deform is thus given by 10. Solutions have been computed for several larger values of l corresponding to $2l = 12, 16$ with no change in the computed solution to three digits. Use of the above numerical parameters to define the filament and of the time step $\Delta t = .01$ insures at least three-figure accuracy in the computed vortex trajectory as those parameters are reduced.

The self-induced velocity of the filament is given by equation (2.26) and Simpson's rule has been employed for those integrals. The derivatives with respect to s , say $\frac{\partial \vec{X}}{\partial s}$ have been computed using the second order central difference scheme according to

$$\frac{\partial \vec{X}}{\partial s} \Big|_{s=s_j} = \frac{\vec{X}_{j+1} - \vec{X}_{j-1}}{2\Delta s} + O(\Delta s^2). \quad (2.62)$$

There are a number of other numerical parameters in the present calculations and a series of numerical tests were carried out to insure the accuracy of the computations. First, for the computations of the vortex trajectory, the real valued integrals corresponding to the calculation of the image induced velocities are all of the Fourier type in k . A transformation in k is employed to cluster the grid near $k = 0$ and the resulting integrals are computed using Simpson's rule. A total of 100 points in k are used to insure three-digit accuracy compared to the solution for 200 points when the distance between the vortex and the cylinder is no less than

two core radii. The integrals in the angular variable α (see equations 2.41-2.43) are calculated using a uniform mesh. A grid size $\Delta\alpha = 2\pi/40$ is employed to insure 3 digit accuracy at all times compared with the solutions for $\Delta\alpha = 2\pi/80$. In addition, the number of modes in the azimuthal direction must be specified; here again, several different values were tried corresponding to 8, 10 and 12 modes with no difference in the computed solution for the filament position to three digits.

Second, the computations of the image induced velocities at the surface of the cylinder used in the evaluation of the surface pressure field are performed using a different procedure. As mentioned earlier, because the airframe surface is fixed and a computational grid is easily defined, it is more efficient computationally to use the Fast Fourier Transform (FFT) technique in the pressure calculations. The Fourier transform of any flow quantity, is defined as

$$\hat{G}(m, k) = \int_{-\infty}^{\infty} \int_{-\pi}^{\pi} G(\theta, z) e^{-im\theta - ikz} d\theta dz \quad (2.63)$$

where $m = 0, \pm 1, \pm 2, \pm 3, \dots$ is the transform variable corresponding to θ and k (real) is the transform variable corresponding to z . A finite range $-L \leq z \leq L$ is used in the numerical scheme to represent the infinite range of z . An adequate range of z is determined by comparing the results with the results of larger ranges. Several tests have been conducted to determine the appropriate range and the value $L = 12.8$ is used here to obtain the results. In addition, values of $\Delta z = .05, .1$ and $.2$ were tested with at least two-digit agreement between all three grid sizes; however, to obtain better, more resolved results for the pressure, especially in the latter stages of the calculations, the present results are for $\Delta z = .05$ with the number of points $M_z = 512$. The number of points in the θ direction is taken to be $M_\theta = 32$ which insures at least three-digit accuracy compared with $M_\theta = 64$. The grid employed for the Fourier transform is given by

$$-\pi \leq \theta \leq \pi, \quad \theta_i = (i - M_\theta/2 - 1)\Delta\theta \quad \text{for } i = 1, 2, \dots, M_\theta, \quad (2.64)$$

$$-L \leq z \leq L, \quad z_j = (j - 1 - M_z/2)\Delta z \quad \text{for } j = 1, 2, \dots, M_z, \quad (2.65)$$

$$-\bar{L} \leq k \leq \bar{L}, \quad k_l = (l - 1 - M_z/2)\Delta k \quad \text{for } l = 1, 2, \dots, M_z, \quad (2.66)$$

where the grid spacings $\Delta\theta$, Δz and Δk should satisfy the following relations

$$\Delta\theta = \frac{2\pi}{M_\theta}, \quad \Delta z = \frac{2L}{M_z}, \quad \Delta k = \frac{\pi}{L}, \quad (2.67)$$

and M_z and M_θ are chosen to be a power of 2 in order to use efficiently the Fast Fourier Transform.

Lastly, because the velocities are more sensitive to numerical error than are the filament positions, it has been found necessary to use a much finer grid over the vortex filament in calculating the surface pressure; thus $\Delta s = .025$ in evaluating the Biot-Savart integral (see equations 2.53, 2.54 and 2.58) in all the pressure and pressure gradient calculations to be presented.

2.9 Results

The methodology described in the previous sections is developed by nondimensionalizing the velocity field with respect to W_∞ ; for the case of a stagnant environment $W_\infty = \Gamma^*/a$ and for the mean flow W_∞ corresponds to the velocity along the axis of the cylinder at upstream infinity in the z -direction. This has been done to accommodate the calculation of the boundary-layer flow to be discussed in Chapter 5. However, the results presented in this chapter were generated using the original formulation of Affes and Conlisk (1992) where the velocity field is made dimensionless with respect to downwash velocity at infinity (U_∞) in order to simulate both the forward flight and hover. In this case, the velocity field \vec{U} given by equation (2.19) takes a slightly different form. First, the vortex induced velocity \vec{U}_V described by equation (2.20) is rewritten as

$$\vec{U}_V(s, t) = -\frac{\text{sgn}(\Gamma^*)}{\beta} \int_C \frac{(\vec{X} - \vec{X}') \times \frac{\partial \vec{X}'}{\partial s'} ds'}{\left\{ |\vec{X} - \vec{X}'|^2 + \mu^2 \right\}^{3/2}}, \quad (2.68)$$

where

$$\beta = 4\pi \frac{U_\infty a}{|\Gamma^*|}. \quad (2.69)$$

Similarly, the image induced velocity is modified by including the constant β in the expression of \vec{U}_V , which is given by equation (2.37). The mean flow component \vec{U}_M given by equation (2.17) has another form and is given by

$$\vec{U}_M = \frac{\sin 2\theta}{r^2} \hat{i} - \left(1 + \frac{\cos 2\theta}{r^2} \right) \hat{j} + \alpha \hat{k}, \quad (2.70)$$

where

$$\alpha = \frac{W_\infty}{U_\infty}, \quad (2.71)$$

is the ratio of the downwash velocity at infinity to the mean velocity at infinity in the z -direction. In addition, the dimensionless time t is scaled differently in the original formulation and is defined by

$$t = \frac{U_\infty}{\beta a} t^*, \quad (2.72)$$

where t^* is the dimensional time. Thus the vortex trajectories computed here are obtained according to the evolution equation which has a different form from that given by equation (2.45). Here we have

$$\frac{\partial \vec{X}}{\partial t}(s, t) = \beta \vec{U}. \quad (2.73)$$

Similarly, Euler's equations for the pressure gradients and Bernoulli's equation for the pressure are modified to account for both the new dimensionless velocity and the new time scale. The nondimensional variables defined in Section 2.2 will be used in Chapters 3 and 5.

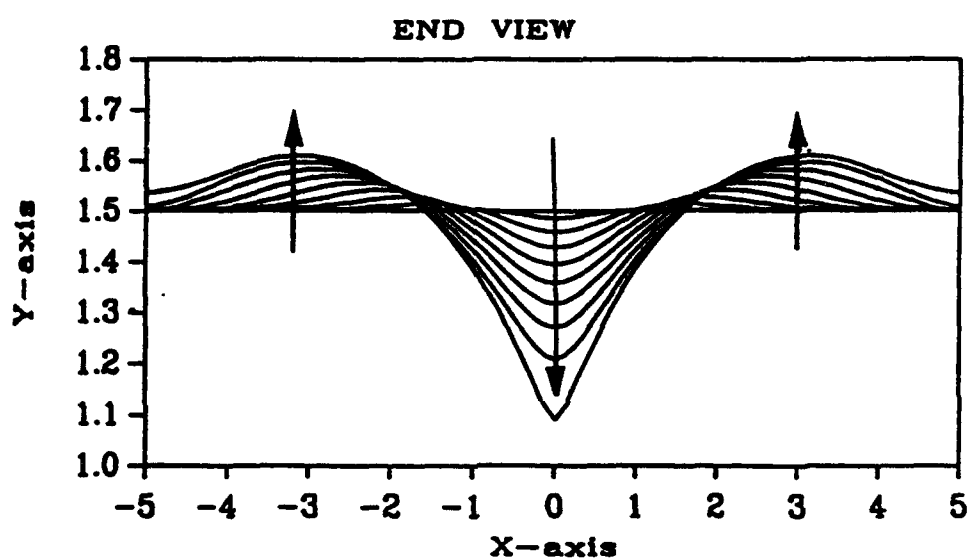
Stagnant Environment

As a benchmark with which to compare the mean flow results we consider the case of a single infinite vortex filament in a stagnant medium. The initial position of the vortex corresponds to a straight filament oriented 90° to the generators of the cylinder at time $t = 0$. This initial position is represented in Cartesian coordinates by $x = s$, $y = 1.5$ and $z = 0$. Here the dimensional velocity scale may be taken to be $|\Gamma^*/a|$ and thus the circulation may be scaled out of the problem. In this case $\bar{U}_M = 0$ in equation (2.70) and $\beta = 4\pi$. The dimensionless core radius is fixed at $a_v = .1$. On Figure 2.1 are the results for the filament positions plotted every ten time steps from time $t = 0$ to $t = 1$; here $\Delta t = .01$. Note that as time increases, the filament increasingly deforms and the head of the vortex begins to move rapidly toward the cylinder. Note however that the motion of the filament is rather slow compared to the mean flow calculations as we will see below. The pressure and pressure gradient shown on Figure 2.2 are plotted every 10 time steps from time $t = 0.1$ to time $t = 0.9$ and at time $t = 0.96$. Note that an adverse pressure gradient emerges as the vortex approaches the airframe. This results in a large-amplitude pressure suction peak on the airframe directly under the head of the vortex. Figure 2.3 shows the pressure distribution on the surface of the cylinder; pressure contour lines are plotted at $t = 0.95$ when the vortex head is one core radius above the cylinder. Note that the area around the suction peak denoted by contour levels A,B,C,D and E covers only a small portion of the cylinder which is indicative of the local character of the influence of the vortex on the cylinder.

The presence of a mean motion as is the case in applications accelerates the development of the pressure field and this situation is considered next.

Mean Flow

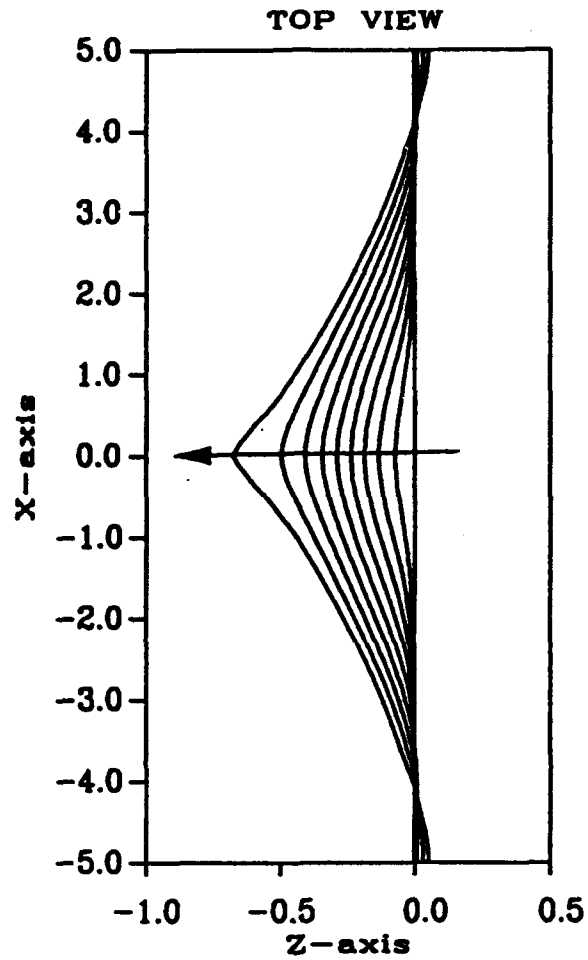
There are three main parameters whose effects are of interest here; these are α , β , and the assumed dimensionless viscous core size, a_v ; the results to be described here are for the original nondimensionlization of Affes and Conlisk (1992) as discussed in the previous subsection. In all the following cases, the initial configuration of the vortex filament is $x = s$, $y = 2.0$ and $z = 0$ and the results are plotted every five time steps beginning at $t=0$. On Figure 2.4 are the results for the filament position for $\alpha = 1$, $\beta = 3$ for the case where the core size is fixed



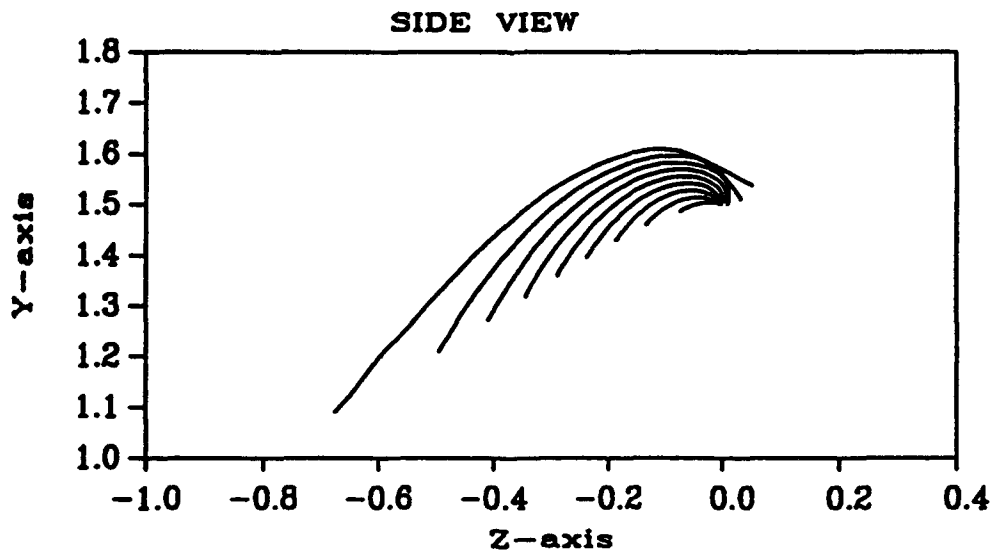
(a)

Figure 2.1: Filament positions for the case of no mean flow. (a) End view, (b) top view, (c) side view. The positions are plotted every 10 time steps starting from $t = 0$. Here $\Delta t = 0.01$ and the vortex core radius $a_v = 0.1$. Arrow denotes increasing time.

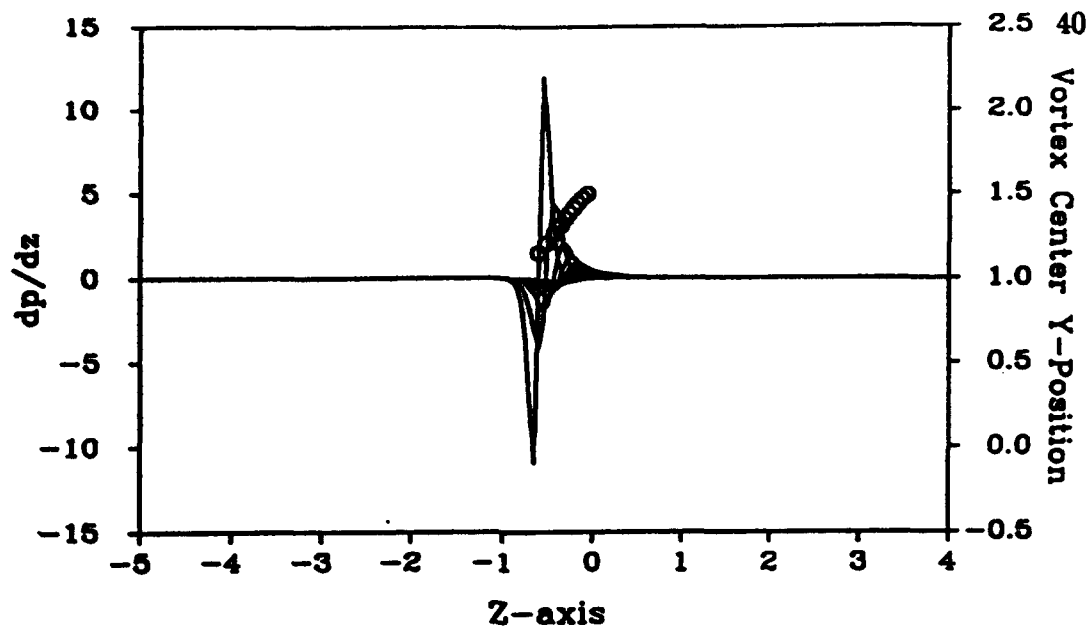
Figure 2.1 (continued)



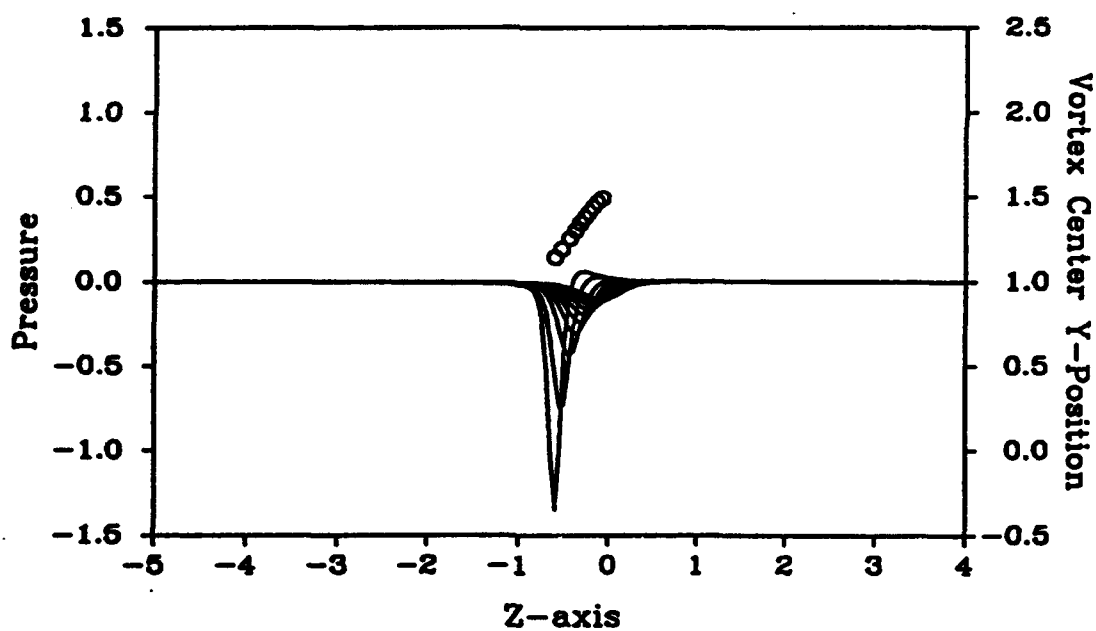
(b)



(c)



(a)



(b)

Figure 2.2: Results for the axial pressure gradient and pressure at $\theta = \pi/2$ for the parameters of Figure 2.1. (a) Pressure gradient, (b) pressure. Here results are plotted every ten time steps ($\Delta t = 0.01$) up to $t = 0.9$ including the results at $t = 0.96$. The circles denote the positions of the vortex center.

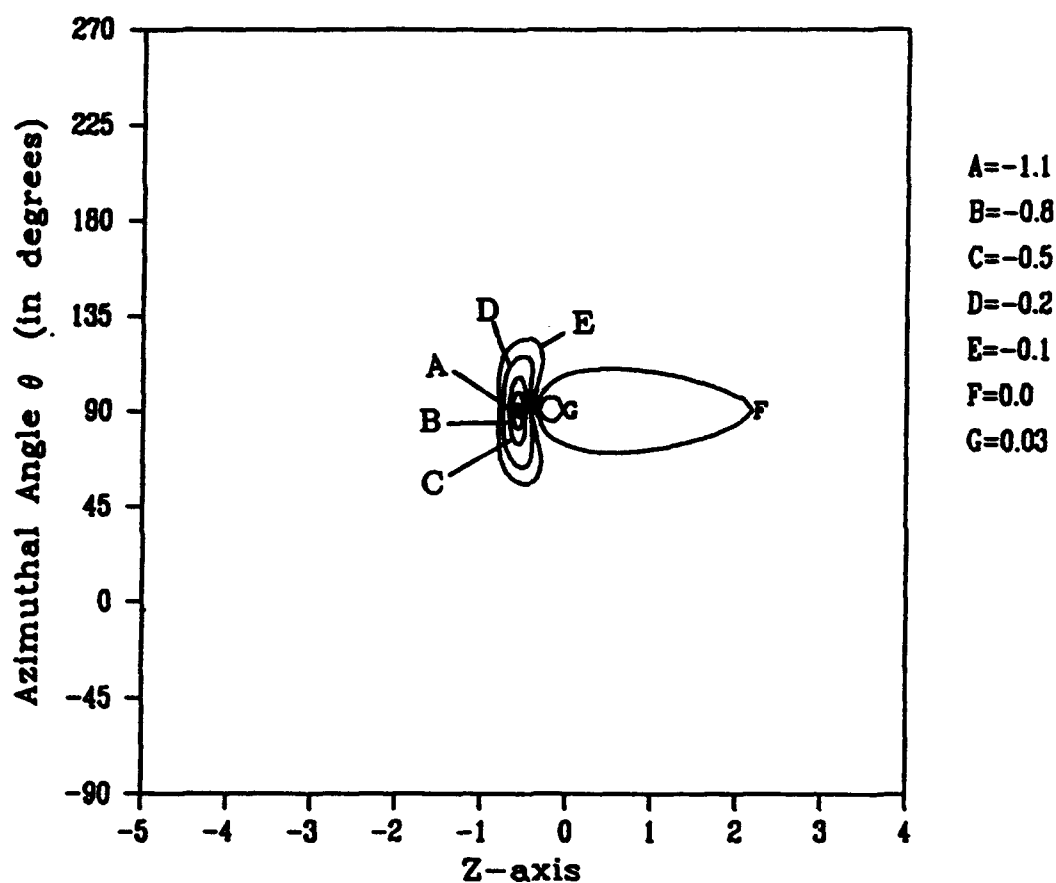


Figure 2.3: Results for surface pressure for the parameters of Figure 2.1. Pressure contours are plotted at different levels given on the side of the figure. Here results are plotted at time $t = 0.95$.

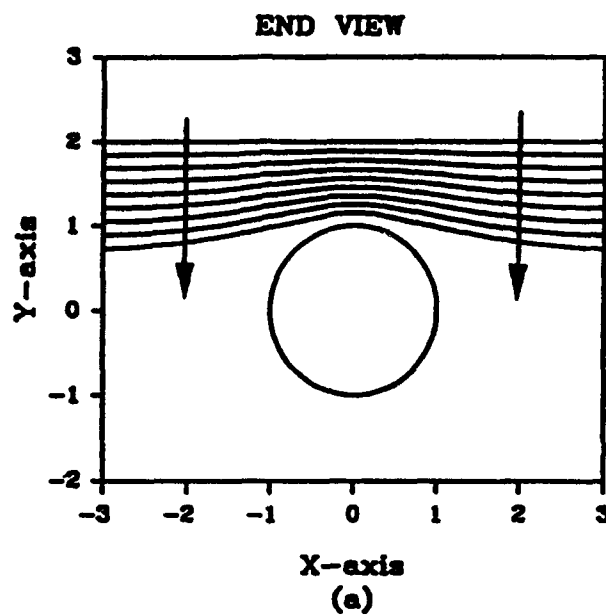
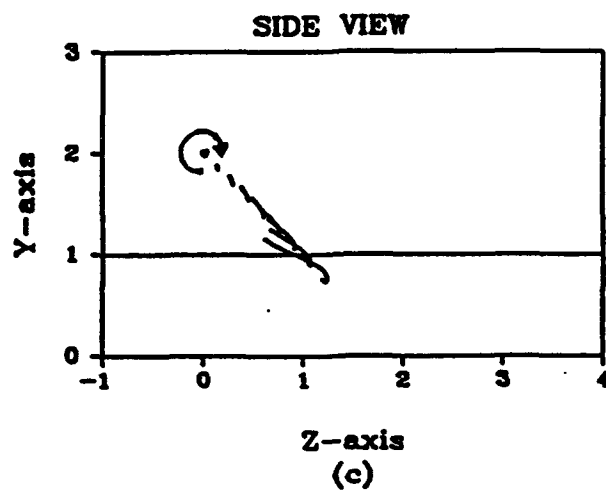
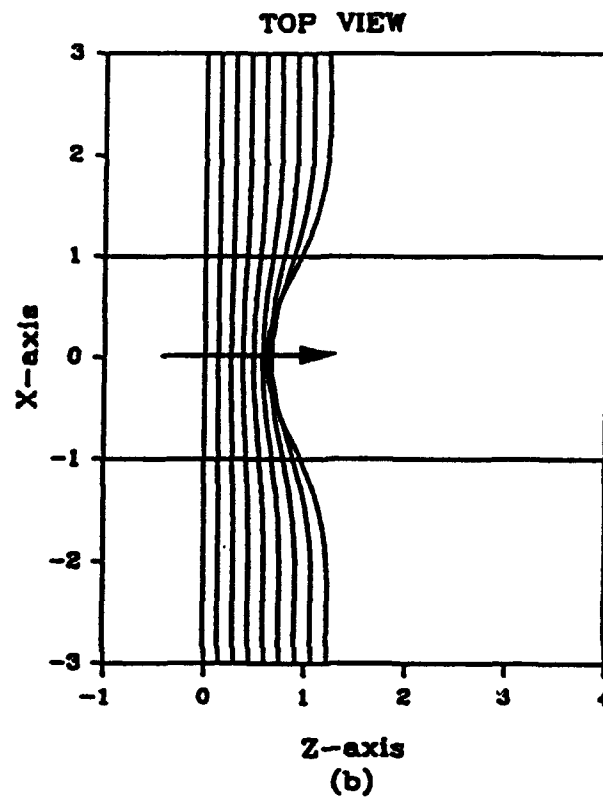


Figure 2.4: Filament positions for the mean flow case where $\alpha = 1.0$, $\beta = 3.0$. (a) End view, (b) top view, (c) side view. Here $\Delta t = 0.01$ and the vortex core radius $a_v = 0.1$. Arrow denotes increasing time. Here positions are plotted every 5 time steps ($\Delta t = 0.01$) up to $t = 0.4$.

Figure 2.4 (continued)



at $a_v = .1$; this results in a value of $\mu = .047$. The sign of the circulation is positive and is also shown and corresponds to the experimental situation of Liou, Komerath, and McMahon (1990) (see also Brand et. al 1989 and Brand 1989). Similar results are obtained for the case of $\alpha = 2$ and they are shown in Figure 2.5; here the convection distance in the z direction is larger because the mean axial flow is larger; the qualitative characteristics of this case are similar to those of Figure 2.4. Note the deformation of the vortex filament as it approaches the airframe; on this figure, the calculation was stopped after 40 time steps and thus the total time of the calculation is $t = .4$; at the last time shown, the head of the vortex is just over one core radius from the cylinder. Soon after this time a kink begins to appear in the vortex at the midpoint $s = 0$ and the calculation fails. The effect of vortex core size is depicted on Figure 2.6 for the case of $\alpha = 2$, and $\beta = 3$. Here $a_v = .05$ and note that the results are very similar to the previous results except in the latter few time steps; in particular the vortex head moves faster toward the cylinder with a slower speed in the z -direction, a situation not evident in the larger core result (Figure 2.5); similar results are noted for the $\alpha = 1$ case. At the last time step shown for $a_v = .05$, the head of the vortex is just over one core radius from the cylinder and the total dimensionless time of the calculation is $t = .4$.

For all the results shown so far, the sign of the circulation has been assumed positive; the experimental situation described by Bi and Leishman (1990,1991) and Leishman and Bi (1990) may be modeled to a first approximation by merely switching the sign of the circulation. The experimental conditions correspond to $\alpha = 1.72$, $\beta = 2.4$; the core size has been fixed at .1. On Figure 2.7 are the results for a advance ratio of .075. Here, because β is smaller than that used in the previous case the total time of the calculation is longer and the computations are stopped at $t = 0.45$. The end view of the filament motion is similar to the previous results; however the other two views are substantially different. Note in particular the side view where the trajectory suggests a grazing type of motion rather than a direct collision. We note here, however that because of the presence of the downwash, the vortex head will eventually collide with the airframe, although at a substantially different angle than is the case for positive circulation. It should be noted also that the initial position of the vortex does not necessarily correspond to that of the experiments of Bi and Leishman (1991); moreover, the vortex core radius has been fixed as noted above. Consequently, quantitative comparison of the present results with the data of Bi and Leishman (1990,1991) must await future work. However, it is believed that the essential features of the vortex motion may be captured using the present model.

The rather mild filament curvature induced by the cylinder belies the striking nature of the pressure field under the vortex. In all subsequent results the axial pressure gradient on the airframe $\frac{\partial p}{\partial z}$ is plotted at $\theta_0 = \pi/2$ at the time steps corresponding to those plotted for the filament positions; however, the pressure

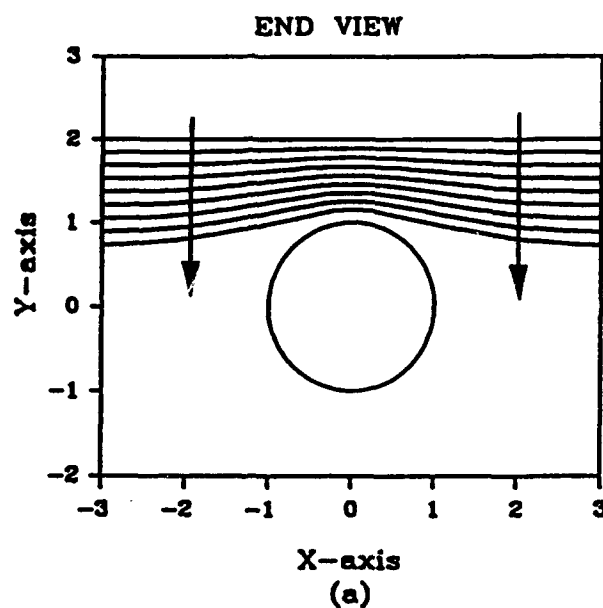
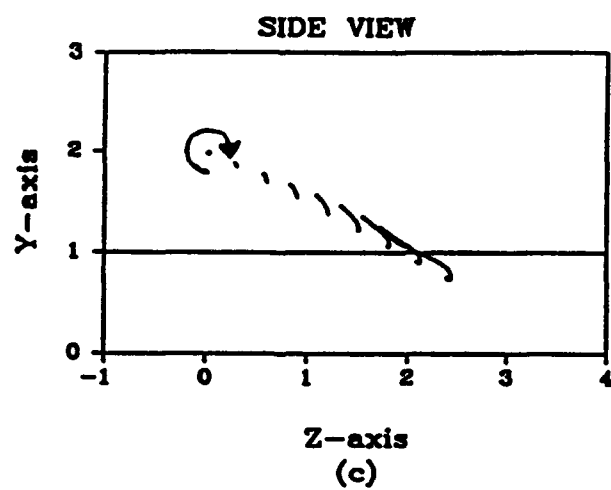
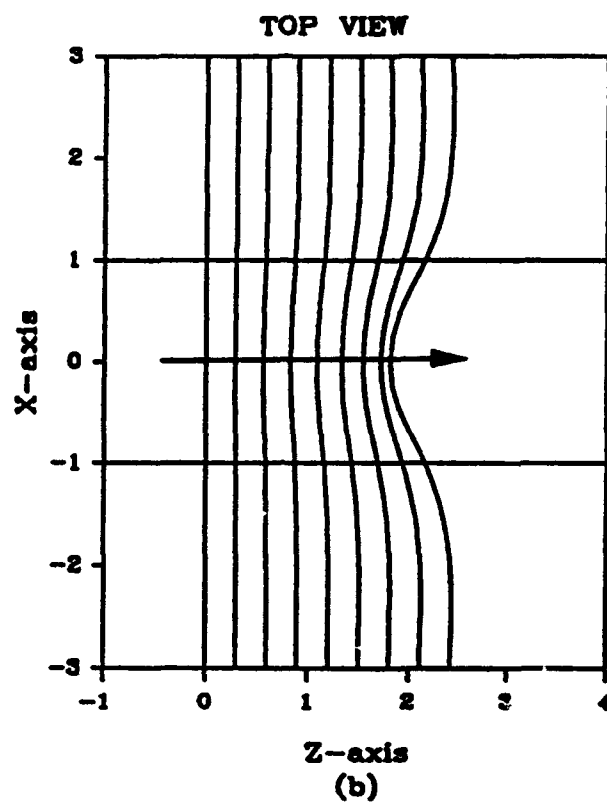


Figure 2.5: Filament positions for the mean flow case where $\alpha = 2.0$, $\beta = 3.0$. (a) End view, (b) top view, (c) side view. Here $\Delta t = 0.01$ and the vortex core radius $a_v = 0.1$. Arrow denotes increasing time. Here positions are plotted every 5 time steps ($\Delta t = 0.01$) up to $t = 0.4$.

Figure 2.5 (continued)



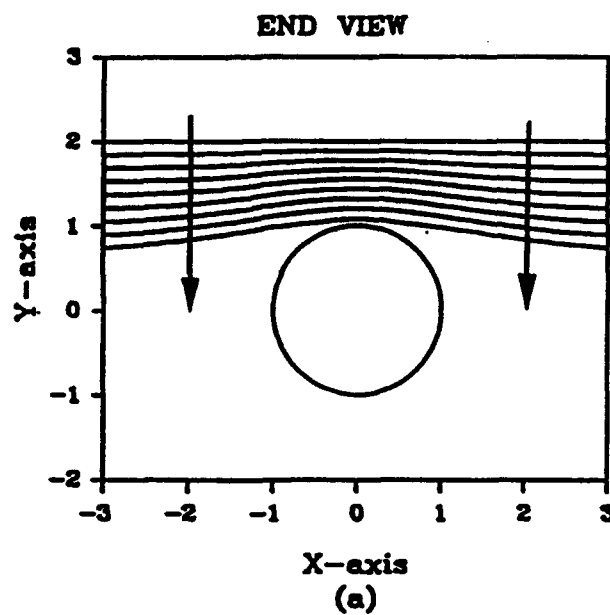
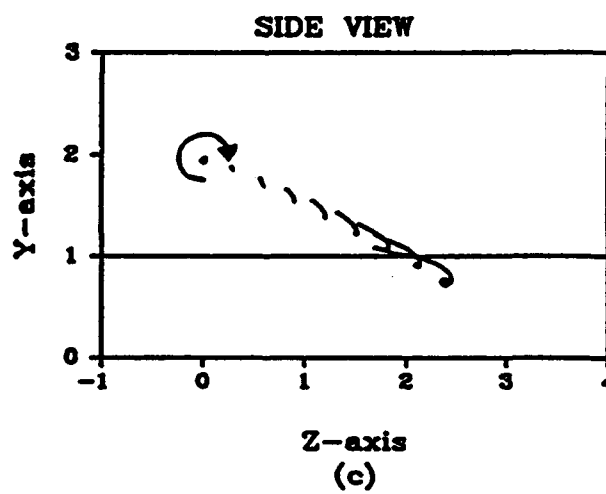
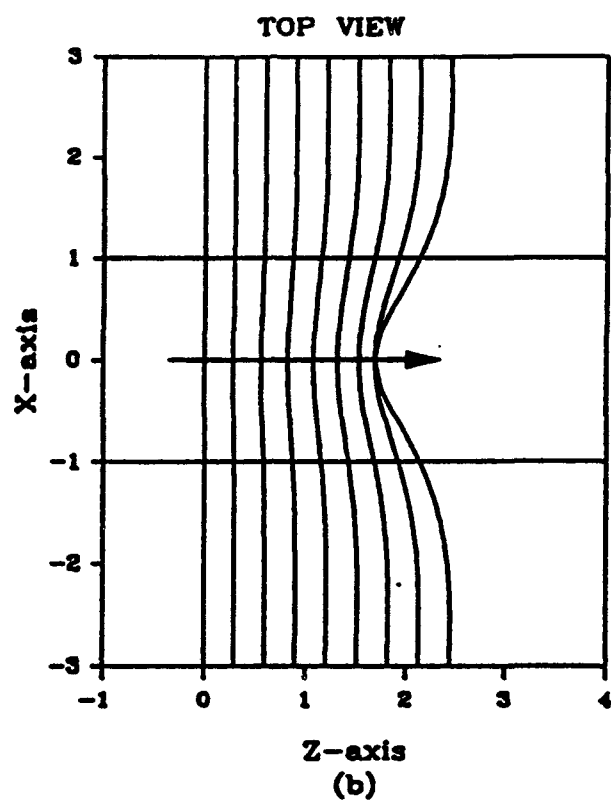


Figure 2.6: Filament positions for the mean flow case where $\alpha = 2.0$, $\beta = 3.0$. (a) End view, (b) top view, (c) side view. Here $\Delta t = 0.01$ and the vortex core radius $a_v = 0.05$. Arrow denotes increasing time. Here positions are plotted every 5 time steps ($\Delta t = 0.01$) up to $t = 0.4$.

Figure 2.6 (continued)



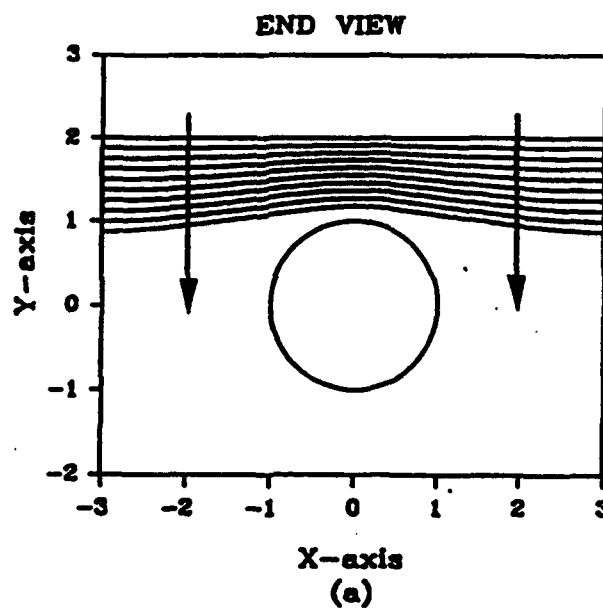
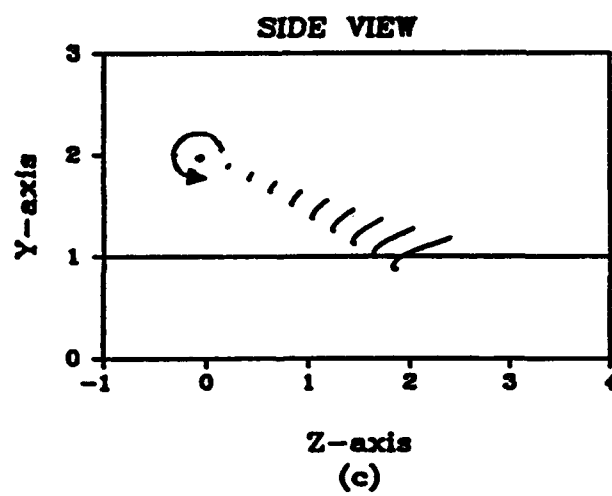
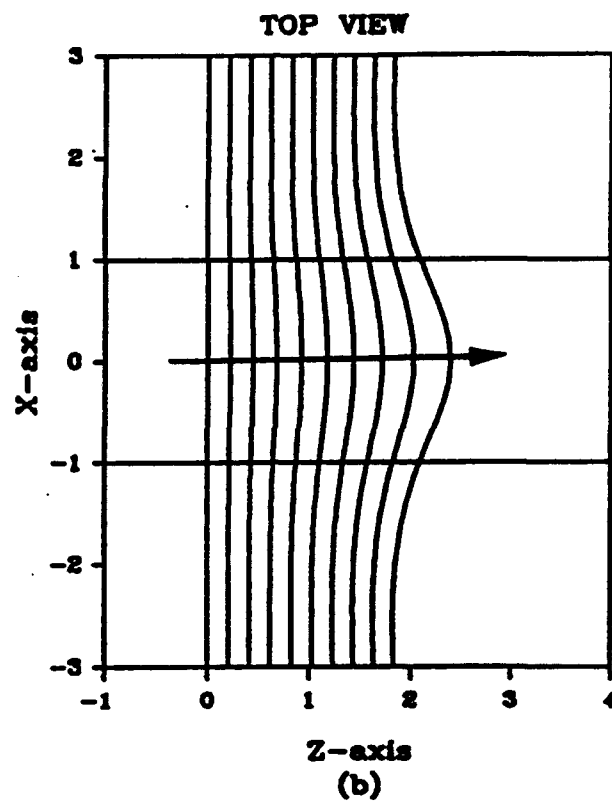


Figure 2.7: Filament positions for the case of Bi and Leishman where $\alpha = 1.72$, $\beta = 2.4$. (a) End view, (b) top view, (c) side view. Here $\text{sgn}(\Gamma) = -1$, $\Delta t = 0.01$ and the vortex core radius $a_v = 0.1$. Arrow denotes increasing time. Here positions are plotted every 5 time steps ($\Delta t = 0.01$) up to $t = 0.45$.

Figure 2.7 (continued)



gradient and pressure initially are not plotted. On Figure 2.8 are the results for the pressure gradient and pressure for the parameters of Figure 2.4. Also shown is the relative position of the vortex head. Note the emergence of a large adverse pressure gradient just downstream of the head of the vortex. The adverse pressure gradient causes a large suction peak to form at the axial location of the head of the vortex. On Figure 2.9 are lines of constant pressure plotted around the cylinder at $t=0.4$. Note the focusing of the pressure valley in the z -direction. Similar results are observed for the case of $\alpha = 2$, $\beta = 3$ depicted on Figure 2.10; the difference in the pressure results at the earlier times is due to the difference in the filament position. However the magnitude of the maximum suction peak is nearly equal in both cases; this is believed to be due to the fact that the local filament position near the pressure evaluation point is very similar in each case. On Figure 2.11 are lines of constant pressure plotted around the cylinder at $t=0.4$. On Figure 2.12, the core size $a_v = .05$ and all other parameters are as on Figure 2.10; here the results are plotted every five time steps beginning at time $t = .05$. The last time step shown on Figure 2.12 corresponds to $t = .37$ and at this time the vortex head position is at nearly the same position as that for the parameters of Figure 2.10 at time $t = .4$. Consequently, the maximum suction peak in each case is nearly equal although the time evolution of the peak is substantially different. This can be seen by noting that in the early stages of the calculation when the vortex is many core radii from the cylinder, the pressure traces in each case are nearly the same; after $t = .3$ as the vortex approaches the cylinder the two solutions begin to deviate.

Finally, on Figure 2.13 are results for negative circulation corresponding to the filament evolution depicted on Figure 2.7. Note that the character of the solution for both the pressure and the pressure gradient is much different than for the case of positive circulation described in the results above. The magnitude of the adverse pressure gradient and the pressure should be compared with Figure 2.10; note that the negative circulation yields much larger values in the latter stages of the calculation. This appears to be due to the fact that the negative value of the circulation induces a larger total axial velocity on the airframe than is the case with the positive value of the circulation. It should be noted here that in the work of Bi and Leishman (1991), the results for the pressure distribution are plotted as a function of time at fixed locations on the airframe; in the present case the results have been plotted at a number of locations on the airframe for several times. On Figure 2.14 are lines of constant pressure plotted around the cylinder at $t=0.4$. The pressure values are given. The precise details of the pressure field in the Bi and Leishman (1991) work depend on the relative position of the pressure sensors on the airframe and several different types of pressure traces have been identified. In particular, the form of presentation of the Bi and Leishman (1991) work may be obtained by fixing attention on a specific point on the airframe and observing the behavior of the pressure at successive times. The present results appear to

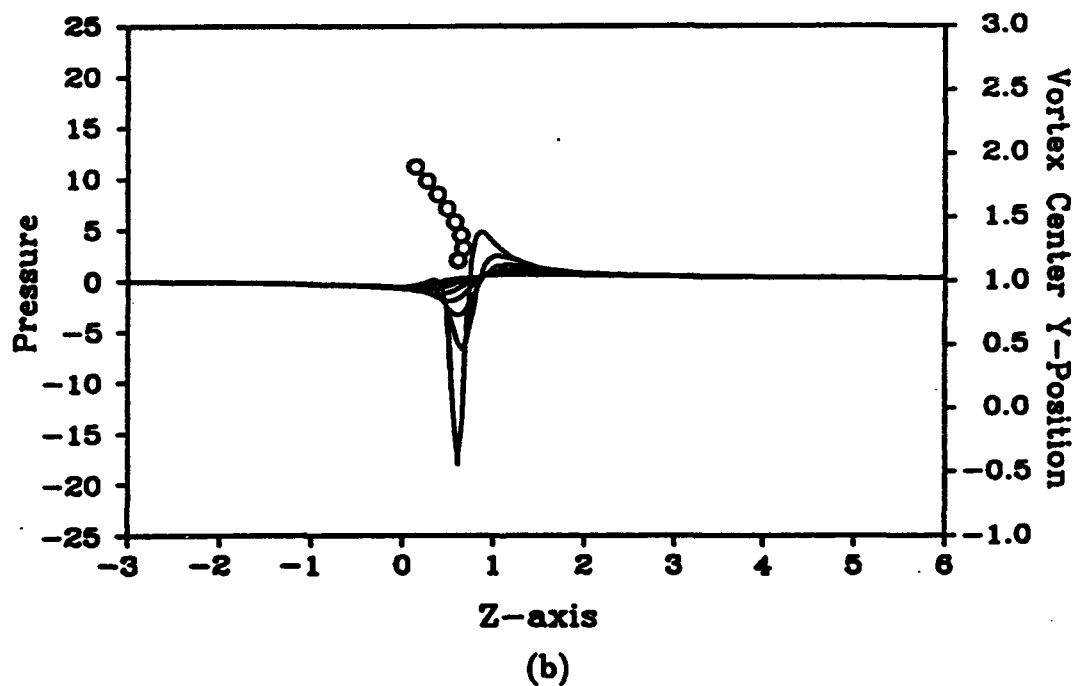
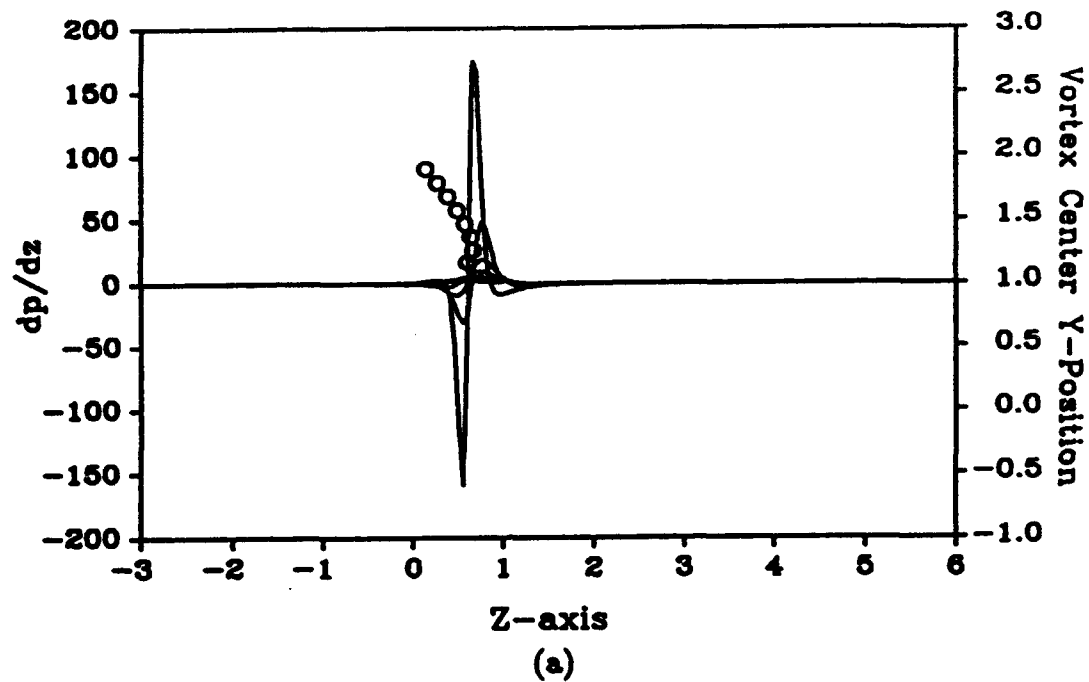


Figure 2.8: Results for the axial pressure gradient and pressure at $\theta = \pi/2$ for the parameters of Figure 2.4 where $\alpha=1$ and $\beta = 3$. (a) Pressure gradient, (b) pressure. Here results are plotted every 5 time steps ($\Delta t = 0.01$) starting from $t = 0.05$ and ending at $t = 0.4$. The circles denote the positions of the vortex center.

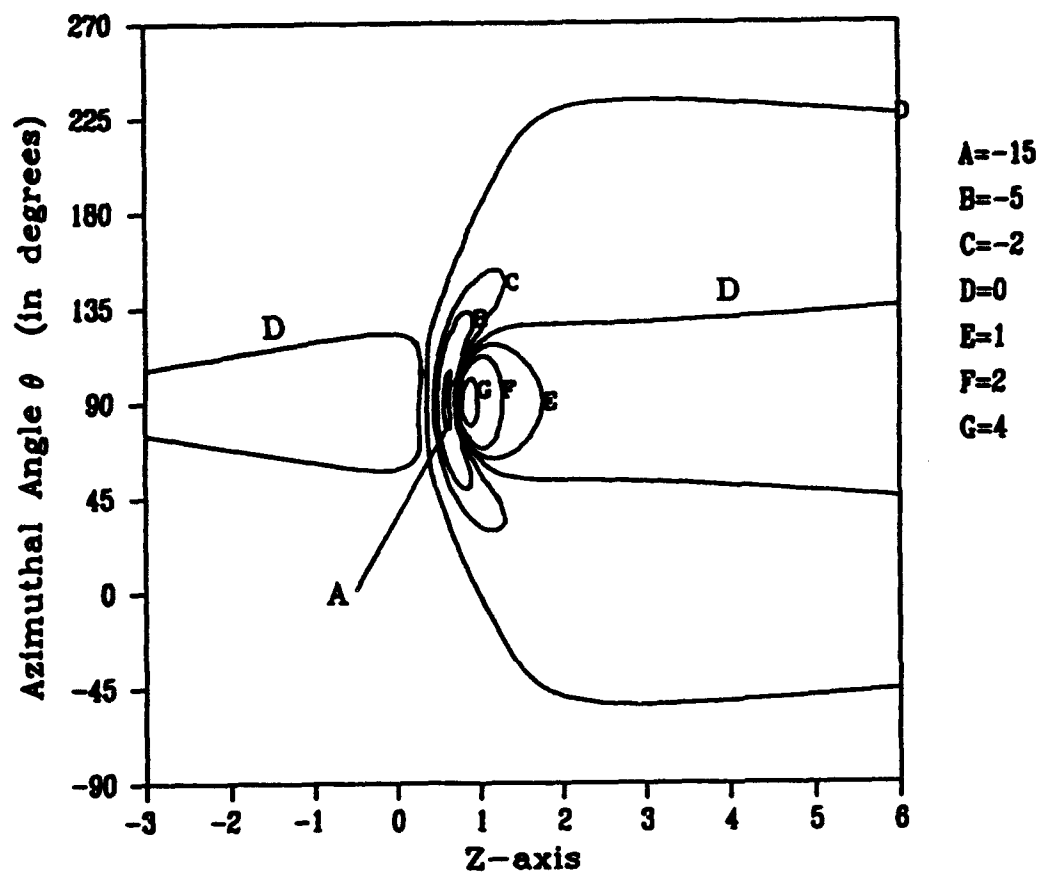
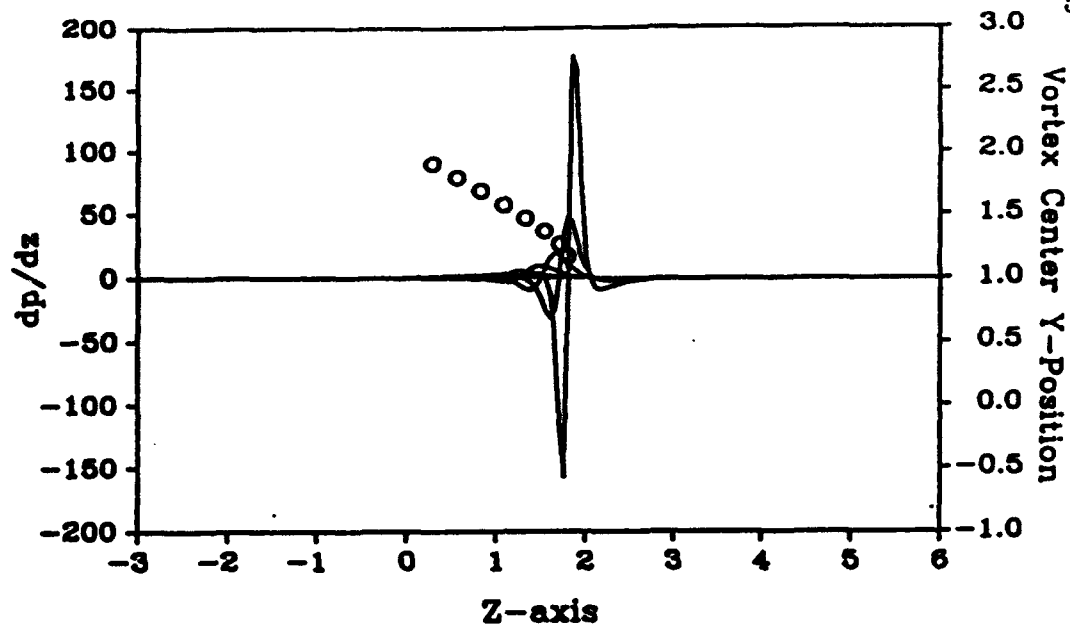
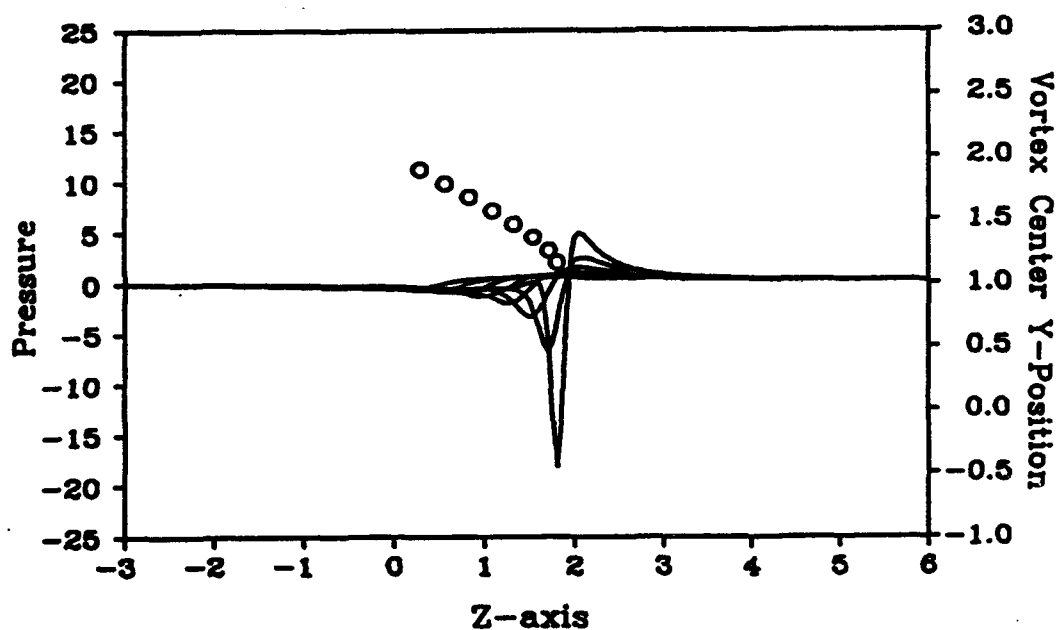


Figure 2.9: Results for surface pressure for the parameters of Figure 2.4 where $\alpha=1$ and $\beta=3$. Pressure contours are plotted at different levels given on the side of the figure. Here results are plotted at time $t=0.4$.



(a)



(b)

Figure 2.10: Results for the axial pressure gradient and pressure at $\theta = \pi/2$ for the parameters of Figure 2.5 where $\alpha=2$ and $\beta = 3$. (a) Pressure gradient, (b) pressure. Here results are plotted every 5 time steps ($\Delta t = 0.01$) starting from $t = 0.05$ and ending at $t = 0.4$. The circles denote the positions of the vortex center.

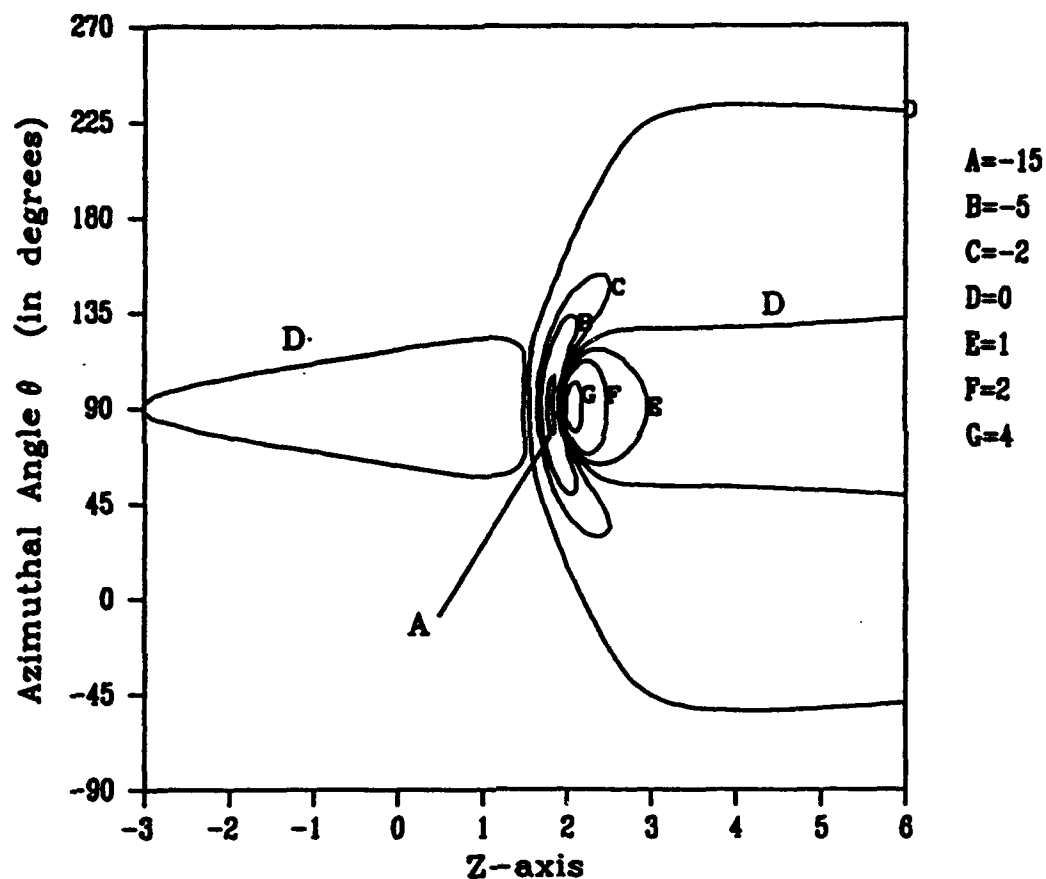


Figure 2.11: Results for surface pressure for the parameters of Figure 2.5 where $\alpha=2$ and $\beta=3$. Pressure contours are plotted at different levels given on the side of the figure. Here results are plotted at time $t=0.4$.

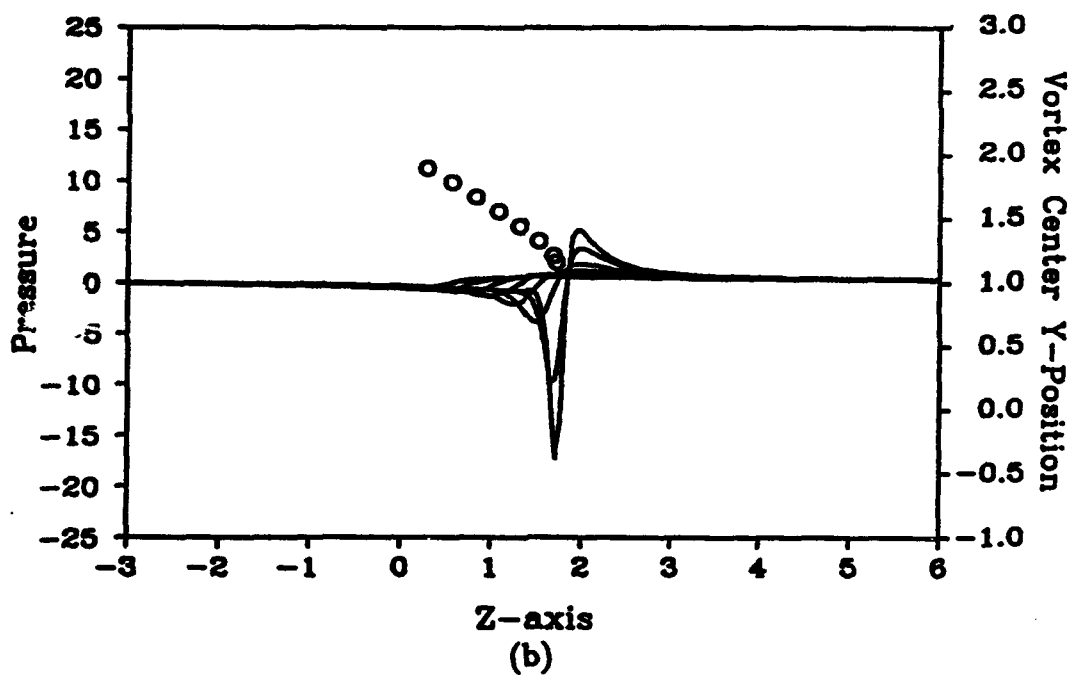
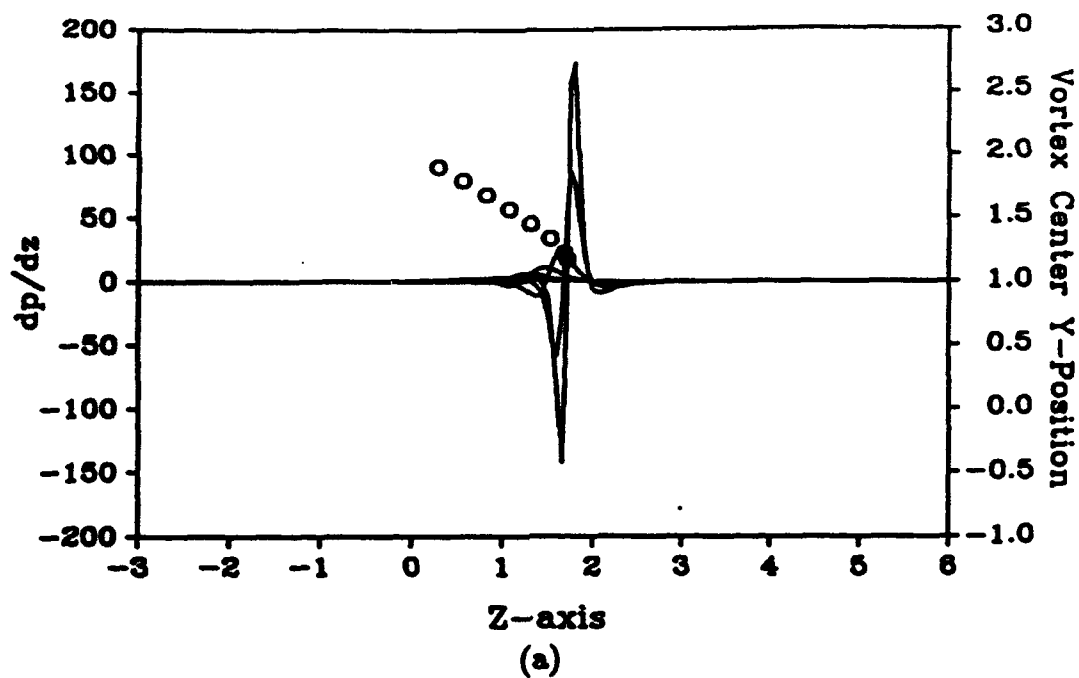


Figure 2.12: Results for the axial pressure gradient and pressure at $\theta = \pi/2$ for the parameters of Figure 2.6 where $\alpha=2$, $\beta=3$ and $a_v=0.05$. (a) Pressure gradient, (b) pressure. Here results are plotted every 5 time steps ($\Delta t = 0.01$) starting from $t = 0.05$ with the exception that the last time step corresponds to $t = 0.37$ instead of $t = 0.4$. The circles denote the positions of the vortex center.

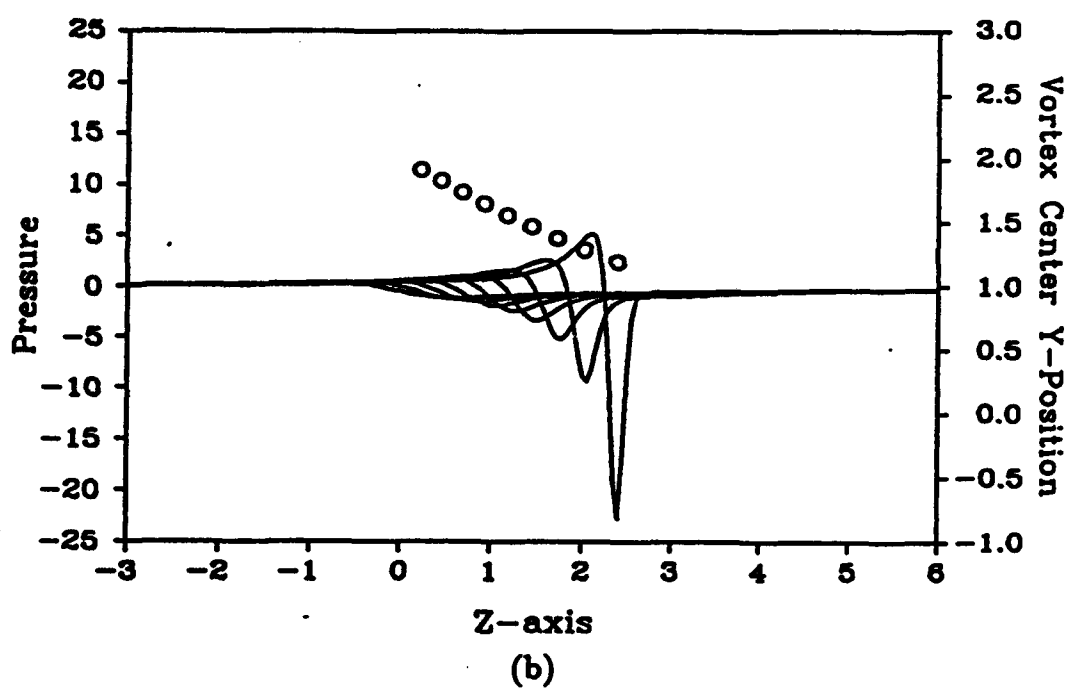
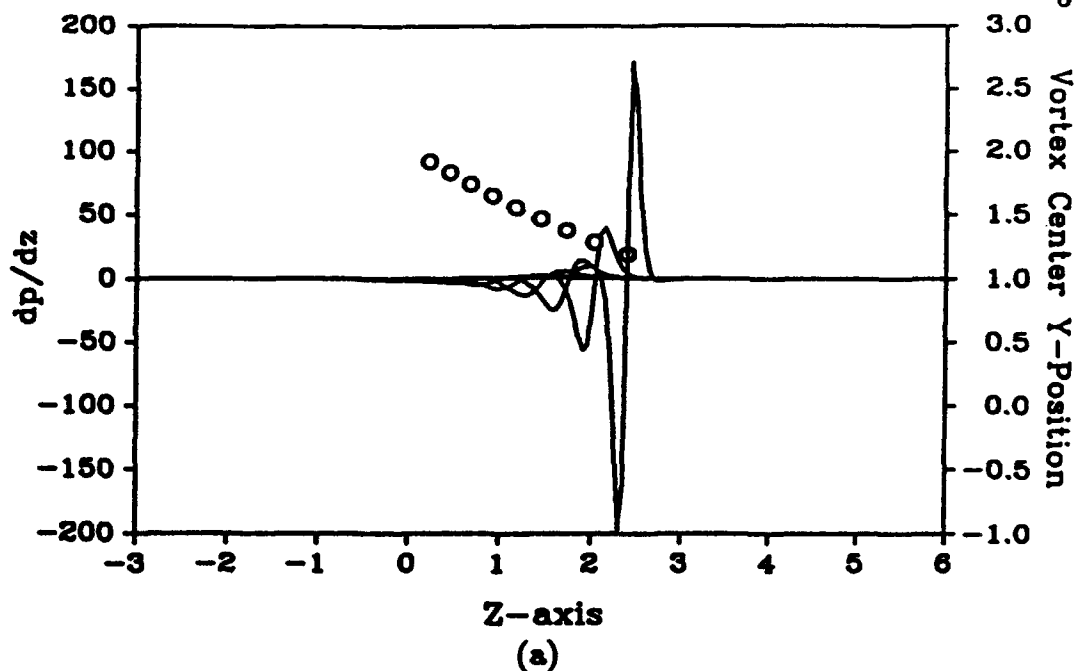


Figure 2.13: Results for the axial pressure gradient and pressure at $\theta = \pi/2$ for the parameters of Figure 2.7 where $\alpha = 1.72$ and $\beta = 2.4$. (a) Pressure gradient, (b) pressure. Here results are plotted every 5 time steps ($\Delta t = 0.01$) starting from $t = 0.05$ and ending at $t = 0.45$. The circles denote the positions of the vortex center.

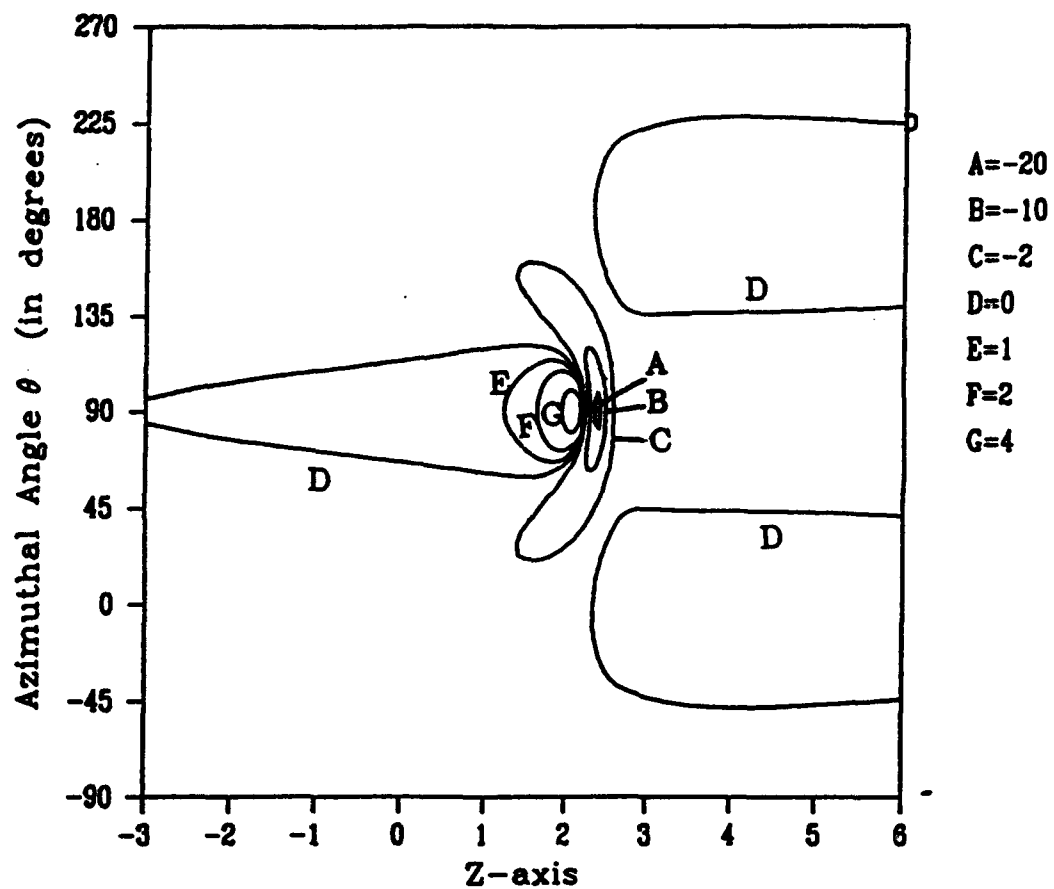


Figure 2.14: Results for surface pressure for the parameters of Figure 2.7 where $\alpha = 1.72$ and $\beta = 2.4$. Pressure contours are plotted at different levels given on the side of the figure. Here results are plotted at time $t = 0.45$.

be consistent with those of Bi and Leishman (1991) during the period prior to vortex-airframe collision in that they indicate a rapid drop in pressure with time as the vortex approaches. The magnitude of the drop is dependent on the relative position of the sensor point and the position of vortex impact as described in Bi and Leishman (1991).

2.10 Vortex Structure

As mentioned earlier, the value of μ in equation (2.23) is obtained assuming that the vortex core structure is locally axisymmetric. To investigate the possible modification of this structure as the filament approaches the cylinder, the velocity field around the core has been investigated. The velocity field relative to the vortex filament at $s = 0$ has been calculated at $\bar{r} = a_v$, where \bar{r} denotes a local radial coordinate attached to the filament and these results are shown on Figure 2.15 for the case of $\alpha = 2$ and $\beta = 3$; the vortex core size has been fixed at .1. In this section the variable θ refers to the local angular coordinate relative to the vortex core as depicted on Figure 2.15. Note that for much of the time the azimuthal velocity (relative to the filament) is constant at just over -6 ; however, very late in the calculation, some azimuthal variation begins to emerge. This coincides with the development of a finite radial velocity at this location. A rapid increase in the magnitude of the azimuthal velocity occurs around $\theta = 270^\circ$ which coincides with the portion of the vortex nearest the cylinder. In the work of Callegari and Ting (1978), the image-induced component of the local velocity field around the vortex is zero and the azimuthal velocity just outside the vortex is the free vortex axisymmetric solution; therefore the core flow will remain axisymmetric if it had originally been axisymmetric. Investigation of the local velocity field at points removed from $s = 0$; namely at $s = 1, 4$ reveals that the flow is indeed nearly axisymmetric at the vortex boundary for all times. It should be mentioned that the azimuthal direction with respect to the core of the vortex filament at $\theta = 270^\circ$ corresponds to the axial flow (z -direction) with respect to the cylinder.

The question of how the vortex structure may be altered as the filament approaches the cylinder can now be addressed. The video tape (Komerath 1991) of the experiments of Liou, et al (1990) indicates (from the side view) that the vortex core undergoes a rapid change as the airframe is approached. In particular, it is noted that a local rapid flattening of the originally circular core takes place just prior to impact with the cylinder. This suggests that the vortex core may be deformed in a quasi-elliptical manner. This phenomenon is depicted on Figure 2.16 (Komerath 1992) where the vortex core is denoted by the dark region at the end of the arrow. This phenomenon had also been observed earlier by Simons, Pacifico, and Jones (1966). Investigation of the video tape results indicates that this rapid flattening apparently begins when the filament is still outside the boundary layer

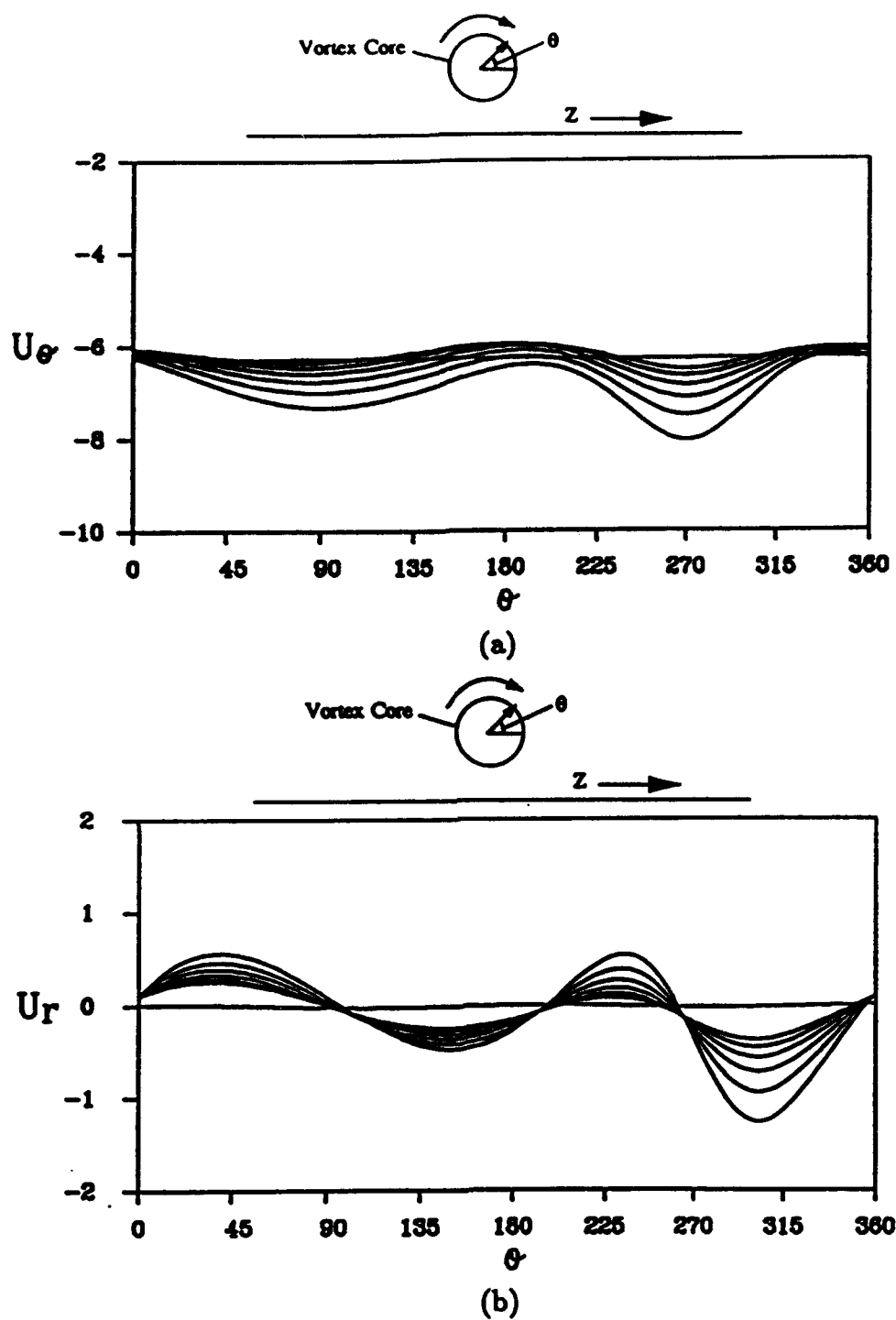
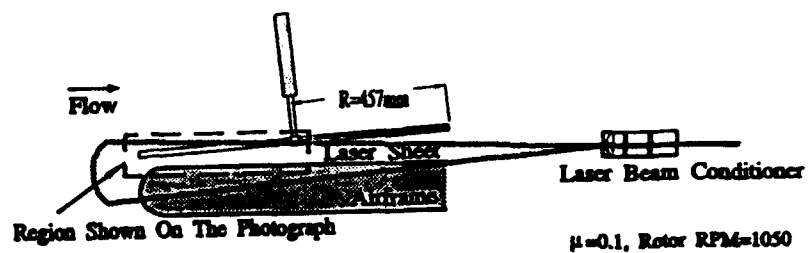
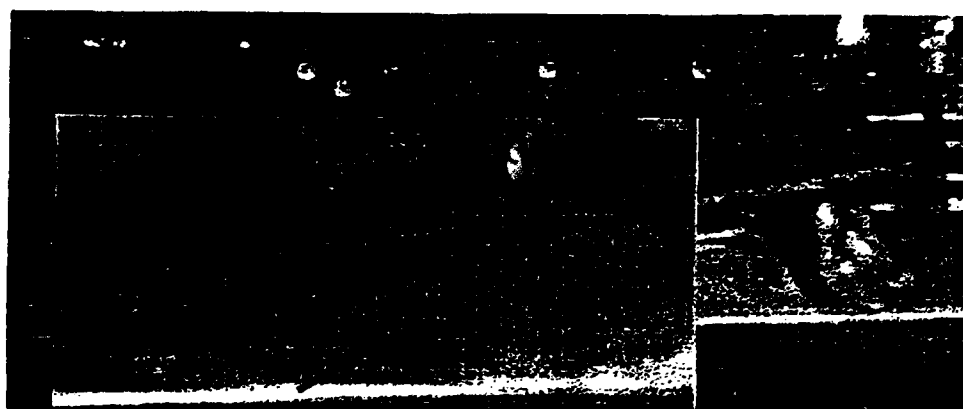


Figure 2.15: Azimuthal and radial velocity relative to the vortex core at the assumed vortex core radius $\bar{r} = a_v$ around the vortex as a function of local polar angle. The curves are plotted at $t=0$ (straight line) and at latter times, $t=.35, .36, .37, .38, .39$ and $.4$. These results are for $s = 0$. Here $\alpha = 2$, $\beta = 3$ and $a_v = .1$.



(a)



(b)

Figure 2.16: (a) Flattening of the vortex core as it approaches the cylinder (Komerath 1992). The vortex core is denoted by the dark region at the end of the arrow. (b) A close-up view of the vortex core.

and during this period, a large change in the time evolution of filament curvature does not appear to occur (Liou et. al 1990, Brand et. al 1989, Brand 1989, and Affes and Conlisk 1991). It is difficult to determine the time scale of this deformation; however, the numerical results indicate that the time scale is much faster than the time scale of the vortex evolution process and is probably related to the dimension of the vortex core although this point needs further clarification.

The genesis of the deformation of the vortex core appears to lie in the breakdown of local vortex core symmetry alluded to above (see Chapter 6). As the vortex approaches the cylinder, the image induced velocity gets progressively larger until it eventually influences the azimuthal velocity field in the vortex core; since the image induced azimuthal velocity is not axisymmetric with respect to the vortex core, the velocity within the core of the vortex must deviate from the simple Rankine vortex model assumed. This loss of symmetry will result, by local continuity in the emergence of finite radial and axial velocities within the vortex core (if such an axial velocity did not exist prior to the strong interaction); the numerical results suggest that this process begins when the vortex is still outside the boundary layer. As Figure 2.15 and the other calculations at $s = 1, 4$ (not shown) indicate, this process occurs locally around the points of the filament which are close enough to the cylinder.

In addition, the vortex undergoes a significant stretching along its own axis at points near the center ($s=0$) as it approaches the cylinder. This is evident when the vortex is embedded in a symmetric mean downwash and vortex points near $s = 0$ tend to move in the direction of the mean flow. The stretching of the vortex may be illustrated by the three plots shown on Figure 2.17. The arc length τ measured along the vortex filament and with origin coinciding with $s = 0$ is plotted vs. s on Figure 2.17(a) at various times $t=0, .1, .2, .3$ and $.4$. Here, we consider the case where $\alpha=2$ and $\beta=3$ and initially we assume that $\tau = s$ at $t = 0$. Note as time increases τ deviates from its distribution at $t = 0$ which is represented by the straight line. At each value of s the vertical spacing between the initial straight line curve and the subsequent curves indicates the amount of stretching performed by each material point along the vortex. Figures 2.17(b) and 2.17(c) show the velocity along the axis of the vortex U_r and its rate of change $\frac{\partial U_r}{\partial s}$ respectively. Note that the locations along the vortex which undergo significant stretching are associated with increasingly high values of U_r as well as $\frac{\partial U_r}{\partial s}$ centered locally around $s = 0$ as time increases.

Finally, it should be noted that the striking emergence of the strong adverse axial pressure gradient spike indicated in Figures 2.8 to 2.14 is characteristic of many flows generated by vortex motions (Conlisk 1989 and Peridier and Walker 1989) and is expected to play a crucial role in the subsequent local destruction of the vortex, and in the development of the boundary layer.

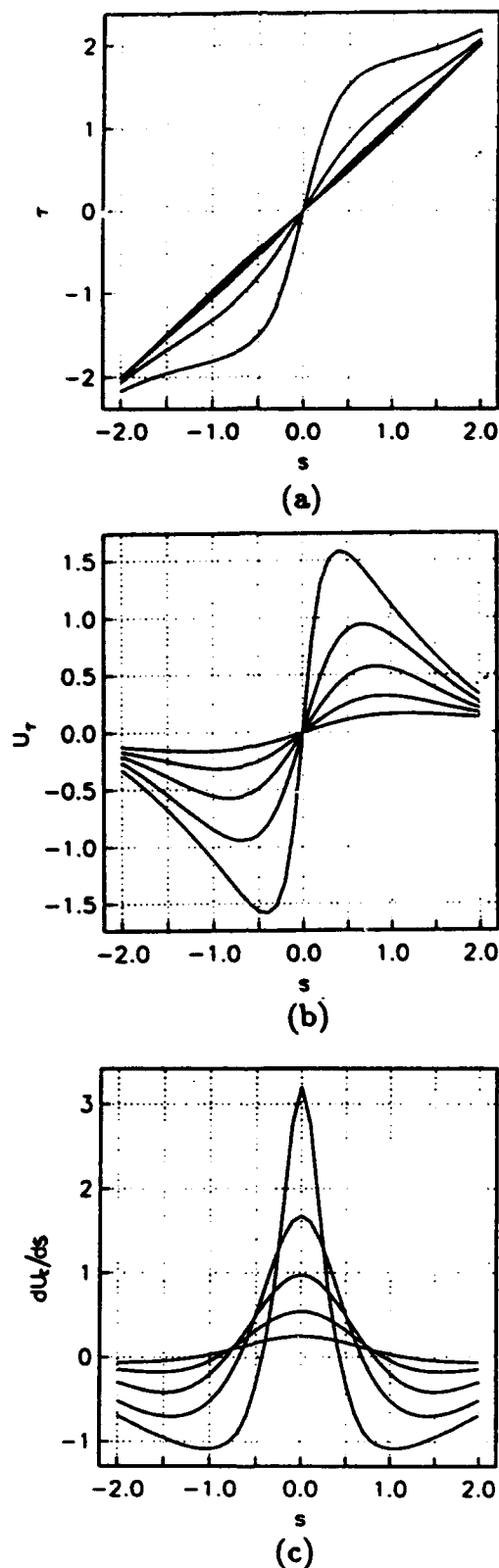


Figure 2.17: Stretching of the vortex as illustrated by the plots of (a) the arc length τ v.s. s , (b) the tangential velocity U_τ v.s. s , (c) $\frac{\partial U_\tau}{\partial s}$ v.s. s . The results correspond to the mean flow case where $\alpha=2$ and $\beta=3$, and they are shown at various times $t=0, .1, .2, .3$ and $.4$.

2.11 Summary

In the present Chapter the motion of a three-dimensional vortex filament outside a circular cylinder has been considered. We have considered the effect of mean flow, vortex core size and the relative magnitude of mean downwash and mean axial flow on the evolution of the vortex. It has been shown that the effect of core size is relatively minor until late in the calculation when the vortex core passes within several core radii of the cylinder surface; some variation in the trajectory of the vortex and in the pressure field on the cylinder are then seen to occur. The presence of the mean flow in the calculation hastens the development of a strong interaction of the vortex with the cylinder as expected. The relative importance of the mean downwash and the axial flow also has the expected result; the vortex reaches the cylinder in a shorter axial distance than for the case of α smaller.

In particular, three major conclusions may be drawn from these calculations. First, the motion of the vortex induces a very strong axial adverse pressure gradient on the cylinder under the vortex which results in a very strong negative pressure spike; this negative pressure spike has also been observed in recent experimental work (Liou et al. 1990, Brand et al. 1990 and Brand 1989). Second, the curvature of the vortex appears to remain finite as it approaches the cylinder and no kinks arise in the vortex profile. This result is also consistent with experimental results (Liou et al. 1990, Brand et al. 1989 and Brand 1989) and suggests that rapid changes in the filament profile are not responsible for the subsequent changes in the vortex structure as it approaches the cylinder. Finally, the present numerical results suggest that the vortex core flow will deviate substantially from the axisymmetric solution assumed as the vortex approaches the airframe. This may be the physical mechanism for the large flattening of the vortex core flow seen in experiments (Simons et al. 1966, Liou et al. 1990 and Komerath 1991).

Having developed the methodology to calculate the advance of the tip-vortex toward the airframe, we now apply this methodology for the parameters of the experiments of Professor Komerath and his colleagues at Georgia Tech.

CHAPTER III

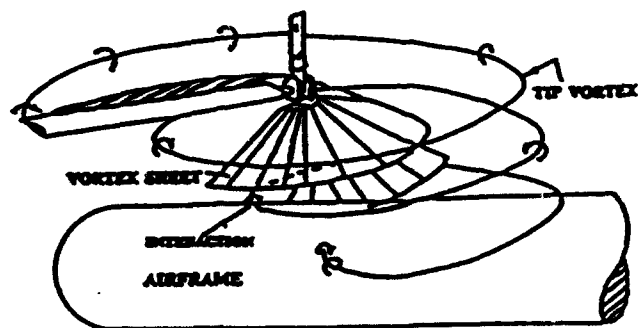
Comparison with Experiments

3.1 Introduction

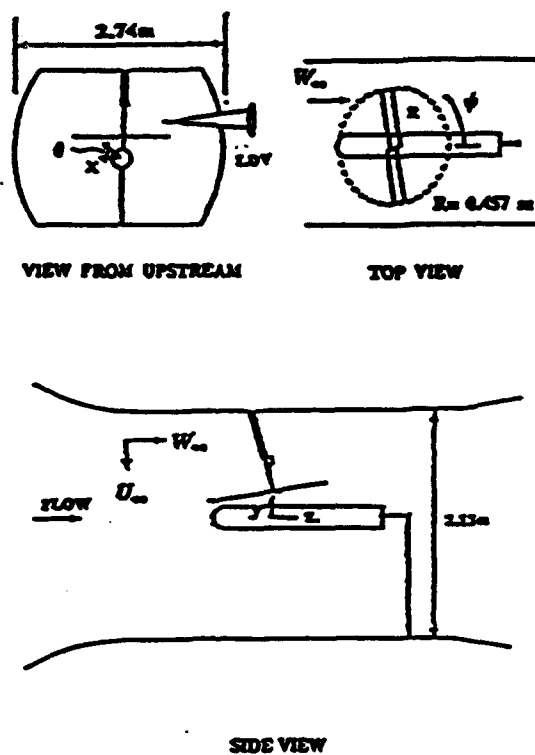
Because the vortex system shed by helicopter blades is very complex and the helicopter airframe is in general of very complex shape as well, it is clear that in order to be able to understand and compute the flow about the entire helicopter airframe, much more information about the interaction of a single vortex with a simplified airframe is desirable. In this chapter we present detailed comparisons between experimental and analytical/numerical results for the interaction of a single vortex filament with an airframe. The purpose of the present work is to present quantitative comparisons of the experimental and analytical/numerical results based on the methods developed in Chapter 2 of this work. Comparisons between theory and experiment will be made in the areas of vortex evolution and pressure distribution on the airframe prior to vortex impact. The physical situation and the experimental configuration are shown in Figure 3.1.

The work of Lorber and Egolf (1990) (and some additional references therein) represents a large-scale computational effort to compute the entire wake flow and its interaction with a simulated helicopter fuselage; they also present results for the pressure for the airframe geometry considered by Liou et. al (1990), Brand et. al (1990) and Bi and Leishman (1990). They were able to capture the effect of blade passage qualitatively; however, the location and amplitude of the pressure spike due to the effect of the tip vortex are not well reproduced (see Figure 16 of that work). The work of Mavris, Komerath, and McMahon (1989) was mainly concerned with the modeling of the mean pressure on a helicopter airframe; they were also able to capture the unsteady blade passage effect using a simple two-dimensional airfoil (in a uniform freestream) model.

It is useful at this point to discuss the factors which influence the pressure distribution on the airframe based on the experimental results referred to above; for definiteness, and since the experimental results are relevant to the top of the



(a)



(b)

Figure 3.1: (a) The wake of a single-bladed rotor in low-speed forward flight. (b) Experimental configuration and coordinate system.

airframe, we confine the discussion to this portion of the airframe. The following comments apply to the case of advance ratio $\mu=.1$, although similar comments apply to other advance ratios. A complete presentation of the experimental results over an entire period for the case of $\mu=.075$ is given in Brand et. al (1990) and Brand (1989).

Figure 3.2 shows phase-resolved pressure data acquired along the top of the airframe during the vortex interaction (Komerath 1992). Here the pressure is normalized by $\frac{1}{2}\rho W_\infty^2$ where W_∞ is the mean velocity along the generators of the cylinder. On Figure 3.2, the sharp peaks occurring at rotor phase $\psi = 0^\circ$ and 180° are due to the passage of the two-bladed rotor over the airframe. These diminish downstream, reflecting the decrease of rotor tangential velocity towards the rotor hub. The oblique features on the figure are the pressure traces of the vortex-surface interaction. The deep valley in the pressure beginning about 10 degrees after blade passage is due primarily to the tip vortex impinging on the surface; the amplitude of this valley reaches a maximum near the time of vortex impact with the cylinder and this amplitude decreases as the vortex moves farther downstream and below the airframe. The effect of the tip vortex appears to be significant from about $\psi \sim 10^\circ$ to $\psi \sim 60^\circ$ when the portion of the tip vortex impacts the top of the airframe. From about $\psi = 60^\circ$ to $\psi = 162^\circ$ the effect of the balance of the rotor wake is significant; this is reflected in the presence of the valley which appears at about $\psi = 40^\circ$ and $\psi = 220^\circ$ and diverges away from the tip trace. The blade passage effect again begins to be felt about $\psi = 150^\circ$ and reaches a maximum at about $\psi = 180^\circ$ and the cycle repeats again. The present work is concerned with the influence of the tip filament on the airframe; hence, the time period of interest is from approximately $\psi \sim 10^\circ$ to $\psi \sim 60^\circ$. Of course, precise values of ψ depend on the advance ratio and other parameters.

The goal of the present work is to determine whether the present analytical and computational techniques can adequately predict the motion of the tip vortex and the induced pressure distribution on the airframe. The parameters of interest correspond to advance ratios of $\mu = .075, .1$; other experimental parameters are as in Brand, Komerath and McMahon (1990) and Brand (1989).

The plan of this Chapter is as follows. First, the experimental apparatus and methodology used by Professor Komerath and his colleagues at the Georgia Institute of Technology are outlined. Second, some computational aspects involved in modeling the complex flow field around the airframe are then discussed. Finally, detailed results for the vortex trajectory and the pressure distribution on the airframe are presented.

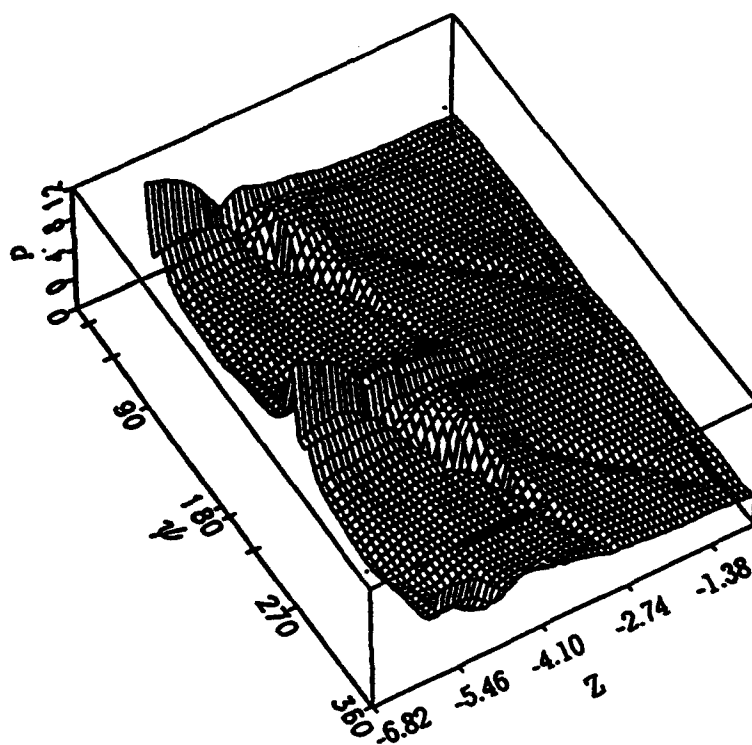


Figure 3.2: Three-dimensional perspective view of the experimental unsteady pressure variation along the airframe surface (Komerath 1992). The advance ratio is $\mu = .1$. Note the blade passage effect near $\psi = 0^\circ, 180^\circ, 360^\circ$. The regime of interest in the present modeling effort is indicated by the additional tick marks.

3.2 Experimental Methods used by Komerath et al.

For completeness, it is useful to review the experimental methods employed in the work of Professor Komerath and his colleagues at Georgia Tech (Affes et al. 1992). The experimental results discussed here are an extension of the results of Liou, Komerath and McMahon (1990) (see also Brand, McMahon, and Komerath 1990 and Brand 1989). They used laser doppler velocimetry to measure the velocity in the vicinity of the filament and obtained results for the pressure on the surface of the cylinder under the impinging vortex. The physical situation and the experimental configuration are shown in Figure 3.1.

All the experimental measurements were performed in the John J. Harper wind tunnel at the Georgia Institute of Technology. The experimental configuration is shown on Figure 3.1. The vortex is generated at the tip of each of the two, constant-chord, untwisted NACA0015 blades of a rotor turning at 2100rpm; thus the wake geometry is periodic with period π . The radius of the rotor is .457m and the airframe model is a cylinder of radius .067m. The rotor is tilted at an angle of 6° to the vertical. Complete details of the design of the experimental configuration has been presented in previous work by Liou et. al (1990), Brand et. al (1990) and Brand (1989). Two distinct sets of experimental data are of interest in the present work; these are tip vortex position and unsteady pressure data on the airframe. We discuss the measurement and characteristics of each in some detail in what follows.

The tip vortex position at each time step was determined by strobed laser sheet visualization. The flow was uniformly seeded with atomized mineral oil and the vortex cores were thus seen as regions devoid of light-scattering material; videography was employed to quantify the trajectories. A pulsed copper vapor laser was employed to acquire images of the vortex core with 25-nanosecond temporal resolution to see the changes in shape as the vortex approaches the airframe. To capture the image of the moving vortex core, an argon ion laser sheet was strobed near the fundamental frequency of the rotor which is 70 Hz; data was taken at successive values of the azimuthal angle ψ which is essentially a timelike variable. Since the rotor consists of two blades, two vortex filaments 180 degrees apart in age exist simultaneously; for example the tip vortex filament present at 210° coexists with the filament present at 390° which was shed from the previous blade. Once the data for the vortex trajectory were taken at a given value of ψ , the video tape was reviewed and positions of the vortex core, visible as dark spots, were plotted on the image of a square grid placed at the measuring plane. The rotor azimuth was determined as follows: since the strobing frequency is not equal to the rotor frequency, the rotor azimuth changes slowly from frame to frame. By counting the time taken for the azimuth to describe 360° , the rotor azimuth is calculated. The accuracy here is of the order of three degrees, limited by the 0.1 second least count

of the camera clock.

The error in the measurement of the vortex positions is estimated to be approximately 15mm which is about twice the average vortex core radius over the regime $\psi = 0$ to $\psi = 60^\circ$, which corresponds approximately to the time of impact for $\mu = .1$. Here ψ is measured from the beginning of a period and μ is the advance ratio which is defined by $\mu = \frac{W_\infty}{R\Omega}$ where W_∞ is the axial mean flow velocity, R is the rotor radius and Ω is the angular velocity of the rotor. The results of the measurements of the vortex position at $\psi = 0$ are used to define the initial conditions for the numerical calculations.

The unsteady component of the pressure was measured by the use of 18 microphone ports mounted flush with the airframe. Four microphone ports were available at any given time and additional measurement locations were obtained by moving the microphones from port to port as described in detail by Brand(1989). The microphones are about 3mm in radius and sampling of the signals was synchronized with a pulse from a rotor shaft encoder so that the azimuthally resolved data could be obtained. The nominal spacing between the microphones is 38 mm. The microphone output signal was sampled at 1-degree increments of rotor azimuth and averaged over each 6-degree interval. The results at each 6-degree interval are then summed with similar data from 100 subsequent revolutions of the rotor. Details of the data reduction procedure are also given by Brand (1989).

3.3 Modelling of the Experiments

The calculation of the flow field due to a generalized three-dimensional vortex filament in the presence of a cylinder is described in detail in Chapter 2; in what follows we discuss the specifics of the application of the theory to the experimental configuration. The physical situation is depicted on Figure 3.1(b); here (x, y, z) and (r, θ, z) denote Cartesian and polar coordinates with origin at the center of the cylindrical airframe. In general the flow field consists of that induced by the vortex itself, that induced by the image field due to the vortex and to any other mean motion in which the vortex may be embedded. As discussed in Chapter 2 the mean streaming motion will satisfy the solid wall boundary condition at the cylinder surface and so the problem reduces to calculating the effect of the image in the cylinder. Here all lengths have been made dimensionless on the cylinder radius denoted by a and the velocity field has been made dimensionless on W_∞ which is the free-stream velocity component along the airframe. Here $W_\infty = 10\text{m/sec}$ for the advance ratio $\mu = 0.1$ and $W_\infty = 7.5\text{m/sec}$ for the case $\mu = 0.075$. For future reference, in the experiments, the rotor radius is .457 m and the airframe radius is .067 m.

The simplest way to model the effect of the downwash velocity on the vortex is to use the two-dimensional potential flow past a circular cylinder along with a

constant velocity in the direction of the generators of the cylinder to simulate forward flight. In the coordinate system of Figure 3.1 this steady streaming motion is given by equation (2.17). There $\gamma = \frac{U_\infty}{W_\infty}$ is the ratio of the mean velocity at infinity in the y -direction to the characteristic velocity W_∞ which is the mean streaming flow along the cylinder at upstream infinity. Note that this mean distribution is symmetric with respect to the y -axis and thus the characteristic asymmetry of the motion of the tip vortex seen in experiments will not occur (Liou, Komerath, and McMahon 1990).

To better model the steady mean flow (both downwash and axial mean flow components), a simplified model which captures the essential characteristics of the asymmetry of the vortex motion has been developed. It should be noted that the mean flow is modified only in the region underneath the rotor; outside this region, the mean flow is considered symmetric and corresponds to that described by equation (2.17). The model consists of introducing the velocities $v(x)$ and $w(x)$ which are linear functions of x to represent the undisturbed (i.e. not affected by the presence of the cylinder) and asymmetric mean flow in the y and z directions respectively in the region of rotor influence. These functions are obtained by interpolating time-averaged experimental values measured at the end points of the vortex filament; these points are located at about 3 or 4 cylinder radii from the airframe and their motion is most affected by the free streaming flow and the blade passage. Thus, the undisturbed asymmetric mean flow which corresponds to a constant vorticity field is given by

$$\vec{U}_A = v(x)\hat{j} + w(x)\hat{k}, \quad (3.1)$$

where

$$v(x) = Ax + B, \quad (3.2)$$

$$w(x) = Cx + D. \quad (3.3)$$

Here A, B, C and D are constants which are determined from the experimental conditions at the beginning of the computational time domain ($t = \psi = 0$). A detailed discussion of the calculation of these constants appears in Section 3.4. Note that in the symmetric mean flow given by equation (2.17) which is used to describe the mean flow outside the region influenced by the rotor, the value of $\gamma = \frac{U_\infty}{W_\infty}$ is chosen to correspond to the absolute value of B appearing in equation (3.2). A physical estimate of U_∞ used in the present calculations for both advance ratios $\mu = 0.1$ and $\mu = 0.075$ will be given in the next section. The velocity field defined by equations (3.2) and (3.3) is depicted in Figure 3.3 where the cylinder is immersed in a constant shear flow. Because the flow is assumed inviscid, the resulting vortical flow field is preserved in time and no generation or dissipation of vorticity will occur. In order to find the asymmetric mean flow around the cylinder, we use the classical decomposition of a vector field into an irrotational component

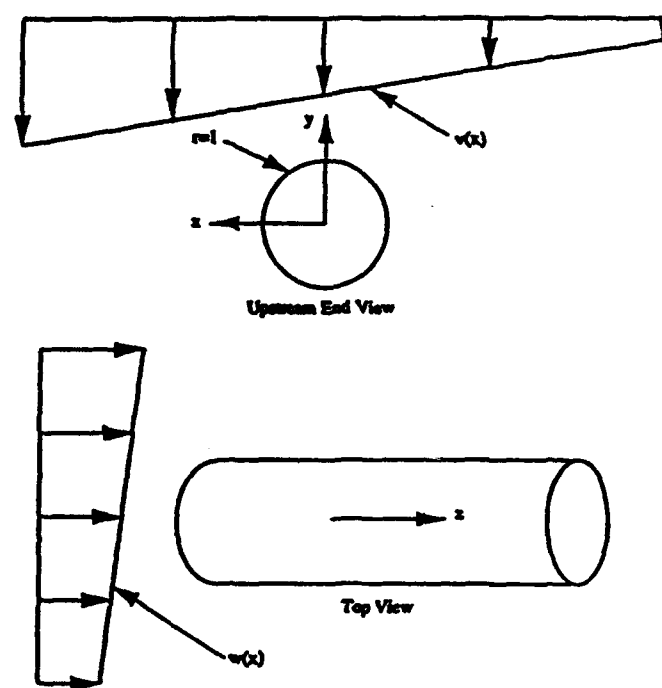


Figure 3.3: Sketch of the mean flow viewed from upstream and top of the cylinder. Note the linear profiles of the downwash $v(x)$ and the the axial flow $w(x)$.

and a rotational one. A theoretical outline of this decomposition method is given by Lamb (1932, p. 208) and an excellent review of the different theoretical work on this issue is given by Richardson and Cornish (1977). Thus, using this method, the asymmetric velocity field \vec{U}_{AM} for the mean flow may be written as

$$\vec{U}_{AM} = \vec{U}_A + \nabla \Phi \quad (3.4)$$

where Φ is a scalar potential. Here

$$\nabla \Phi = \vec{v}, \quad (3.5)$$

is the velocity perturbation due to the presence of the cylinder. Equation (3.5) ensures that the equation $\nabla \times \vec{v} = 0$ is satisfied identically and since the flow is assumed incompressible, Φ satisfies

$$\nabla^2 \Phi = 0. \quad (3.6)$$

The above equation is subject to the boundary conditions

$$\frac{\partial \Phi}{\partial r} = -v(x) \sin \theta \text{ at } r = 1, \text{ and } \Phi \text{ is finite as } r \rightarrow \infty, \quad (3.7)$$

where $\frac{\partial \Phi}{\partial r}$ is the negative of the radial component of \vec{U}_A and is given by

$$\frac{\partial \Phi}{\partial r} = -\frac{A}{2} r \sin 2\theta - B \sin \theta. \quad (3.8)$$

Note that the constants C and D do not appear in the above equation, and thus the mean streaming motion along the axis is not affected by the presence of the cylinder. To obtain the solution to the boundary value problem defined by equations (3.6) and (3.7) we use a finite Fourier transform in the θ -direction; defining the Fourier transform of Φ as

$$\hat{\Phi} = \int_{-\pi}^{\pi} \Phi e^{-im\theta} d\theta, \quad (3.9)$$

the transform solution $\hat{\Phi}$ satisfies

$$\frac{\partial^2 \hat{\Phi}}{\partial r^2} + \frac{1}{r} \frac{\partial \hat{\Phi}}{\partial r} - \frac{m^2}{r^2} \hat{\Phi} = 0. \quad (3.10)$$

After applying the boundary conditions (3.7) in the transform space, a solution for $\hat{\Phi}$ is obtained

$$\hat{\Phi} = \begin{cases} \mp i\pi \frac{A}{2|m|} r^{-|m|}, & \text{for } m = \pm 2, \\ \mp i\pi \frac{B}{|m|} r^{-|m|}, & \text{for } m = \pm 1, \\ 0, & \text{otherwise.} \end{cases} \quad (3.11)$$

Using the inversion formulas for the transform as given in Churchill (1972 p. 379), it may easily be shown that

$$\Phi(r, \theta) = \frac{A \sin 2\theta}{4r^2} + B \frac{\sin \theta}{r}. \quad (3.12)$$

Thus the resulting mean flow takes the form

$$\vec{U}_{AM} = (U_{AMr} \cos \theta - U_{AM\theta} \sin \theta)\hat{i} + (U_{AMr} \sin \theta + U_{AM\theta} \cos \theta)\hat{j} + w(x)\hat{k}, \quad (3.13)$$

where U_{AMr} and $U_{AM\theta}$ are respectively the radial and azimuthal components of the asymmetric mean flow and are given by

$$U_{AMr} = \left[Ar \cos \theta \left(1 - \frac{1}{r^4} \right) + B \left(1 - \frac{1}{r^2} \right) \right] \sin \theta, \quad (3.14)$$

and

$$U_{AM\theta} = -\frac{A}{2r^3} + \left[Ar \cos \theta \left(1 + \frac{1}{r^4} \right) + B \left(1 + \frac{1}{r^2} \right) \right] \cos \theta. \quad (3.15)$$

To advance the vortex filament, the induced velocity field on the filament is calculated; each point is then advanced according to the evolution equation (2.45). Here the time scale t is defined by

$$t = \frac{W_\infty}{a} t^*, \quad (3.16)$$

where t^* is dimensional. The total velocity field is thus given by

$$\vec{U} = \vec{U}_I + \vec{U}_V + \vec{U}_{AM}, \quad (3.17)$$

where the velocity \vec{U} has been nondimensionalized on W_∞ .

The components \vec{U}_I and \vec{U}_V are the velocity fields in the Cartesian system due to the image of the filament in the cylinder and the free vortex respectively (see Chapter 2). As described in Chapter 2, the time evolution of the vortex is computed using a fourth-order Runge-Kutta method in time; the Biot-Savart integral (equation 2.9) is evaluated using Simpson's rule and the Fourier integrals involved in evaluating the image-induced velocity field at points off the vortex (on the surface of the cylinder) are computed using the Fast Fourier Transform procedure developed by Cooley and Tukey (1965). The pressure on the airframe is computed from Bernoulli's equation given by equation (2.50) and, as in Chapter 2, is made dimensionless according to

$$p = \frac{p^* - p_\infty}{\frac{1}{2}\rho W_\infty^2}, \quad (3.18)$$

where ρ is the density of the fluid and p^* is the dimensional pressure.

3.4 Experimental Conditions

There are a number of considerations involving the motion of the tip vortex in the experiments and these issues are addressed in this section. In general, the initial position of the filament is given by

$$\vec{X}(s, t = 0) = x_s \hat{i} + y_s \hat{j} + z_s \hat{k};$$

in the present work the initial position of the vortex is specified by using the experimental data of Liou, Komerath, and McMahon (1990) for $\mu = .1$ at $\psi = 0$; in this case there are nineteen data points across the vortex. To better resolve the vortex filament, these data points were used to interpolate (second order interpolation) once to obtain 37 points along the filament. The experimental data ranges from $x = -3.07$ to $x = 3.07$; to avoid a discontinuity in slope at each end of the filament, additional points were added so that the vortex ends are assumed to be straight for $|x| > 5$. The parametric variable s ranges from -5 to 5 with the grid spacing in s , $\Delta s = .167$. For the case of $\mu = .075$, the experimental data set for the vortex position is not as extensive as that for $\mu = .1$. Consequently, the same initial condition was used for this case as that described above but shifted to agree with the experimental centerline vortex position (i.e. from a side view) at $\psi = 0$. Because of the proximity of the vortex to the airframe, this procedure should be adequate to describe the subsequent vortex motion and instantaneous pressure distribution on the airframe.

The determination of the undisturbed and asymmetric mean downwash $v(x)$ which is given by equation (3.2) is a bit more difficult. To estimate the downwash velocity in the experiments, the velocities of the vortex on the advancing and retreating sides of the rotor far from the cylinder are estimated using the data between the values $\psi_{abs} = 330$ and $\psi_{abs} = 540$. (Here ψ_{abs} is measured from the instant of creation of the helix defining the tip-vortex.) The resulting downwash $v(x)$ is then obtained by linear interpolation between these two points. Using this procedure, the coefficients of $v(x)$ are approximated by $A = -0.208$ and $B = -0.557$ for the advance ratio $\mu = 0.1$. Since the magnitude of the dimensional downwash is kept the same for both advance ratios $\mu = 0.1$ and $\mu = 0.075$ and the velocity is made dimensionless with respect to W_∞ , the values of A and B (see equation 3.2) for $\mu = 0.1$ are divided by 0.75 in the case $\mu = 0.075$. This results in a dimensional quantity $U_\infty = 5.57$ m/sec which is used to describe the symmetric mean flow (equation 2.17) outside the region affected by the rotor.

The determination of the undisturbed asymmetric axial mean flow given by equation (3.3) is not trivial. From a fundamental point of view, the motion of the tip vortex is driven by the blade passage effect, by the balance of the rotor wake, by the image of the vortex in the airframe, and by its own self-induced motion. Consider the case of the advance ratio, $\mu = .1$; direct calculation of the

axial mean flow speed from the definition of μ yields $W_\infty = 10\text{m/sec}$ and this value was initially used in the calculations. Comparison of the position of the vortex at $\psi = 30^\circ$ and at $\psi = 60^\circ$ (ψ is measured from the beginning of the period; see below) with the experimental data reveals that the vortex traveled significantly farther downstream than is evident in the calculations. To investigate this phenomenon, the velocity at the two ends of the vortex was estimated based on the results presented by Liou, Komerath, and McMahon (1990). Because the ends of the filament are relatively far from the airframe, the ends should move at approximately the mean flow speed. This calculation reveals that the ends move at a velocity somewhat greater than 10m/sec ; moreover, each end of the vortex travels at a different speed depending on whether it is on the retreating or advancing side of the rotor. Consequently, matching the experimental values at the ends of the filament, the resulting coefficients of $w(x)$ are given by $C = 0.045$ and $D = 1.315$. When this adjustment is made, the comparison with experiment is much better on the advancing side of the rotor as well as on the retreating side of the rotor.

The time scale of the motion may be calculated simply by using the definition of the angular speed of the rotor. This was done and for both values of the advance ratio, $\Delta\psi = 6^\circ$ corresponds to about .00048 seconds; in dimensionless form this requires a value of $\Delta t = .0711$ for $\mu = .1$ and $\Delta t = .0533$ for $\mu = .075$. The accuracy of the solution for this value of the time step was checked by halving Δt for the case of $\mu = .1$ with no change in the computed results. The absolute value of the dimensional circulation has been estimated at $1.5\text{ m}^2/\text{sec}$ (Liou, Komerath, and McMahon 1990) which results in a dimensionless circulation of $\Gamma=2.2$.

The experimental work has suggested that significant axial flow is present in the core. However, since the azimuthal velocity within the core is much greater than the axial velocity, the incorporation of this effect into the calculations makes little difference in the results (Affes and Conlisk 1991). The assumed core size of the vortex is a key parameter in the problem. The core radius was measured from copper laser sheet flow visualization data and was found to range from between .2 to .4 inches as the vortex approached the airframe; the increase in core radius is believed to be due to diffusion effects. For the calculations a mean radius equal to .3 inches was thus assumed. This results in a dimensionless core radius of about .11 (Komerath 1991).

The pressure gradient has been calculated from the Euler equations and the pressure has been calculated from Bernoulli's equation. To calculate the surface speeds requires the inversion of two Fourier transforms in the θ and z directions and the evaluation of an integral over the vortex filament. The Fast Fourier Transform is employed for both transforms; 64 modes in the θ direction have been employed and 512 modes in the z direction have been used. The grid spacing in the z direction is $\Delta z = .05$ and so the computational spacing of the grid points corresponds to about one-half of a dimensionless vortex core radius. All of the grid parameters

described in the pressure calculation have been tested for accuracy. The integral over the vortex filament is evaluated in the same manner as that employed in the calculation of the vortex position. However, because the velocities are more sensitive to numerical error than are the filament positions, it has been found necessary to use a much finer grid over the vortex filament and thus $\Delta s = \frac{1}{96}$ in all the pressure and pressure gradient calculations to be presented.

3.5 Results

As mentioned earlier, the evolution of the tip vortex and the induced pressure distribution on the airframe are of primary interest in the present study. The experimental results correspond to nominal advance ratios of .075 and .1. We consider the case of .1 first. On Figure 3.4 are the top and upstream end views of the vortex trajectory plotted at two subsequent times corresponding to $\psi = 30^\circ$ and $\psi = 60^\circ$; the circles are the experimental data points. Here ψ is measured from the beginning of the period; in general, the absolute age of the vortex in the experiments is $\psi_{abs} = \psi + 360^\circ$. The error bars correspond to about 15mm which is about one vortex diameter. Note the good agreement between theory and experiment especially at $\psi = 30^\circ$. At $\psi = 60^\circ$ the vortex is about to impact the airframe and some uncertainty in the precise position of the vortex near impact does exist; consequently, those experimental data points nearest the airframe should be viewed with caution. This is probably the reason for the rather substantial differences between the experiments and the computed results in the top view of the vortex position at $\psi = 60^\circ$.

On Figure 3.5 is a typical pressure gradient $\frac{\partial p}{\partial z}$ induced on the airframe for $\mu = .1$ for several values of ψ ; the computed side view of the vortex center position ($s=0$) is represented by the open circles which are not drawn to scale. Note the strong adverse pressure gradient that develops as the vortex approaches. Moreover, as ψ increases the pressure gradient becomes more focused locally in space; in addition, it is apparent that a short time scale is also emerging as evidenced by the rapid increase in the amplitude of the pressure gradient from $\psi = 42^\circ$ to $\psi = 54^\circ$.

The pressure distribution along the top of the airframe is depicted on Figure 3.6; each of the crosses corresponds to the experimental data points and the open circle(not drawn to scale) denotes the side view of the computed vortex center position along the top of the airframe. For the smaller values of ψ the effect of blade passage is rather substantial as can be seen by the positive pressure values upstream of the vortex. As ψ increases, the effect of blade passage diminishes until by $\psi = 48^\circ$, the effect of the tip vortex is dominant locally. Although the computed results slightly over-predict the experimental result in the later stages, the agreement is certainly very good. Note the excellent agreement with the experimental data

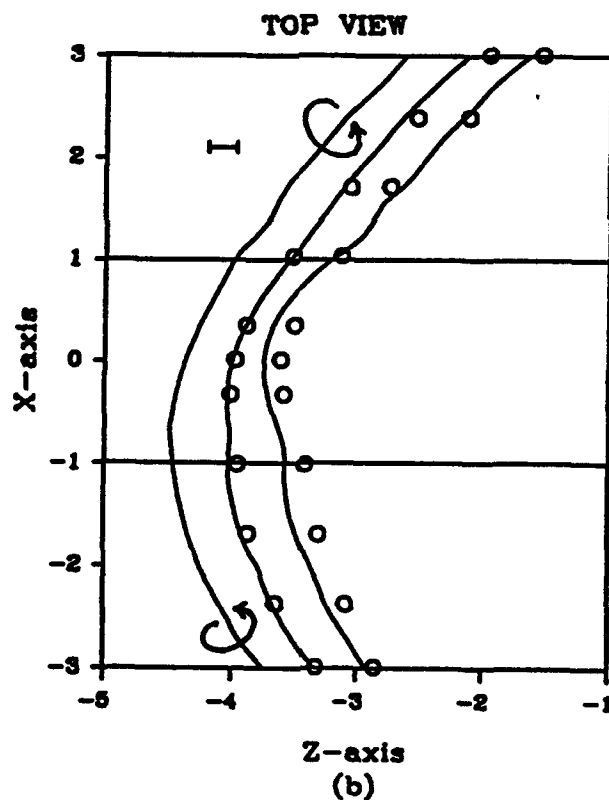
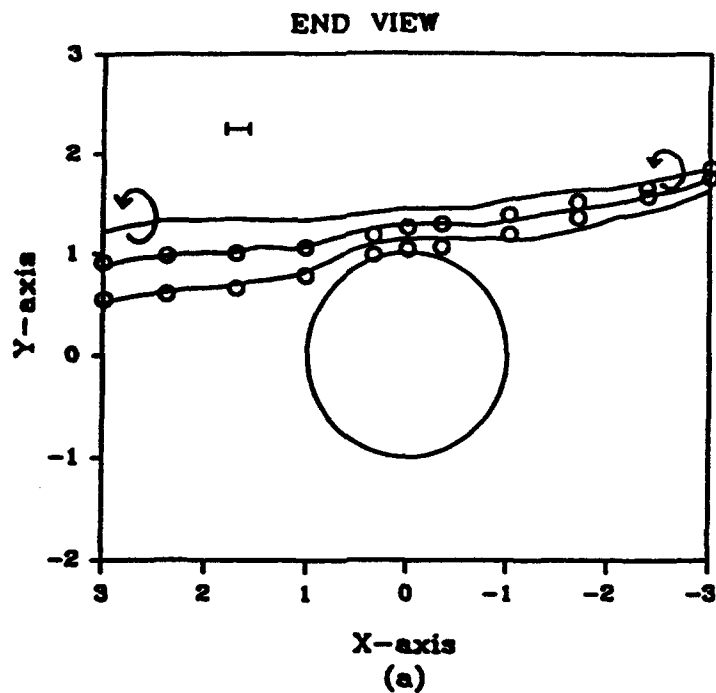


Figure 3.4: The vortex trajectory for advance ratio $\mu = .1$. (a) Upstream end view; (b) top view. The circles denote the experimental results (not to scale for the vortex core); the times shown are for $\psi = 0$ (the initial condition), $\psi = 30^\circ$, and $\psi = 60^\circ$. The error bar in the experiments is also shown. The arrows indicate the sense of vortex circulation ($\Gamma > 0$).

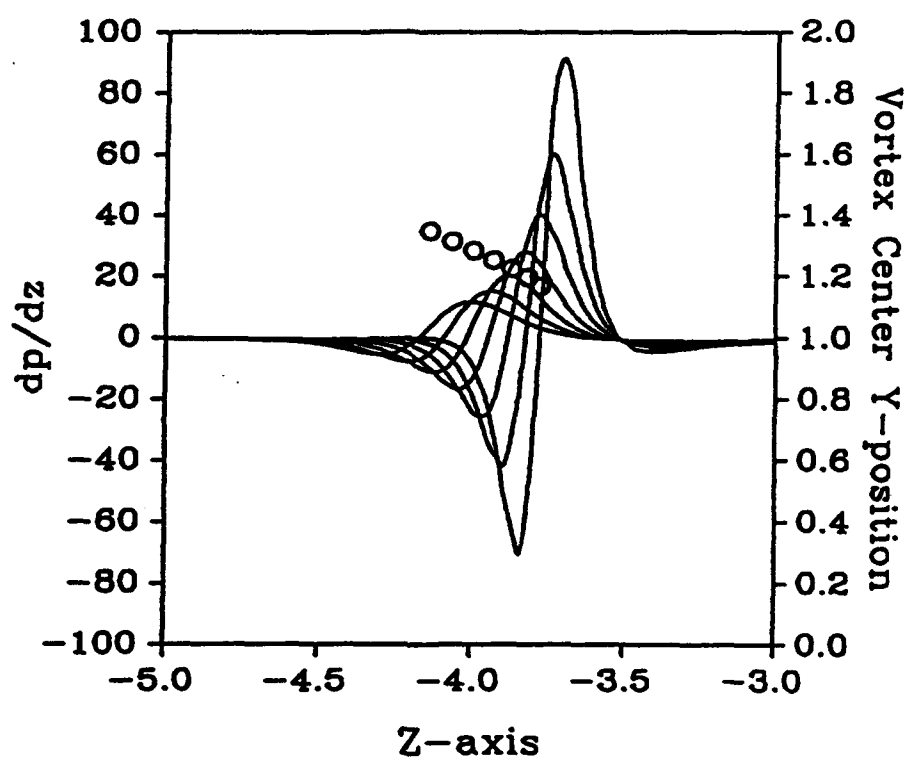


Figure 3.5: Pressure gradient $\frac{\partial p}{\partial z}$ for $\mu = .1$ along the top of the airframe for several values of $\psi = 18^\circ, 24^\circ, 30^\circ, 36^\circ, 42^\circ, 48^\circ$ and 54° . The amplitude of the pressure gradient spike increases as ψ increases. The open circles are side views of the computed vortex center ($s = 0$) position.

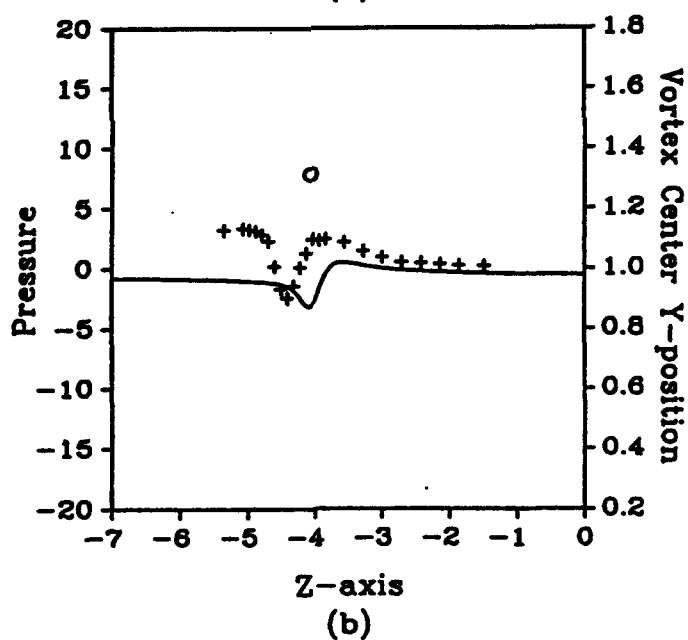
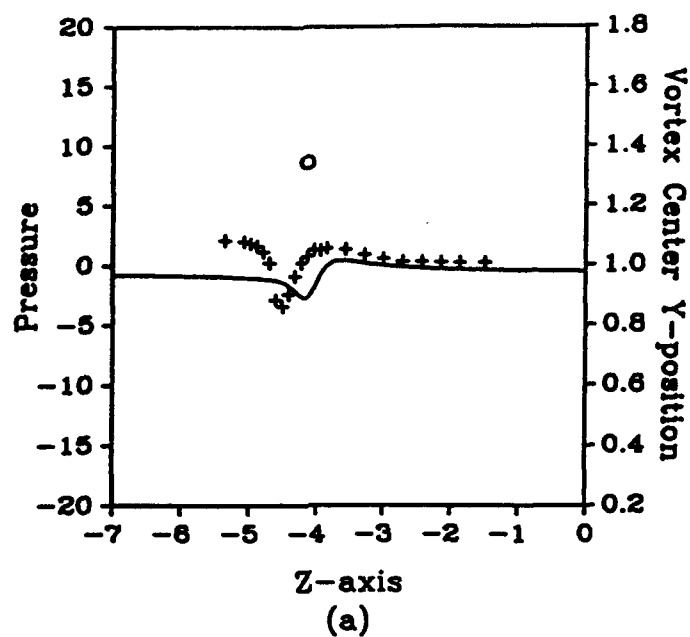


Figure 3.6: Pressure distribution along the top of the airframe for several values of ψ for $\mu = .1$. The circle is the side view of the computed vortex center ($s = 0$) position. (a) $\psi = 18^\circ$, (b) $\psi = 24^\circ$, (c) $\psi = 30^\circ$, (d) $\psi = 36^\circ$, (e) $\psi = 42^\circ$, (f) $\psi = 48^\circ$, (g) $\psi = 54^\circ$.

Figure 3.6 (continued)

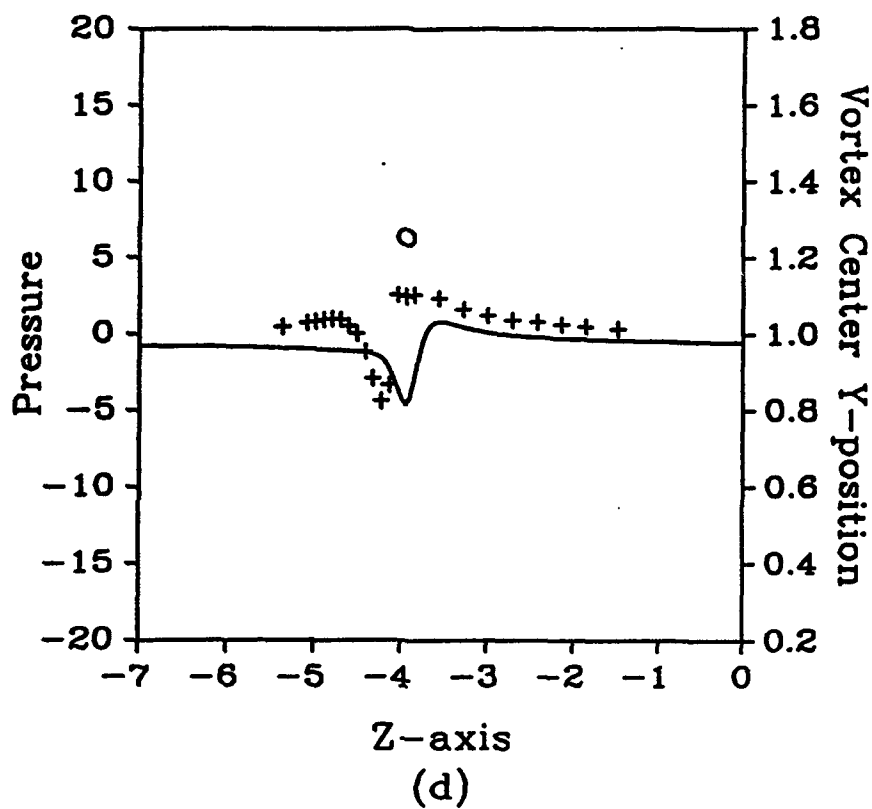
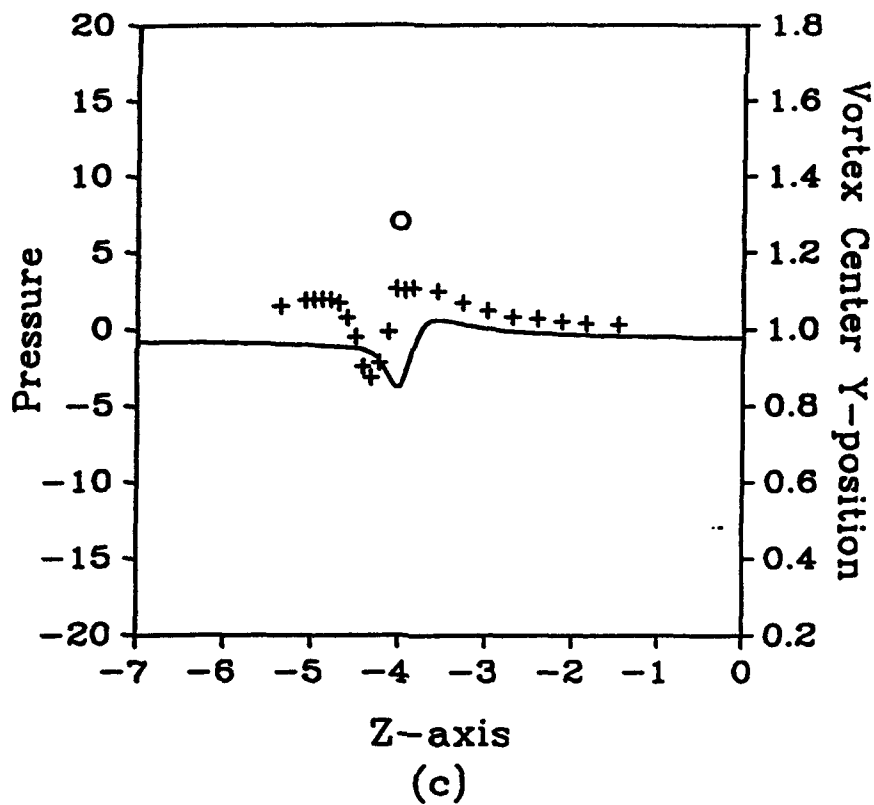


Figure 3.6 (continued)

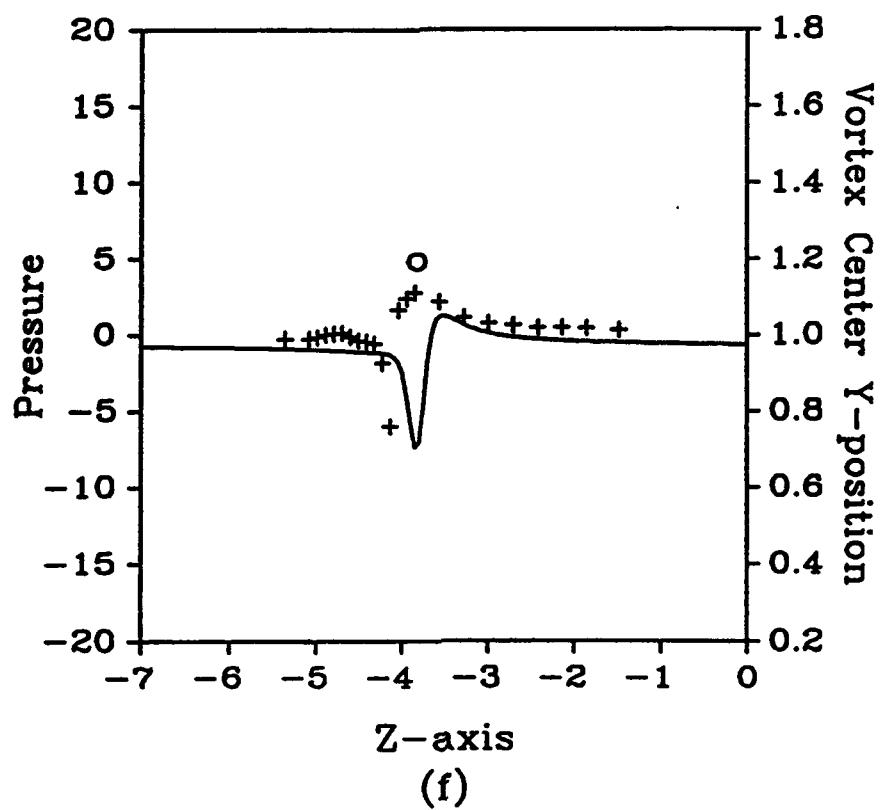
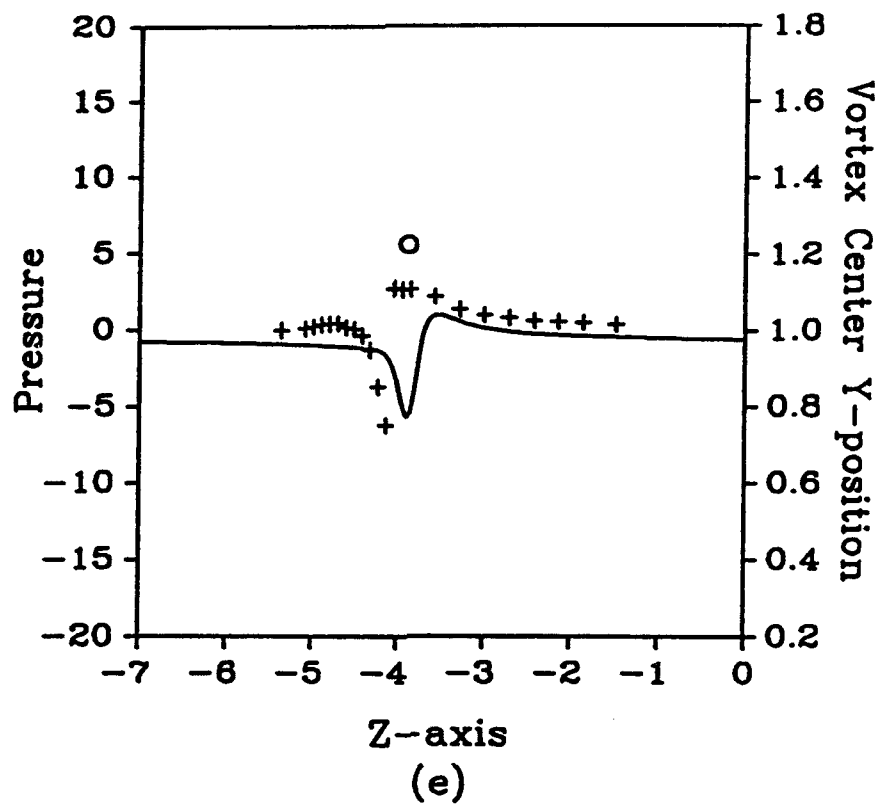
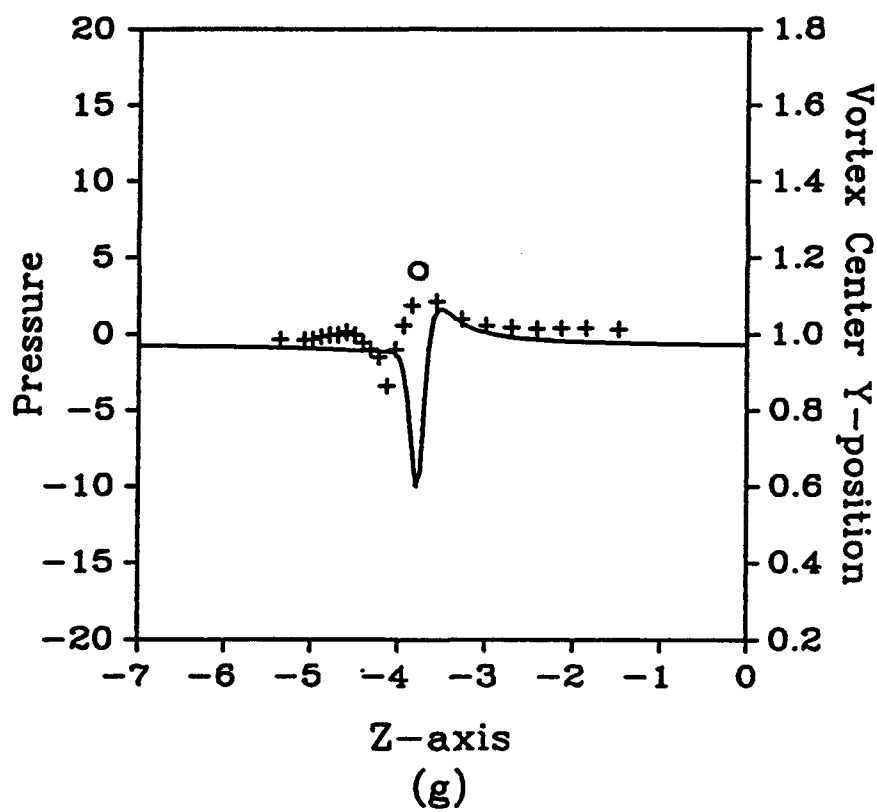


Figure 3.6 (continued)



downstream of the vortex. There is apparent in the results a shift in the position of the suction peak relative to the computed position of the vortex center; this may be due to uncertainty in the precise position of the vortex center in the experiments.

For the case of $\mu = .1$ the experimental data suggests that the effect of the airframe on the vortex core flow begins to be felt at about $\psi = 54^\circ$. This is manifest in a sudden decrease in the amplitude of the suction peak at this time. The present results do not show this trend at $\psi = 54^\circ$, thus establishing the approximate region of validity of the present model.

On Figure 3.7 is depicted the pressure gradient for the case of $\mu = .075$ for $\psi = 18^\circ$ to $\psi = 42^\circ$ in increments of 6° . These results are similar in form to the case of $\mu = .1$; however, it is apparent that in the later stages of the calculations the amplitude of the peak is higher. On Figure 3.8 are the corresponding results for the pressure. As with the earlier results the blade passage effect is evident at the lower values of ψ ; as the vortex moves toward the airframe, the tip vortex again becomes more dominant and the present analytical/computational effort appears to adequately capture the phenomenon.

The contribution of the unsteady term $\frac{\partial \phi}{\partial t}$ to the pressure p appearing in equation (2.50) has also been investigated. The results from both cases of $\mu = .1$ and $\mu = .075$ show that $\frac{\partial \phi}{\partial t}$ comprises a major part of the pressure during the initial stages from $\psi = 0^\circ$ to $\psi = 30^\circ$. In the latter stages, $\frac{\partial \phi}{\partial t}$ has only a slight effect on the pressure suction peak; however, it remains the major factor in the growth of the positive pressure hump appearing downstream of the suction peak.

3.6 Summary

In the present work the experimental results produced by Professor Komerath and his colleagues at the Georgia Institute of Technology have been compared with the results of a simplified model for this interaction. Results have been presented for the vortex path and the pressure distribution for two advance ratios indicative of low-speed forward flight. The experimental and analytical/numerical results are in substantial agreement for both the pressure and the vortex path during the time period prior to vortex impact. While some of the experimental data itself has been employed to determine the mean flow speed far from the airframe, the present analytical/computational effort is substantially free of fit parameters and may thus be termed a predictive effort. Estimates for the initial position of the vortex, the circulation of the vortex, and the vortex core radius have been determined directly from the experiments. In particular, it has been shown that the position and magnitude of the suction peak induced on the airframe can be adequately predicted using a three-dimensional potential flow analysis during the time period from the onset of strong interaction with the airframe until just prior to the vortex-airframe collision.

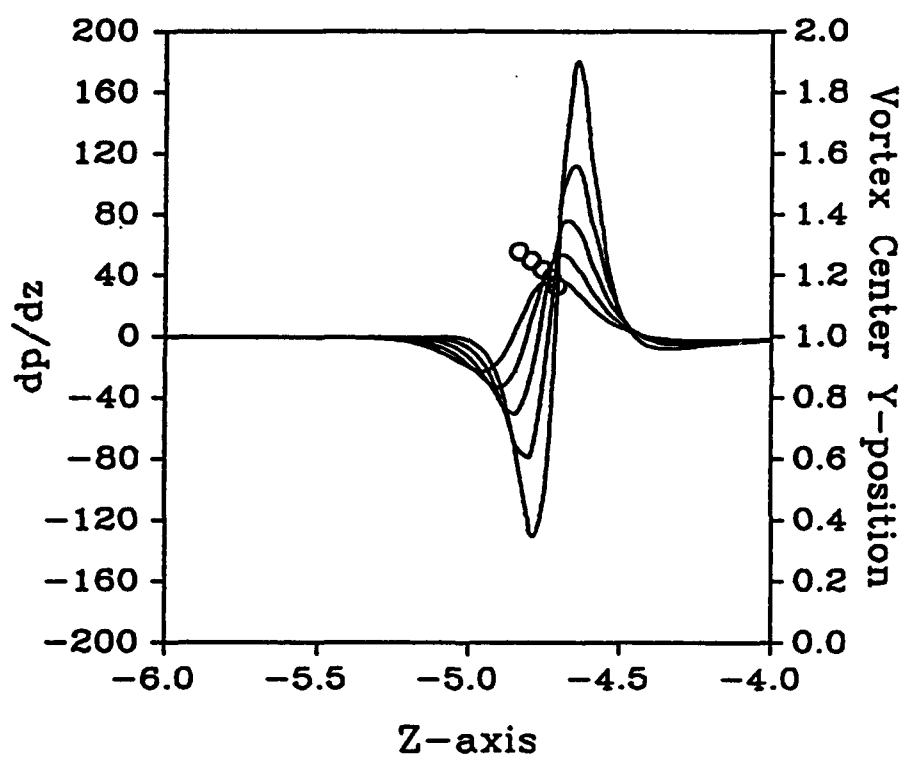


Figure 3.7: Pressure gradient $\frac{\partial p}{\partial z}$ for $\mu = .075$ along the top of the airframe for several values of $\psi = 18^\circ, 24^\circ, 30^\circ, 36^\circ$ and 42° . The amplitude of the pressure gradient spike increases as ψ increases. The open circles are side views of the computed vortex center ($s = 0$) position.

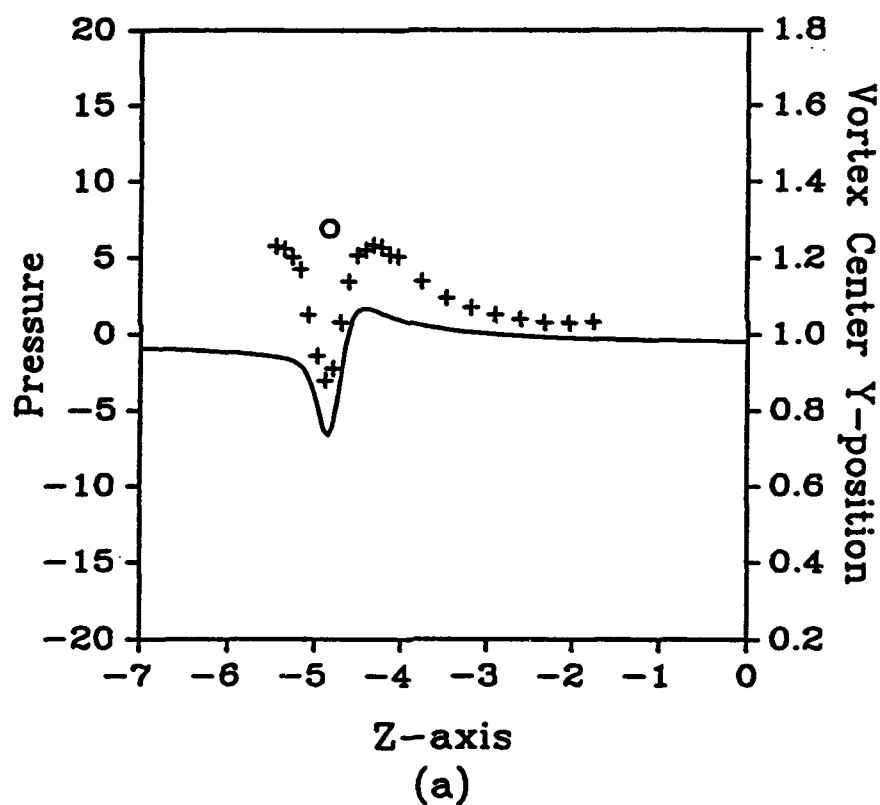


Figure 3.8: Pressure distribution along the top of the airframe for several values of ψ for $\mu = .075$. The circle is the side view of the computed vortex center ($s = 0$) position. (a) $\psi = 18^\circ$, (b) $\psi = 24^\circ$, (c) $\psi = 30^\circ$, (d) $\psi = 36^\circ$, and (e) $\psi = 42^\circ$.

Figure 3.8 (continued)

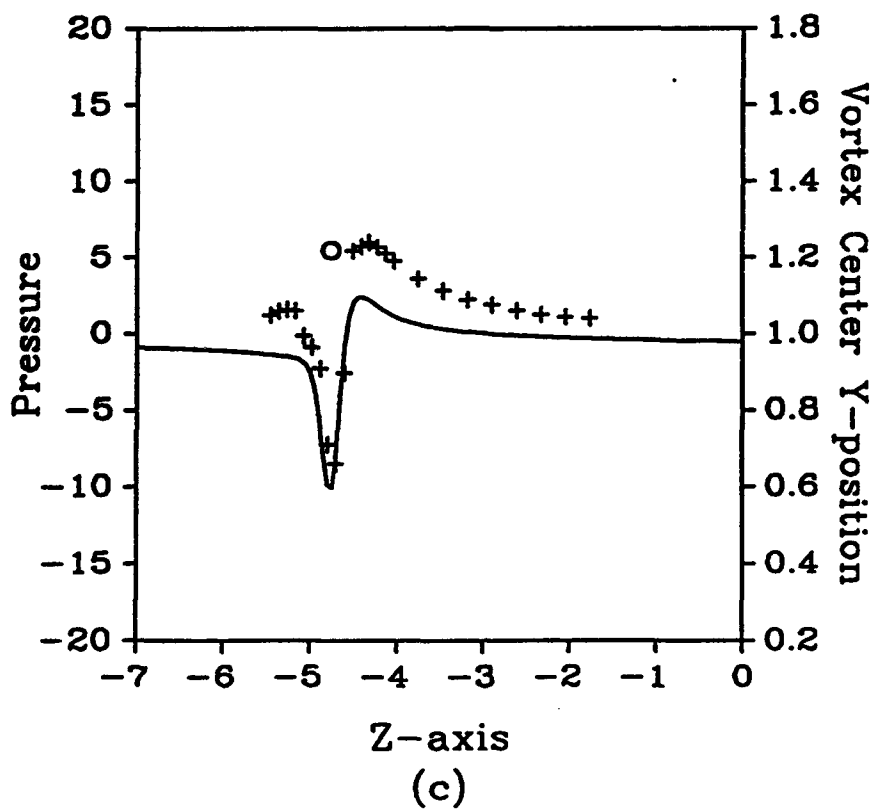
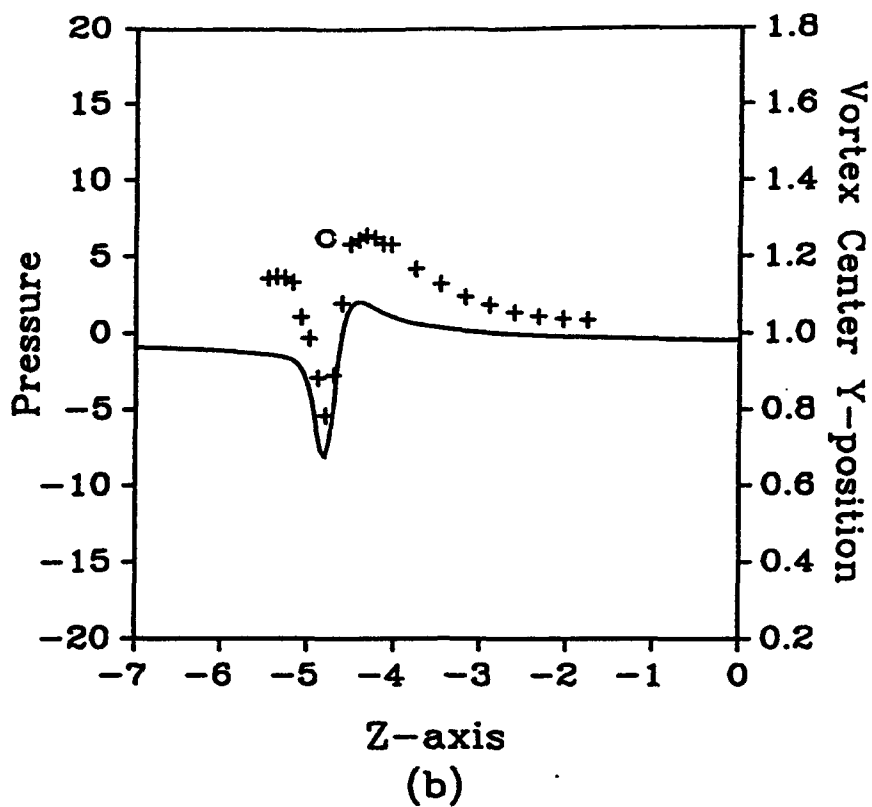
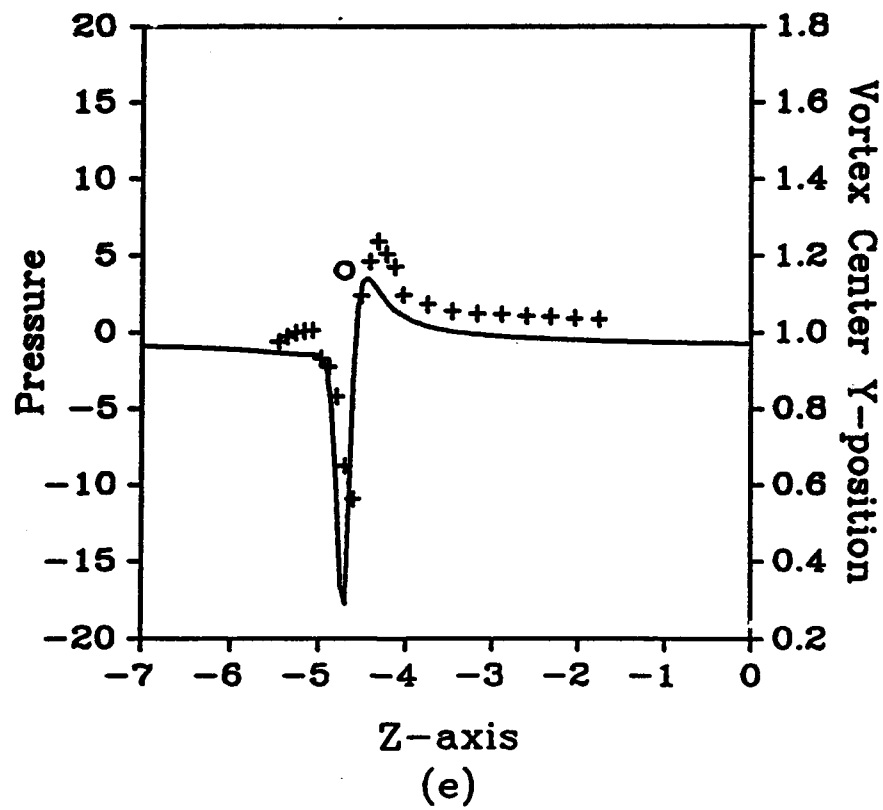
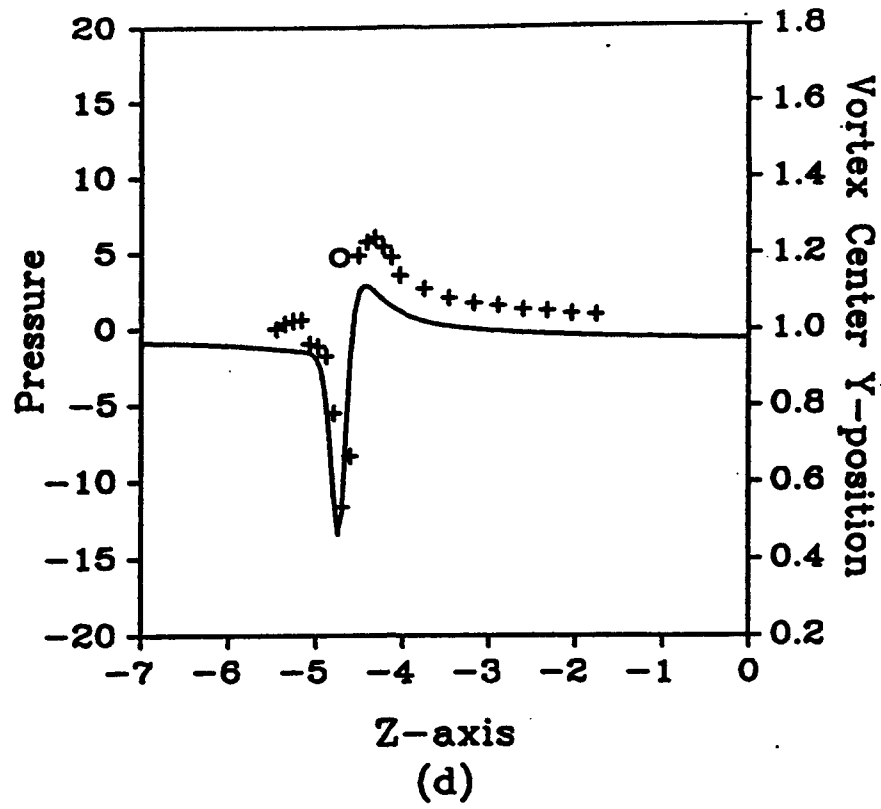


Figure 3.8 (continued)



The development of a very strong suction peak coincides with the emergence of a very large adverse pressure gradient, a feature which is often responsible for initiating boundary layer separation (see Chapter 5).

The scale of the sharp pressure gradients which generate the deep suction peaks in the pressure distribution on the top of the airframe are short in both space and time; this feature of the flow suggests that a purely computational approach to the present problem is likely to fail. This includes both those methods which involve convection of inviscid vortex filaments as well as direct computations of the Navier-Stokes equations. Consider, for example, in the present problem, a Navier-Stokes computation in which there are 200 points in each of the three coordinate directions; for simplicity, consider a cartesian coordinate system. Suppose that the computation is to be based on the Georgia Tech configuration and that the total computational domain is based on the lengths $L_x = L_z = 2R + \Delta R$ where R is the rotor radius $R = .457m$ and $L_y = 2H + H + D_{airframe} + 2H = .82m$, where H is the rotor to airframe gap and is about .14m. The diameter of the airframe is .134m. Note that this is a rather limited domain for a computational approach. Then the grid sizes are $\Delta x = \Delta z = .00625m$ and $\Delta y = .004m$. As discussed previously, a typical vortex radius is about .3in=.0076m and the boundary layer thickness is about .002m based on the airframe radius and axial speed W_∞ . Thus, in the present hypothetical computation, there would be *no* points within the boundary layer, and only one grid point to represent the vortex core. Moreover, since the three velocity components and the pressure need to be computed, for the present number of grid points, 32Mwords of memory are required for a single time step. This is about the size of the typically available memory in a standard supercomputer(say Cray YMP) calculation. Clearly, this situation is not tenable and suggests that the asymptotic approach taken in the present work is the only viable approach for accurate resolution of the small length and time scales which emerge in the present problem, given the present computational environment. In this spirit, in preparation for the consideration of the three dimensional boundary layer flow, the axisymmetric, two dimensional boundary layer flow is considered next.

CHAPTER IV

The Impulsively Started Two-Dimensional Boundary-Layer Flow Past a Circular Cylinder

4.1 Introduction

In this chapter we consider the analysis of the boundary-layer flow about the impulsively started cylinder in two dimensions using Fourier transform techniques. The purpose of this investigation is to provide a test of the accuracy and efficiency of the numerical algorithm which will be extended in Chapter 5 to calculate the three-dimensional boundary-layer on a cylinder induced by a generalized convecting vortex filament.

The two-dimensional boundary-layer flow past an impulsively started cylinder has been considered by many researchers. From this problem a basic understanding of the unsteady separation mechanisms which may occur in two dimensions has emerged. It has been recognized that the boundary-layer flow generated by an impulsively started cylinder is characterized by a finite time separation singularity which occurs at the surface after about .75 diameter movement (van Dommelen 1981). Evidence of the emergence of the singularity of the unsteady boundary-layer equations was first given by van Dommelen and Shen (1980). In their work, the boundary-layer flow past a suddenly started cylinder is calculated using a Lagrangian method. The presence of a singularity is indicated by, according to the Lagrangian formulation, the formation of a stationary point at which the y -position becomes singular. Here, the Lagrangian y -position of a fluid particle is given by the continuity integral (see van Dommelen 1981 p. 30) as

$$y = \int_{wall}^{\xi, \eta} \frac{ds}{|\nabla x|}$$

where s denotes the arc length along the line of constant x through (ξ, η) . Note that the continuity integral shows that the y -position may become singular where

$|\nabla x|$ approaches zero. Here $x = x(\xi, \eta, t)$ denotes the streamwise Lagrangian particle position. Simply stated, the stationary point develops at some location (ξ_s, η_s) at time t_s where

$$\frac{\partial x}{\partial \xi} = \frac{\partial x}{\partial \eta} = 0.$$

In the Eulerian formulation evidence of subsequent singular behavior is indicated by the local behavior of the displacement thickness as time increases. Their best estimate of this time when the boundary-layer flow becomes singular is $t_s = 1.5$ with the singularity occurring at a location $x_s = 111^\circ$ downstream of the front stagnation point. This is consistent with the experimental observations by Bouard and Coutenceau (1980) who investigate the early stages of the development of the wake behind an impulsively started cylinder. The emergence of a finite time singularity was later confirmed analytically by Cowley (1983) and Ingham (1984) who used a series extension method and a series truncation method, respectively.

Other numerical results have also been produced by other investigators. For example, Telionis and Tsahalis (1974) developed a numerical method using an upwind differencing scheme to account for flow reversal; however, they experienced breakdown with singular appearance at about $t \simeq 1.4$. The numerical algorithm of Cebeci (1979) which uses an Eulerian Keller box-scheme breaks down at time $t=1.4$. The work of Cebeci (1979) is consistent with previous work in that the boundary-layer flow is free of singularity for $t < 1.4$ although his results have been shown to be somewhat unreliable at larger times. On the other hand, van Dommelen (1981) and van Dommelen and Shen (1980) using the Lagrangian method show that the appearance of the singular behavior occurs at about $t \simeq 1.5$. Wu (1985) has adopted the Lagrangian method developed by van Dommelen and Shen (1980) to calculate the two-dimensional incompressible boundary-layer flow generated by an impulsively started elliptic cylinder at different angles of attack and two thickness ratios. An excellent review of other numerical methods employed to solve the impulsively started flow about a circular cylinder can be found in van Dommelen (1981).

The methodology developed in the present work to compute the boundary-layer flow past an impulsively started circular cylinder is considered next.

4.2 The Inviscid Flow

For simplicity, we consider the inviscid flow to correspond to the (r, θ) components of the inviscid flow field described by equation (2.17) for $\gamma = 1$. The physical situation and the coordinate system are shown in Figure 4.1. It can be shown that by integrating \tilde{U}_M , the velocity potential for the two-dimensional flow past the

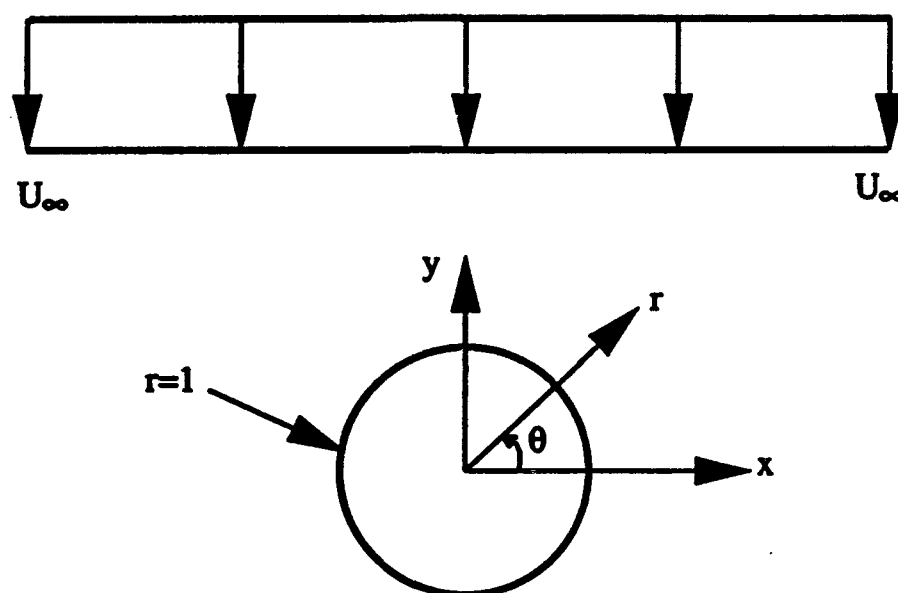


Figure 4.1: Geometry and coordinate system employed for the two-dimensional impulsively-started cylinder.

circular cylinder is given by

$$\phi_M = -\left(1 + \frac{1}{r}\right) \sin \theta, \quad (4.1)$$

where r is the nondimensional radius used in Chapter 2. Therefore, by taking the gradient of ϕ_M in polar coordinates, the velocity components may be written as

$$U_{Mr} = -\left(1 - \frac{1}{r^2}\right) \sin \theta, \quad (4.2)$$

and

$$U_{M\theta} = -\left(1 + \frac{1}{r^2}\right) \cos \theta. \quad (4.3)$$

At the surface of the cylinder where $r = 1$, the velocities and pressure gradients can be obtained by using the above equations and Euler's equations respectively, we have

$$U_{Mr} |_{r=1} = 0, \quad (4.4)$$

$$U_{M\theta} |_{r=1} = -2 \cos \theta, \quad (4.5)$$

$$\frac{\partial p}{\partial r} |_{r=1} = 0, \quad (4.6)$$

and

$$\frac{\partial p}{\partial \theta} |_{r=1} = 2 \sin 2\theta. \quad (4.7)$$

Note that $U_{M\theta}$ at the surface is not zero because the inviscid solution is not uniformly valid. The θ -component of the velocity is reduced to relative rest on the cylinder wall by an unsteady viscous boundary-layer which is considered next.

4.3 Boundary-Layer Formulation

In general, the viscous flow around a circular cylinder is governed by the Navier-Stokes equations and the continuity equation which, in an incompressible medium, are given in polar coordinates by

$$\frac{1}{r} \frac{\partial}{\partial r}(r \bar{u}_r) + \frac{1}{r} \frac{\partial \bar{u}_\theta}{\partial \theta} = 0, \quad (4.8)$$

$$\frac{D\bar{u}_r}{Dt} - \frac{\bar{u}_\theta^2}{r} = -\frac{\partial p}{\partial r} + \frac{1}{Re} \left[\nabla^2 \bar{u}_r - \frac{\bar{u}_r}{r^2} - \frac{2}{r^2} \frac{\partial \bar{u}_\theta}{\partial \theta} \right], \quad (4.9)$$

$$\frac{D\bar{u}_\theta}{Dt} + \frac{\bar{u}_\theta \bar{u}_r}{r} = -\frac{1}{r} \frac{\partial p}{\partial \theta} + \frac{1}{Re} \left[\nabla^2 \bar{u}_\theta - \frac{\bar{u}_\theta}{r^2} + \frac{2}{r^2} \frac{\partial \bar{u}_r}{\partial \theta} \right], \quad (4.10)$$

where $\bar{u}_r, \bar{u}_\theta$ are the nondimensional radial and azimuthal velocities. ∇^2 is the Laplace operator defined as

$$\nabla^2 = \frac{\partial^2}{\partial r^2} + \frac{1}{r} \frac{\partial}{\partial r} + \frac{1}{r^2} \frac{\partial^2}{\partial \theta^2}$$

and

$$\frac{D}{Dt} = \frac{\partial}{\partial t} + \bar{u}_r \frac{\partial}{\partial r} + \frac{\bar{u}_\theta}{r} \frac{\partial}{\partial \theta}$$

is the material derivative. Here $Re = \frac{U_\infty a}{\nu}$ is the Reynolds number, with ν the kinematic viscosity and U_∞ is the characteristic velocity.

However, for high Reynolds numbers the flow can be regarded as inviscid except at a thin boundary layer near the cylinder wall where the viscosity is not negligible. In order to describe the flow in this thin layer, we use the following scaled variables defined as

$$u_\theta = \bar{u}_\theta, \quad u_r = \bar{u}_r \sqrt{Re}, \quad y = (r - 1) \sqrt{Re}. \quad (4.11)$$

Substituting these relationships into equations (4.8)-(4.10) and dropping the terms of the order $Re^{-1/2}$, the boundary-layer equations for the flow past a cylinder are given by

$$\frac{\partial u_r}{\partial y} + \frac{\partial u_\theta}{\partial \theta} = 0, \quad (4.12)$$

$$\frac{\partial u_\theta}{\partial t} + u_r \frac{\partial u_\theta}{\partial y} + u_\theta \frac{\partial u_\theta}{\partial \theta} = -\frac{\partial p}{\partial \theta} + \frac{\partial^2 u_\theta}{\partial y^2}. \quad (4.13)$$

Equations (4.12) and (4.13) are subject to the initial and boundary conditions

$$u_r, u_\theta \text{ specified at } t = 0,$$

$$u_r = u_\theta = 0 \text{ at } y = 0, \quad u_\theta \rightarrow U_\theta|_{r=1} \text{ as } y \rightarrow \infty, \quad (4.14)$$

where $U_\theta|_{r=1}$ is the inviscid velocity component in the θ given by equation (4.5).

To describe the motion subsequent to $t = 0$, it is convenient to use Rayleigh variables according to

$$\eta = \frac{y}{2\sqrt{t}},$$

and the governing equations (4.12) and (4.13) become

$$\frac{\partial u_r}{\partial \eta} + 2\sqrt{t} \frac{\partial u_\theta}{\partial \theta} = 0, \quad (4.15)$$

$$4t \frac{\partial u_\theta}{\partial t} - 2\eta \frac{\partial u_\theta}{\partial \eta} - \frac{\partial^2 u_\theta}{\partial \eta^2} = -4t \frac{\partial p}{\partial \theta} + R_\theta, \quad (4.16)$$

where

$$R_\theta = -4t \left(\frac{u_r}{2\sqrt{t}} \frac{\partial u_\theta}{\partial \eta} + u_\theta \frac{\partial u_\theta}{\partial \theta} \right). \quad (4.17)$$

Let u_θ^0 denote the velocity distribution at $t=0$; then taking the limit of equation (4.16) as $t \rightarrow 0$, an equation for u_θ^0 is obtained

$$2\eta \frac{\partial u_\theta^0}{\partial \eta} + \frac{\partial^2 u_\theta^0}{\partial \eta^2} = 0, \quad (4.18)$$

which is subject to the following boundary conditions

$$u_\theta^0 = 0 \text{ at } \eta = 0, \quad u_\theta^0 = U_\theta|_{r=1}, \text{ as } \eta \rightarrow \infty. \quad (4.19)$$

The solution to equation (4.18) is given by

$$u_\theta^0 = -2 \cos \theta \operatorname{erf} \eta. \quad (4.20)$$

In what follows, we assume that the flow at subsequent times after $t = 0$ is a perturbation from the initial solution given by equation (4.20). Let \tilde{u} be the perturbation, then the total velocity can be written as

$$u_\theta = \tilde{u}_\theta + u_\theta^0. \quad (4.21)$$

In addition, let

$$u_r = 2\sqrt{t}(\tilde{u}_r + u_r^0), \quad (4.22)$$

where u_r^0 is the radial velocity that corresponds to u_θ^0 and is obtained from the continuity equation. The solution for u_r^0 may be obtained analytically and is given by

$$u_r^0 = -2 \sin \theta \left(\eta \operatorname{erf} \eta + \frac{1}{\sqrt{\pi}} e^{-\eta^2} - \frac{1}{\sqrt{\pi}} \right). \quad (4.23)$$

Substituting equations (4.22) and (4.23) into (4.15) and (4.16), and using equation (4.7), the boundary-layer equations become

$$\frac{\partial \tilde{u}_r}{\partial \eta} + \frac{\partial \tilde{u}_\theta}{\partial \theta} = 0, \quad (4.24)$$

$$4t \frac{\partial \tilde{u}_\theta}{\partial t} - 2\eta \frac{\partial \tilde{u}_\theta}{\partial \eta} - \frac{\partial^2 \tilde{u}_\theta}{\partial \eta^2} = -4t \sin 2\theta + \tilde{R}_\theta, \quad (4.25)$$

where

$$\tilde{R}_\theta = -4t \left[(\tilde{u}_r + u_r^0) \frac{\partial}{\partial \eta} (\tilde{u}_\theta + u_\theta^0) + (\tilde{u}_\theta + u_\theta^0) \frac{\partial}{\partial \theta} (\tilde{u}_\theta + u_\theta^0) \right]. \quad (4.26)$$

Note that the term \tilde{R}_θ contains all the nonlinear inertia terms. Treatment of these terms to obtain a numerical solution will be discussed next.

4.4 Numerical Methods

The numerical scheme used in this study is a combination of finite-difference methods and the Fourier transform methods. First, the Fourier transform method is employed to calculate the derivatives with respect to the θ -direction; second, central finite differences are used to approximate all derivatives with respect to η . Finally, the implicit Crank-Nickolson marching technique is employed to advance the solution in time.

The discretization in the η direction consists of dividing the domain into $N - 1$ equal intervals; thus, the grid points are defined by

$$\eta_j = (j - 1)\Delta\eta \quad \text{for } j = 1, 2, \dots, N, \quad (4.27)$$

where N is the total number of points used across the boundary-layer and $\Delta\eta$ is the grid size. The boundary condition in the y -direction is imposed at some large but finite value of η , say $\eta = \eta_{max}$. In general, η_{max} is determined by testing larger values until the change in the results becomes negligible. The finite difference and the Crank-Nickolson techniques can then be applied in η and t , which yields

$$4\left(t - \frac{1}{2}\Delta t\right) \frac{\tilde{u}_\theta^t - \tilde{u}_\theta^{t-\Delta t}}{\Delta t} - \eta \left(\frac{\partial \tilde{u}_\theta^t}{\partial \eta} + \frac{\partial \tilde{u}_\theta^{t-\Delta t}}{\partial \eta} \right) - \frac{1}{2} \left(\frac{\partial^2 \tilde{u}_\theta^t}{\partial \eta^2} + \frac{\partial^2 \tilde{u}_\theta^{t-\Delta t}}{\partial \eta^2} \right) = \frac{1}{2} (\tilde{P}_\theta^t + \tilde{P}_\theta^{t-\Delta t}), \quad (4.28)$$

where

$$\tilde{P}_\theta = -4t \frac{\partial p}{\partial \theta} + \tilde{R}_\theta. \quad (4.29)$$

The first and the second derivatives of \tilde{u}_θ with respect to η are evaluated by using central differencing; let u_j^n denote \tilde{u}_θ at $\eta = \eta_j$ and $t = (n - 1)\Delta t$ then we have

$$\left(\frac{\partial u}{\partial \eta} \right)_j^n = \frac{(u_{j+1}^n - u_{j-1}^n)}{2\Delta\eta} + O(\Delta\eta^2), \quad (4.30)$$

and

$$\left(\frac{\partial^2 u}{\partial \eta^2} \right)_j^n = \frac{(u_{j+1}^n - 2u_j^n + u_{j-1}^n)}{\Delta\eta^2} + O(\Delta\eta^2). \quad (4.31)$$

The final discretized form of the equations results in a tridiagonal system which may be written as

$$a_j u_{j-1}^{n+1} + b_j u_j^{n+1} + c_j u_{j+1}^{n+1} = -a_j u_{j-1}^n + d_j u_j^n - c_j u_{j+1}^n + e_j, \quad (4.32)$$

where

$$a_j = \frac{1}{2}\eta_j \frac{\Delta t}{\Delta \eta} - \frac{1}{2} \frac{\Delta t}{\Delta \eta^2}, \quad (4.33)$$

$$b_j = 4t^{n+\frac{1}{2}} + \frac{\Delta t}{\Delta \eta^2}, \quad (4.34)$$

$$c_j = -\frac{1}{2}\eta_j \frac{\Delta t}{\Delta \eta} - \frac{1}{2} \frac{\Delta t}{\Delta \eta^2}, \quad (4.35)$$

$$d_j = 4t^{n+\frac{1}{2}} - \frac{\Delta t}{\Delta \eta^2}, \quad (4.36)$$

$$e_j = +\frac{1}{2} (\bar{P}_\theta^{n+1} + \bar{P}_\theta^n). \quad (4.37)$$

The tridiagonal system given in equation (4.32) may be written in matrix form as

$$\begin{bmatrix} b_2 & c_2 & & & \\ a_3 & b_3 & c_3 & & \\ & \ddots & \ddots & \ddots & \\ & & a_{N-2} & b_{N-2} & c_{N-2} \\ & & & a_{N-1} & b_{N-1} \end{bmatrix} \begin{bmatrix} u_2 \\ u_3 \\ \vdots \\ u_{N-2} \\ u_{N-1} \end{bmatrix} = \begin{bmatrix} R_2 \\ R_3 \\ \vdots \\ R_{N-2} \\ R_{N-1} \end{bmatrix}$$

where

$$R_j = -a_j u_{j-1}^n + d_j u_j^n - c_j u_{j+1}^n + e_j \text{ for } j = 3, \dots, N-2, \quad (4.38)$$

and since $u = 0$ at $\eta = 0$ and is finite at $\eta = \eta_{max}$, we have

$$R_{N-1} = -a_{N-1} u_{N-2}^n + d_{N-1} u_{N-1}^n - c_{N-1} (u_N^{n+1} + u_N^n) + e_{N-1}, \quad (4.39)$$

and

$$R_2 = d_2 u_2^n - c_2 u_3^n + e_2. \quad (4.40)$$

The truncation errors for the differencing scheme are of order (Δt^2) and $(\Delta \eta^2)$ because of the central differencing used here.

To compute the nonlinear terms appearing in \bar{R}_θ Fourier transform techniques are employed to compute all the derivatives in the θ -direction while finite difference methods are used to compute the η derivatives. The Finite Fourier transform of any flow quantity is defined as

$$\hat{G}(m) = \int_{-\pi}^{\pi} G(\theta) e^{-im\theta} d\theta \quad (4.41)$$

where $m = 0, \pm 1, \pm 2, \pm 3 \dots$ is the transform variable. The discretization of the Fourier transform is carried out as follows. The grid points θ_i are defined by

$$\theta_i = (i - 1 - M/2)\Delta\theta \text{ for } i = 1, 2, \dots, M, \quad -\pi \leq \theta \leq \pi, \quad (4.42)$$

where the grid spacing $\Delta\theta$ is defined as

$$\Delta\theta = \frac{2\pi}{M}, \quad (4.43)$$

and M is chosen to be power of 2 in order to use efficiently the fast Fourier transform (Cooley and Tukey 1965).

The computation of terms involving differentiation with respect to θ is explained as follows. Consider the term $\frac{\partial \tilde{u}_\theta}{\partial \theta}$ which appears in \tilde{R}_θ ; the velocity \hat{u}_θ which is the forward Fourier transform of \tilde{u}_θ is computed. To obtain $\frac{\partial \tilde{u}_\theta}{\partial \theta}$, the quantity $im\hat{u}_\theta$ is inverted back to the physical domain using the inverse Fourier transform. The two terms are then multiplied together to obtain the required result in the physical domain. All other derivatives in θ are obtained in a similar way. It is to be noted that since the θ -derivatives of u_θ are not numerically differentiated, there is no need for a special differencing scheme to incorporate the possibility of reversed flow. Each point in the physical space θ corresponds to a full range of points in spectral space; the possibility that regions of reversed flow may exist is automatically taken into account by the Fourier transform. The iteration scheme used here is summarized as follows. The scheme consists of two main loops. Within the outer loop, the boundary-layer equations are solved for each time step iteratively. At each specific time step, using the prescribed boundary conditions and pressure gradients which are known solutions of the inviscid flow, one subroutine is called to compute \tilde{R}_θ using previously iterated values of \tilde{u}_θ as an initial guess. The tridiagonal system for the new iterate \tilde{u}_θ is then solved using the Thomas algorithm. The process is repeated until the change of \tilde{u}_θ in successive iterations is less than a specified absolute tolerance value; in this case 10^{-5} is used. The calculation then continues to the outer loop where time marching is performed. In solving (4.25) for \tilde{u}_θ , under-relaxation is used according to the formulas

$$\hat{u}_\theta = \omega \hat{u}_\theta^{\text{new}} + (1 - \omega) \hat{u}_\theta^{\text{old}}.$$

Typically, for $\omega = 0.8$, 10-15 iterations or sweeps of the mesh in the interior are required to obtain convergence. It should be noted that within each iteration, a new value of the normal velocity \tilde{u}_r is computed by using the continuity equation (4.24). This involves the integration of $\frac{\partial \tilde{u}_\theta}{\partial \theta}$ with respect to η ; the integration is performed numerically using Simpson's rule.

In order to ensure good accuracy, a grid size study was conducted. Table 4.1 shows the results for the azimuthal velocity u_θ computed with different grid sizes $\Delta\eta = .1, .05, .025$ at $t = 1.4$ where $\eta_{\max} = 8$, $\Delta t = 0.0025$ and $\Delta\theta = \frac{2\pi}{256}$. Here we choose the location where $\theta = -11\pi/16$ ($\theta = -56.25^\circ$) which is about 35.25° downstream of the location of the singularity ($\theta_s = -21^\circ$ at the time $t_s = 1.5$, see van Dommelen and Shen 1980). The reason we choose this location is that flow reversal exists at this point and inaccuracies are most likely to arise first in this

region. Notice that $\Delta\eta = 0.05$ ensures at least three-digit accuracy and will be used to obtain the results. In Table 4.1 the total number of points N which correspond $\Delta\eta = .1, .05, .025$ are respectively $N=81, 161$ and 321 . Table 4.2 also shows the results for $\Delta\theta = \frac{2\pi}{256}$, $\Delta\theta = \frac{2\pi}{512}$ and $\Delta\theta = \frac{2\pi}{1024}$; here the results correspond to time $t = 1.4$ and are shown at fixed $\eta = 0.05$ using $\Delta t = 0.0025$. In addition, Table 4.3 shows the effect of varying Δt . The results are shown at the same location and time employed in Table 4.2 and Table 4.1 with $\Delta\theta = \frac{2\pi}{512}$. An appropriate value of η_{max} has also been determined. $\eta_{max} = 8$ and $\eta_{max} = 12$ were tested and $\eta_{max} = 8$ is sufficient for three digit accuracy; this value corresponds approximately to y_{max} employed by Xiao et al (1990).

4.5 Results and Discussion

Numerical results have been obtained for the resolved grid system corresponding to $\Delta\eta = .05$, $\Delta\theta = 2\pi/512$ and $\Delta t = .001$. Computed results for the displacement thickness δ^* , wall shear τ_w and the streamline flow patterns are obtained using the definitions of δ^* , τ_w and the streamfunction ψ which are given by

$$\delta^* = \int_0^y \left(1 + \frac{u_\theta}{2 \cos \theta} \right) dy,$$

$$\tau_w = \frac{\partial u_\theta}{\partial y} \Big|_{y=0}$$

and

$$\psi(y) = \int_0^y u_\theta dy'.$$

Note that in this chapter, ψ denotes streamfunction and not rotor blade angle as in the previous chapter.

The results of van Dommelen (1981) and Xiao et al (1990) for the displacement thickness and the wall shear are shown in Figures 4.2 and 4.3. The same results are reproduced by using the methodology of the present work and they are shown in Figures 4.4 and 4.5. Figure 4.4 shows the temporal development of the displacement thickness δ^* which is magnified by a factor $Re^{1/2}$ in order to obtain an $O(1)$ quantity. Note that before $t=1.4$, the displacement thickness is almost monotonic. However, at times subsequent to $t=1.4$, the displacement thickness grows sharply and then drops quickly, forming a spike-like structure. This was also observed by van Dommelen (1981) and Xiao et al (1990) as noted on Figure 4.2. It should be noted that the times shown in van Dommelen results correspond exactly to twice the times shown in the present work. This is due to the choice of the mean free stream away from the cylinder.

Table 4.1: Effect of $\Delta\eta$ on the azimuthal velocity at $t=1.4$

η	$\Delta\eta=0.1$	$\Delta\eta=0.05$	$\Delta\eta=0.025$
0.20	0.51403E+00	0.51315E+00	0.51297E+00
0.40	0.71678E+00	0.71551E+00	0.71525E+00
0.60	0.72443E+00	0.72303E+00	0.72275E+00
0.80	0.62538E+00	0.62415E+00	0.62389E+00
1.00	0.47298E+00	0.47190E+00	0.47164E+00
1.20	0.29575E+00	0.29445E+00	0.29412E+00
1.40	0.10678E+00	0.10528E+00	0.10489E+00
1.60	-0.85423E-01	-0.86957E-01	-0.87359E-01
1.80	-0.27230E+00	-0.27390E+00	-0.27431E+00
2.00	-0.44637E+00	-0.44821E+00	-0.44867E+00
2.20	-0.60186E+00	-0.60413E+00	-0.60470E+00
2.40	-0.73474E+00	-0.73753E+00	-0.73825E+00
2.60	-0.84306E+00	-0.84633E+00	-0.84717E+00
2.80	-0.92720E+00	-0.93072E+00	-0.93164E+00
3.00	-0.98948E+00	-0.99297E+00	-0.99389E+00
3.20	-0.10335E+01	-0.10367E+01	-0.10375E+01
3.40	-0.10632E+01	-0.10659E+01	-0.10666E+01
3.60	-0.10825E+01	-0.10846E+01	-0.10852E+01
3.80	-0.10945E+01	-0.10961E+01	-0.10965E+01
4.00	-0.11017E+01	-0.11028E+01	-0.11031E+01
4.20	-0.11059E+01	-0.11066E+01	-0.11069E+01
4.40	-0.11082E+01	-0.11087E+01	-0.11089E+01
4.60	-0.11095E+01	-0.11099E+01	-0.11099E+01
4.80	-0.11102E+01	-0.11104E+01	-0.11105E+01
5.00	-0.11106E+01	-0.11107E+01	-0.11108E+01
5.20	-0.11108E+01	-0.11109E+01	-0.11109E+01
5.40	-0.11109E+01	-0.11110E+01	-0.11110E+01
5.60	-0.11110E+01	-0.11110E+01	-0.11110E+01
5.80	-0.11110E+01	-0.11111E+01	-0.11111E+01
6.00	-0.11111E+01	-0.11111E+01	-0.11111E+01

Table 4.2: Effect of $\Delta\theta$ on the azimuthal velocity at $t=1.4$

η	$\Delta\theta = \frac{2\pi}{256}$	$\Delta\theta = \frac{2\pi}{512}$	$\Delta\theta = \frac{2\pi}{1024}$
0.20	0.51403E+00	0.51389E+00	0.51411E+00
0.40	0.71678E+00	0.71664E+00	0.71700E+00
0.60	0.72443E+00	0.72479E+00	0.72522E+00
0.80	0.62538E+00	0.62727E+00	0.62771E+00
1.00	0.47298E+00	0.47632E+00	0.47668E+00
1.20	0.29575E+00	0.29872E+00	0.29903E+00
1.40	0.10678E+00	0.10893E+00	0.10925E+00
1.60	-0.85423E-01	-0.83251E-01	-0.82954E-01
1.80	-0.27230E+00	-0.26986E+00	-0.26961E+00
2.00	-0.44637E+00	-0.44391E+00	-0.44371E+00
2.20	-0.60186E+00	-0.59954E+00	-0.59940E+00
2.40	-0.73474E+00	-0.73252E+00	-0.73254E+00
2.60	-0.84306E+00	-0.84123E+00	-0.84120E+00
2.80	-0.92720E+00	-0.92573E+00	-0.92574E+00
3.00	-0.98948E+00	-0.98841E+00	-0.98844E+00
3.20	-0.10335E+01	-0.10328E+01	-0.10328E+01
3.40	-0.10632E+01	-0.10629E+01	-0.10629E+01
3.60	-0.10825E+01	-0.10824E+01	-0.10824E+01
3.80	-0.10945E+01	-0.10946E+01	-0.10946E+01
4.00	-0.11017E+01	-0.11019E+01	-0.11019E+01
4.20	-0.11059E+01	-0.11061E+01	-0.11061E+01
4.40	-0.11082E+01	-0.11085E+01	-0.11085E+01
4.60	-0.11095E+01	-0.11098E+01	-0.11098E+01
4.80	-0.11102E+01	-0.11105E+01	-0.11105E+01
5.00	-0.11106E+01	-0.11108E+01	-0.11108E+01
5.20	-0.11108E+01	-0.11110E+01	-0.11110E+01
5.40	-0.11109E+01	-0.11111E+01	-0.11111E+01
5.60	-0.11110E+01	-0.11111E+01	-0.11111E+01
5.80	-0.11110E+01	-0.11111E+01	-0.11111E+01
6.00	-0.11111E+01	-0.11111E+01	-0.11111E+01

Table 4.3: Effect of Δt on the azimuthal velocity $t=1.4$

η	$t = 0.005$	$t = 0.0025$	$t = 0.00125$
0.20	0.51403E+00	0.51389E+00	0.51359E+00
0.40	0.71678E+00	0.71655E+00	0.71607E+00
0.60	0.72443E+00	0.72416E+00	0.72364E+00
0.80	0.62538E+00	0.62517E+00	0.62474E+00
1.00	0.47298E+00	0.47295E+00	0.47271E+00
1.20	0.29575E+00	0.29588E+00	0.29578E+00
1.40	0.10678E+00	0.10698E+00	0.10693E+00
1.60	-0.85423E-01	-0.85203E-01	-0.85227E-01
1.80	-0.27230E+00	-0.27211E+00	-0.27213E+00
2.00	-0.44637E+00	-0.44620E+00	-0.44621E+00
2.20	-0.60186E+00	-0.60169E+00	-0.60166E+00
2.40	-0.73474E+00	-0.73454E+00	-0.73445E+00
2.60	-0.84306E+00	-0.84284E+00	-0.84268E+00
2.80	-0.92720E+00	-0.92697E+00	-0.92676E+00
3.00	-0.98948E+00	-0.98925E+00	-0.98903E+00
3.20	-0.10335E+01	-0.10333E+01	-0.10331E+01
3.40	-0.10632E+01	-0.10630E+01	-0.10628E+01
3.60	-0.10825E+01	-0.10823E+01	-0.10822E+01
3.80	-0.10945E+01	-0.10943E+01	-0.10942E+01
4.00	-0.11017E+01	-0.11016E+01	-0.11015E+01
4.20	-0.11059E+01	-0.11058E+01	-0.11057E+01
4.40	-0.11082E+01	-0.11082E+01	-0.11082E+01
4.60	-0.11095E+01	-0.11095E+01	-0.11095E+01
4.80	-0.11102E+01	-0.11102E+01	-0.11102E+01
5.00	-0.11106E+01	-0.11106E+01	-0.11106E+01
5.20	-0.11108E+01	-0.11108E+01	-0.11108E+01
5.40	-0.11109E+01	-0.11109E+01	-0.11109E+01
5.60	-0.11110E+01	-0.11110E+01	-0.11110E+01
5.80	-0.11110E+01	-0.11110E+01	-0.11110E+01
6.00	-0.11111E+01	-0.11111E+01	-0.11111E+01

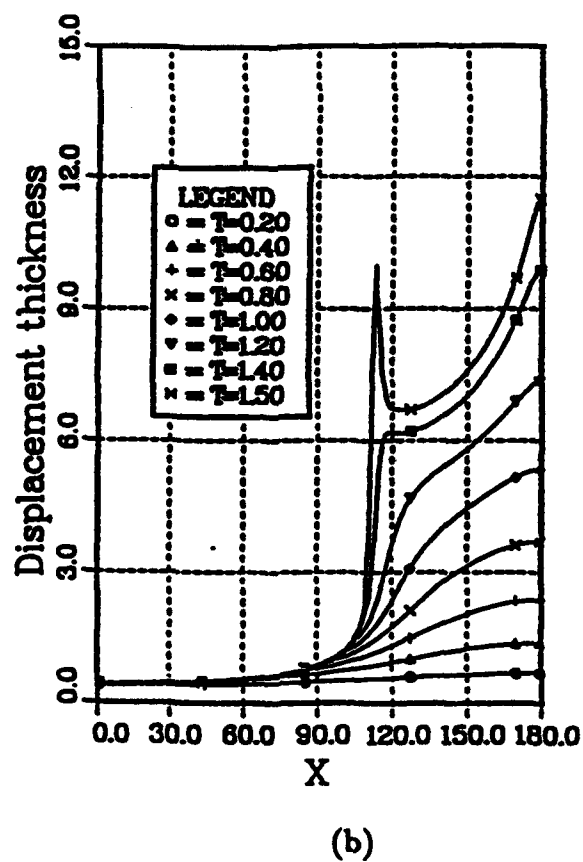
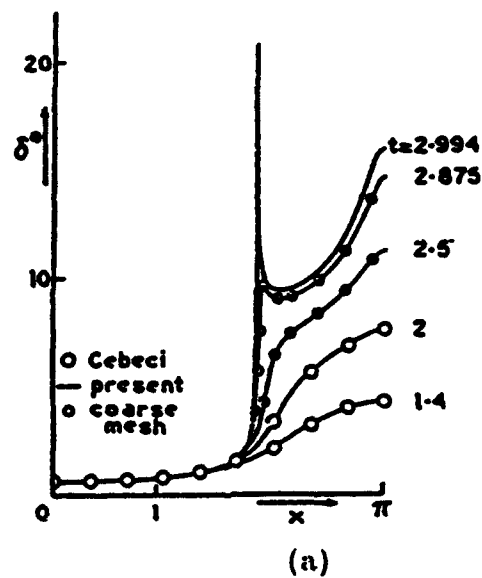
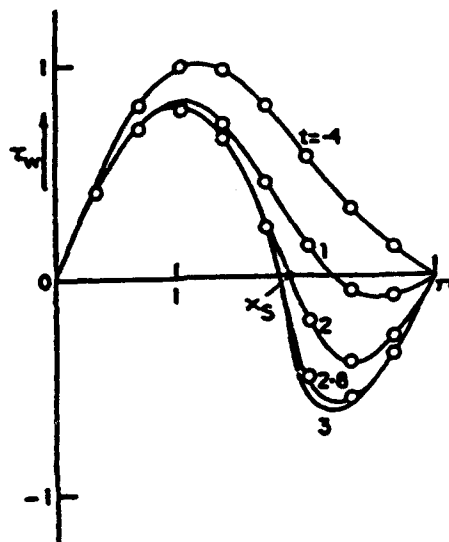
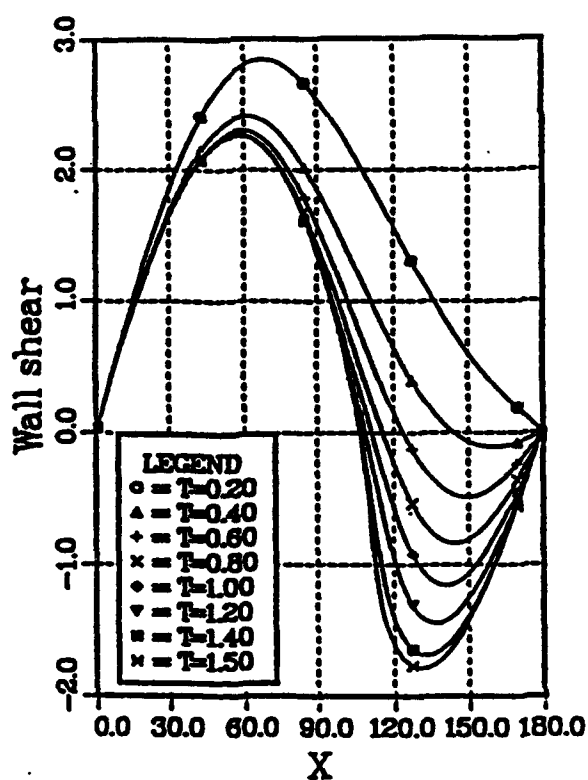


Figure 4.2: Temporal development of the displacement thickness. (a) From van Dommelen (1981) using the Lagrangian method, (b) from Xiao et al. (1990) using a non-iterative method with upwind differencing. Note that the time scale in (b) is half of that in (a).



(a)



(b)

Figure 4.3: Temporal development of wall shear. (a) From van Dommelen (1981) using the Lagrangian method, (b) from Xiao et al. (1990) using a non-iterative method with upwind differencing. Note that the time scale in (b) is half of that in (a).

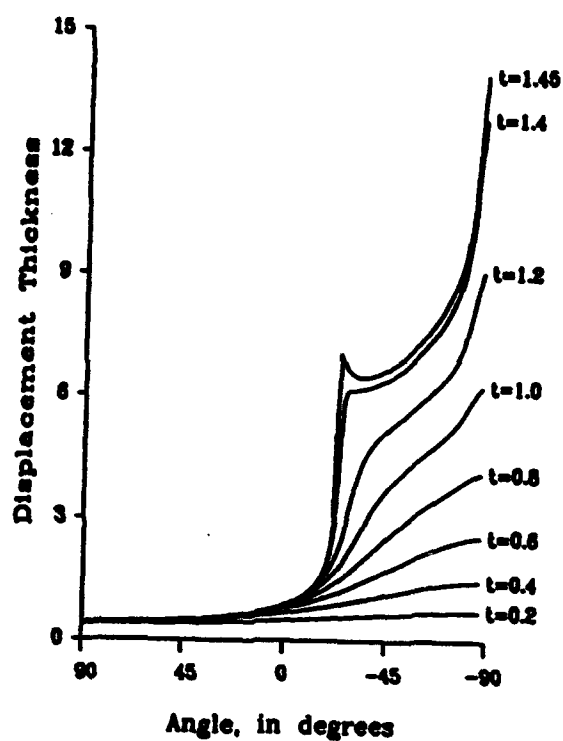


Figure 4.4: Temporal development of the displacement thickness computed in the present work.

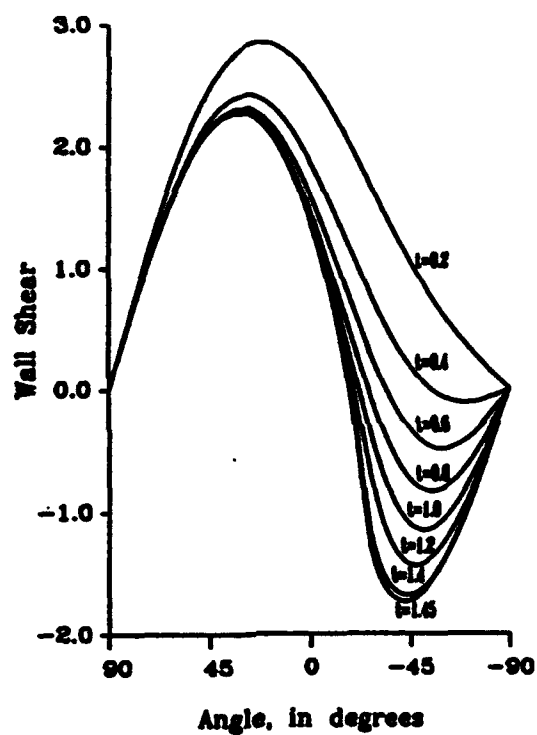


Figure 4.5: Temporal development of the wall shear computed in the present work.

van Dommelen (1981) used $\gamma = 0.5$ (as shown in equation 4.2) instead of $\gamma = 1$ as in the present work. According to van Dommelen (1981), the singularity is interpreted here as an indication of the "eruption" of the boundary-layer on an $O(Re^{-1/2})$ boundary-layer scale. It should be noted that in the boundary-layer approximation the Reynolds number is assumed infinite; in the actual physical situation, on the body scale, the eruption is no more than a local bulging of the infinitely thin boundary-layer. Figure 4.5 shows the evolution of the wall shear stress; the results are consistent with those of van Dommelen (1981) and agree very well with those of Xiao et al. (1990) as shown in Figure 4.3. Note that the wall shear gradient becomes steeper as the singularity is approached, however it remains regular at all times. Streamline patterns at $t = 0.2, 0.4, 0.6, 0.8, 1.0, 1.2, 1.4$ and 1.45 are shown in Figure 4.6. Because $Re \rightarrow \infty$, the flow patterns represent a greatly expanded view of the flow in the infinitely thin boundary-layer ring around the cylinder. Similar to the spike structure in the displacement thickness which is observed at $t = 1.45$, a hump in the streamline patterns is also detected near the singularity.

At later times ($t > 1.46$) the current computational scheme suffers some numerical instabilities which originate at the leading and the trailing edges of the cylinder. This is believed to be due to the non-resolved grid at these locations and clustering of the grid near these points is required to eliminate these oscillations. No attempt has been made in the current investigation to introduce a transformation variable along the θ -direction to cluster the grid near the stagnation points. However, more points must be used with a uniform grid in order to stabilize the numerical computations beyond $t=1.46$.

4.6 Summary

Fourier Transform techniques combined with the Crank Nicolson scheme are employed to solve the unsteady two-dimensional boundary-layer flow past a circular cylinder which is suddenly set in motion in a direction normal to its axis. This type of flow has been well studied and it has been shown by van Dommelen and Shen that this flow is characterized by the emergence of a finite time singularity at $t_s = 1.5$ and at the location $x_s = 111^\circ$ downstream from the front stagnation point. The results of Xiao et al. (1990) also confirm this phenomenon using a non-iterative scheme with upwind-differencing of the convective term. The present results agree very well up to $t = 1.45$ with the results of van Dommelen and Shen (1980) and the results of Xiao et al. (1990). The present numerical scheme becomes unstable at later times and no attempt has been made to remove the numerical instabilities which originate at the front and rear stagnation points. As suggested by Xiao et al. (1990) clustering of the grid at these points is necessary to resolve the numerical computations. The Fourier Transform technique proves to be very

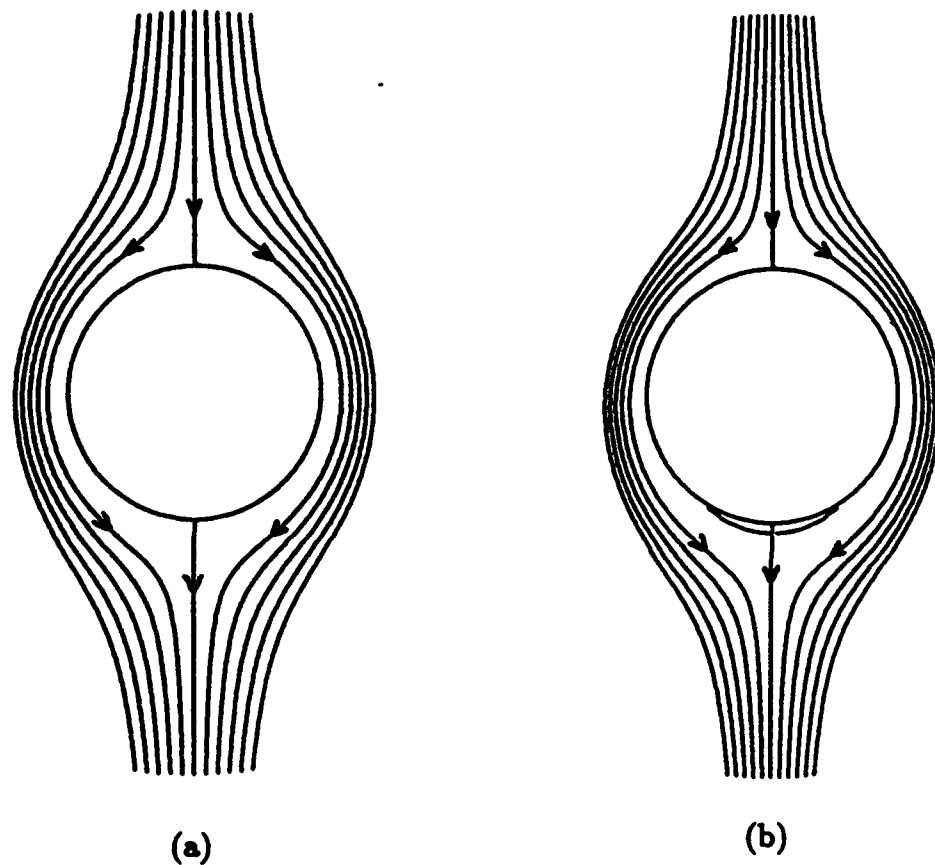


Figure 4.6: Instantaneous streamline patterns for the boundary-layer flow past an impulsively started circular cylinder. The results are shown for the times (a) $t=0.2$, (b) $t=0.4$, (c) $t=0.6$, (d) $t=0.8$, (e) $t=1.0$, (f) $t=1.2$, (g) $t=1.4$, (h) $t=1.45$. The boundary-layer and the recirculating regions are greatly expanded in the normal direction, and not to scale.

Figure 4.6 (continued)

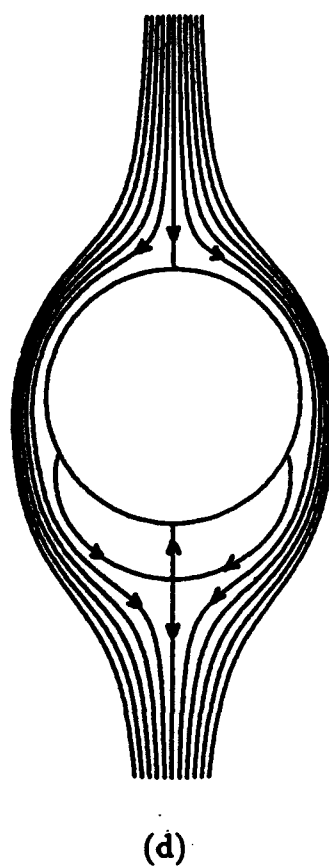
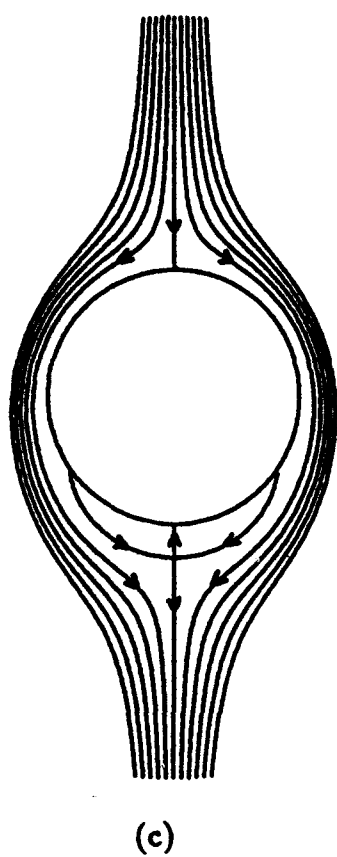
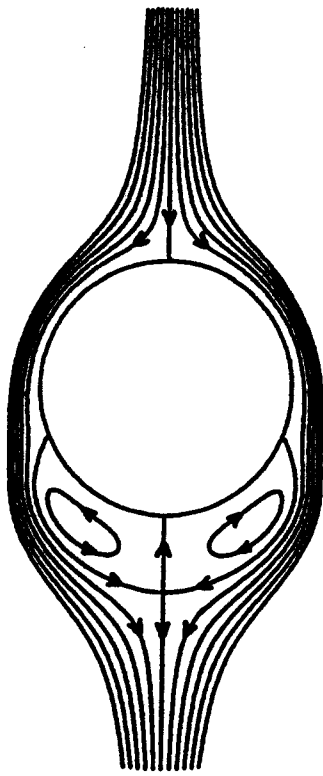
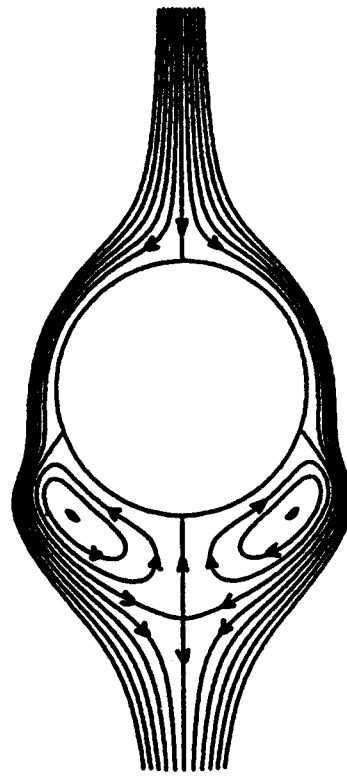


Figure 4.6 (continued)

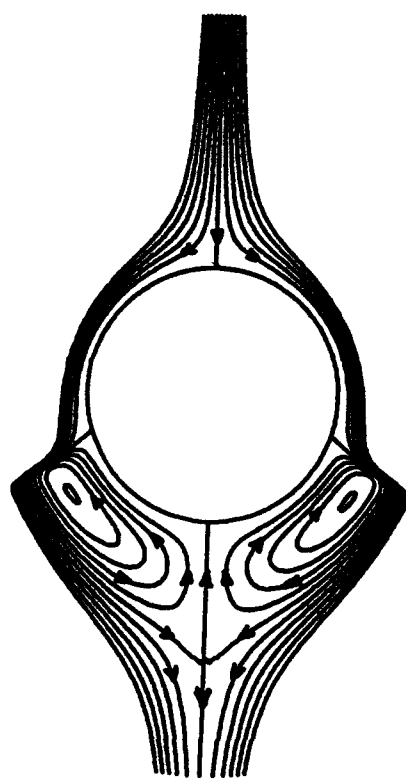


(e)

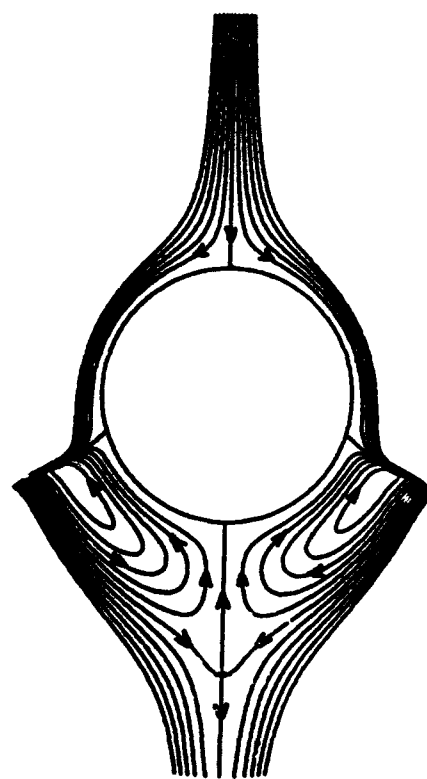


(f)

Figure 4.6 (continued)



(g)



(h)

accurate at early times; for instance, up to $t=0.5$ only 64 modes in θ are needed to ensure 4 digit accuracy. However, in regions of large variation (at later times) many more points are needed to remove the numerical oscillations.

CHAPTER V

The Boundary Layer Induced by a Vortex Impinging on an Airframe

5.1 Introduction

In Chapters 2 and 3 the trajectory of a three-dimensional vortex filament convecting above a cylinder has been calculated. In particular, the evolution of the vortex filament in space and time is obtained when the vortex is embedded in a stagnant medium, in a symmetric mean flow and in an asymmetric mean flow which is typical of applications. The initial configuration of the vortex is arbitrary; however, in order to simplify the problem, a straight filament configuration is used as an initial condition for both the stagnant medium case and the symmetric mean flow case. In this chapter, for each of the cases mentioned above, the nature of the unsteady boundary-layer flow induced on the cylinder surface by the moving vortex is investigated. As shown in Chapters 2 and 3, the effects of the interaction of the tip-vortex with the cylinder are associated with the development of large and extremely unsteady adverse pressure gradients especially in the z direction which, in the first two cases mentioned above, is perpendicular to the vortex centerline. Although in the actual situation the boundary-layer flow on the airframe due to the convecting tip vortices is periodic in time, the results reported in this work are calculated by assuming that the effects of viscosity become important suddenly at $t=0$; at subsequent times $t > 0$ a thin unsteady boundary-layer flow develops at the cylinder surface as the vortex filament convects above the cylinder. This approach corresponds to the situation where the cylinder is suddenly immersed in an irrotational flow field obtained by superimposing the mean streaming motion and the velocity field due to a free vortex. Then for an initial interval of time the motion of the flow is irrotational everywhere except within a thin layer adjoining the cylinder surface. In this case, the inviscid surface velocity is computed instantaneously from knowledge of the effect of the cylinder geometry on the irrotational flow field.

The boundary-layer problem consists of solving the unsteady three-dimensional boundary-layer equations subject to the boundary conditions determined from the inviscid flow problem discussed in Chapter 2 and 3. Since, for the first two cases, the computation of the boundary-layer flow is performed in a moving frame of reference traveling with the z -component of the vortex head speed, a slight modification of the Euler equations and Bernoulli's equation must be performed. In addition, for the case of the stagnant medium, and the symmetric mean inviscid flow, the initial condition of the vortex is different from that employed in Chapter 2. Consequently, the inviscid flow results are re-examined and results for the quantities directly relevant to the calculation of the boundary-layer flow are presented. For the case where the inviscid flow corresponds to that in the actual physical situation (i.e. the asymmetric flow) the results presented in Chapter 3 are employed directly.

The objective of the present chapter is to identify and understand the primary features of the viscous flow on the airframe due to the impinging tip vortex. However, the difficulties associated with such a study are severe; it is well known from previous work that a primary feature of boundary layers induced by vortical structures is the development of a secondary eddy in the boundary layer on the airframe which grows in time and is eventually ejected from the boundary layer (see below). The origin of this reversed flow (i.e. relative to the main stream velocity) begins on the sub-boundary layer scale and may grow to the body scale. For the parameters of the flow of interest in experiments, the genesis of the reversed flow region occurs on the scale of less than 1mm and consequently, the genesis of such a secondary structure cannot be resolved experimentally using present-day, state-of-the-art techniques. Since the size of the secondary eddy may eventually reach body scale, a fully computational approach cannot be used to describe the full range of development because of resolution problems associated with the wide range of length scales (i.e. 0.1mm to about 70mm). Consequently, we describe the initiation of the reversed flow region computationally and use the experimental results produced by Professor Komerath at Georgia Tech to describe the evolution of the secondary eddy experimentally. The focus is on the visualization and computation of the vorticity field, three-dimensional streamline patterns associated with the induced separated flow under the tip-vortex, and the measurement of the induced pressure field on the airframe including the viscous correction.

5.2 The Inviscid Flow

As noted previously, in general, the flow field consists of that induced by the vortex itself, that induced by the image field due to the vortex and to any other mean motion in which the vortex may be embedded. Since, for a vortex embedded in a stagnant medium and in the symmetric mean flow case, the boundary-layer

equations are solved in a frame of reference moving with the vortex head (center of the vortex for the symmetric case), Bernoulli's equation for the pressure and Euler equations for the pressure gradients must be adjusted. Let (r, θ, Z) denote the fixed polar coordinate system; then the new coordinate system whose origin is moving with the vortex head speed U_c is given by (r, θ, z) where

$$z = Z - Z_{Vc}(t).$$

Here, Z_{Vc} is the position of the vortex head in the z direction. Thus in a frame of reference moving with speed U_c , the Bernoulli's equation for the pressure is given by

$$\frac{\partial \phi}{\partial t} + \frac{|\vec{U}|^2}{2} + p + F = f_0(t), \quad (5.1)$$

where

$$F = -U_c(\vec{U} \cdot \hat{k}). \quad (5.2)$$

Here f_0 is the Bernoulli constant obtained by evaluating the left hand side of equation (5.1) at the beginning of the integration path; if all paths begin at $z = -\infty$, then

$$f_0 = \left\{ \frac{1}{2} (U_{M\theta}^2 + U_{Mz}^2) - U_c U_{Mz} \right\}_{z=-\infty}. \quad (5.3)$$

It should be noted that since the velocity field has been made nondimensional with respect to axial mean flow at infinity W_∞ then $U_{Mz} = 1$ at $z = -\infty$.

Similarly, Euler's equations for the pressure gradients, in a frame of reference moving with the vortex center speed, may be written as

$$-\frac{\partial p}{\partial \theta} = \frac{\partial U_\theta}{\partial t} + U_\theta \frac{\partial U_\theta}{\partial \theta} + (U_z - U_c) \frac{\partial U_\theta}{\partial z}, \quad (5.4)$$

$$-\frac{\partial p}{\partial z} = \frac{\partial U_z}{\partial t} + U_\theta \frac{\partial U_z}{\partial \theta} + (U_z - U_c) \frac{\partial U_z}{\partial z}. \quad (5.5)$$

Here, the inviscid surface speed \vec{U} is computed in polar coordinates and its components in both the azimuthal direction and along the axis of the cylinder are composed of image, vortex and mean parts and as in Chapter 2, the total velocities appearing in equations (5.4) and (5.5) are given by

$$U_\theta = U_{I\theta} + U_{V\theta} + U_{M\theta} \quad (5.6)$$

and

$$U_z = U_{Iz} + U_{Vz} + U_{Mz}. \quad (5.7)$$

The surface speeds and the pressure gradients are computed by following the same procedure outlined in Chapter 2. In the next three subsections, some of the inviscid flow results which are directly relevant to the calculation of the boundary-layer flow are presented in a format which is somewhat different from that employed in Chapters 2 and 3.

Stagnant Medium

Before computing the surface speeds, the vortex filament evolution in space and time is obtained first. The vortex is advanced in time according to the evolution equation (2.45) and as in Chapter 2 the nondimensional time defined by

$$t = \frac{|\Gamma|}{a^2} t^*, \quad (5.8)$$

is employed; here t^* is dimensional. The velocity field \vec{U} , which is given by

$$\vec{U} = \vec{U}_I + \vec{U}_V, \quad (5.9)$$

has been nondimensionalized on $\frac{|\Gamma|}{a}$. The vortex is discretized using a mesh size $\Delta s = 0.1$ with a total number of points $M = 101$. The initial position of the vortex corresponds to a straight filament oriented 90° to the generators of the cylinder at time $t = 0$. This initial position is represented in Cartesian coordinates by $x = s$, $y = 1.3$ and $z = 0$; note that the y coordinate of the initial position is different from that employed in Chapter 2. This was done to reduce the number of time steps required to establish the response of the boundary-layer. For this and all subsequent calculations, the dimensionless vortex core radius is fixed at $a_v = .11$. On Figure 5.1 are the results for the filament positions plotted every ten time steps; here $\Delta t = .05$. Note that as time increases, the filament increasingly deforms and the head of the vortex begins to move toward the cylinder. Here the total time of the calculation is about $t = 3.0$ and thus the motion of the filament is rather slow. (It will be noted later that the boundary-layer calculations are stopped after $t = 0.8$.) During this time the vortex filament has barely moved from its initial straight position. Here on Figure 5.1 the results are similar to those shown of Figure 2.1 except, as noted immediately above, a different initial vortex configuration ($y_s = 1.3$ instead of $y_s = 1.5$) and a different time scale are used in this chapter. To examine the temporal development of the inviscid flow as the vortex deforms from $t = 0$ to $t = 0.8$, distributions of the velocity U_z , the pressure gradient $\partial p / \partial z$ and pressure at the symmetry plane are shown in Figure 5.2. It should be noted that because the inviscid flow results (i.e. velocity field, pressure and pressure gradients) are computed concurrently with the boundary-layer flow results, vortex positions computed with $\Delta t = 0.05$ are interpolated in time to yield new positions that correspond to the finer time step employed in the boundary-layer calculations. The same procedure to interpolate the vortex positions in time is also applied to the symmetric and the asymmetric mean flow cases. This issue is discussed in detail at the end of the numerical method section. Note the extremely mild variation of the pressure and pressure gradient with time shown on Figure 5.2. Thus the inviscid flow is slowly varying during the boundary-layer calculations. To obtain a quantitative picture of the surface variation of the pressure and the

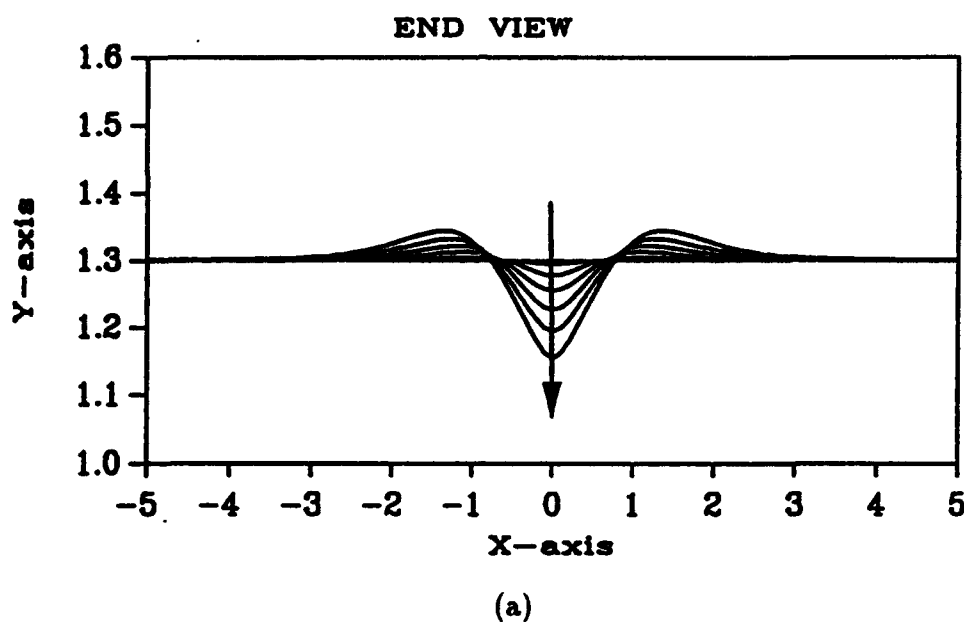


Figure 5.1: Filament positions for the case of no mean flow. (a) End view, (b) top view and (c) side view. The results shown here are slightly different from those shown on Figure 2.1 in that a different initial configuration of the vortex ($x_s=s$, $y_s=1.3$ and $z_s=0$) and a different time scale are employed. Here $\Delta t=0.05$ and the vortex core radius $a_v=0.11$. The filament positions are plotted every 10 time steps starting from $t=0$. The arrow denotes the direction of increasing time; the last time step corresponds to $t=3.0$.

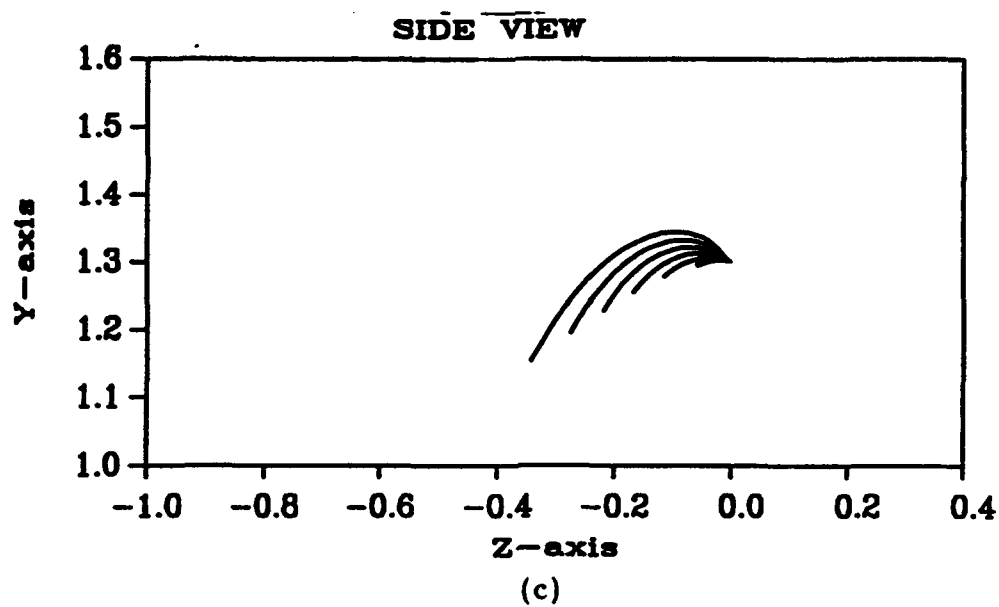
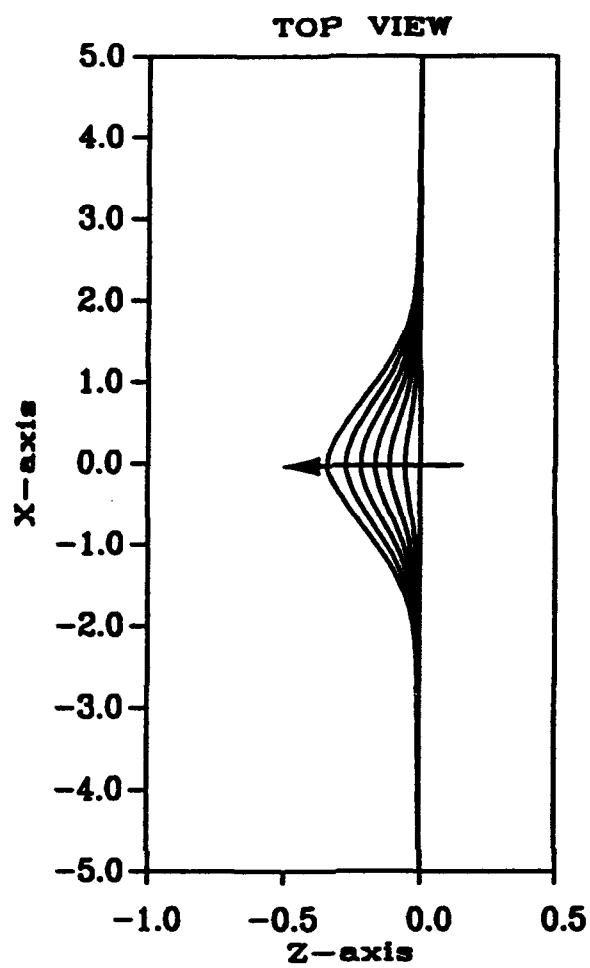


Figure 5.1 (continued)

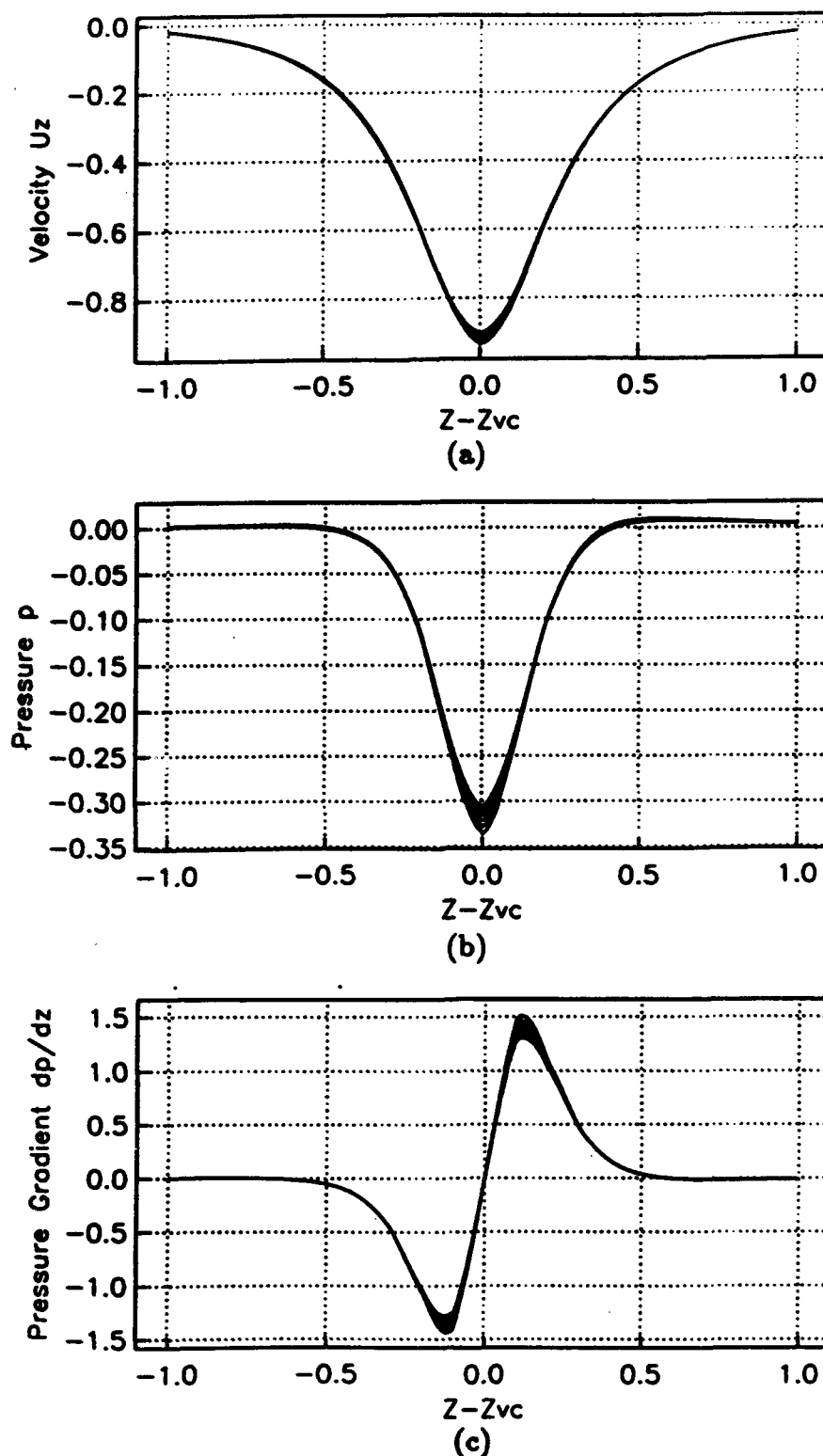


Figure 5.2: Temporal development of the inviscid flow field and the pressure at the top of the cylinder ($r=1$ and $\theta = \pi/2$). (a) The velocity component U_z , (b) the pressure and (c) the pressure gradient $\frac{\partial p}{\partial z}$. Here, the results are for the stagnant medium case and they are plotted at times $t=0.1, 0.2, 0.3, \dots, 0.8$.

velocity field on the cylinder, contours for the azimuthal inviscid velocity U_θ , the axial velocity U_z and the pressure are plotted at $t = 0.6$ respectively in Figure 5.3, 5.4 and 5.5. On Figures 5.6 and 5.7 are the corresponding pressure gradients $\partial p/\partial\theta$ and $\partial p/\partial z$.

Symmetric Mean Flow

Similar to the stagnant medium case, vortex positions are obtained first by advancing the vortex in time according to the evolution equation (2.45). Here, to facilitate the calculation of the boundary-layer flow, we define the dimensionless time according to equation (3.16). The total velocity \vec{U} given by equation (2.19) has been nondimensionalized on W_∞ . The circulation has been made dimensionless according to $\Gamma = \frac{\Gamma^*}{W_\infty a}$. The results shown here are produced by using a dimensional circulation $\Gamma^* = 1.5 \text{ m}^2/\text{sec}$ (Liou, Komerath and McMahon 1990), an effective downwash $U_\infty = 5.5 \text{ m/sec}$ and an effective axial mean velocity $W_\infty = 5.5 \text{ m/sec}$. This situation corresponds to the case where $\alpha=1$ and $\beta=3$ which are defined in the results section of Chapter 2. This results in a dimensionless circulation $\Gamma=4.2$.

The vortex is discretized using a mesh size $\Delta s = 0.1$ with a total number of points $M = 61$. The initial position of the vortex corresponds to a straight filament oriented 90° to the generators of the cylinder at time $t = 0$. This initial position is represented in Cartesian coordinates by $x = s$, $y = 1.5$ and $z = 0$; note that the initial y position of the vortex is different from that employed in Chapter 2. This was done for the same reason as described in the previous subsection. For this and all subsequent calculations, the dimensionless vortex core radius is fixed at $a_v = .11$. On Figure 5.8 is the vortex position plotted every ten time steps for $\Delta t = .01$. Here the total time of the calculation is $t = 0.6$ and as will be shown later the boundary-layer flow calculations are stopped after $t = 0.4$. To examine the temporal development of the inviscid flow as the vortex is convected downward toward the cylinder from $t = 0$ to $t=0.4$, distributions of the velocity U_z , the pressure gradient $\partial p/\partial z$ and pressure at the symmetry plane and at various times are shown in Figure 5.9. Unlike the stagnant medium case, the results show considerable time variation associated with the inviscid mean flow giving rise to larger pressure gradients. It is also worthwhile to investigate the inviscid flow field over the entire surface of the cylinder and this is shown in Figures 5.10-5.14 where constant contour levels for the velocity components U_θ , U_z , the pressure and the pressure gradients are plotted. Note in particular the local character of the development of the axial pressure gradient; this is also reflected in the locally large values of the axial velocity depicted on Figure 5.11. Note in particular that the adverse pressure gradient of value $+5$ extends downstream and off the symmetry plane about 30° indicating the possibility of axially separated flow to that spanwise

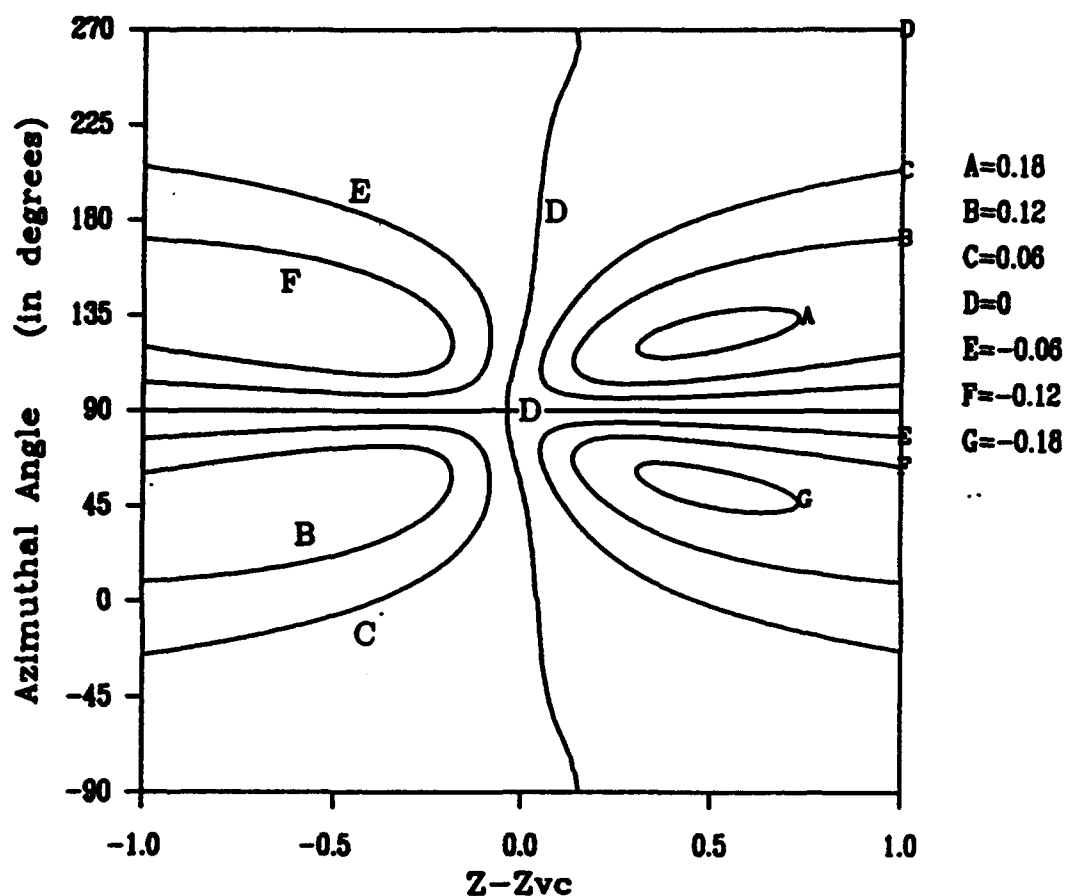


Figure 5.3: Lines of constant azimuthal inviscid velocity U_θ computed around the cylinder at the surface. Here the results are for the stagnant medium case and are plotted at time $t=0.6$.

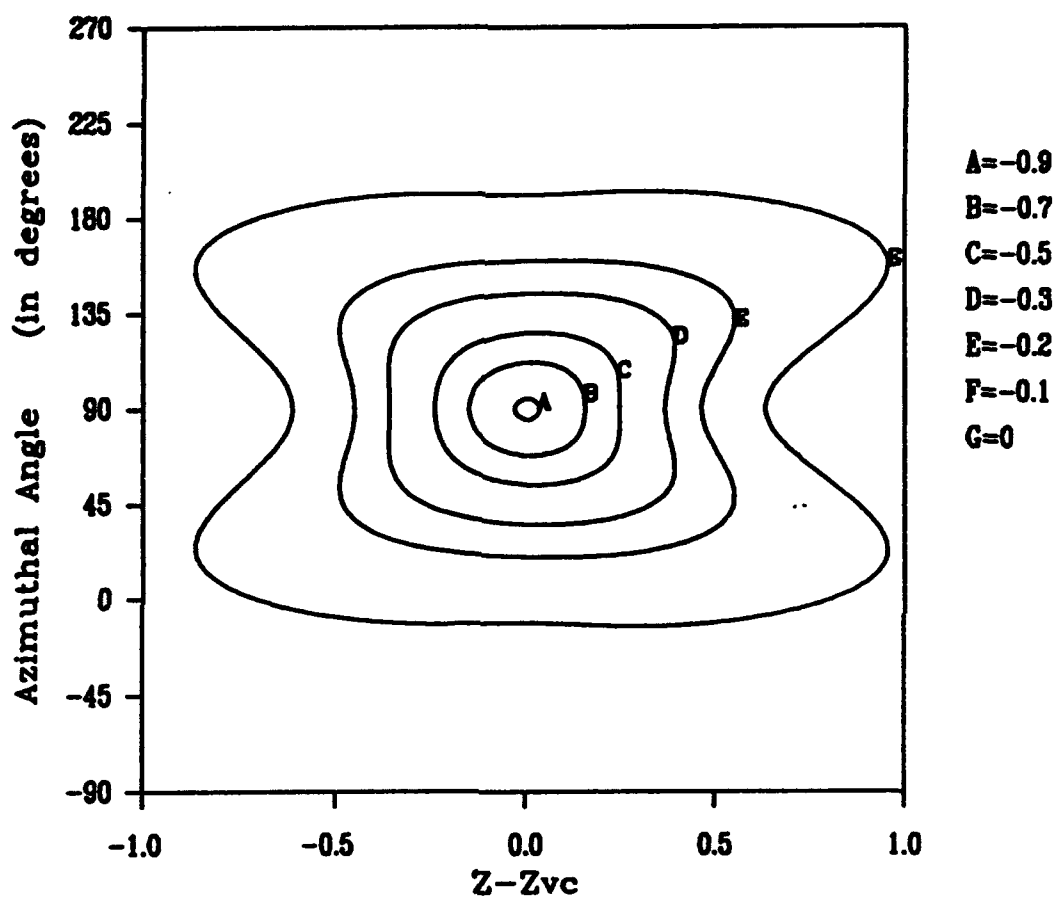


Figure 5.4: Lines of constant axial inviscid velocity U_z computed around the cylinder at the surface. Here the results are for the stagnant medium case and are plotted at time $t=0.6$.

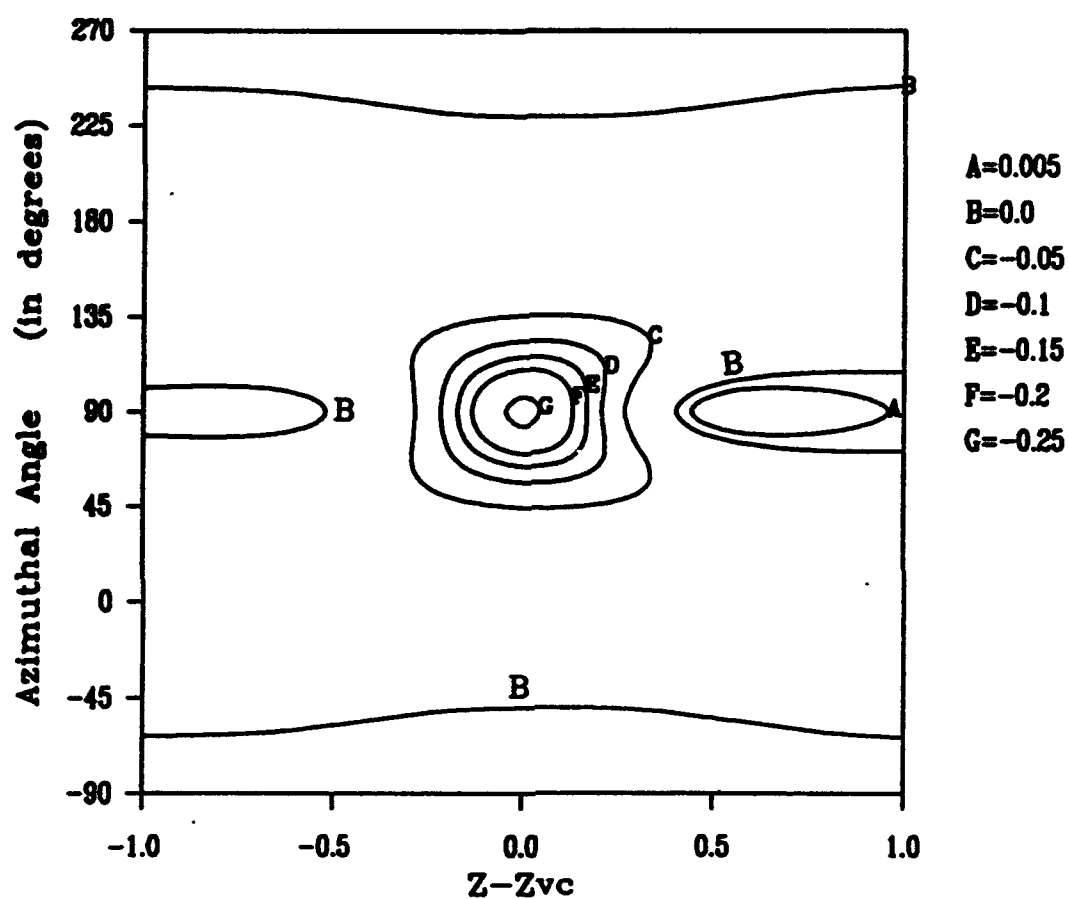


Figure 5.5: Lines of constant pressure p computed around the cylinder at the surface. Here the results are for the stagnant medium case and are plotted at time $t=0.6$.

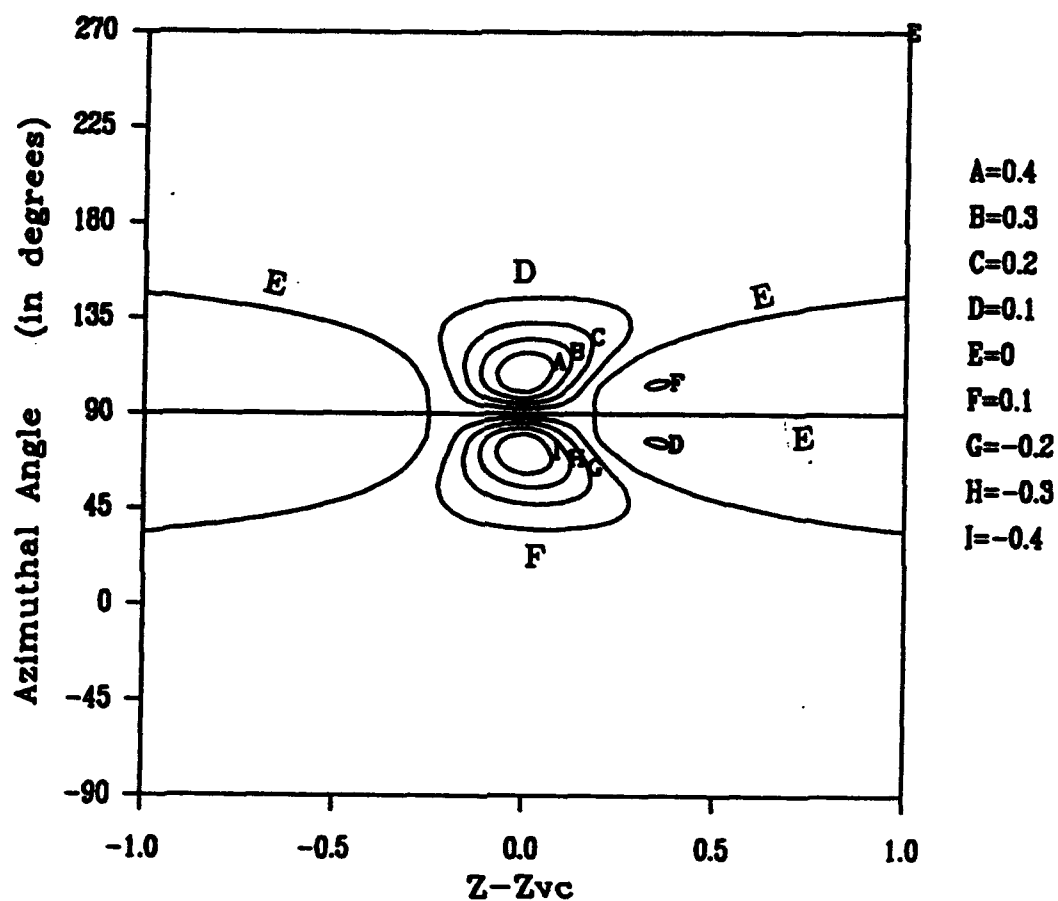


Figure 5.6: Lines of constant pressure gradient $\frac{\partial p}{\partial \theta}$ computed around the cylinder at the surface. Here the results are for the stagnant medium case and are plotted at time $t=0.6$.

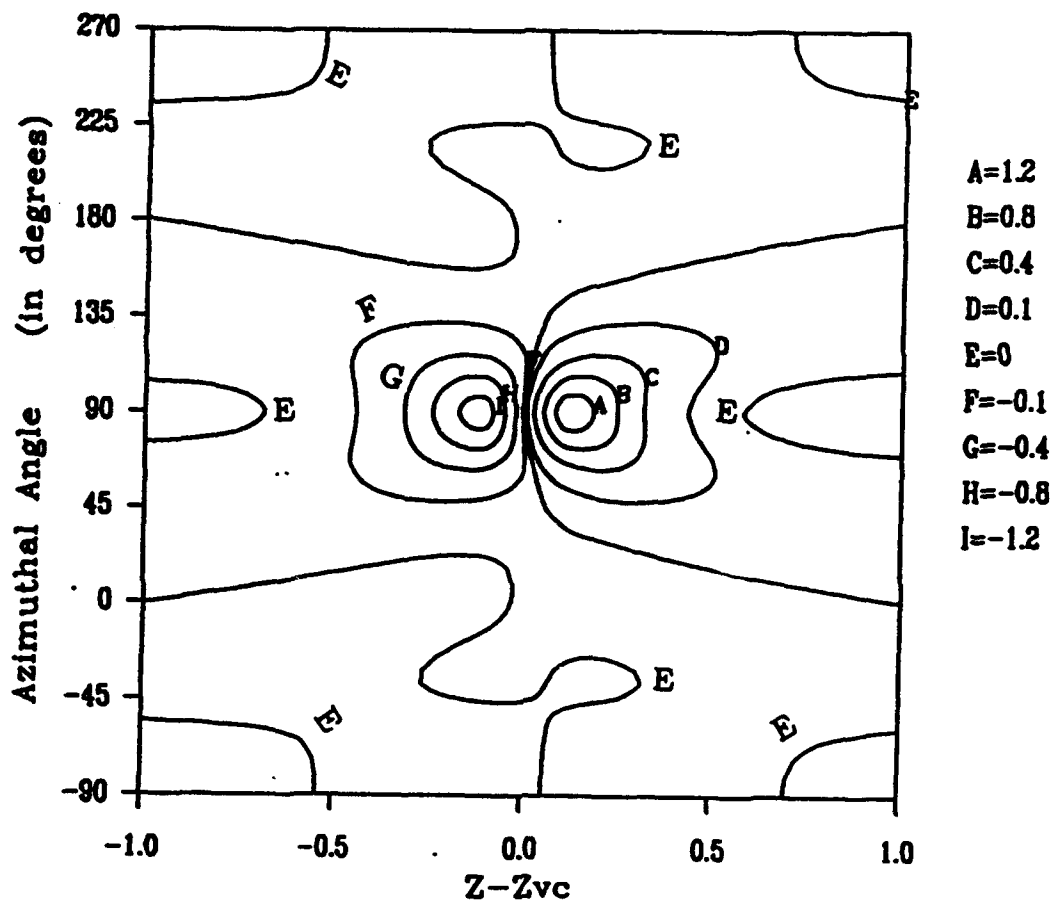


Figure 5.7: Lines of constant pressure gradient $\frac{\partial p}{\partial z}$ computed around the cylinder at the surface. Here the results are for the stagnant medium case and are plotted at time $t=0.6$.

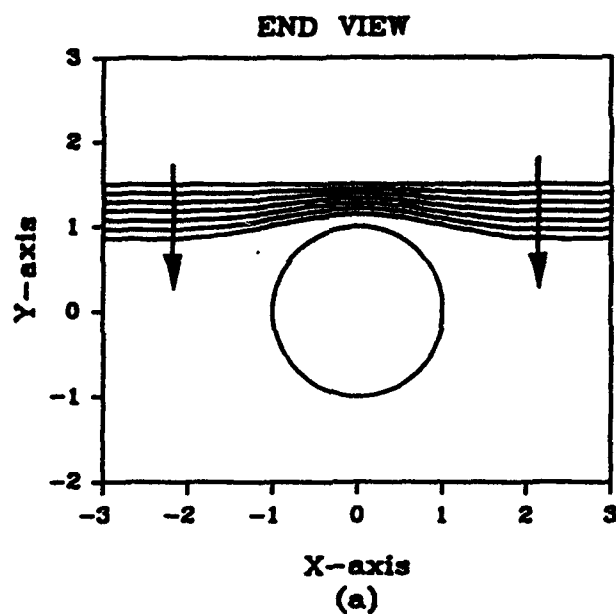


Figure 5.8: Filament positions for the symmetric mean flow case. (a) End view, (b) top view and (c) side view. The initial configuration of the vortex corresponds to $x_s=s$, $y_s=1.5$ and $z_s=0$. Here $\Delta t=0.01$ and the vortex core radius $a_v=0.11$. The filament positions are plotted every 10 time steps starting from $t=0$. The arrow denotes the direction of increasing time; the last time step corresponds to $t=0.6$.

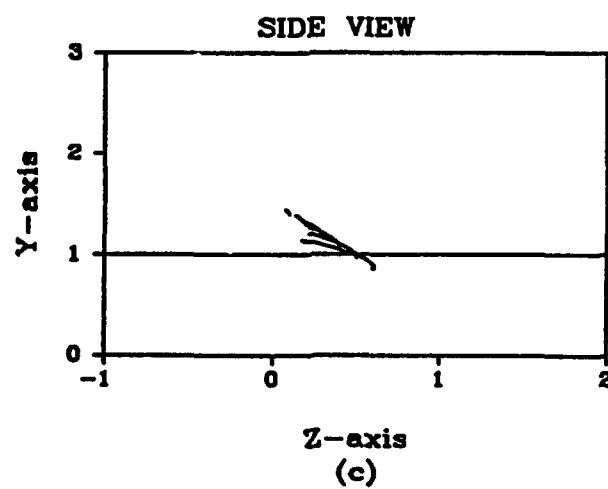
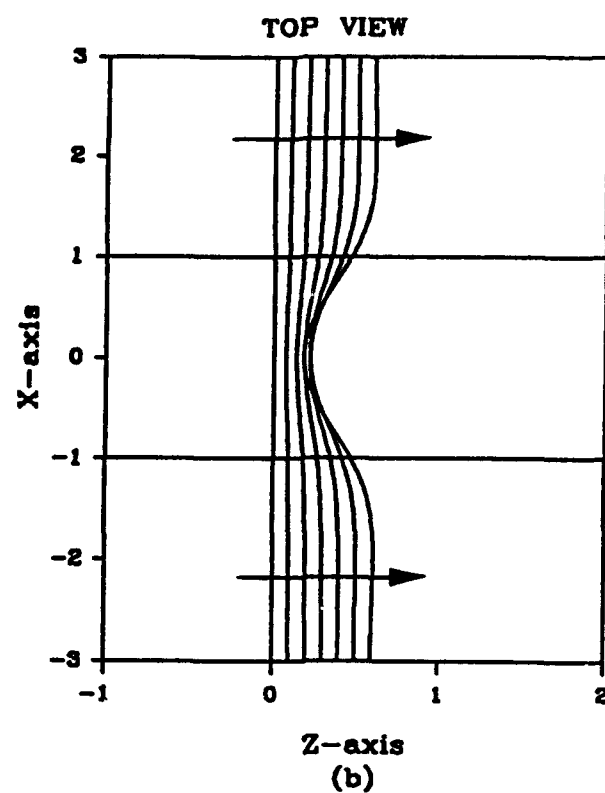


Figure 5.8 (continued)

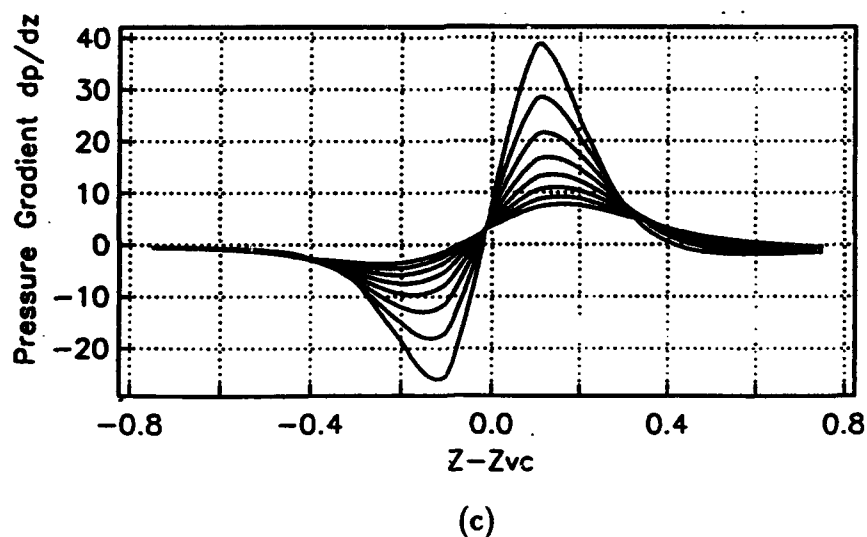
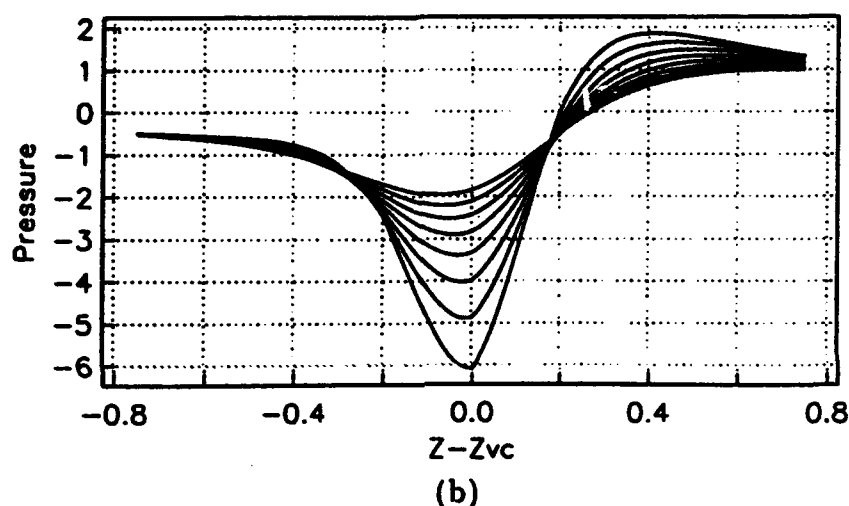
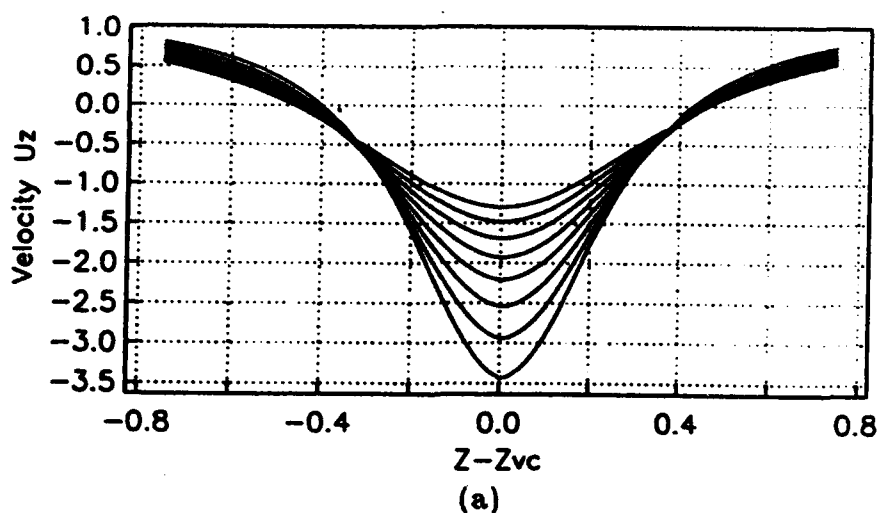


Figure 5.9: Temporal development of the inviscid flow field and the pressure at the top of the cylinder ($r=1$ and $\theta = \pi/2$). (a) The velocity component U_z , (b) the pressure and (c) the pressure gradient $\frac{\partial p}{\partial z}$. Here, the results are for the symmetric mean flow case and are plotted at times $t=0.05, 0.1, 0.15, \dots, 0.4$.

location. Also the axial velocity is negative directly under the vortex but positive at locations significantly removed from the symmetry plane.

Asymmetric Mean Flow: The Rotor Tip Vortex

The asymmetric mean flow formulated in Chapter 3 is used here to generate the inviscid flow results. In particular we consider the case where the advance ratio $\mu=0.1$ and recall that the dimensionless circulation is $\Gamma=2.2$. Since the initial configuration of the vortex used in Chapter 3 is well suited to perform the boundary-layer flow calculations (i.e. the vortex is located close enough to the surface so that its effect on the boundary-layer becomes considerable), there is no need to recompute the vortex trajectories as we did for the stagnant medium and the mean flow cases. Therefore, the vortex trajectories shown in Figure 3.4 will be employed here to compute the pressure gradients and the surface speeds. Recall that the initial vortex configuration is taken directly from experimental measurements where the vortex is of arbitrary shape as shown in Figure 3.4. Recall also that the vortex is discretized using a mesh size $\Delta s=0.167$ with a total number of points $M=61$ and is advanced in time using a time step $\Delta t=0.071$ which corresponds to 6 degrees rotation of the rotor.

Because of the asymmetry of the problem which may adversely affect the numerical solution, a fixed frame of reference is employed to compute the results although some streamline patterns are presented in a moving frame. Here, for simplicity, a new polar coordinate system whose origin coincides with the vortex head position at $t=0$ is employed and is given by (r, θ, z) where

$$z = Z - Z_{V_c}(t = 0).$$

Here, Z_{V_c} is the position of the vortex head in the z direction.

Results for the azimuthal and axial velocities and the pressure gradient $\partial p / \partial z$ are shown in Figures 5.15-5.17 as contours of constant values calculated on the surface of the cylinder. Note that the developing asymmetry of the flow here is very pronounced especially in the axial velocity distribution. Again, noting the axial length scale employed on the figures, the axial velocity field is rapidly varying just underneath the main vortex (Figure 5.16).

5.3 Boundary Layer Formulation

The problem to be solved is the boundary-layer flow on a circular cylinder induced by a convecting three-dimensional vortex filament in a frame of reference traveling with the axial (z) speed of the centerline point of the vortex filament. Following the same procedure as in Chapter 4, we use the following scaled variables to describe the flow in the boundary-layer flow

$$u_z = \bar{u}_z, u_\theta = \bar{u}_\theta, u_r = \bar{u}_r \sqrt{Re}, y = (r - 1) \sqrt{Re}, \quad (5.10)$$

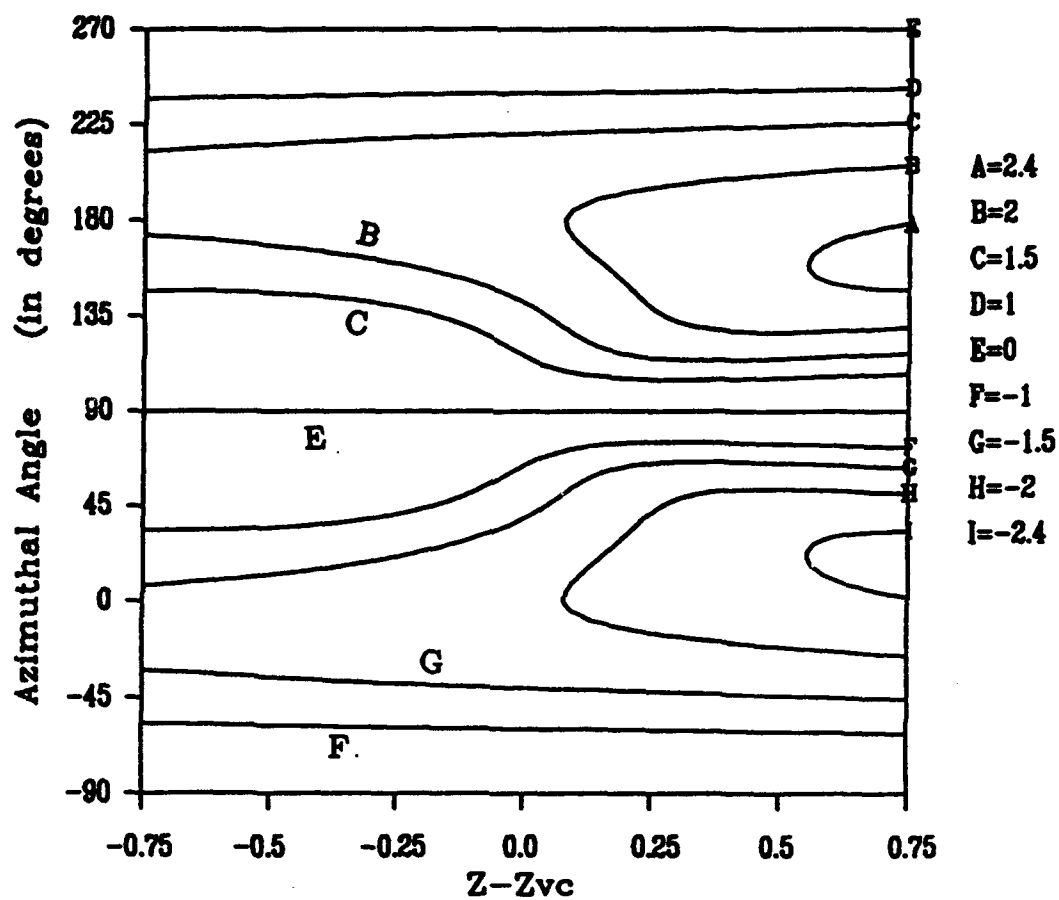


Figure 5.10: Lines of constant azimuthal inviscid velocity U_θ computed around the cylinder at the surface. Here the results are for the symmetric mean flow case and are plotted at time $t=0.3$.

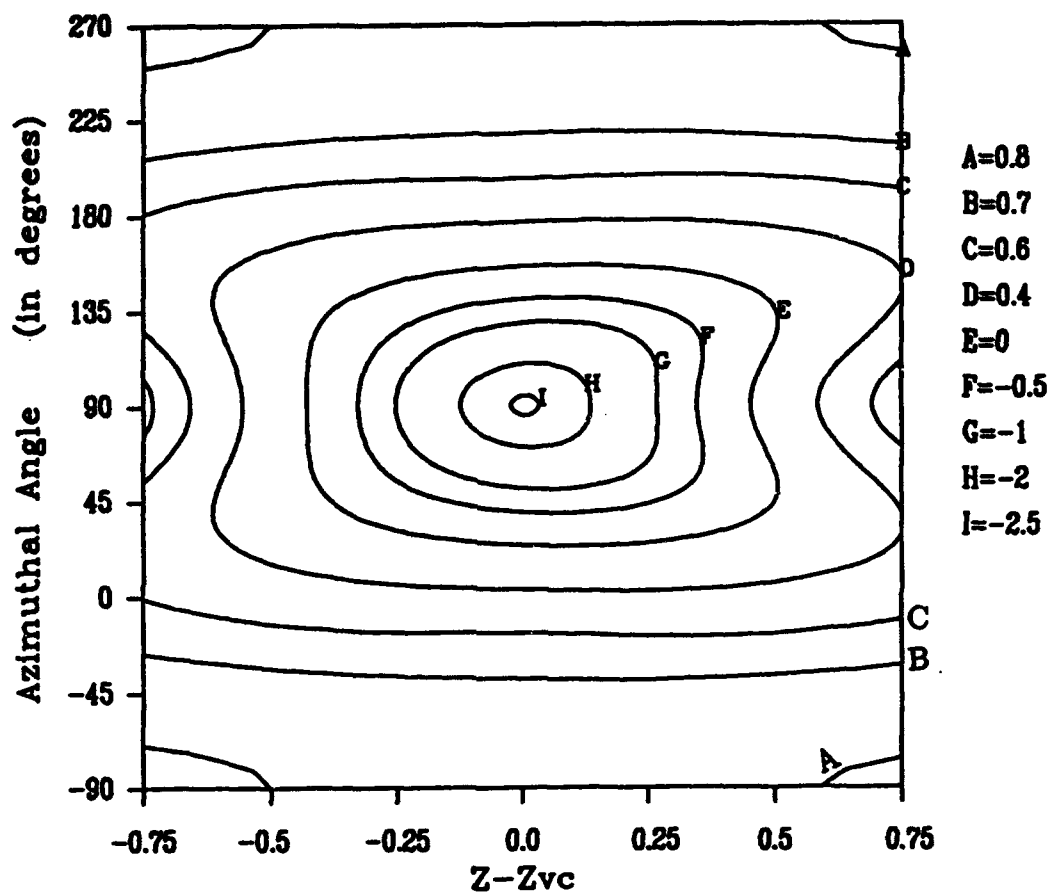


Figure 5.11: Lines of constant axial inviscid velocity U_z , computed around the cylinder at the surface. Here the results are for the symmetric mean flow case and are plotted at time $t=0.3$.

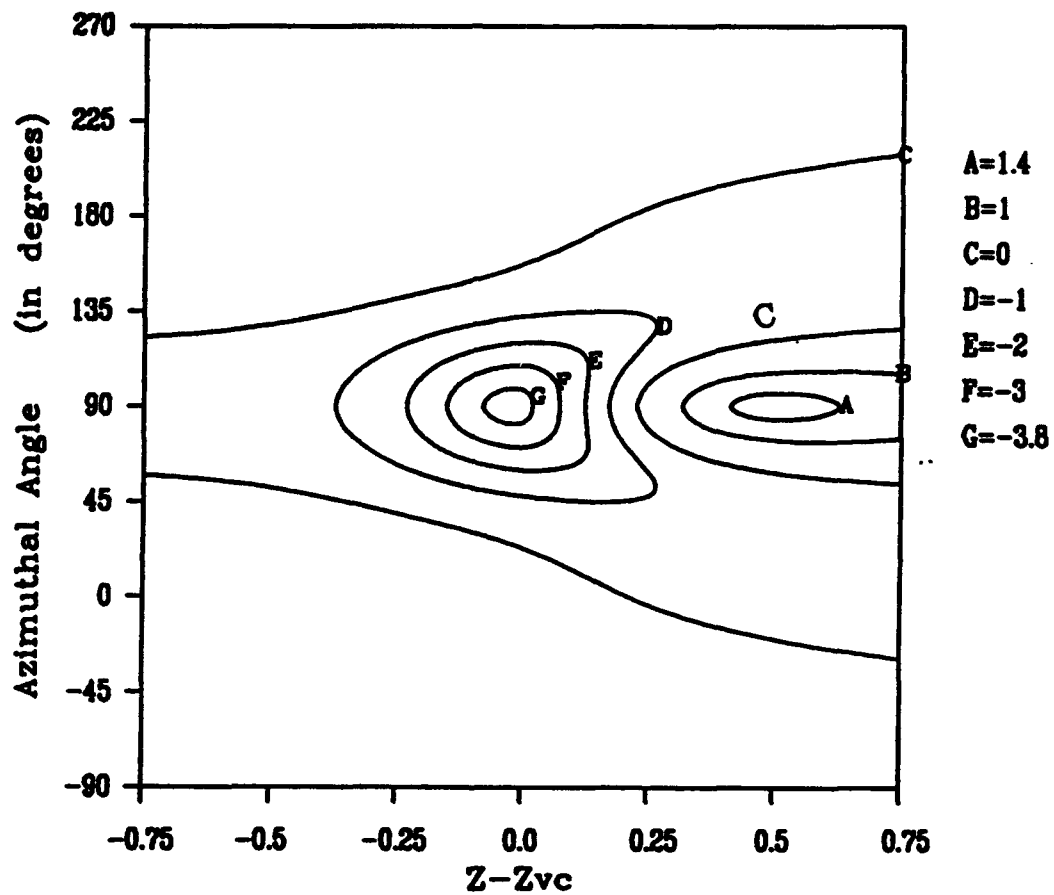


Figure 5.12: Lines of constant pressure p computed around the cylinder at the surface. Here the results are for the symmetric mean flow case and are plotted at time $t=0.3$.

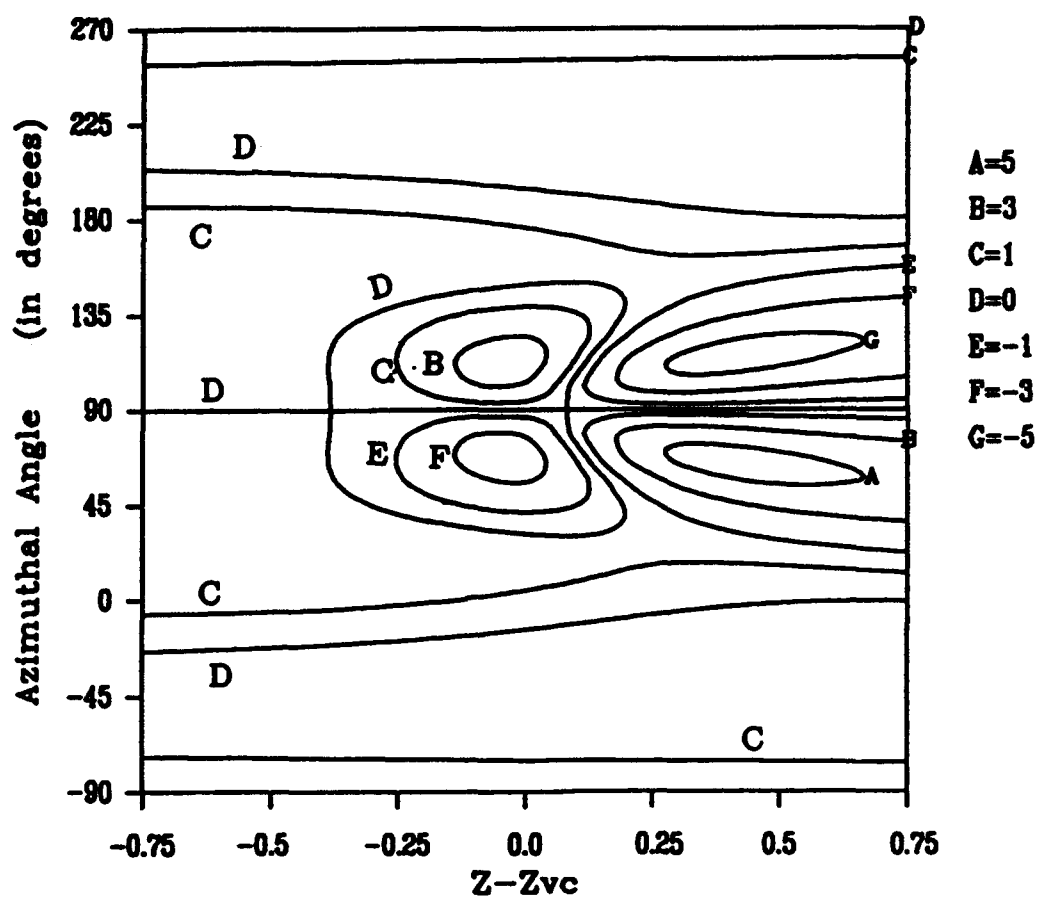


Figure 5.13: Lines of constant pressure gradient $\frac{\partial p}{\partial \theta}$ computed around the cylinder at the surface. Here the results are for the symmetric mean flow case and are plotted at time $t=0.3$.

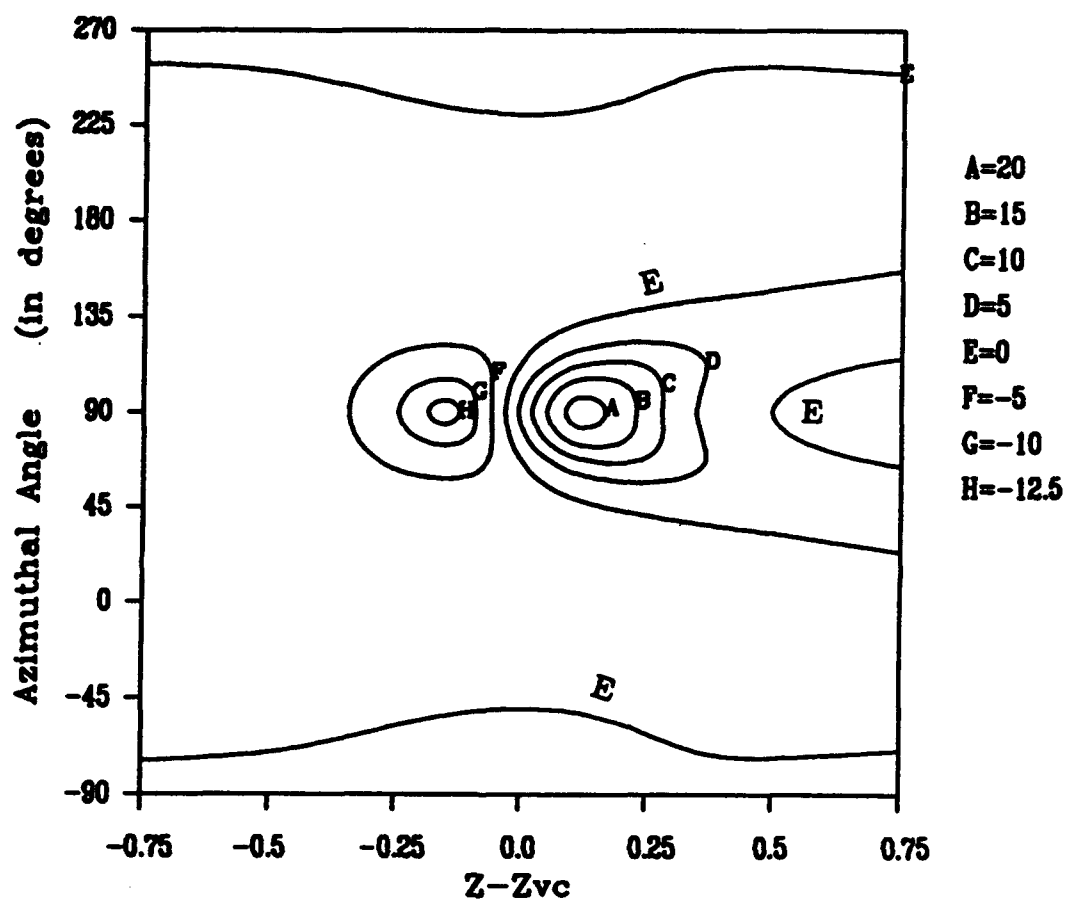


Figure 5.14: Lines of constant pressure gradient $\frac{\partial p}{\partial r}$ computed around the cylinder at the surface. Here the results are for the symmetric mean flow case and are plotted at time $t=0.3$.

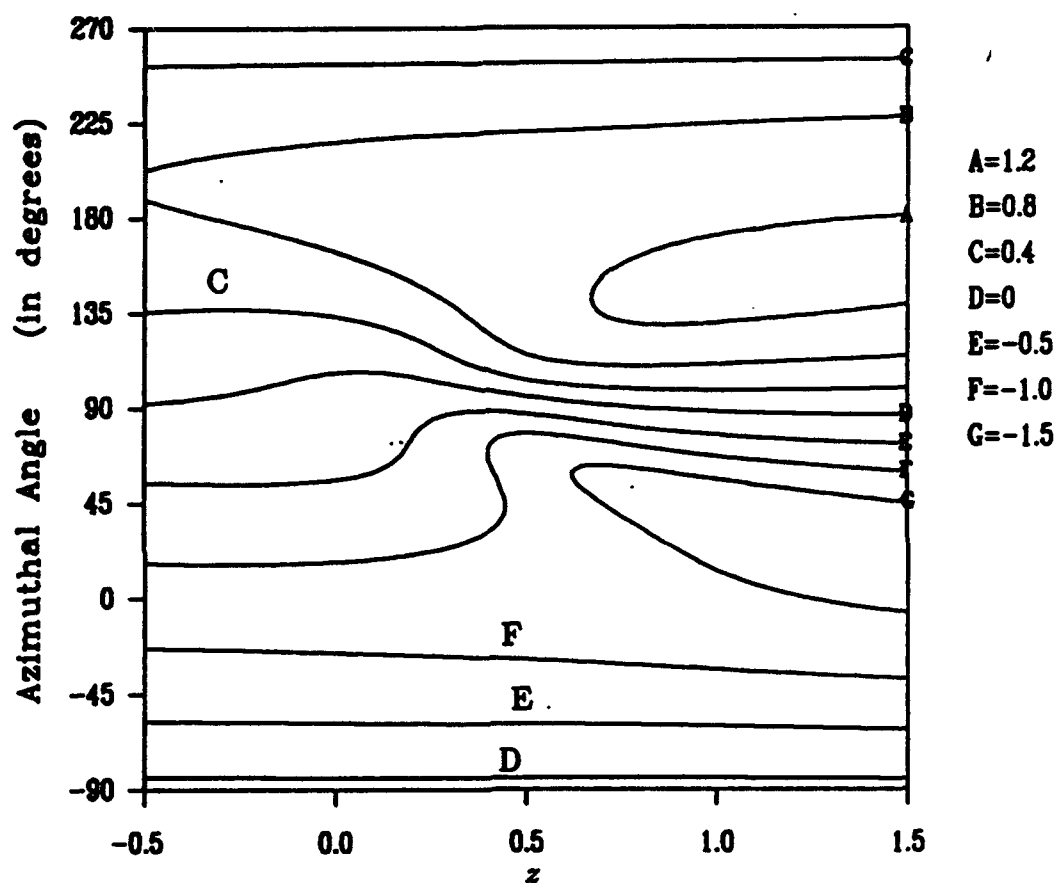


Figure 5.15: Lines of constant azimuthal inviscid velocity U_θ computed around the cylinder at the surface. Here the results are for the asymmetric mean flow case and are plotted at time $t=0.3554$ ($\psi = 30^\circ$). Here $z=Z - Z_{Vc}(t=0)$.

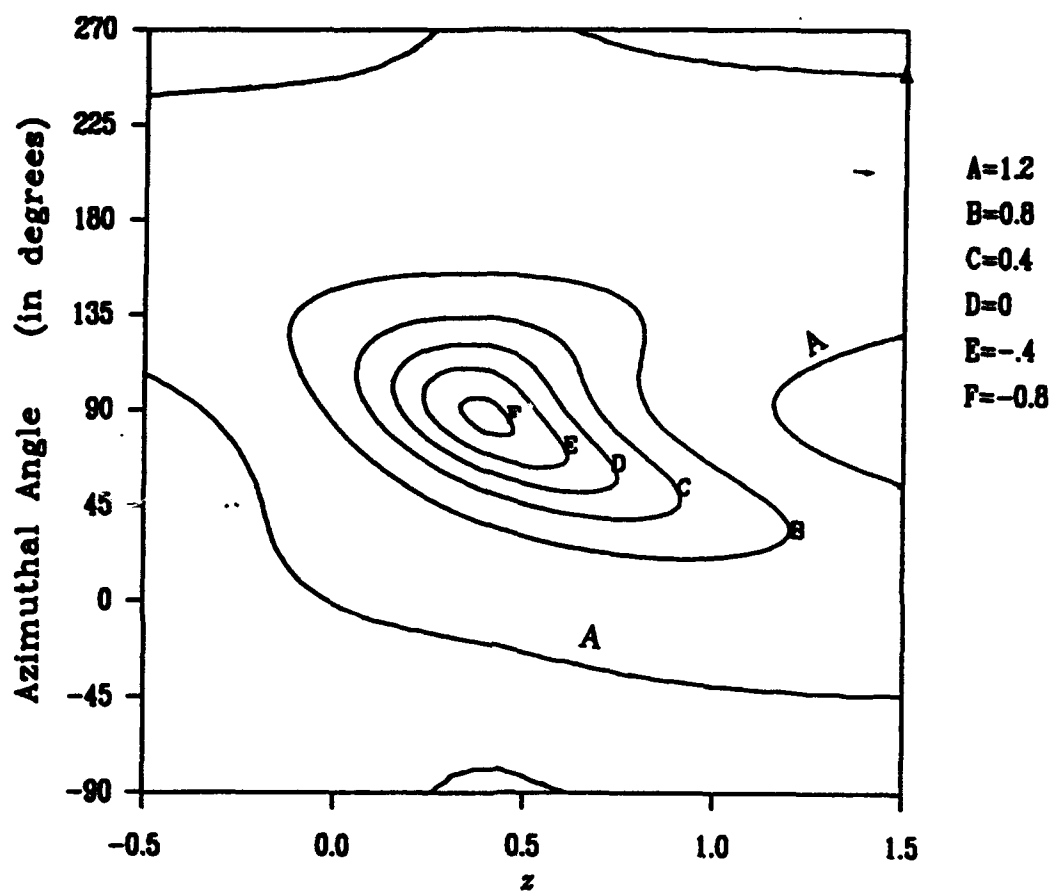


Figure 5.16: Lines of constant axial inviscid velocity U_z computed around the cylinder at the surface. Here the results are for the asymmetric mean flow case and are plotted at time $t=0.3554$ ($\psi = 30^\circ$).

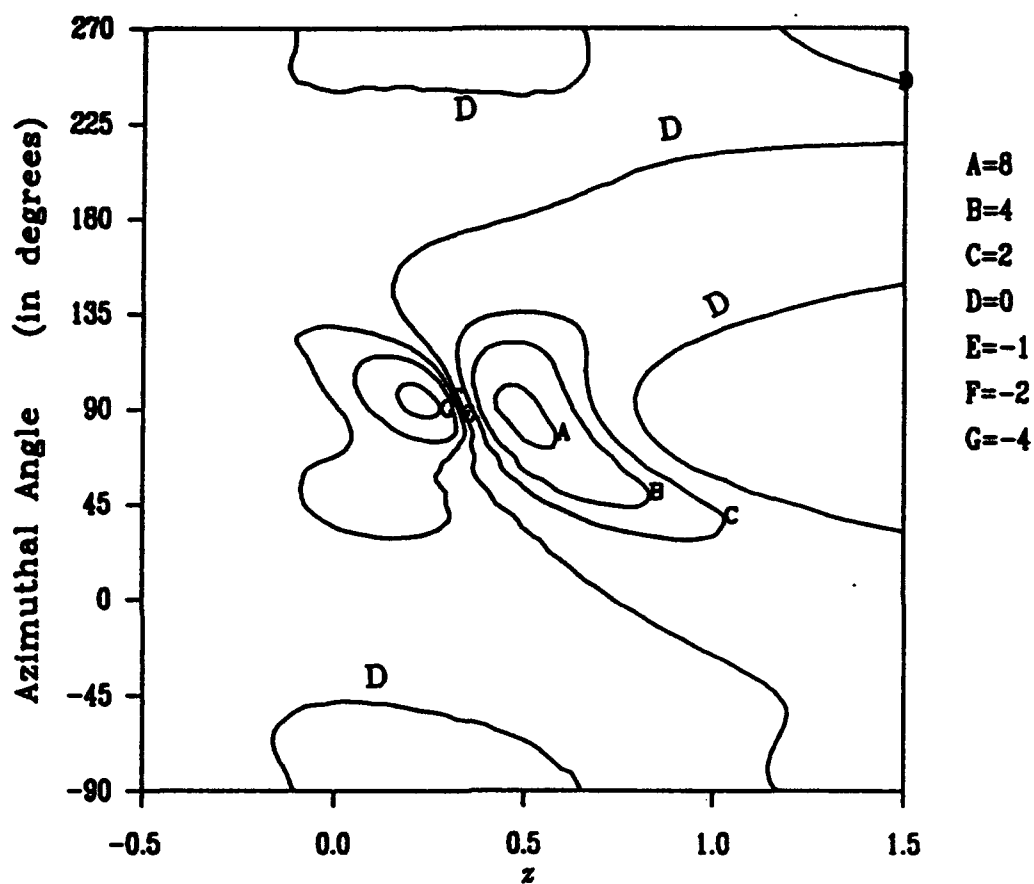


Figure 5.17: Lines of constant pressure gradient $\partial p / \partial z$ computed around the cylinder at the surface. Here the results are for the asymmetric mean flow case and are plotted at time $t=0.3554$ ($\psi = 30^\circ$).

where $Re = W_\infty a / \nu$ is the Reynolds number. Here W_∞ is a characteristic velocity which corresponds to the streamwise flow along the cylinder as $r \rightarrow \infty$ for the case of mean flow or to the circulation of the vortex divided by the cylinder radius for the case of a stagnant medium. Thus, the incompressible, unsteady and three-dimensional boundary-layer equations may be written in polar coordinates as

$$\frac{\partial u_r}{\partial y} + \frac{\partial u_\theta}{\partial \theta} + \frac{\partial u_z}{\partial z} = 0, \quad (5.11)$$

$$\frac{\partial u_\theta}{\partial t} + u_r \frac{\partial u_\theta}{\partial y} + u_\theta \frac{\partial u_\theta}{\partial \theta} + (u_z - U_c) \frac{\partial u_\theta}{\partial z} = -\frac{\partial p}{\partial \theta} + \frac{\partial^2 u_\theta}{\partial y^2}, \quad (5.12)$$

$$\frac{\partial u_z}{\partial t} + u_r \frac{\partial u_z}{\partial y} + u_\theta \frac{\partial u_z}{\partial \theta} + (u_z - U_c) \frac{\partial u_z}{\partial z} = -\frac{\partial p}{\partial z} + \frac{\partial^2 u_z}{\partial y^2}, \quad (5.13)$$

where U_c is the z -component of the vortex center velocity. Note that in the asymmetric mean flow case, where boundary-layer calculations are performed in a fixed frame of reference, U_c is simply set to zero. Details on how the boundary-layer variables are nondimensionalized will be discussed in each of the results sections corresponding to each of the three inviscid flows discussed previously. Equations (5.11)-(5.13) are subject to the initial and boundary conditions which are given by

$$\begin{aligned} u_\theta, u_z &\text{ specified at } t = 0, \\ u_\theta &\rightarrow U_{M\theta} \text{ as } z \rightarrow \pm\infty, \\ u_z &\rightarrow U_{Mz} \text{ as } z \rightarrow \pm\infty, \\ u_r = u_\theta = u_z &= 0 \text{ at } y = 0, \\ u_\theta &\rightarrow U_\theta \text{ as } y \rightarrow \infty, \\ u_z &\rightarrow U_z \text{ as } y \rightarrow \infty, \end{aligned} \quad (5.14)$$

where U_θ and U_z are the inviscid velocity components in the θ and z -directions respectively. Here \vec{U}_M is the mean flow field evaluated at the surface of the cylinder and it denotes the inviscid flow field at locations $z = \pm\infty$ where the effect of the vortex is negligible. It should be noted that for the stagnant medium case $\vec{U}_M = 0$.

To describe the motion subsequent to $t=0$, it is convenient to use Rayleigh variables according to

$$\eta = \frac{y}{2\sqrt{t}},$$

and the governing equations (5.11-5.13) become

$$\frac{\partial u_r}{\partial \eta} + 2\sqrt{t} \frac{\partial u_\theta}{\partial \theta} + 2\sqrt{t} \frac{\partial u_z}{\partial z} = 0, \quad (5.15)$$

$$4t \frac{\partial u_\theta}{\partial t} - 2\eta \frac{\partial u_\theta}{\partial \eta} - \frac{\partial^2 u_\theta}{\partial \eta^2} = -4t \frac{\partial p}{\partial \theta} + R_\theta, \quad (5.16)$$

$$4t \frac{\partial u_z}{\partial t} - 2\eta \frac{\partial u_z}{\partial \eta} - \frac{\partial^2 u_z}{\partial \eta^2} = -4t \frac{\partial p}{\partial z} + R_z, \quad (5.17)$$

where

$$R_\theta = -4t \left(\frac{u_r}{2\sqrt{t}} \frac{\partial u_\theta}{\partial \eta} + u_\theta \frac{\partial u_\theta}{\partial \theta} + (u_z - U_c) \frac{\partial u_\theta}{\partial z} \right), \quad (5.18)$$

$$R_z = -4t \left(\frac{u_r}{2\sqrt{t}} \frac{\partial u_z}{\partial \eta} + u_\theta \frac{\partial u_z}{\partial \theta} + (u_z - U_c) \frac{\partial u_z}{\partial z} \right). \quad (5.19)$$

Let u_z^0 and u_θ^0 denote the initial condition for the flow; then taking the limit of equations (5.16) and (5.17) as $t \rightarrow 0$, an equation for each component u_z^0 and u_θ^0 is obtained according to

$$2\eta \frac{\partial u_\theta^0}{\partial \eta} + \frac{\partial^2 u_\theta^0}{\partial \eta^2} = 0, \quad (5.20)$$

$$2\eta \frac{\partial u_z^0}{\partial \eta} + \frac{\partial^2 u_z^0}{\partial \eta^2} = 0. \quad (5.21)$$

Equations (5.20) and (5.21) are subject to the following boundary conditions

$$u_\theta^0 = 0 \text{ at } \eta = 0, \quad u_\theta^0 = U_\theta^0 \text{ as } \eta \rightarrow \infty, \quad (5.22)$$

and

$$u_z^0 = 0 \text{ at } \eta = 0, \quad u_z^0 = U_z^0 \text{ as } \eta \rightarrow \infty. \quad (5.23)$$

Here U_z^0 and U_θ^0 denote the axial and the azimuthal surface speeds computed from the inviscid flow equations at $t=0$. The solutions to equations (5.20) and (5.21) subject to equations (5.22) and (5.23) are given by

$$u_\theta^0 = U_\theta^0 \text{erf} \eta, \quad (5.24)$$

and

$$u_z^0 = U_z^0 \text{erf} \eta. \quad (5.25)$$

As with the two-dimensional problem, we assume that the flow at times subsequent to $t=0$ is a perturbation from the initial solution given by equations (5.24) and (5.25). Let \tilde{u} be the perturbation, then the velocity components can be written as

$$u_\theta = \tilde{u}_\theta + u_\theta^0, \quad (5.26)$$

and

$$u_z = \tilde{u}_z + u_z^0. \quad (5.27)$$

In addition, let

$$u_r = 2\sqrt{t}(\dot{u}_r + u_r^0), \quad (5.28)$$

where u_r^0 is the new scaled radial velocity and is finite at $t=0$. The solution for u_r^0 may be obtained analytically using the continuity equation and is given by (see equation 4.23)

$$u_r^0 = - \left(\frac{\partial U_\theta^0}{\partial \theta} + \frac{\partial U_z^0}{\partial z} \right) \left(\eta \operatorname{erf} \eta + \frac{1}{\sqrt{\pi}} e^{-\eta^2} - \frac{1}{\sqrt{\pi}} \right). \quad (5.29)$$

Substituting equations (5.26)-(5.28) into equations (5.15)-(5.17), the boundary-layer equations become

$$\frac{\partial \dot{u}_r}{\partial \eta} + \frac{\partial \dot{u}_\theta}{\partial \theta} + \frac{\partial \dot{u}_z}{\partial z} = 0, \quad (5.30)$$

$$4t \frac{\partial \dot{u}_\theta}{\partial t} - 2\eta \frac{\partial \dot{u}_\theta}{\partial \eta} - \frac{\partial^2 \dot{u}_\theta}{\partial \eta^2} = -4t \frac{\partial p}{\partial \theta} + R_\theta, \quad (5.31)$$

$$4t \frac{\partial \dot{u}_z}{\partial t} - 2\eta \frac{\partial \dot{u}_z}{\partial \eta} - \frac{\partial^2 \dot{u}_z}{\partial \eta^2} = -4t \frac{\partial p}{\partial z} + R_z, \quad (5.32)$$

where R_θ and R_z contain all the nonlinear inertia terms. The above equations (5.30)-(5.32) are subject to the modified initial and boundary conditions

$$\dot{u}_r, \dot{u}_\theta, \dot{u}_z = 0 \quad \text{at } t = 0,$$

$$\dot{u}_r, \dot{u}_\theta, \dot{u}_z \rightarrow 0 \quad \text{as } z \rightarrow \pm\infty,$$

$$\dot{u}_r = \dot{u}_\theta = \dot{u}_z = 0 \quad \text{at } y = 0,$$

$$\dot{u}_\theta \rightarrow U_\theta - U_\theta^0 \quad \text{as } y \rightarrow \infty,$$

$$\dot{u}_z \rightarrow U_z - U_z^0 \quad \text{as } y \rightarrow \infty, \quad (5.33)$$

where U_z^0 and U_θ^0 are the inviscid surface speeds at $t=0$, and U_z and U_θ are the corresponding surface speeds at subsequent times t .

For future reference, it is useful to investigate the induced vorticity field. In general, the vorticity field is defined as the curl of the velocity field and is given here in the original unscaled cylindrical coordinates as

$$\vec{\omega} = \frac{1}{r} \left\{ \frac{\partial u_z}{\partial \theta} - r \frac{\partial u_\theta}{\partial z} \right\} \hat{i}_r - \left\{ \frac{\partial u_z}{\partial r} - \frac{\partial u_r}{\partial z} \right\} \hat{i}_\theta + \frac{1}{r} \left\{ \frac{\partial r u_\theta}{\partial r} - \frac{\partial u_r}{\partial \theta} \right\} \hat{i}_z. \quad (5.34)$$

Using the boundary-layer scaled variables defined above and dropping the terms of the order $(Re^{-1/2})$ the scaled vorticity field takes a simpler form and is given by

$$Re^{-1/2} \vec{\omega} = \omega_\theta \hat{i}_\theta + \omega_z \hat{i}_z \quad (5.35)$$

where ω_θ and ω_z are respectively the azimuthal and the axial scaled vorticity components given by

$$\omega_\theta = -\frac{1}{2\sqrt{t}} \frac{\partial u_z}{\partial \eta}, \quad (5.36)$$

and

$$\omega_z = \frac{1}{2\sqrt{t}} \frac{\partial u_\theta}{\partial \eta}. \quad (5.37)$$

In particular, for later use, the enstrophy which is defined as the magnitude of the vorticity vector, is an important quantity in the analysis of the complex three-dimensional structure of the vorticity field. Here the scaled enstrophy is defined as

$$E = \|Re^{-1/2}\vec{\omega}\| = \sqrt{\omega_\theta^2 + \omega_z^2}. \quad (5.38)$$

Similarly, the wall shear components will also be investigated in the present work and they are obtained as follows. In non-dimensional unscaled form the wall-shear components may be written as

$$\tau_{r\theta} = Re^{-1} \left(\frac{1}{r} \frac{\partial u_r}{\partial \theta} + \frac{\partial u_\theta}{\partial r} - \frac{u_\theta}{r} \right) |_{r=1}, \quad (5.39)$$

$$\tau_{rz} = Re^{-1} \left(\frac{1}{r} \frac{\partial u_r}{\partial z} + \frac{\partial u_z}{\partial r} \right) |_{r=1}, \quad (5.40)$$

and

$$\tau_{\theta z} = Re^{-1} \left(\frac{1}{r} \frac{\partial u_z}{\partial \theta} + \frac{\partial u_\theta}{\partial z} \right) |_{r=1}. \quad (5.41)$$

Using the boundary-layer scaled variables defined above, the scaled wall shear components may be written as

$$Re^{1/2}\tau_{r\theta} = \frac{1}{2\sqrt{t}} \frac{\partial u_\theta}{\partial \eta} |_{\eta=0}, \quad (5.42)$$

$$Re^{1/2}\tau_{rz} = \frac{1}{2\sqrt{t}} \frac{\partial u_z}{\partial \eta} |_{\eta=0}. \quad (5.43)$$

Note that the scaled wall shear components given above correspond to the components of scaled vorticity at the wall and thus may be given in terms of ω_θ and ω_z as

$$Re^{1/2}\tau_{r\theta} = \omega_z |_{\eta=0}, \quad (5.44)$$

and

$$Re^{1/2}\tau_{rz} = -\omega_\theta |_{\eta=0}. \quad (5.45)$$

5.4 Numerical Methods

As in the two-dimensional problem discussed in Chapter 4, the numerical scheme used to solve the three-dimensional boundary-layer equations is a combination of finite-difference methods and Fourier transform methods. First, the Finite Fourier transform method is employed to compute all derivatives with respect to θ (see Chapter 4). The derivatives with respect to z are obtained using central finite difference in the calculation of the term $\frac{\partial \tilde{u}_z}{\partial z}$ appearing in the continuity equation and third-order upwind differencing to approximate the z derivatives in the convective terms. In the η direction, a coordinate transformation is employed to cluster the grid near the wall of the cylinder and central finite difference is applied to the resulting derivatives in the normal direction. The implicit Crank-Nicolson marching technique is employed to advance the solution in time.

The coordinate transformation in the η -direction is performed by letting

$$\xi = g(\eta); \quad (5.46)$$

applying this transformation to the boundary-layer equations (5.30)-(5.32) we obtain

$$g' \frac{\partial \tilde{u}_r}{\partial \xi} + \frac{\partial \tilde{u}_\theta}{\partial \theta} + \frac{\partial \tilde{u}_z}{\partial z} = 0 \quad (5.47)$$

$$4t \frac{\partial \tilde{u}_\theta}{\partial t} - (2\eta g' + g'') \frac{\partial \tilde{u}_\theta}{\partial \xi} - g'^2 \frac{\partial^2 \tilde{u}_\theta}{\partial \xi^2} = -4t \frac{\partial p}{\partial \theta} + R_\theta, \quad (5.48)$$

$$4t \frac{\partial \tilde{u}_z}{\partial t} - (2\eta g' + g'') \frac{\partial \tilde{u}_z}{\partial \xi} - g'^2 \frac{\partial^2 \tilde{u}_z}{\partial \xi^2} = -4t \frac{\partial p}{\partial z} + R_z, \quad (5.49)$$

where

$$R_\theta = -4t \left(\frac{g' u_r}{2\sqrt{t}} \frac{\partial u_\theta}{\partial \xi} + u_\theta \frac{\partial u_\theta}{\partial \theta} + (u_z - U_c) \frac{\partial u_\theta}{\partial z} \right), \quad (5.50)$$

$$R_z = -4t \left(\frac{g' u_r}{2\sqrt{t}} \frac{\partial u_z}{\partial \xi} + u_\theta \frac{\partial u_z}{\partial \theta} + (u_z - U_c) \frac{\partial u_z}{\partial z} \right), \quad (5.51)$$

where $g' = d\xi/d\eta$ and $g'' = d^2\xi/d\eta^2$. Here the coordinate transformation used in η is given by

$$\eta = \frac{2\xi}{1-\xi}, \quad (5.52)$$

where ξ ranges from 0 to 0.75 which gives $\eta_{max}=6$.

For simplicity, let u denote either velocity component \tilde{u}_θ or \tilde{u}_z ; then by applying the Crank-Nicolson scheme in t to the momentum equations we obtain

$$4\left(t - \frac{1}{2}\Delta t\right) \frac{u^t - u^{t-\Delta t}}{\Delta t} - \left(\eta g' + \frac{1}{2}g''\right) \left(\frac{\partial u^t}{\partial \xi} + \frac{\partial u^{t-\Delta t}}{\partial \xi}\right)$$

$$-\frac{1}{2}g'^2 \left(\frac{\partial^2 u^t}{\partial \xi^2} + \frac{\partial^2 u^{t-\Delta t}}{\partial \xi^2} \right) = \frac{1}{2} (P^t + P^{t-\Delta t}), \quad (5.53)$$

where

$$P = -4t \frac{\partial p}{\partial \theta} + R_\theta, \quad (5.54)$$

for the θ momentum equation or

$$P = -4t \frac{\partial p}{\partial z} + R_z, \quad (5.55)$$

for the z -momentum equation. Following the same procedure outlined in Chapter 4, the first and the second derivatives of u with respect to ξ are evaluated by using central differencing and the final discretized form of the equations results in a tridiagonal system which may be written as

$$a_j u_{j-1}^{n+1} + b_j u_j^{n+1} + c_j u_{j+1}^{n+1} = -a_j u_{j-1}^n + d_j u_j^n - c_j u_{j+1}^n + e_j, \quad (5.56)$$

where

$$a_j = \frac{1}{2} \left(\eta_j g'_j + \frac{1}{2} g''_j \right) \frac{\Delta t}{\Delta \xi} - \frac{1}{2} g'^2_j \frac{\Delta t}{\Delta \xi^2}, \quad (5.57)$$

$$b_j = 4t^n + g'^2_j \frac{1}{2} + \frac{\Delta t}{\Delta \eta^2}, \quad (5.58)$$

$$c_j = -\frac{1}{2} \left(\eta_j g'_j + \frac{1}{2} g''_j \right) \frac{\Delta t}{\Delta \xi} - \frac{1}{2} g'^2_j \frac{\Delta t}{\Delta \xi^2}, \quad (5.59)$$

$$d_j = 4t^{n+\frac{1}{2}} - g'^2_j \frac{\Delta t}{\Delta \eta^2}, \quad (5.60)$$

and

$$e_j = \frac{1}{2} (P^{n+1} + P^n). \quad (5.61)$$

A third-order upwind differencing scheme to treat the convective terms in the z direction is employed in the present work and the method is described as follows. The third-order upwind differencing is illustrated for a typical convective term $f \frac{\partial u}{\partial z}$ by (Leonard 1984)

$$\left(f \frac{\partial u}{\partial z} \right)_i = \begin{cases} f_i (2u_{i+1} + 3u_i - 6u_{i-1} + u_{i-2}) / 6\Delta z + O(\Delta z^3) & \text{for } f_i > 0, \\ f_i (-u_{i+2} + 6u_{i+1} - 3u_i - 2u_{i-1}) / 6\Delta z + O(\Delta z^3) & \text{for } f_i < 0, \end{cases} \quad (5.62)$$

which may be written in a more compact form as

$$\left(f \frac{\partial u}{\partial z} \right)_i = f_i \frac{-u_{i+2} + 8u_{i+1} - 8u_{i-1} + u_{i-2}}{12\Delta z}$$

$$+ |f_i| \frac{u_{i+2} - 4u_{i+1} + 6u_i - 4u_{i-1} + u_{i-2}}{12\Delta z} + O(\Delta z^3). \quad (5.63)$$

The iteration scheme used here is summarized as follows. The scheme consists of two main loops. Within the outer loop, the boundary-layer equations are solved for each time step iteratively. At each specific time step, using the prescribed boundary conditions and pressure gradients which are known solutions of the potential flow, two subroutines are called to compute R_θ and R_z using previously iterated values of \tilde{u}_θ and \tilde{u}_z as an initial guess. The tridiagonal systems for the new iterates \tilde{u}_θ and \tilde{u}_z are then solved using the Thomas algorithm. The process is repeated until the solution for either component \tilde{u}_θ or \tilde{u}_z converges to four significant figures at each grid point in the computational domain. If $u_{i,j,k}^m$ denotes the m th iterate for the solution at the (i,j,k) node in (r,θ,z) grid domain, the convergence criterion used to produce the results is

$$\left| \frac{u_{i,j,k}^m - u_{i,j,k}^{m-1}}{u_{i,j,k}^{m-1}} \right| < 10^{-4}.$$

The calculation then continues to the outer loop where time marching is performed. In solving equations (5.48) and (5.49) for \tilde{u}_θ and \tilde{u}_z , under-relaxation is used according to the formulas

$$\tilde{u}_\theta = \Omega_\theta \tilde{u}_\theta^{\text{new}} + (1 - \Omega_\theta) \tilde{u}_\theta^{\text{old}}$$

$$\tilde{u}_z = \Omega_z \tilde{u}_z^{\text{new}} + (1 - \Omega_z) \tilde{u}_z^{\text{old}}$$

where Ω_θ and Ω_z are the relaxation factors. In all the calculations, using relaxation factors that vary from 0.8 at the initial calculations to 0.4 at the later times, 15 to 25 iterations are required to obtain a converged solution.

The accuracy of the scheme was checked by conducting a grid size study in ξ, z, θ and t . The agreement between different grid sizes and time-steps is very good especially at early times up to $t = 0.7$ for the stagnant medium case. Solutions at $t=0.8$ are also well resolved outside the region just underneath the vortex. Based on these tests, it is found that 61 points across the boundary layer are sufficient to insure two-figure accuracy in the computed velocities. The number of points in the θ direction is taken to be $M_\theta = 64$ which insures three digit accuracy when compared with $M_\theta = 128$. The inviscid flow is well resolved for this value of M_θ . In the stagnant medium case, the time step in the present results is taken to be $\Delta t = 0.00625$ here which ensures at least three digit accuracy in the early stages of the calculation. In addition, the boundary condition in the y -direction is imposed at some large but finite value of η , say $\eta = \eta_{\text{max}}$. In general, η_{max} is determined by testing larger values until the change in the results becomes negligible; $\eta_{\text{max}} = 6$ and 10 were tested and the value $\eta_{\text{max}} = 6$ is sufficient for three digit accuracy.

The grid size study was conducted for the case of stagnant medium and is shown as follows. Table 5.1 shows the results for u_z for $\Delta\xi = .025, .0125, .00625$ at $t = .6$ where $\eta_{max} = 6$, $\Delta t = 0.0125$ and $\Delta\theta = \frac{2\pi}{64}$. Here we choose the location where $\theta = 7\pi/16$ which is slightly off the symmetry plane ($\theta = \pi/2$) to the right and at a location $z = -0.25$ just inside the region of reversed flow. Notice that $\Delta\xi = 0.0125$ ensures at least three-digit accuracy and will be used to obtain the results. Table 5.2 also shows the results for $\Delta\theta = \frac{2\pi}{32}$, $\Delta\theta = \frac{2\pi}{64}$ and $\Delta\theta = \frac{2\pi}{128}$; here the results correspond to time $t = 0.6$ and are shown at fixed $\xi = 0.0125$ using $\Delta t = 0.0125$. Table 5.3 shows the effect of varying Δz . The results are shown at the same location and time employed in Table 5.2 and Table 5.1 with $\Delta\theta = \frac{2\pi}{64}$ and $\xi = 0.0125$. Note that the results are not as resolved as for other grid sizes however a two-digit accuracy is still maintained. Finally in Table 5.4 are results for different grid sizes of Δt . Here $\Delta t = 0.025, .0125$ and 0.00625 are employed and results correspond to the same location used in the other tables. As for the stagnant medium case, a grid size study has been conducted for the other two mean flow cases and the grid sizes used in the stagnant medium case yield similar numerical resolution as for the symmetric and the asymmetric mean flow cases. Therefore, in this chapter, the spatial grid sizes $\xi = 0.0125$, $\Delta\theta = \frac{2\pi}{64}$ and $\Delta z = 0.025$, which are used to generate the boundary-layer flow results for the stagnant medium case, are also employed to compute the boundary-layer flow for the other two mean flow cases.

To speed up the computations of the boundary-layer flow, the inviscid flow results which serve as boundary conditions for the boundary layer flow problem are generated by using grid sizes which are somewhat coarser than those employed in Chapters 2 and 3. Recall that the numerical accuracy of the inviscid flow results is very sensitive to the distance between the vortex and the cylinder and that the results reported in Chapters 2 and 3 are resolved up to the point where the vortex is one core radius away from the cylinder. In this chapter, the vortex filament is more than two core radii away from the cylinder during the boundary-layer computations and so the use of a coarser grid (double the grid size used in Chapters 2 and 3) is expected to yield a numerical accuracy comparable to that required in Chapters 2 and 3. In all cases, in this Chapter, $\Delta\theta = 2\pi/32$ and $\Delta z = 0.1$ are used to generate the inviscid flow solutions.

It should be noted that since more grid points are required to resolve the boundary layer calculations, in all cases studied here, the inviscid flow results computed on a relatively coarse grid are interpolated using cubic splines to give results on a finer grid. The inviscid flow solution is computed on a range $-12.8 \leq z \leq 12.8$ using a grid size $\Delta z = 0.1$. However, for stagnant medium and the symmetric mean flow cases, only the range $-1.5 \leq z \leq 1.5$, which contains 31 inviscid grid points, is employed to compute the boundary-layer solution since the inviscid surface speeds and pressure gradients decay rapidly in z (Figures 5.2 and 5.9). On the other hand,

Table 5.1: Effect of $\Delta\xi$ on the axial velocity u_z at $t=0.6$

η	$\Delta\xi=0.025$	$\Delta\xi=0.0125$	$\Delta\xi=0.00625$
0.0000	0.00000E+00	0.00000E+00	0.00000E+00
0.0513	0.84159E-02	0.84066E-02	0.84043E-02
0.1053	0.13345E-01	0.13327E-01	0.13322E-01
0.1622	0.14697E-01	0.14669E-01	0.14662E-01
0.2222	0.12414E-01	0.12376E-01	0.12367E-01
0.2857	0.64807E-02	0.64326E-02	0.64206E-02
0.3529	-0.30737E-02	-0.31338E-02	-0.31489E-02
0.4242	-0.16175E-01	-0.16249E-01	-0.16267E-01
0.5000	-0.32699E-01	-0.32789E-01	-0.32811E-01
0.5806	-0.52474E-01	-0.52583E-01	-0.52610E-01
0.6667	-0.75281E-01	-0.75410E-01	-0.75442E-01
0.7586	-0.10085E+00	-0.10100E+00	-0.10104E+00
0.8571	-0.12887E+00	-0.12904E+00	-0.12908E+00
0.9630	-0.15897E+00	-0.15915E+00	-0.15919E+00
1.0769	-0.19070E+00	-0.19089E+00	-0.19093E+00
1.2000	-0.22360E+00	-0.22377E+00	-0.22381E+00
1.3333	-0.25710E+00	-0.25723E+00	-0.25727E+00
1.4783	-0.29055E+00	-0.29063E+00	-0.29064E+00
1.6364	-0.32317E+00	-0.32317E+00	-0.32317E+00
1.8095	-0.35405E+00	-0.35396E+00	-0.35394E+00
2.0000	-0.38217E+00	-0.38203E+00	-0.38200E+00
2.2105	-0.40658E+00	-0.40644E+00	-0.40640E+00
2.4444	-0.42654E+00	-0.42646E+00	-0.42644E+00
2.7059	-0.44171E+00	-0.44175E+00	-0.44175E+00
3.0000	-0.45229E+00	-0.45245E+00	-0.45249E+00
3.3333	-0.45897E+00	-0.45920E+00	-0.45926E+00
3.7143	-0.46272E+00	-0.46296E+00	-0.46302E+00
4.1538	-0.46458E+00	-0.46477E+00	-0.46482E+00
4.6667	-0.46519E+00	-0.46550E+00	-0.46553E+00
5.2727	-0.46681E+00	-0.46554E+00	-0.46570E+00
6.0000	-0.46211E+00	-0.46211E+00	-0.46211E+00

Table 5.2: Effect of $\Delta\theta$ on the axial velocity u_z at $t=0.6$

η	$\Delta\theta = \frac{2\pi}{32}$	$\Delta\theta = \frac{2\pi}{64}$	$\Delta\theta = \frac{2\pi}{128}$
0.0000	0.00000E+00	0.00000E+00	0.00000E+00
0.0513	0.84159E-02	0.84071E-02	0.84285E-02
0.1053	0.13345E-01	0.13327E-01	0.13371E-01
0.1622	0.14697E-01	0.14667E-01	0.14736E-01
0.2222	0.12414E-01	0.12371E-01	0.12468E-01
0.2857	0.64807E-02	0.64213E-02	0.65490E-02
0.3529	-0.30737E-02	-0.31541E-02	-0.29920E-02
0.4242	-0.16175E-01	-0.16283E-01	-0.16082E-01
0.5000	-0.32699E-01	-0.32843E-01	-0.32601E-01
0.5806	-0.52474E-01	-0.52668E-01	-0.52380E-01
0.6667	-0.75281E-01	-0.75539E-01	-0.75206E-01
0.7586	-0.10085E+00	-0.10119E+00	-0.10082E+00
0.8571	-0.12887E+00	-0.12932E+00	-0.12891E+00
0.9630	-0.15897E+00	-0.15955E+00	-0.15910E+00
1.0769	-0.19070E+00	-0.19145E+00	-0.19099E+00
1.2000	-0.22360E+00	-0.22452E+00	-0.22406E+00
1.3333	-0.25710E+00	-0.25821E+00	-0.25778E+00
1.4783	-0.29055E+00	-0.29184E+00	-0.29146E+00
1.6364	-0.32317E+00	-0.32462E+00	-0.32429E+00
1.8095	-0.35405E+00	-0.35560E+00	-0.35534E+00
2.0000	-0.38217E+00	-0.38377E+00	-0.38356E+00
2.2105	-0.40658E+00	-0.40815E+00	-0.40798E+00
2.4444	-0.42654E+00	-0.42801E+00	-0.42787E+00
2.7059	-0.44171E+00	-0.44305E+00	-0.44292E+00
3.0000	-0.45229E+00	-0.45350E+00	-0.45336E+00
3.3333	-0.45897E+00	-0.46005E+00	-0.45990E+00
3.7143	-0.46272E+00	-0.46371E+00	-0.46355E+00
4.1538	-0.46458E+00	-0.46552E+00	-0.46536E+00
4.6667	-0.46519E+00	-0.46608E+00	-0.46592E+00
5.2727	-0.46681E+00	-0.46789E+00	-0.46768E+00
6.0000	-0.46211E+00	-0.46211E+00	-0.46211E+00

Table 5.3: Effect of Δz on the axial velocity u_z at $t=0.6$

η	$\Delta z=0.05$	$\Delta z=0.025$	$\Delta z=0.0125$
0.0000	0.00000E+00	0.00000E+00	0.00000E+00
0.0513	0.84159E-02	0.82679E-02	0.82348E-02
0.1053	0.13345E-01	0.13039E-01	0.12970E-01
0.1622	0.14697E-01	0.14218E-01	0.14110E-01
0.2222	0.12414E-01	0.11745E-01	0.11591E-01
0.2857	0.64807E-02	0.56001E-02	0.53943E-02
0.3529	-0.30737E-02	-0.41928E-02	-0.44582E-02
0.4242	-0.16175E-01	-0.17562E-01	-0.17895E-01
0.5000	-0.32699E-01	-0.34386E-01	-0.34795E-01
0.5806	-0.52474E-01	-0.54493E-01	-0.54985E-01
0.6667	-0.75281E-01	-0.77657E-01	-0.78238E-01
0.7586	-0.10085E+00	-0.10360E+00	-0.10428E+00
0.8571	-0.12887E+00	-0.13199E+00	-0.13277E+00
0.9630	-0.15897E+00	-0.16244E+00	-0.16332E+00
1.0769	-0.19070E+00	-0.19449E+00	-0.19548E+00
1.2000	-0.22360E+00	-0.22763E+00	-0.22871E+00
1.3333	-0.25710E+00	-0.26125E+00	-0.26239E+00
1.4783	-0.29055E+00	-0.29465E+00	-0.29582E+00
1.6364	-0.32317E+00	-0.32703E+00	-0.32815E+00
1.8095	-0.35405E+00	-0.35751E+00	-0.35849E+00
2.0000	-0.38217E+00	-0.38516E+00	-0.38591E+00
2.2105	-0.40658E+00	-0.40909E+00	-0.40955E+00
2.4444	-0.42654E+00	-0.42864E+00	-0.42878E+00
2.7059	-0.44171E+00	-0.44350E+00	-0.44335E+00
3.0000	-0.45229E+00	-0.45384E+00	-0.45347E+00
3.3333	-0.45897E+00	-0.46034E+00	-0.45984E+00
3.7143	-0.46272E+00	-0.46400E+00	-0.46348E+00
4.1538	-0.46458E+00	-0.46590E+00	-0.46544E+00
4.6667	-0.46519E+00	-0.46663E+00	-0.46635E+00
5.2727	-0.46681E+00	-0.46891E+00	-0.46879E+00
6.0000	-0.46211E+00	-0.46211E+00	-0.46211E+00

Table 5.4: Effect of Δt on the axial velocity u_z at $t=0.6$

η	$\Delta t=0.025$	$\Delta t=0.0125$	$\Delta t=0.00625$
0.0000	0.00000E+00	0.00000E+00	0.00000E+00
0.0513	0.82747E-02	0.82679E-02	0.82661E-02
0.1053	0.13053E-01	0.13039E-01	0.13036E-01
0.1622	0.14240E-01	0.14218E-01	0.14213E-01
0.2222	0.11774E-01	0.11745E-01	0.11738E-01
0.2857	0.56371E-02	0.56001E-02	0.55904E-02
0.3529	-0.41474E-02	-0.41928E-02	-0.42047E-02
0.4242	-0.17508E-01	-0.17562E-01	-0.17576E-01
0.5000	-0.34323E-01	-0.34386E-01	-0.34403E-01
0.5806	-0.54420E-01	-0.54493E-01	-0.54512E-01
0.6667	-0.77575E-01	-0.77657E-01	-0.77679E-01
0.7586	-0.10351E+00	-0.10360E+00	-0.10363E+00
0.8571	-0.13189E+00	-0.13199E+00	-0.13202E+00
0.9630	-0.16233E+00	-0.16244E+00	-0.16247E+00
1.0769	-0.19438E+00	-0.19449E+00	-0.19452E+00
1.2000	-0.22751E+00	-0.22763E+00	-0.22767E+00
1.3333	-0.26113E+00	-0.26125E+00	-0.26128E+00
1.4783	-0.29453E+00	-0.29465E+00	-0.29468E+00
1.6364	-0.32693E+00	-0.32703E+00	-0.32706E+00
1.8095	-0.35743E+00	-0.35751E+00	-0.35753E+00
2.0000	-0.38510E+00	-0.38516E+00	-0.38517E+00
2.2105	-0.40908E+00	-0.40909E+00	-0.40910E+00
2.4444	-0.42866E+00	-0.42864E+00	-0.42864E+00
2.7059	-0.44355E+00	-0.44350E+00	-0.44348E+00
3.0000	-0.45391E+00	-0.45384E+00	-0.45382E+00
3.3333	-0.46042E+00	-0.46034E+00	-0.46031E+00
3.7143	-0.46409E+00	-0.46400E+00	-0.46398E+00
4.1538	-0.46597E+00	-0.46590E+00	-0.46588E+00
4.6667	-0.46666E+00	-0.46663E+00	-0.46661E+00
5.2727	-0.46890E+00	-0.46891E+00	-0.46891E+00
6.0000	-0.46211E+00	-0.46211E+00	-0.46211E+00

for the asymmetric mean flow case, a range $-2 \leq z \leq 2$, which contains 41 inviscid grid points, is employed to compute the boundary-layer solution. Here, as for the symmetric flow cases, the inviscid surface speeds and pressure gradients (not shown in this work) also decay rapidly in z . In all cases, cubic spline approximation is employed to represent the inviscid solution at points between the inviscid grid points giving an effective viscous grid size in the z -direction of 0.025. In addition, cubic spline interpolation is employed in the θ -direction to represent the inviscid flow solution on a finer viscous θ grid. Finally, the z -ranges quoted above have been compared with larger domains in z with no change in the computed results.

In addition, since the time step employed to advance the vortex in time is relatively larger than that required for the boundary-layer calculations, vortex positions are interpolated in time by repeatedly halving the time step until the new positions correspond to the required finer time step. Note that this time interpolation procedure has been also applied to all the symmetric and the asymmetric mean flow cases. For instance, the time steps (employed to advance the vortex filament in time) $\Delta t = 0.05$ for the stagnant medium, $\Delta t = 0.05$ for the symmetric mean flow and $\Delta t = 0.0711$ for the asymmetric mean flow have been reduced respectively to $\Delta t = 0.00625$, $\Delta t = 0.0025$ and $\Delta t = 0.00444$ in the calculations of the boundary-layer flow. Here a standard second-order interpolation scheme is used to obtain values at mid-intervals. Recall that vortex positions are computed separately and then stored in a data file which is used to compute the inviscid flow field, pressure and pressure gradients.

5.5 Results

In this section, results for each of the three types of outer inviscid flow are presented; in each case the non-dimensionalization employed is given and the results are presented in dimensionless form.

Stagnant Medium

For the stagnant medium case, the boundary-layer variables have been made dimensionless according to

$$\theta = \theta^*, \quad z = \frac{z^*}{a}, \quad y = \left(\frac{r^*}{a} - 1\right) Re^{1/2}, \quad t = \frac{|\Gamma^*|}{a^2} t^*,$$

$$u_r = \frac{a u_r^*}{|\Gamma^*|} Re^{1/2}, \quad u_\theta = \frac{a u_\theta^*}{|\Gamma^*|}, \quad u_z = \frac{a u_z^*}{|\Gamma^*|}, \quad (5.64)$$

where a is the radius of the cylinder, Γ^* is the circulation of the vortex. Here the asterisk indicates dimensional variables. $Re = |\Gamma^*| / \nu$ is the Reynolds number.

The pressure p^* is non-dimensionalized on $\rho \left(\frac{|\Gamma^*|}{a} \right)^2$ where ρ is the density of the fluid. In the present work the three-dimensional streamline patterns are obtained by solving the equations

$$\frac{d\theta}{u_\theta} = \frac{dy}{u_r} = \frac{dz}{u_z} = dS, \quad (5.65)$$

where S is a parameter that measures the distance along a given streamline. These equations are approximated using simple forward differences for the derivatives. For example, in the (z, η) plane, the above equations are numerically approximated according to

$$\eta - \eta_0 = \frac{u_{r0}}{2\sqrt{t}} \Delta S, \quad z - z_0 = u_{z0} \Delta S \quad (5.66)$$

where (u_{r0}, u_{z0}) are the instantaneous velocities at an arbitrary initial point (η_0, z_0) at a given time t . Each streamline in the (z, η) plane is traced by selecting a step ΔS according to (Hon and Walker 1987)

$$(u_z^2 + u_\theta^2 + u_r^2) \Delta S = 0.005. \quad (5.67)$$

It should be noted that because the points defining a streamline do not coincide with the mesh grid points in the (z, θ, η) plane, three-dimensional linear interpolation must be used to compute the three velocity components. Some experimentation in the location of the origin of the streamlines is required, especially in the three-dimensional rendering to be described below. In this regard, to limit computer time a maximum of 3000 points along a streamline are plotted; thus those streamlines which appear to end in the fluid are the result of this arbitrary limiting procedure and are not in violation of the fundamental tenet that a streamline cannot end in the fluid.

The results to be presented here correspond to the vortex trajectories shown on Figure 5.1 and the inviscid flow field depicted on Figures 5.2-5.7. On Figure 5.18 are the results for the streamline patterns plotted at various times corresponding to $t = .3, .6$, and $.8$. The results are plotted in the coordinate system traveling with the speed of the vortex head in the axial direction defined in Section 5.2. All the results to be presented here are for an (η, θ, z) grid corresponding to 61, 64, and 121 points, respectively with $\Delta t = .00625$. Grid and time step accuracy studies as shown by Tables 5.1-5.4 indicate that the present solutions are resolved to at least two figure accuracy up to time $t = .7$ for these parameters. Note the development of a reversed flow eddy which grows in time; at time $t = .8$ kinks appear in the streamlines and boundary layer fluid is expected to eventually erupt into the main inviscid stream. Note that fluid from off the symmetry plane is entrained into the swirling flow, which is strongest on the symmetry plane, and is then ejected in the upstream direction. The swirling fluid motion begins off the symmetry plane at roughly $\theta = 65^\circ$ (see below Figure 5.25). The streamline patterns of Figure 5.18

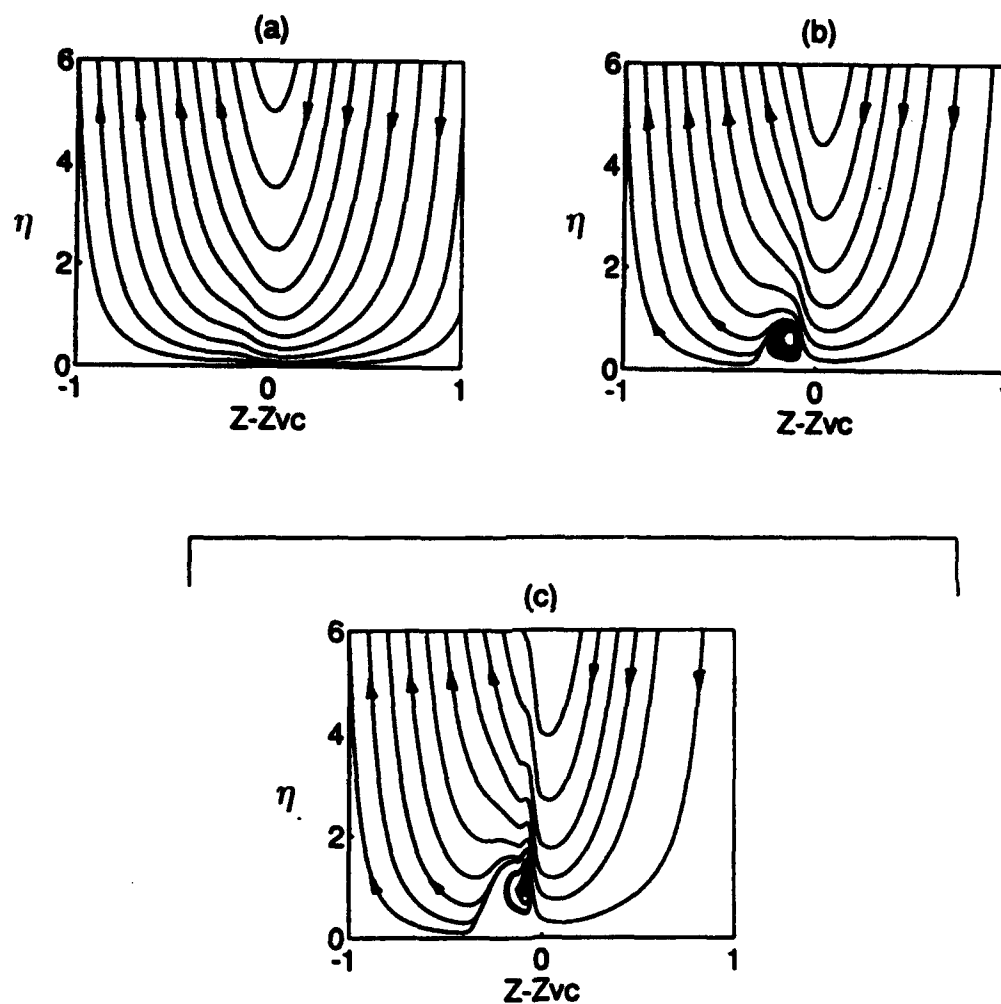
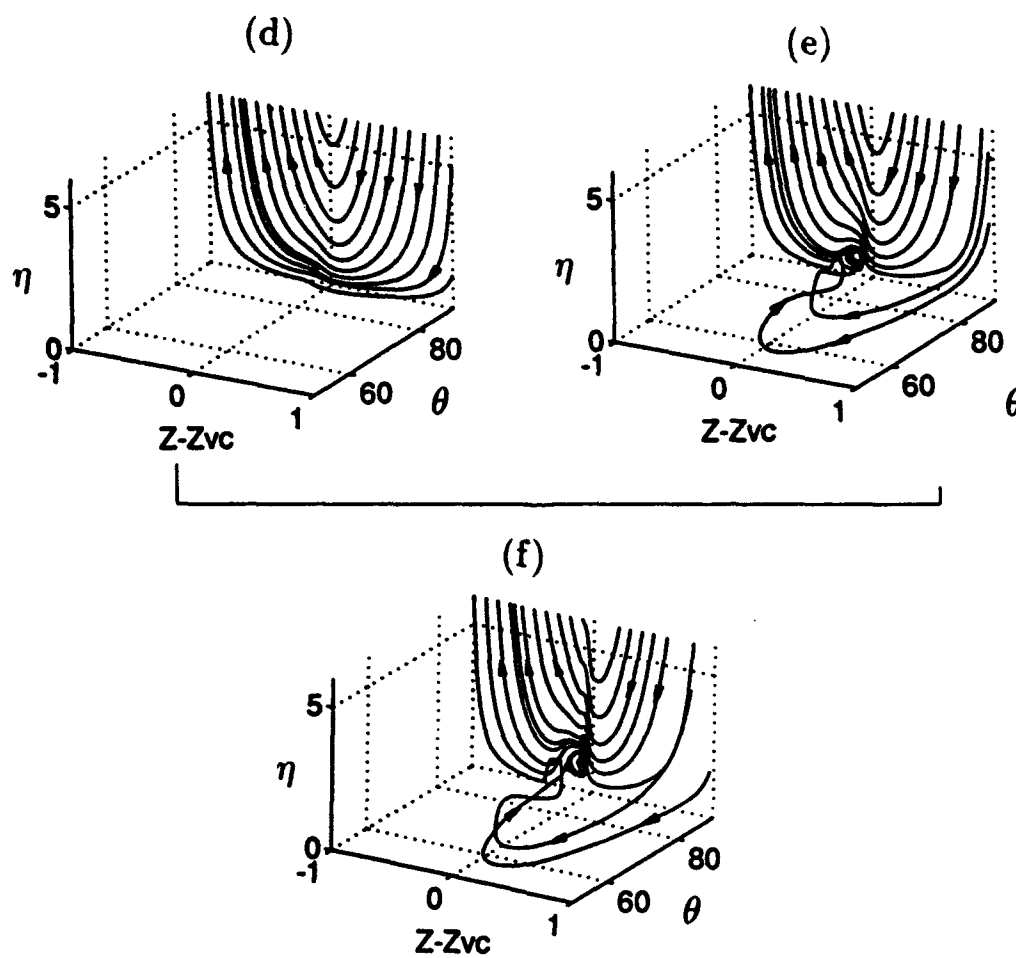


Figure 5.18: Streamline patterns for the stagnant medium at $\theta=\pi/2$ plotted at various times. In the symmetry plane at (a) $t=0.3$, (b) $t=0.6$, (c) $t=0.8$; and a fully three-dimensional view at (d) $t=0.3$, (e) $t=0.6$, (f) $t=0.8$.

Figure 5.18 (continued)



are depicted in the frame of reference traveling with the speed of the vortex head in the z -direction.

There are two $(r-z)$ planes of symmetry in which $u_\theta=0$ which are located on the top of the cylinder at $\theta=\pi/2$ and on the bottom at $\theta=-\pi/2$. Results for the streamline patterns in the bottom plane ($\theta=-\pi/2$; not shown) show no indication that a secondary eddy exists and the secondary flow patterns are very weak. This suggests the presence of a concentration of azimuthal vorticity deep within the boundary-layer which wraps around the cylinder and whose magnitude varies strongly in the θ -direction. This is apparent in the results depicted on Figure 5.19 where lines of constant total azimuthal vorticity, which is defined by equation (5.36), are plotted at several azimuthal locations around the cylinder. The flow in the boundary-layer is symmetric about $\theta = \pi/2$ and so only one-half of the results are plotted. Figures 5.19(a)-5.19(f) show respectively the distributions of the azimuthal vorticity across the boundary-layer in the planes, $\theta=\pi/2$, $3\pi/8$, $\pi/4$, 0 , $-\pi/4$ and $-\pi/2$. Here the range of η shown on the figure is reduced since at higher values of η the flow is practically inviscid and the azimuthal vorticity is near zero there. The constant azimuthal vorticity lines for each of the values of θ are plotted in increments of .02 from -1.4 to 1.4. On Figure 5.19(a) are the constant azimuthal vorticity lines for time $t = .6$ at $\theta = \pi/2$ and note the concentration of azimuthal vorticity directly under the main vortex. The dark region corresponds to absolute values of the azimuthal vorticity above .3. For Figures 5.19(a) and 5.19(b), positive values of the azimuthal vorticity appear outside of the zero azimuthal vorticity line which is marked with an arrow; inside the zero azimuthal vorticity line, the azimuthal vorticity is negative. Note that the clustering of the azimuthal vorticity patterns has diminished as θ varies from the top of the cylinder $\theta = \pi/2$ to $\theta = 3\pi/8$; the maximum positive azimuthal vorticity is reduced from 1.366 to .774 while the negative azimuthal vorticity has dropped from -.458 to -.0266. For Figures 5.19(c)-5.19(f) the values of the azimuthal vorticity deep within the boundary-layer are all positive and the maximum value is 0.398 at $\theta = \pi/4$. Note also that the magnitude of the azimuthal vorticity continues to diminish until at $\theta = -\pi/2$ the maximum is about 0.043. Clearly the present results indicate that the "strength" of the secondary eddy spawned within the boundary-layer diminishes rapidly away from $\theta = \pi/2$.

Of particular interest is the investigation of the time evolution of the zero vorticity line. On Figure 5.20 the lines of constant total azimuthal vorticity at $\theta = \pi/2$ are plotted at various times by excluding the negative values. In this way the zero azimuthal vorticity line can be easily located since, for the stagnant medium case, it is a closed line that is attached to the cylinder wall; inside the zero azimuthal vorticity line, is the negative azimuthal vorticity region. The results are shown for the times $t=0.3$, .4, .5, .6, .7 and .8. Note the increase in the size of the negative azimuthal vorticity region (which is inside the zero vorticity line) as

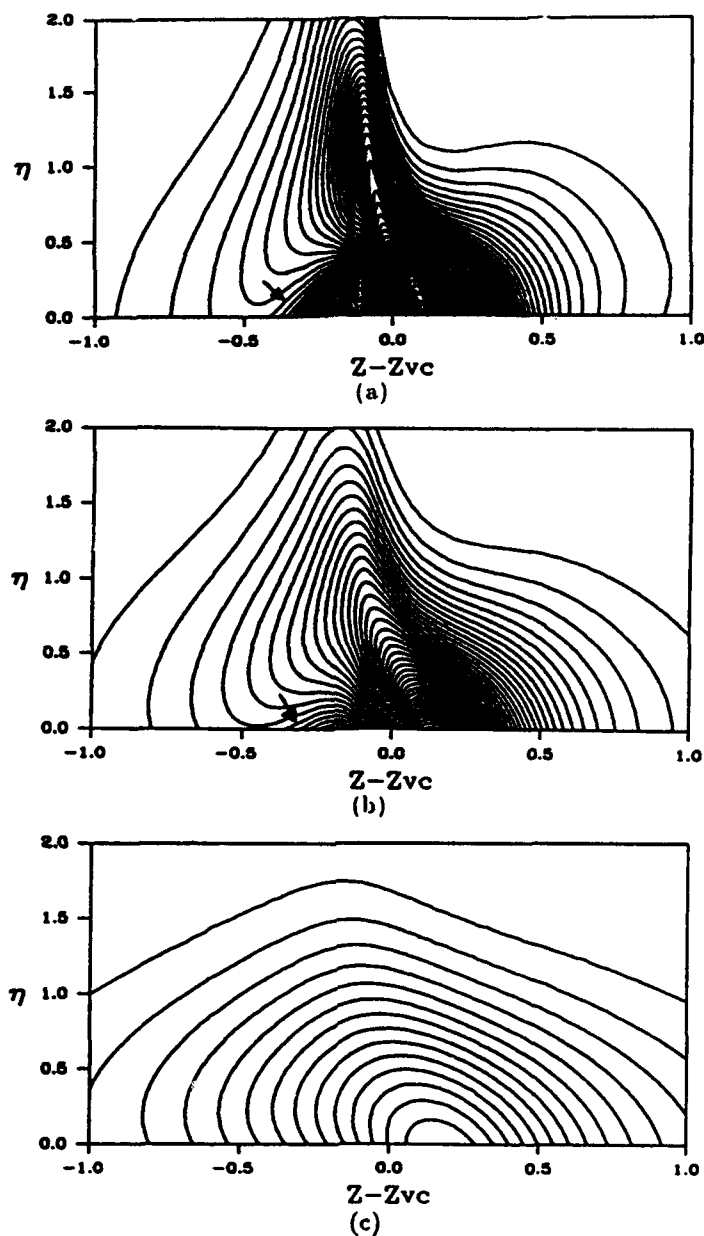
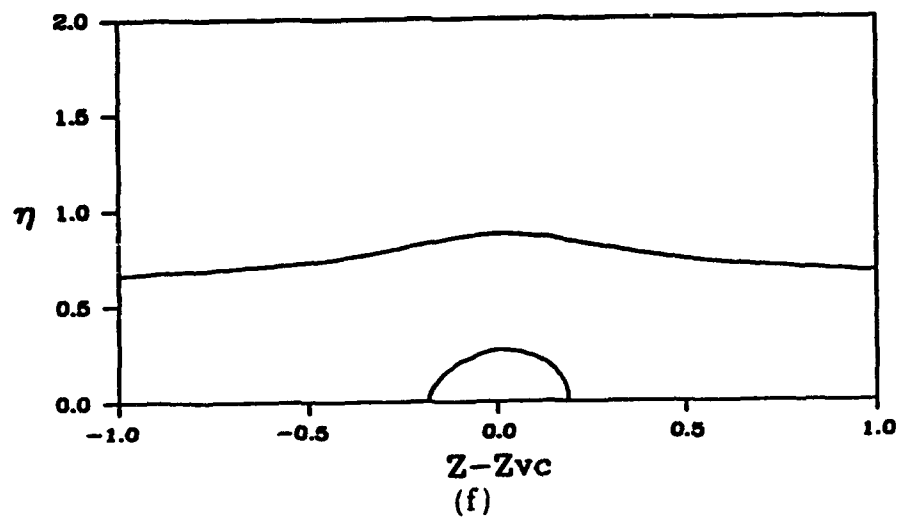
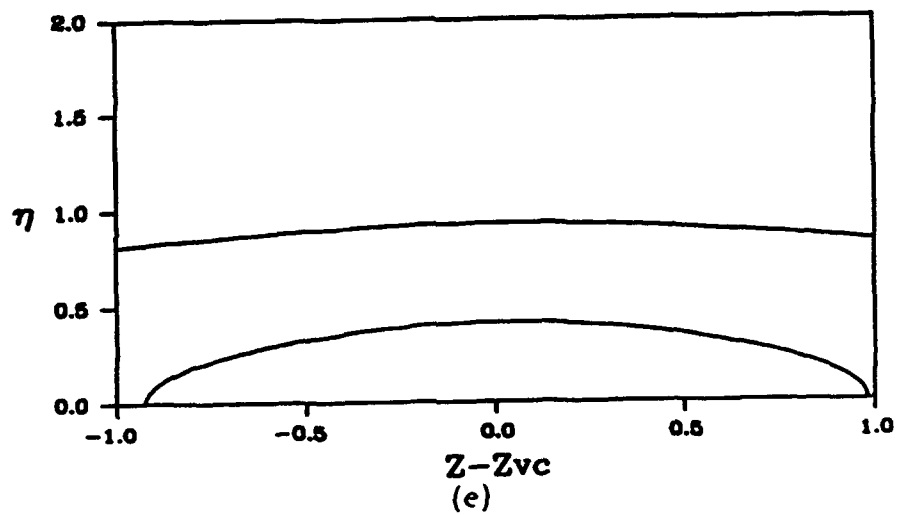
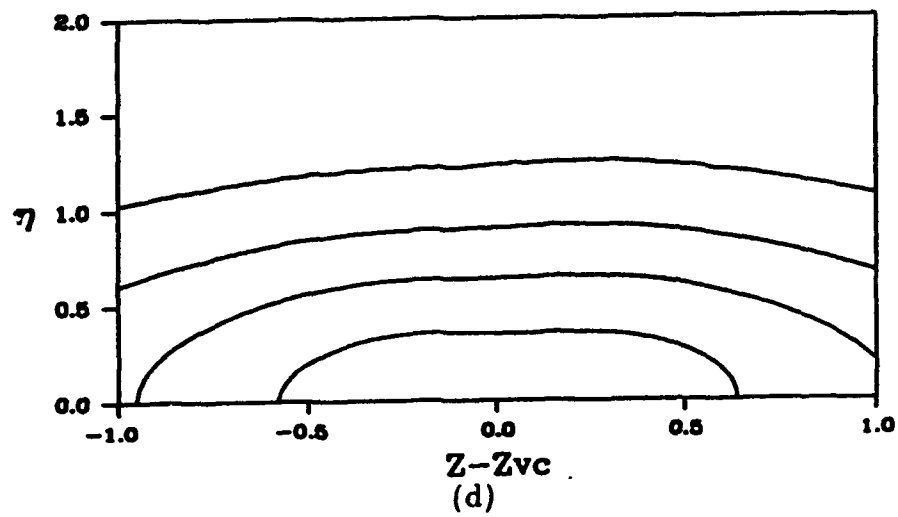


Figure 5.19: Lines of constant total azimuthal vorticity ω_θ at $t=0.6$ for several azimuthal locations around the cylinder: (a) $\theta=\pi/2$, (b) $\theta=3\pi/8$, (c) $\theta=\pi/4$, (d) $\theta=0$, (e) $\theta=-\pi/4$, (f) $\theta=-\pi/2$. The results are for the stagnant medium case where the boundary-layer flow is symmetric about $\theta = \pi/2$. The line of $\omega_\theta=0$ is marked by an arrow.

Figure 5.19 (continued)



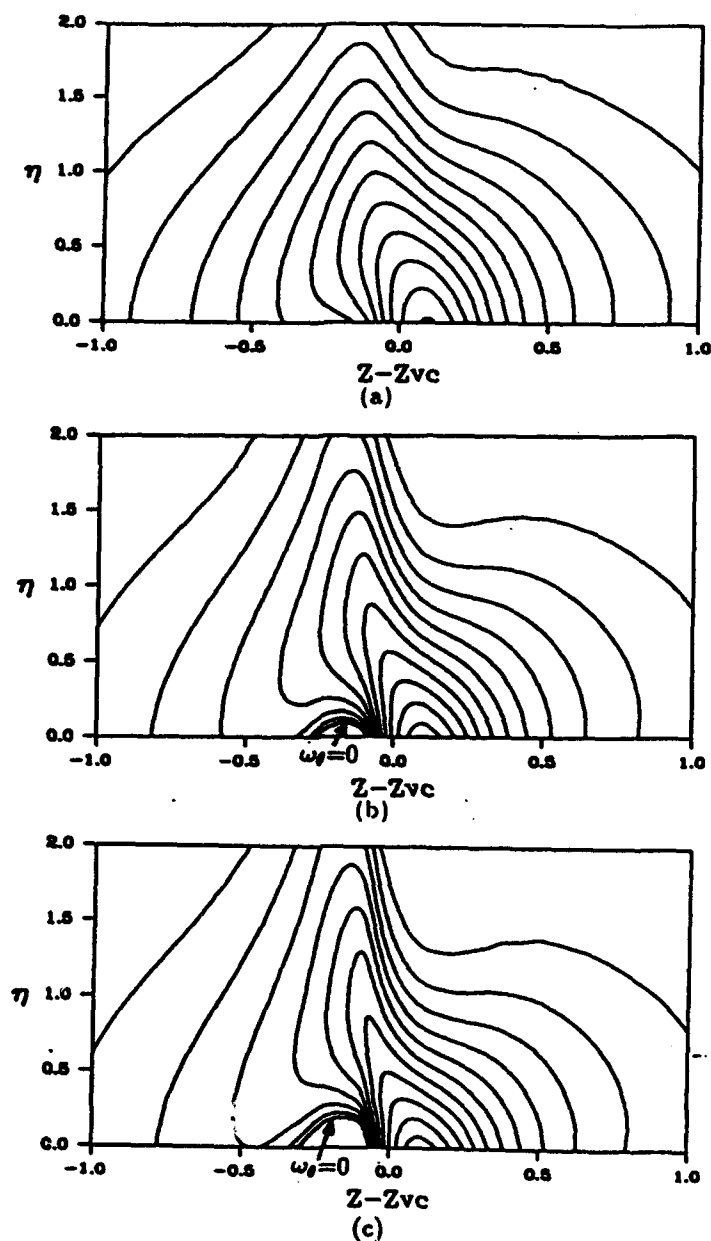
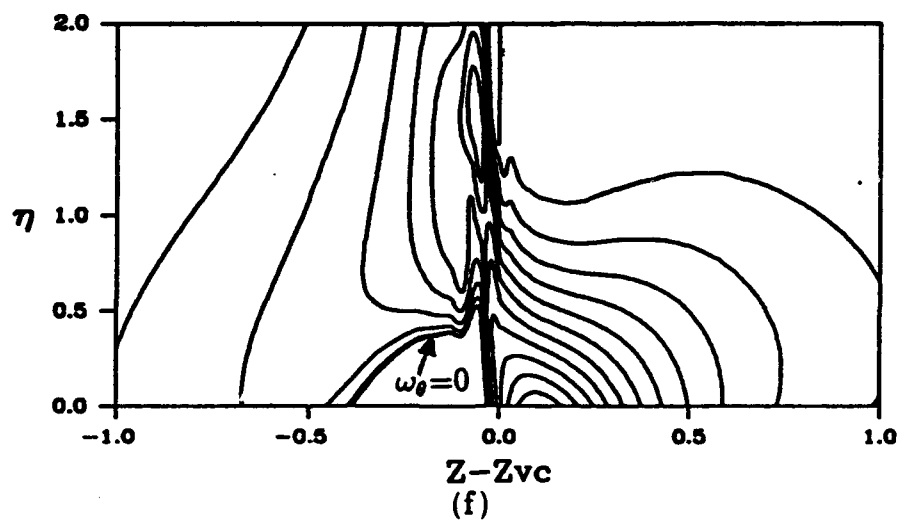
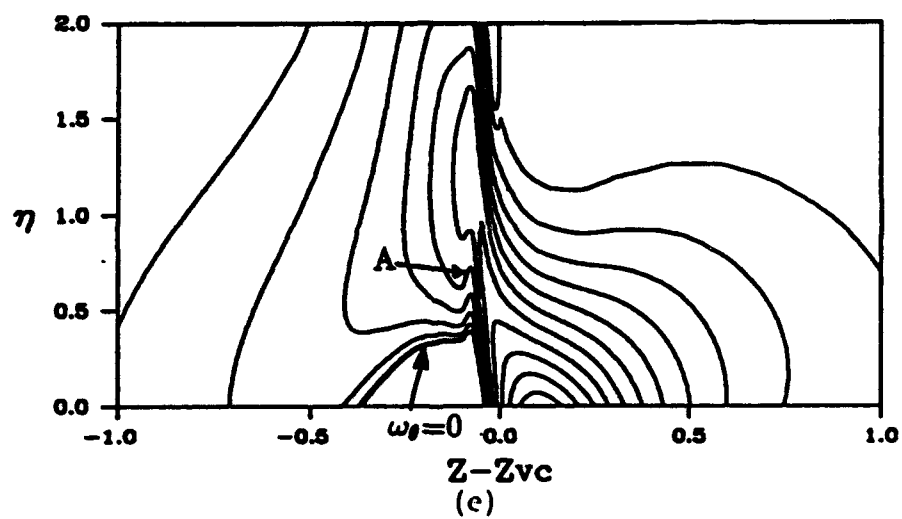
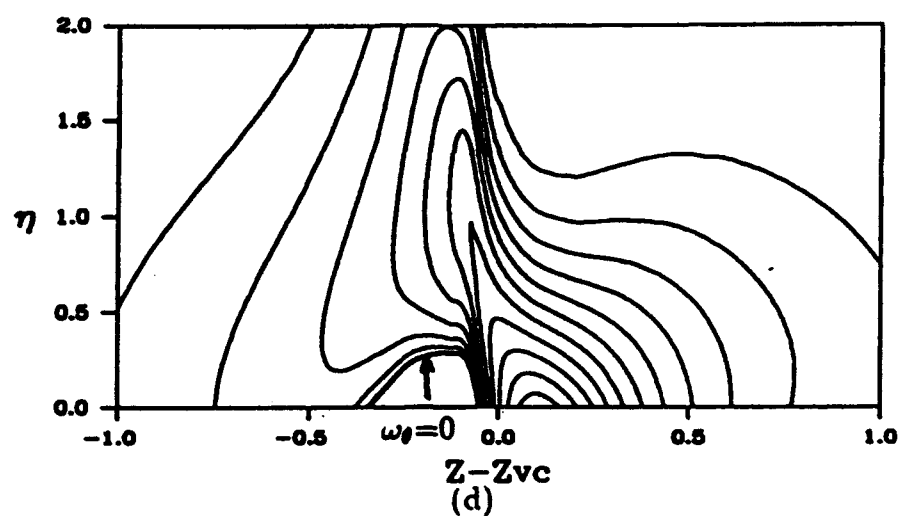


Figure 5.20: Temporal development of the azimuthal vorticity ω_θ in the symmetry plane $\theta = \pi/2$. Here the results are for the stagnant medium case and they are shown as lines of constant ω_θ which are plotted at various times: (a) $t=0.2$, (b) $t=0.4$, (c) $t=0.5$, (d) $t=0.6$, (e) $t=0.7$, (f) $t=0.8$. The line of $\omega_\theta=0$ is marked by an arrow.

Figure 5.20 (continued)



time increases and also note the spike-like structure of the zero azimuthal vorticity line at the latter times especially at $t = 0.8$. In these figures the zero azimuthal vorticity line is labeled. On Figure 5.20(e) ($t=0.7$) the zero azimuthal vorticity line touches the wall at about $z = -0.05$ and at $z = -0.35$. As stated by Peridier and Walker (1989) for the corresponding two-dimensional problem, the eruption of the boundary-layer will occur in the vicinity of a zero vorticity line. By using Lagrangian techniques they are able to predict both the location and the time at which the boundary-layer flow becomes singular. The azimuthal vorticity patterns plotted as contours of constant values show a developing inverted "V" shape in the region just underneath the primary vortex; this inverted "V" pattern becomes considerably stretched in the vertical direction as the singularity is approached. The singular point is expected at the first occurrence of a stationary point on the zero vorticity line. In three dimensions the singularity is defined as the location of vanishing gradient of an oblique Lagrangian coordinate (van Dommelen and Cowley 1990), while, simultaneously, the vorticity vector vanishes. In the present case, the azimuthal vorticity vanishes along the line indicated on Figure 5.20; in addition, by symmetry, the axial vorticity vanishes along the plane $\theta = \pi/2$. Consequently, the vorticity vector vanishes along the curve indicated in Figure 5.20. It should be noted that there are other locations where the azimuthal vorticity vanishes (Figure 5.19); however, inspection of the numerical results indicates that there are no other locations of vanishing axial vorticity. Thus, the present situation is similar to the laterally symmetric separation case considered by van Dommelen and Cowley (1990) and the singularity is expected to occur somewhere along the zero azimuthal vorticity line. It is difficult within the framework of the present Eulerian calculations to determine where the singularity will occur and at what time. However, initial calculations of the behavior of the maximum displacement velocity in the latter stages of the calculations indicate a behavior $u_{r,max} \sim (t_s - t)^{-7/4}$ which is consistent with the predictions of Elliott, Cowley, and Smith (1983). Indeed, the present results indicate that the constant azimuthal vorticity lines on the symmetry plane develop in a manner similar to the two-dimensional problem described by Peridier and Walker (1989) and are consistent with the development of a singularity there.

At later times in the calculation the accuracy of the numerical results near $z = 0$ is suspect and to investigate this, we show on Figure 5.21 the effect of varying Δz on the azimuthal vorticity distribution at $t = 0.8$. Results for $\Delta z = 0.025$, $\Delta z = 0.0125$ and $\Delta z = 0.00625$ are shown respectively on Figure 5.21(a), 5.21(b) and 5.21(c). Note that the azimuthal vorticity lines near $z=0$ become more focused as the grid size Δz is reduced which is consistent with the two-dimensional results near the singular time of Peridier and Walker (1989). See for instance Figure 4.5(c) of their work.

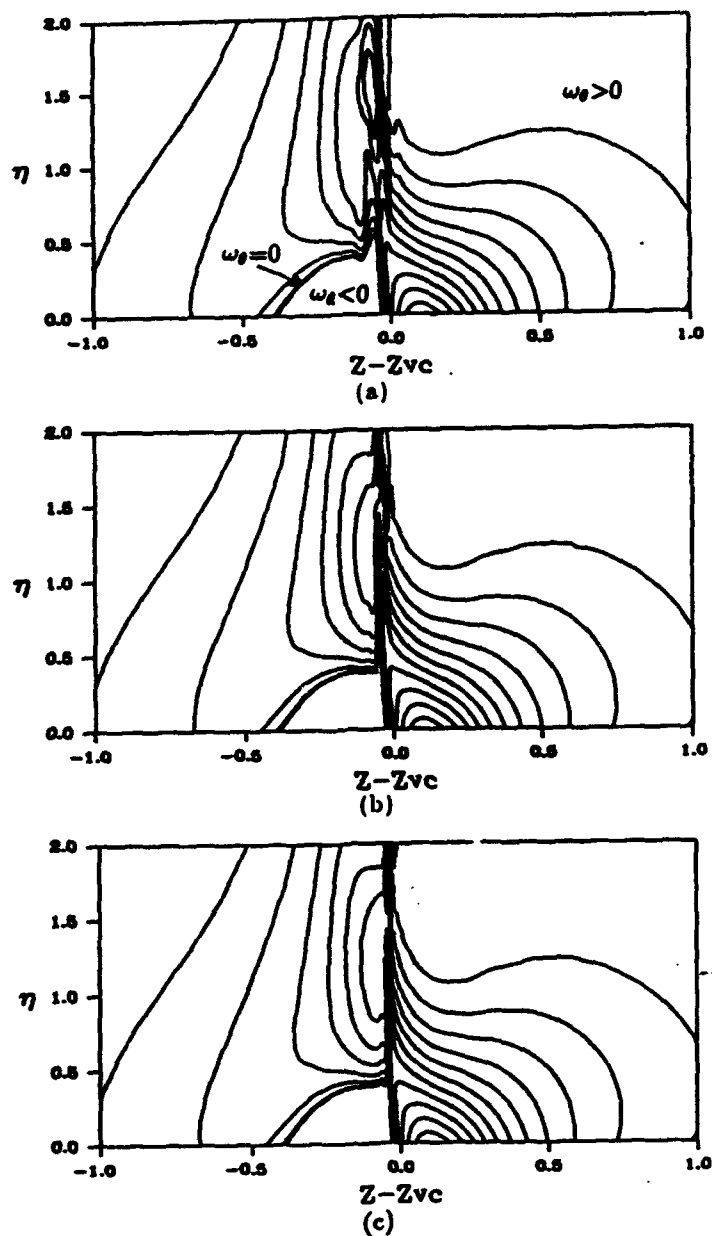


Figure 5.21: The effect of the grid size Δz on the computed azimuthal vorticity component which is plotted as contour lines in the symmetry plane $\theta = \pi/2$. Here the results are for the stagnant medium case and are plotted at time $t=0.8$ for 3 grid sizes: (a) $\Delta z=0.025$, (b) $\Delta z=0.0125$, (c) $\Delta z=0.00625$.

On Figure 5.22 is the temporal development of the radial velocity at $\theta = \pi/2$ for times $t = .1$ to $.8$ in increments of $.1$ plotted as a function of distance along the cylinder centerline. Note the rapid growth of the velocity as time increases; shortly after this time the numerical scheme breaks down; the results at time $t = .8$ should be viewed as qualitative. It is useful to note that the results depicted on this figure provide the temporal limits on the application of boundary-layer theory to finite Reynolds numbers since $Re^{-1/2}u_r \ll 1$ for boundary-layer theory to apply.

On Figure 5.23 is another view of the development of the large radial velocity at the boundary layer edge. Here lines of constant radial velocity at the edge of the boundary-layer around the cylinder are plotted for times $t = 0.2$, $t = 0.4$, $t = 0.6$ and $t = 0.8$. Note that at points removed from $\theta = \pi/2$, the edge velocity is varying somewhat slowly. Near $\theta = \pi/2$, however, there is a local rapid variation just under the head of the vortex, especially at time $t = .8$. At $t = 0.8$ the lines of constant radial velocity depicted on Figure 5.23(d) show that the negative values correspond to a valley shape with smooth base while the positive values represent a mountain-like shape with pointed top located inside the level "A" contour line.

To investigate the effect of the boundary-layer flow on the wall of the cylinder, the surface streamlines are plotted for three times on Figure 5.24. These lines are obtained by taking the limit of the ratio of the azimuthal and axial surface speeds as the cylinder is approached. These lines thus are the result of solving a nonlinear ordinary differential equation with the right hand side corresponding to the ratio of the appropriate surface stresses. The solution of the equation is obtained in a manner similar to the solution of the two and three-dimensional streamline patterns themselves. At the early time ($t = .3$) these patterns show very little activity. However, by $t = .6$ there appears a nodal point of attachment (N) near the upstream end of the secondary eddy with a saddle point of separation (S) appearing downstream (see Figures 5.18 and 5.19; see also Lighthill (1963; Figure II. 11, p. 77)). This situation is consistent with the surface singularity rule for an infinite body described by Tobak and Peake (1982). Note that the skin friction lines just adjacent to the dividing lines leading to the saddle point of separation do not intersect normally and are thus not additional singular points. This is shown in the expanded view depicted on Figure 5.24(d).

On Figure 5.25 are the lines of constant azimuthal vorticity at the wall plotted at $t = 0.6$. Note the presence of a zero azimuthal vorticity line which encloses the region defined by the node of attachment and the saddle point of separation seen in the wall streamline patterns. Outside of the zero line on Figure 5.25 the flow is nominally attached.

On Figure 5.26 the temporal development of the profiles of the velocity component u_z is shown. The axial velocity profiles are plotted at various times $t = 0.2$, 0.3 , 0.4 , 0.5 and 0.6 . For each time level the profiles are plotted at 9 z locations which are equally spaced and centered around the point $z = Z - Z_{V_c} = -0.25$. The

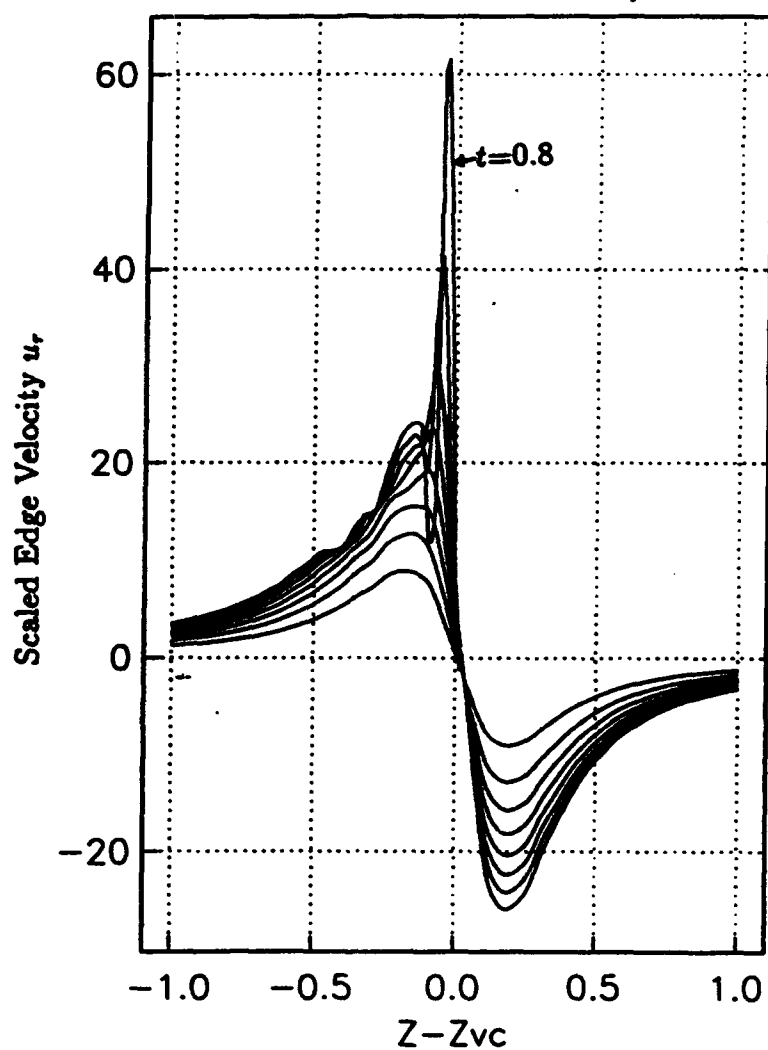


Figure 5.22: Temporal development of the radial velocity at the edge of the boundary-layer evaluated in the symmetry plane $\theta = \pi/2$. Here the results are for the stagnant medium case and they are plotted at several times $t=0.1, 0.2, 0.3, \dots, 0.8$.

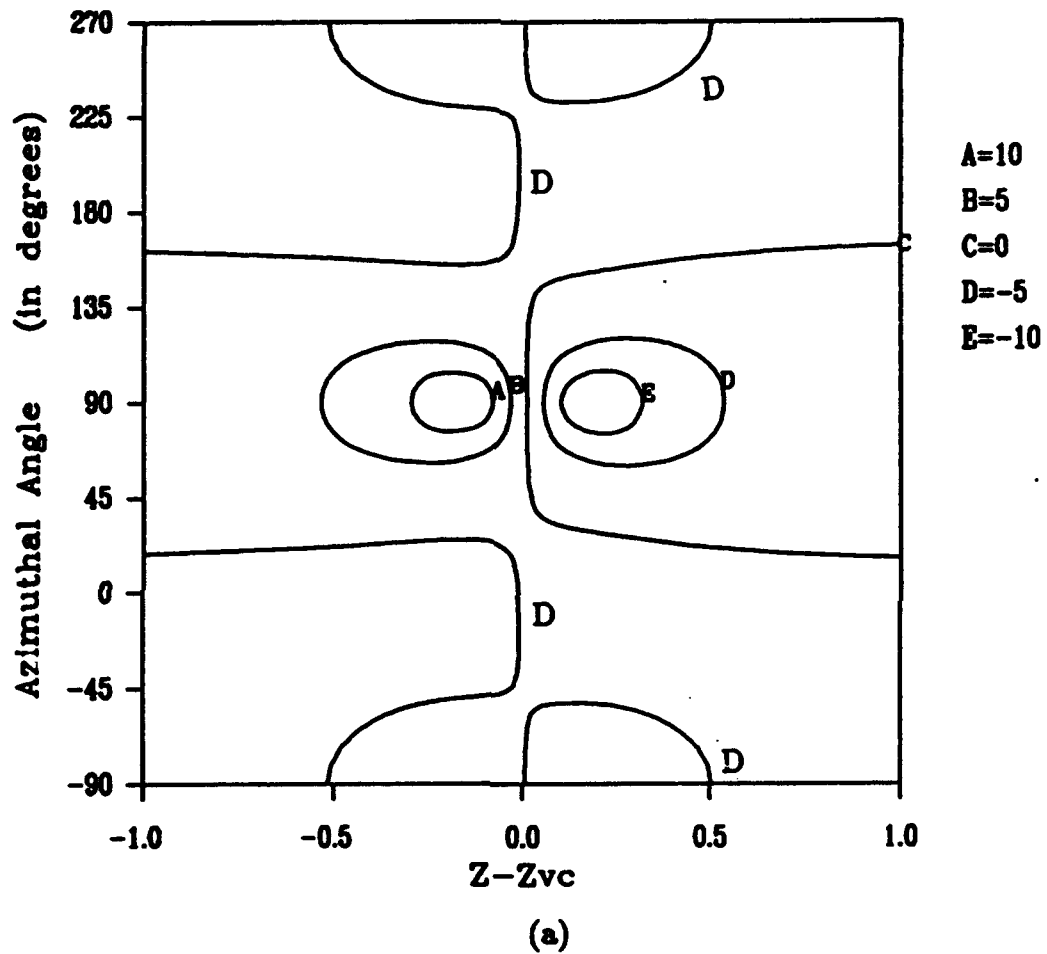


Figure 5.23: Lines of constant radial velocity u_r at the edge of the boundary-layer plotted around the cylinder for various times. (a) $t = 0.2$, (b) $t = 0.4$, (c) $t = 0.6$, (d) $t = 0.8$. Here the results are for the stagnant medium case where the flow is symmetric about $\theta = \pi/2$ (or 90°). The values of u_r are shown.

Figure 5.23 (continued)

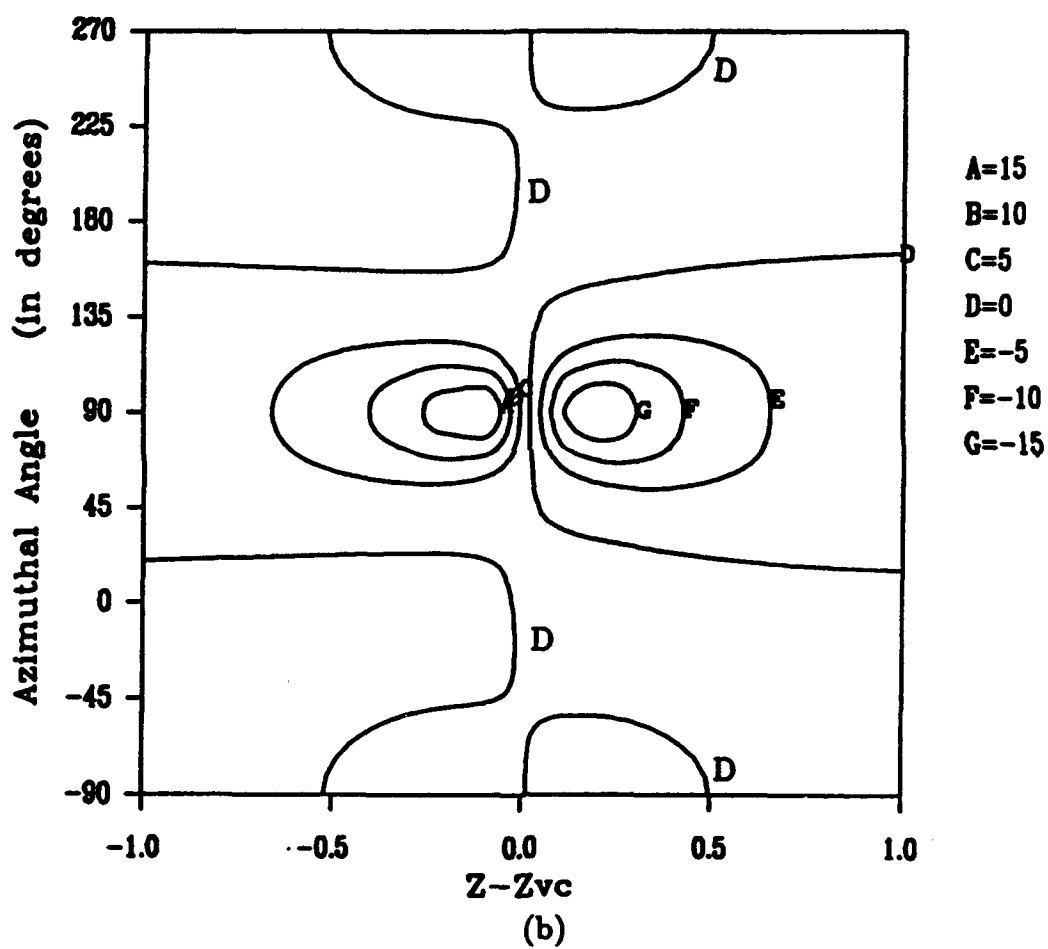


Figure 5.23 (continued)

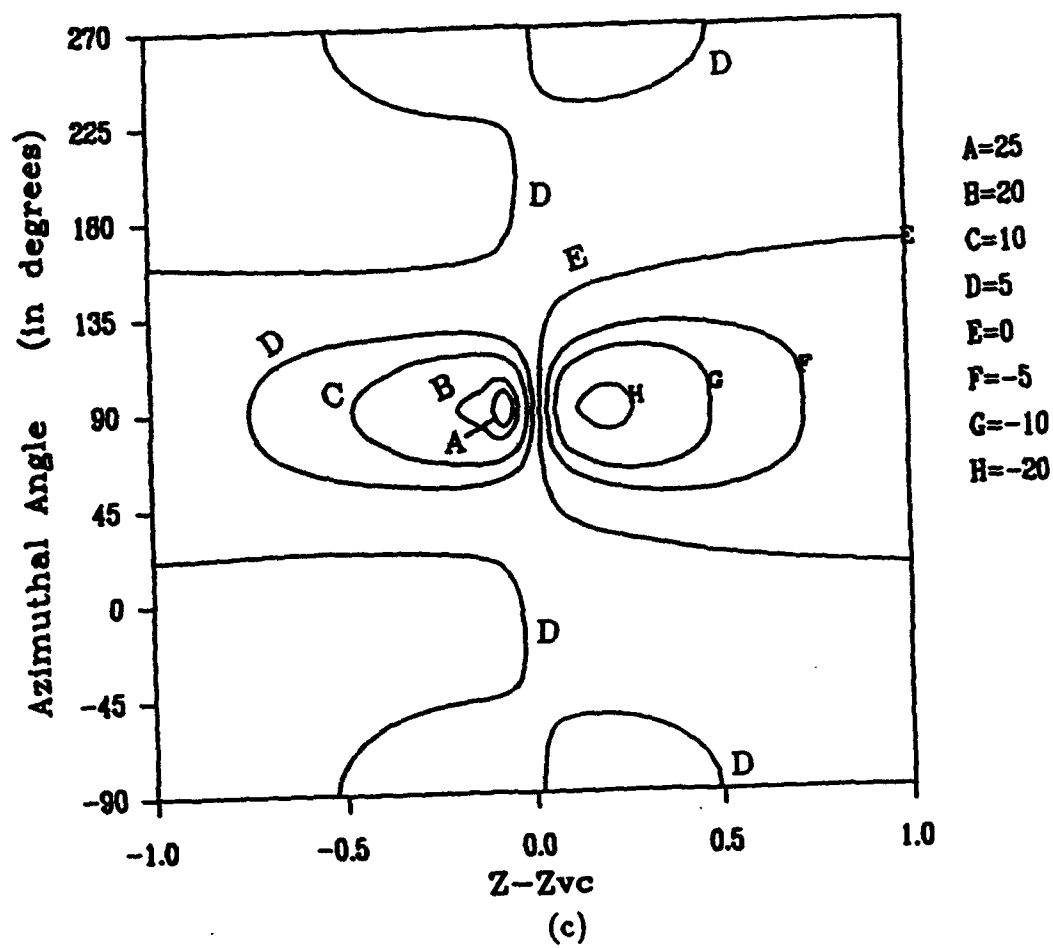
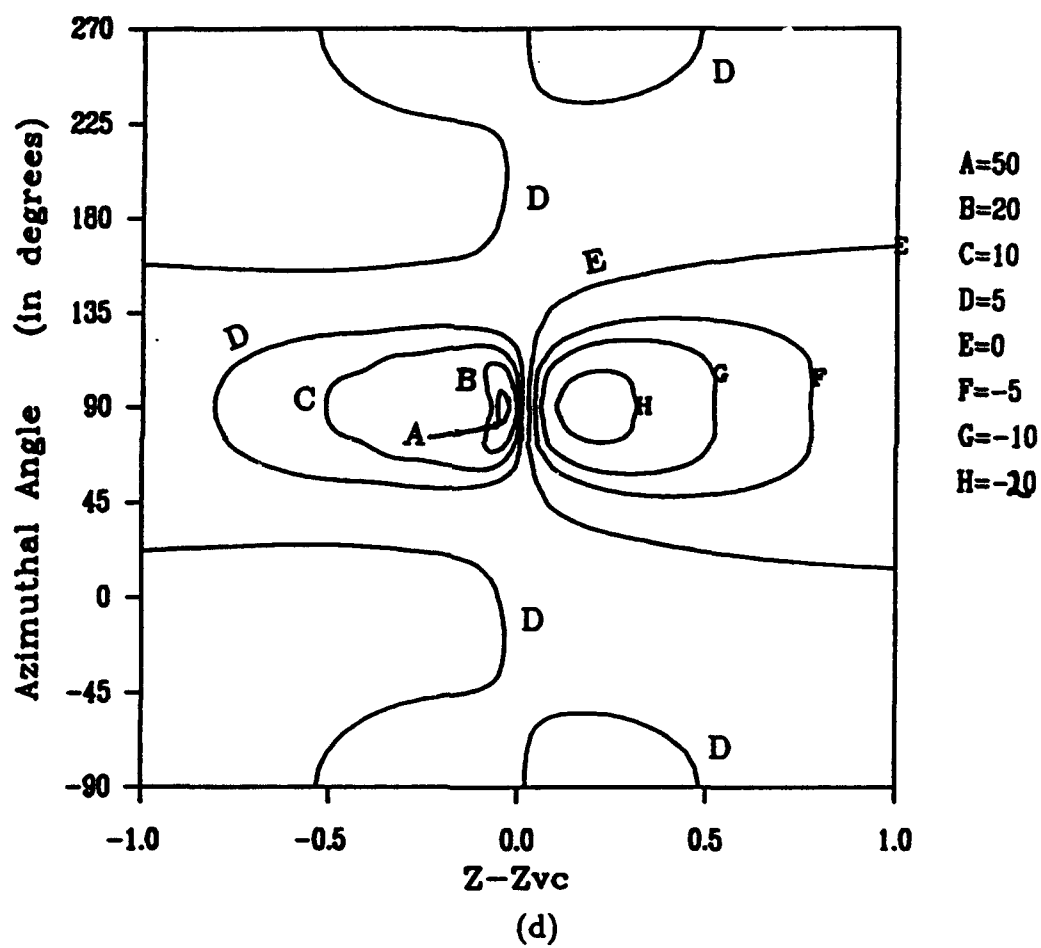


Figure 5.23 (continued)



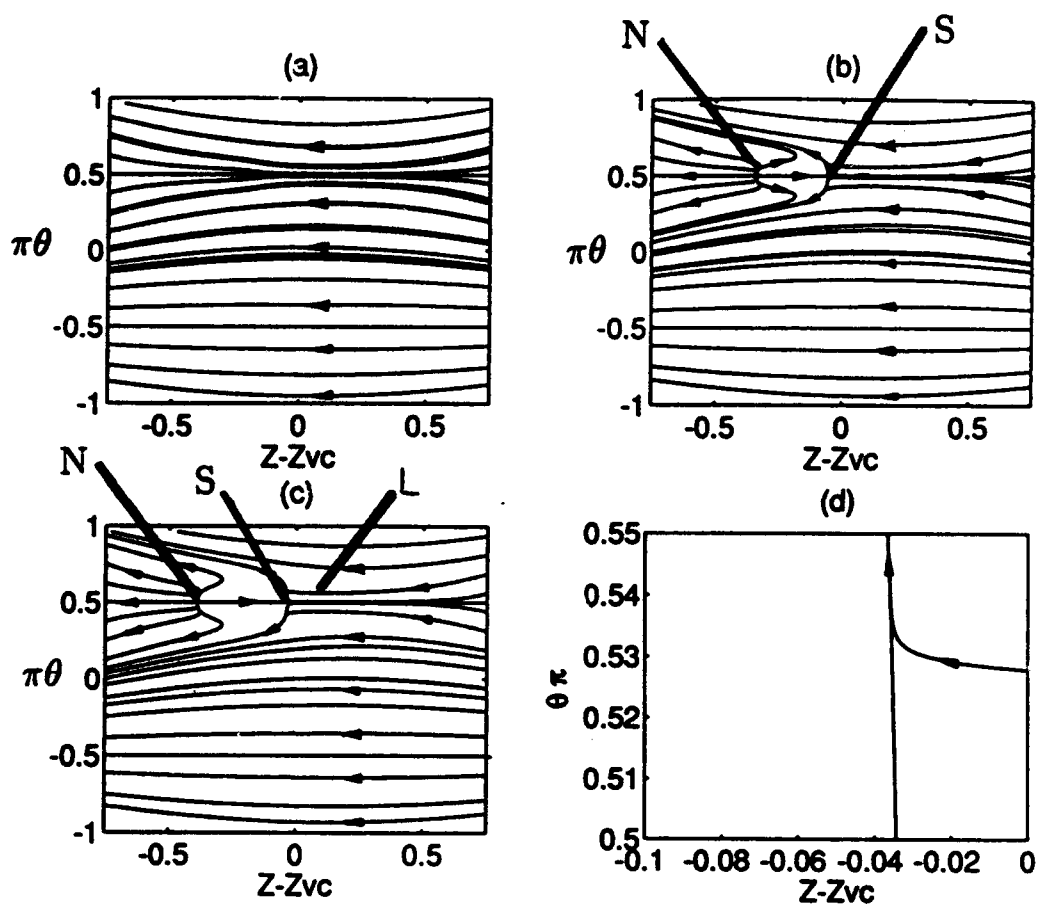


Figure 5.24: Surface streamlines for the stagnant medium at various times showing the development of a nodal point of attachment (N) and a saddle point of separation (S). (a) $t = 0.3$, (b) $t = 0.6$, (c) $t = 0.8$; (d) expanded view of the surface streamline labelled L.

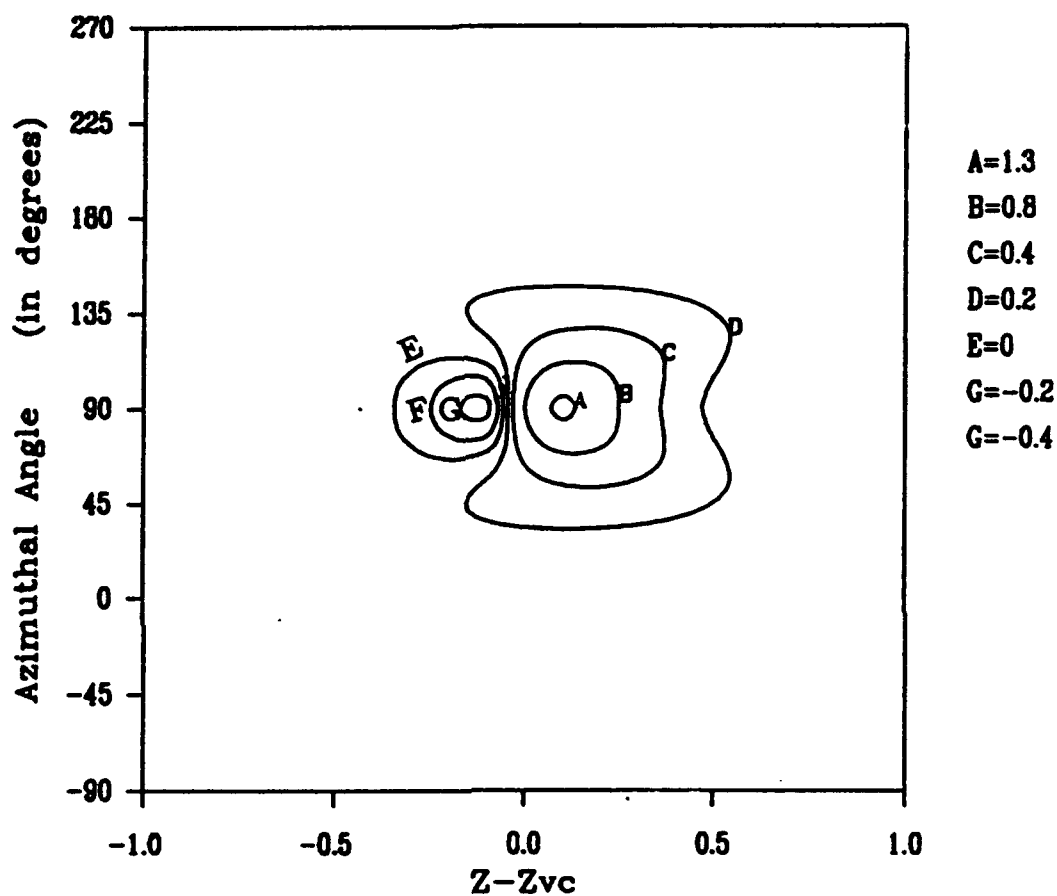


Figure 5.25: Lines of constant azimuthal vorticity ω_θ evaluated at the wall of the cylinder and plotted around the cylinder for the time $t=0.6$. Here the results are for the stagnant flow case where the flow is symmetric about $\theta=\pi/2$ (or 90°). The values of ω_θ are shown.

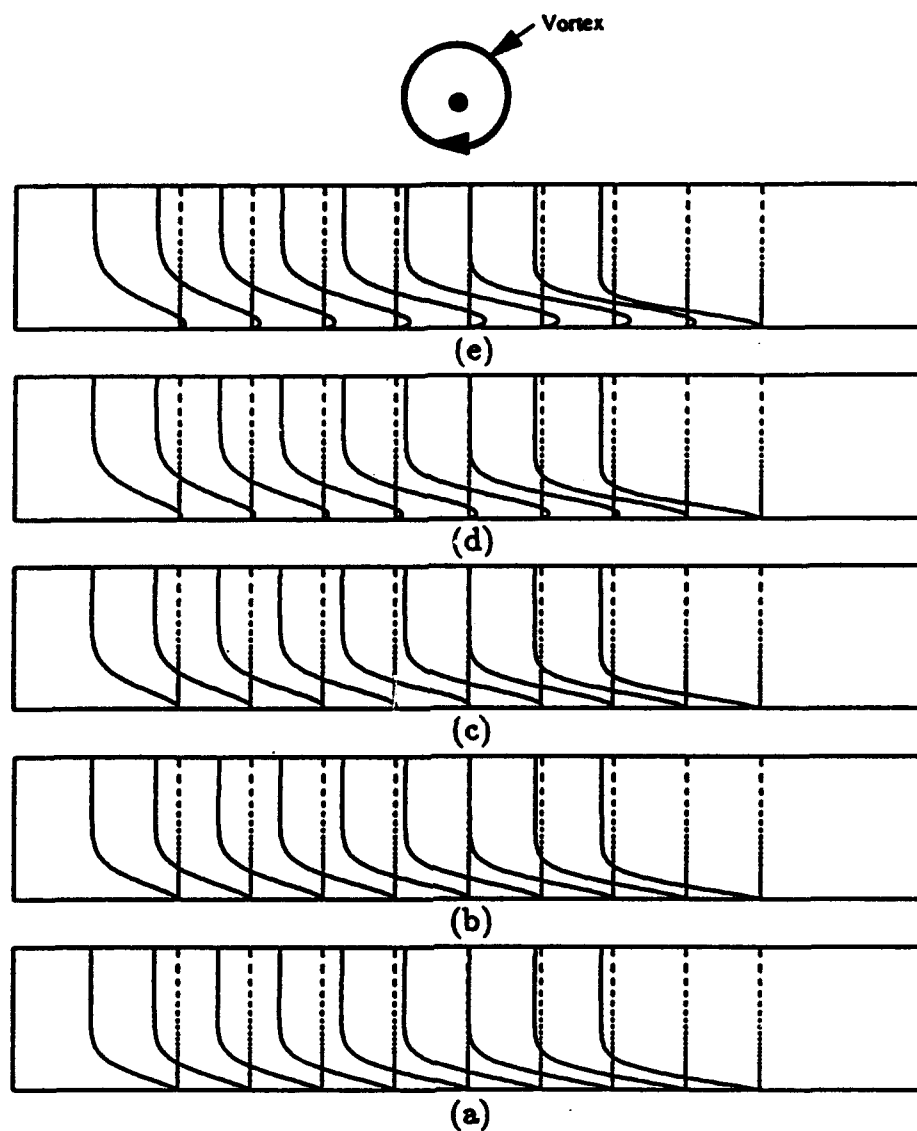


Figure 5.26: Temporal development of the velocity profiles of u_z plotted across the boundary-layer for the stagnant medium ($0 \leq \eta \leq 6$) at various times: (a) $t=0.2$, (b) $t=0.3$, (c) $t=0.4$, (d) $t=0.5$, (e) $t=0.6$. The profiles are shown at 9 equally spaced locations which are centered around $z = Z - Z_{Vc} = -0.25$ and separated by $\Delta z = 0.025$.

z interval between two profiles corresponds to the grid size $\Delta z = 0.025$. The vertical lines which are shown by the discontinuous lines correspond to the locations where the axial velocity is zero at each axial station. At the wall all axial velocity profiles intersect with these vertical lines. Above the wall, if the profiles are shown to the left of these vertical lines then the axial velocity is negative and it is positive otherwise. Here the velocity profiles are plotted across the boundary-layer for $0 \leq \eta \leq 6$. Note the development of a forward flow region near the wall as time increases indicating the presence of a secondary eddy; the velocity $u_z < 0$ throughout the balance of the boundary-layer since the edge axial velocity is negative as indicated on Figure 5.2.

On Figure 5.27 are results for the enstrophy defined by equation (5.38). From the enstrophy, a quantitative picture of the complex three-dimensional vorticity field can be obtained. On Figure 5.27(a) and 5.27(b) are contours of enstrophy which are shown at the surface of the cylinder $\eta = 0$ and at $\eta = .286$ respectively. Note that the largest value of the enstrophy occurs in the center of the oval-shaped region which is located at about $z = Z - Z_{V_c} = .1$ just ahead of the head of the main vortex. Additional calculations of the axial vorticity values on the wall reveal that this component is much smaller than the azimuthal component and so the enstrophy on the wall is dominated by the azimuthal component of vorticity. Note, however that the magnitude of the vorticity rapidly decreases away from $\theta = \pi/2$ and away from the immediate axial location of the main vortex. The enstrophy distribution at $\eta = .286$ exhibits somewhat smaller values when compared with the distribution at $\eta = 0$; however the maximum value at this level occurs in the same vicinity as on Figure 5.27(a).

On Figure 5.27(c) is the surface of constant enstrophy; the value of enstrophy is 0.27. Note from this three-dimensional surface the .27 value exists only very close to the wall except at a local region just underneath the main vortex denoted by the local bulge in the surface well above the wall. Although it is difficult to see, there are actually two separate surfaces on Figure 5.27(c). The presence of the secondary eddy is indicated by the bubble-like surface located below and to the left of the thumb-like structure on Figure 5.27(c). It should be noted that the enstrophy involves vorticities having opposite sign; however, since the enstrophy is always positive, regions where the vorticity may change sign and regions of small absolute values of the vorticity are indistinguishable. Note, in fact, the very small region of near zero vorticity in the middle of the region plotted on Figure 5.27(a) and the extended region small vorticity upstream of the scar on Figure 5.27(b). Referring to Figure 5.25, the small near-zero vorticity region on Figure 5.30(a) corresponds to a change in sign of azimuthal vorticity.

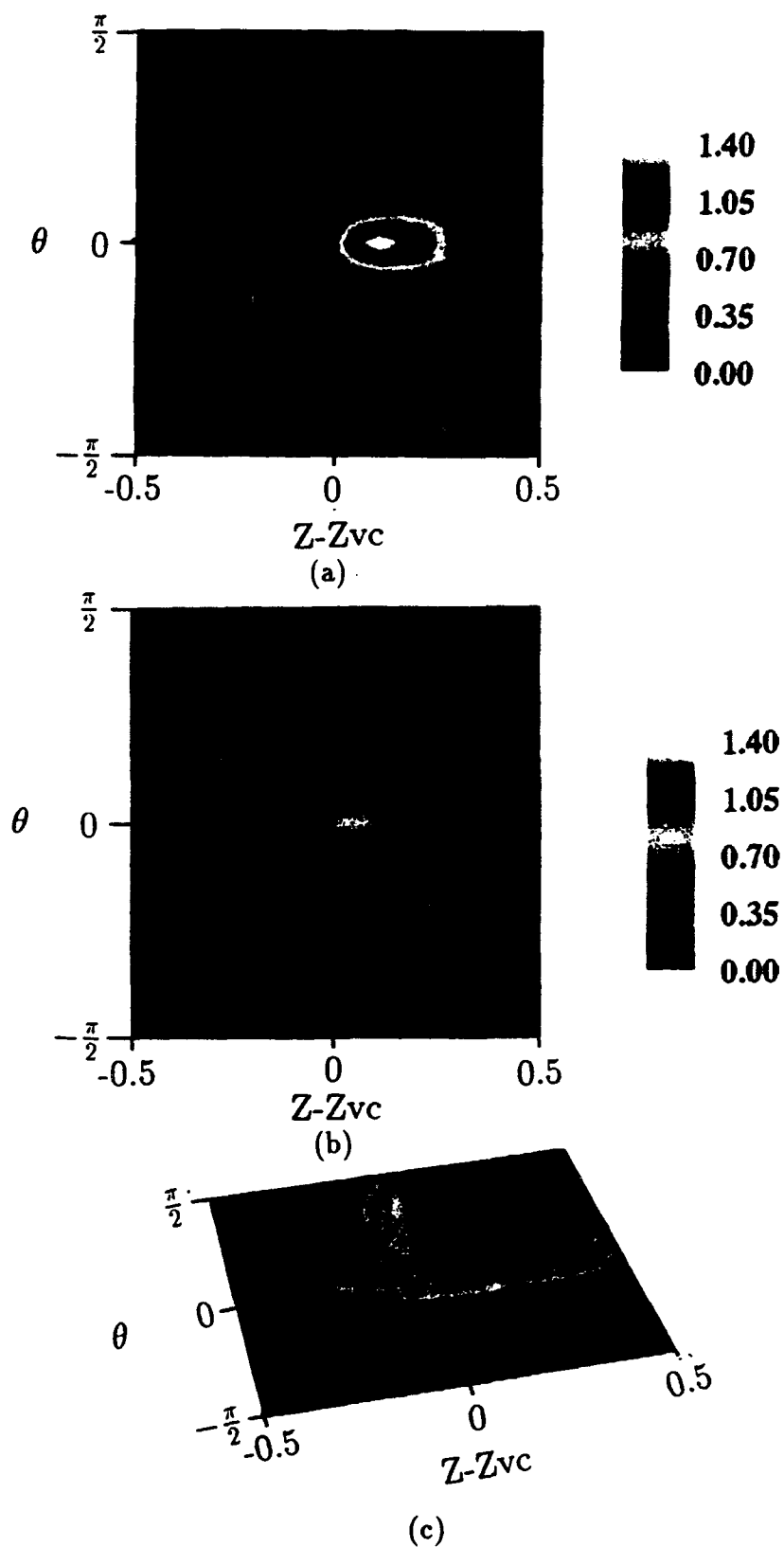


Figure 5.27: Contours of constant enstrophy which are shown by: (a) $\eta=0$, (b) $\eta=.268$, (c) surface of the constant value equal to .27. Here the results are for the stagnant medium case and are plotted at $t=.7$.

Symmetric Mean Flow

The results to be presented here correspond to the symmetric vortex configuration depicted on Figure 5.8; here, the boundary-layer variables have been made dimensionless according to

$$\theta = \theta^*, \quad z = \frac{z^*}{a}, \quad y = \left(\frac{r^*}{a} - 1\right)Re^{1/2}, \quad t = \frac{W_\infty}{a}t^*,$$

$$u_r = \frac{u_r^*}{W_\infty}, \quad u_\theta = \frac{u_\theta^*}{W_\infty}, \quad u_z = \frac{u_z^*}{W_\infty}, \quad (5.68)$$

where a is the radius of the cylinder, W_∞ is the mean velocity in the z direction; the asterisk indicates dimensional variables and $Re = W_\infty a / \nu$ is the Reynolds number. The pressure p^* is non-dimensionalized on ρW_∞^2 where ρ is the density of the fluid. It should be noted that the results presented here correspond to the dimensionless circulation $\Gamma = \frac{\Gamma^*}{W_\infty a} = 4.2$. All the results to be presented here are for an (η, θ, z) grid corresponding to 61, 64, and 121 points, respectively with $\Delta t = .0025$. Grid and time step accuracy studies have been made and the present solutions are resolved to at least two figure accuracy at time $t = .3$ for these parameters.

On Figure 5.28 are the results for the streamline patterns at several different times corresponding to $t = .1, .2, .3$, and $.4$. Figures 5.28(a-d) are the results on the symmetry plane while Figures 5.28(e-h) a fully three-dimensional view. By time $t = 0.3$ the secondary eddy is developing rapidly and is characterized by a nodal point at the middle of the spiral with a saddle point adjacent to it (Figure 5.28(c)); fluid entering the spiral passes out azimuthally as shown on Figure 5.28(h) which is a three-dimensional view of the reversed flow region. Note however, that the extent of the eddy is not large in the azimuthal direction until $t = 0.4$. It should also be mentioned that all of the streamlines that begin off the symmetry plane originate at about $\eta = 1$ far above the wall. These streamline patterns are depicted in the frame of reference traveling with the speed of the vortex head in the z -direction. The flow patterns depicted on Figures 5.28(a-d) satisfy the topological requirement given by Tobak and Peake (1982; rule 4) that the number of nodal points off the boundary plus one-half the number of nodal points on the boundary minus the same quantity for the saddle points must be zero. On Figures 5.28(a,b) there is one node and two saddles on the wall. On Figures 5.28(c,d) there are two nodes off the boundary, no nodes on the boundary; there is one saddle off the boundary and two saddles on the boundary. Here the position of the main vortex has been considered a nodal point which is consistent with the definition of Tobak and Peake (1982).

As with the stagnant medium case, there are two $(r - z)$ planes of symmetry in which $u_\theta = 0$ which are located on the top and bottom of the cylinder. Results

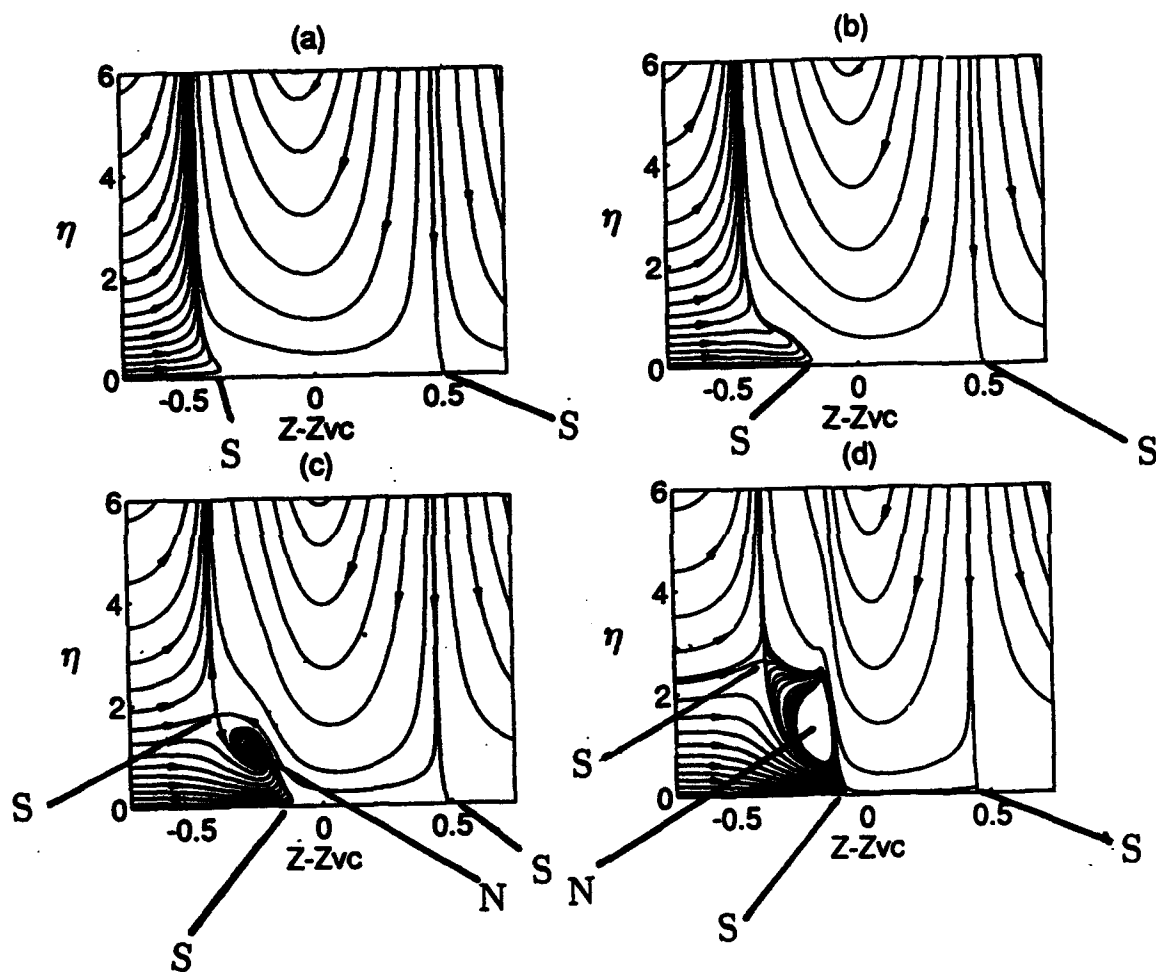
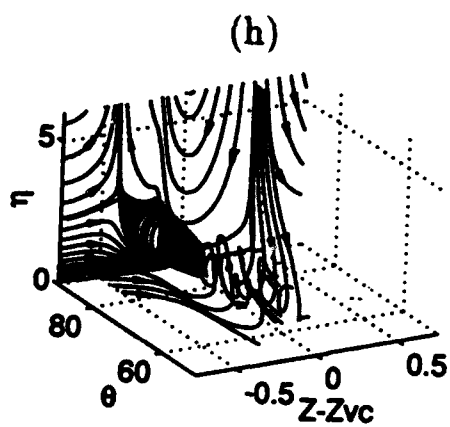
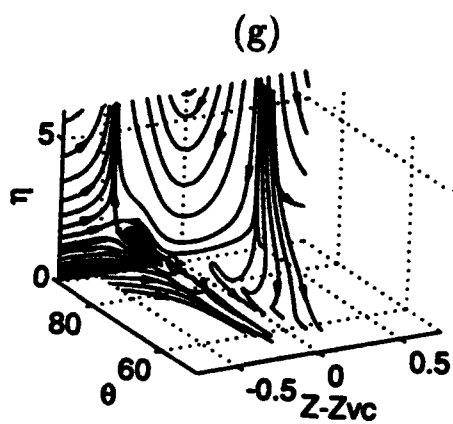
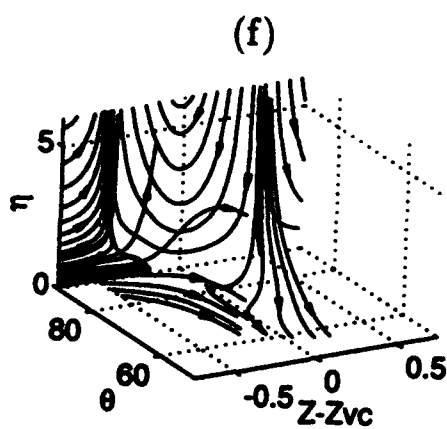
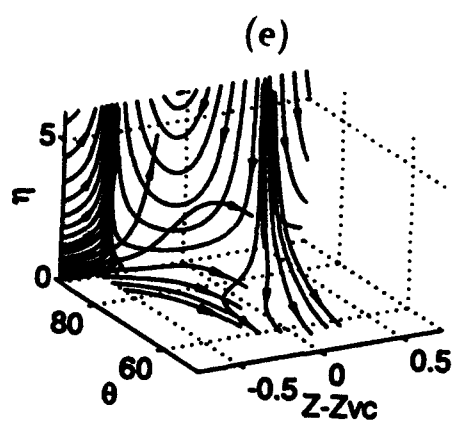


Figure 5.28: Streamline patterns for the symmetric mean flow plotted at various times. On the symmetry plane at (a) $t=0.1$, (b) $t=0.2$, (c) $t=0.3$, (d) $t=0.4$; and a fully three-dimensional view at (e) $t=0.1$, (f) $t=0.2$, (g) $t=0.3$, (h) $t=0.4$.

Figure 5.28(continued)



for the streamline patterns in the bottom plane ($\theta = -\pi/2$; not shown) indicate that the flow patterns are dominated by the two-dimensional base flow.

On Figure 5.29 are vector plots of the velocity field deep within the boundary layer on planes $z = Z - Z_{Vc} = \text{constant}$ at time $t = 0.4$. The upper edge of the field is at $\eta = 2$. Note that the azimuthal velocity is toward the symmetry plane very near the wall and away from the symmetry plane farther above and that the flow to the symmetry plane occurs only locally in $z = Z - Z_{Vc}$. These plots should be compared with the streamline plots on the previous figure.

On Figure 5.30 are lines of constant azimuthal vorticity ω_θ plotted at several azimuthal locations around the cylinder. On Figure 5.30(a) are the constant azimuthal vorticity lines for time $t = .3$ at $\theta = \pi/2$ and note the concentration of azimuthal vorticity directly under the main vortex. The dark region corresponds to absolute values of the azimuthal vorticity above 1.2 which is three times larger than the corresponding value for the stagnant medium. The constant azimuthal vorticity lines for each of the values of θ on Figure 5.30 are plotted in increments of .1 from -8 to 8. Figures 5.30(a)-5.30(f) correspond respectively to distributions of the azimuthal vorticity across the boundary-layer in the planes, $\theta = \pi/2, 3\pi/8, \pi/4, 0, -\pi/4$ and $-\pi/2$. On Figure 5.30(a-c) the maximum positive azimuthal vorticity is reduced from 7.90 to .432 while the negative azimuthal vorticity has dropped from -2.75 to -.615. For Figures 5.30(d)-5.30(f) the values of the azimuthal vorticity deep within the boundary-layer are all negative and the maximum negative -0.894 at $\theta = \pi/4$. Note that the maximum negative value of azimuthal vorticity at $\theta = -\pi/2$ is -.732 which is close to that at $\theta = 0$; this is indicative of the fact that in the bottom half of the cylinder the flow is dominated by the two-dimensional mean flow effect and the effects of the main vortex are small.

The time evolution of both the azimuthal vorticity and zero azimuthal vorticity lines in the symmetry plane $\theta = \pi/2$ are shown respectively on Figures 5.31 and 5.32. On Figure 5.31 the lines of constant azimuthal vorticity at $\theta = \pi/2$ are plotted at various times $t = 0.1, .3$ and $.4$. Note the focusing of azimuthal vorticity lines toward the location $z=0$ as time evolves. By excluding the negative values, the zero azimuthal vorticity line can be easily located and on Figure 5.32 the zero azimuthal vorticity lines are labeled. Unlike the stagnant medium case where the zero azimuthal vorticity line is a closed line that touches the wall at two locations and is not present at early times, in the mean flow case the zero azimuthal vorticity lines do exist in the boundary-layer starting from the initial condition of the flow.

As depicted in Figure 5.32 the zero azimuthal vorticity line in the region just downstream of the separation bubble tends, near the wall, to be very close to the zero axial velocity line shown in Figure 5.33 and marked by an arrow.

On Figure 5.34 is the temporal development of the radial velocity at $\theta = \pi/2$ for times $t = .05$ to $.4$ in increments of $.05$ plotted as a function of distance along

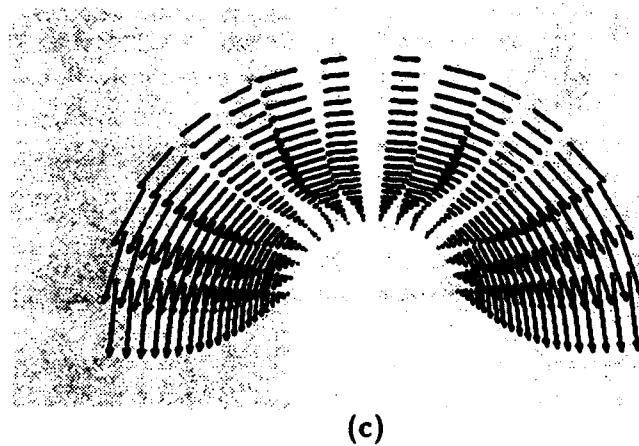
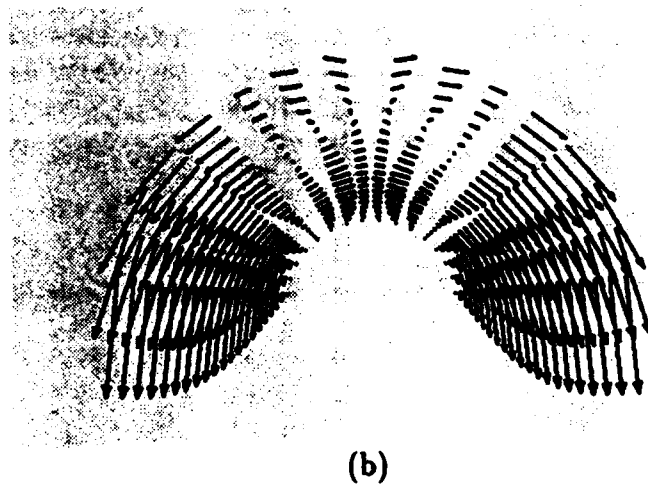
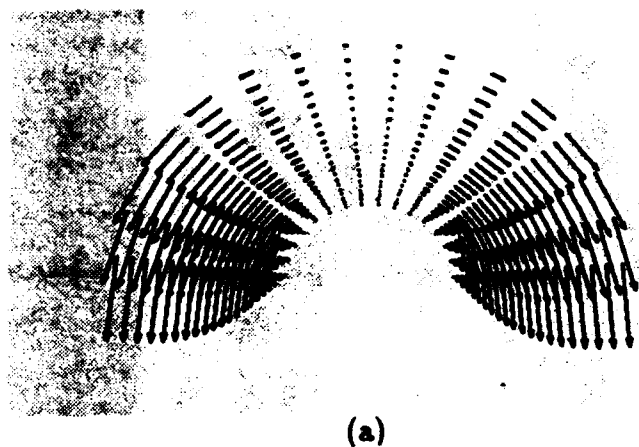


Figure 5.29: Vector plots of the velocity field at various locations in $Z - Z_{Vc}$ at $t = 0.4$ across the boundary layer. The upper edge on the Figure is at $\eta = 2$; the edge of the boundary layer is at $\eta = 6$. (a) $Z - Z_{Vc} = -0.3$, $Z - Z_{Vc} = -0.125$, (c) $Z - Z_{Vc} = 0$.

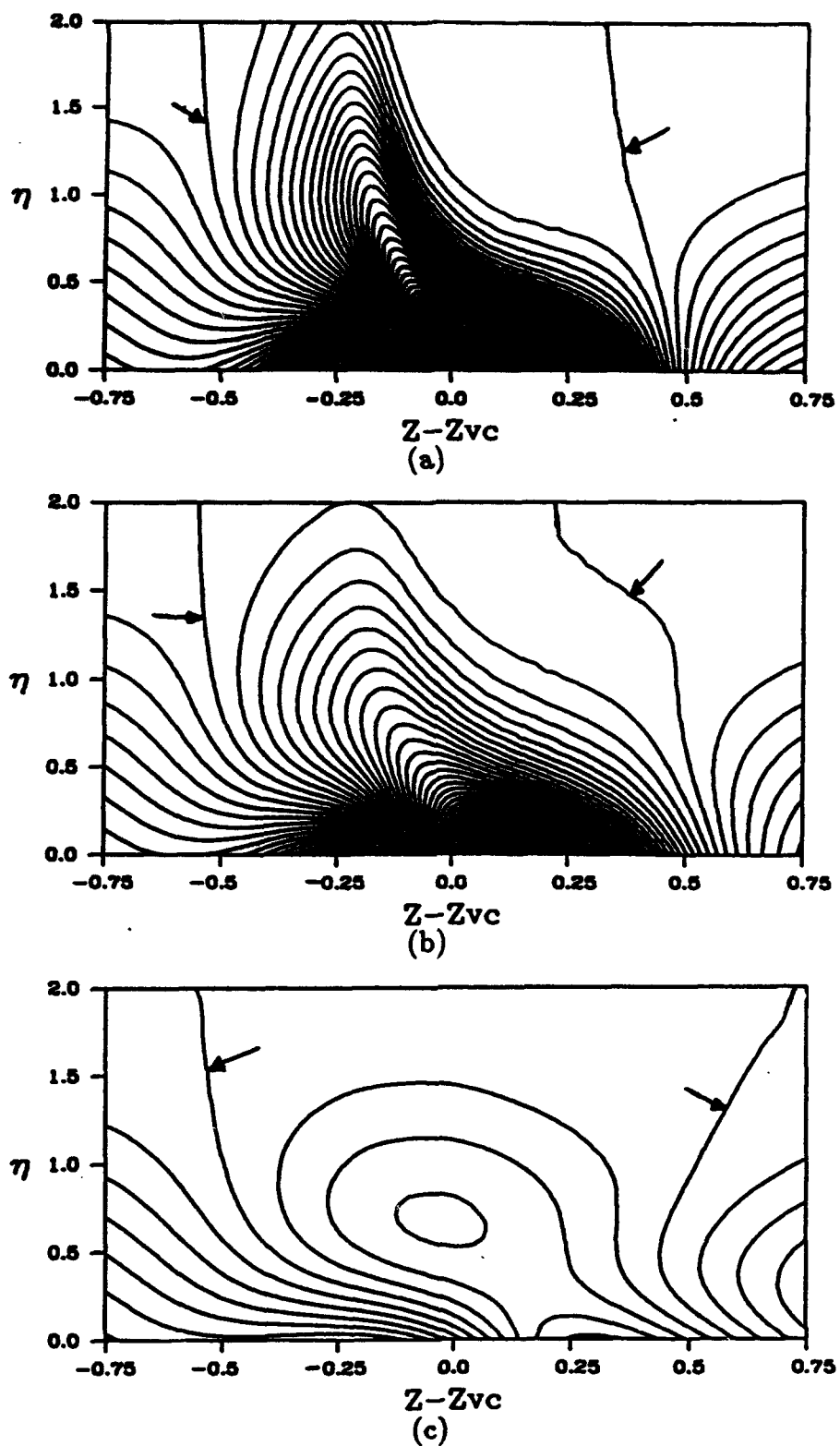
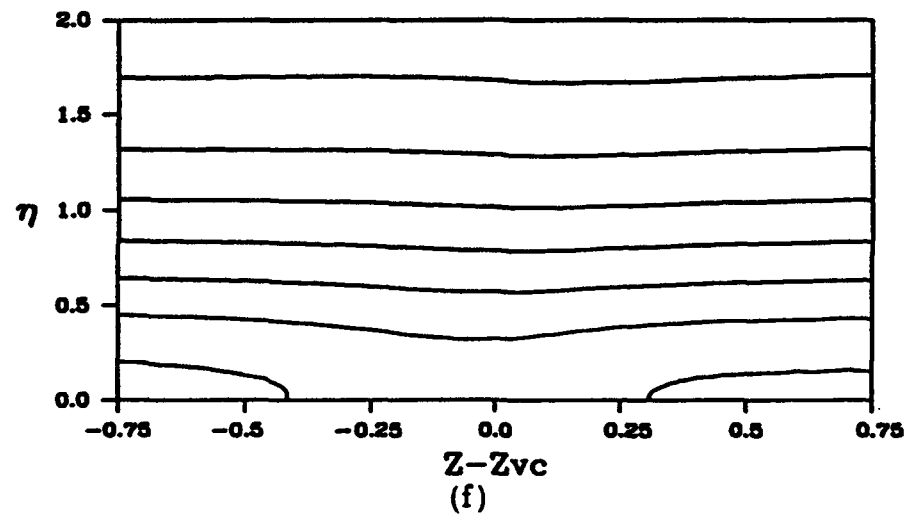
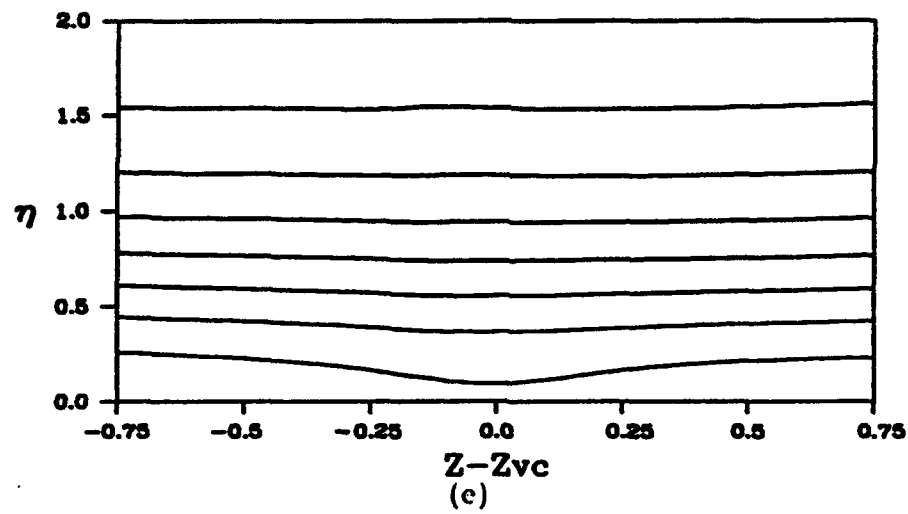
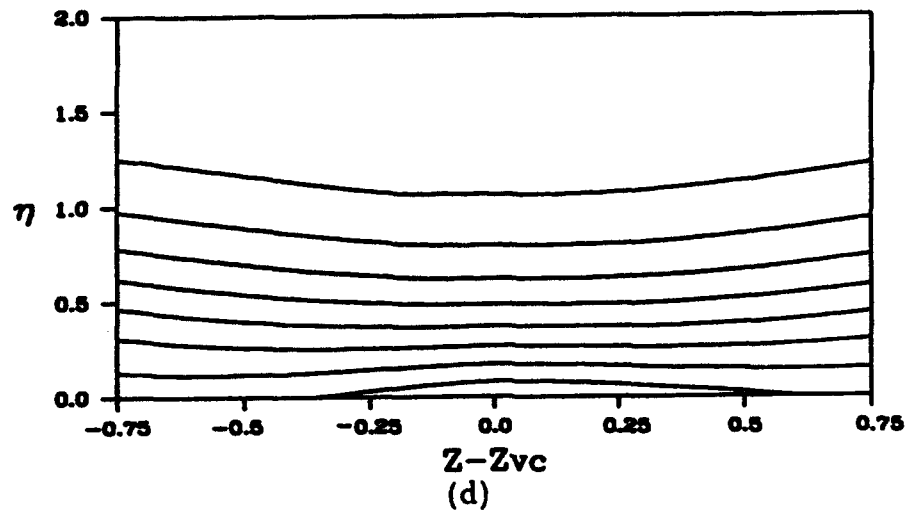


Figure 5.30: Lines of constant azimuthal vorticity ω_θ at $t=0.3$ for several azimuthal locations around the cylinder: (a) $\theta=\pi/2$, (b) $\theta=3\pi/8$, (c) $\theta=\pi/4$, (d) $\theta=0$, (e) $\theta=-\pi/4$, (f) $\theta=-\pi/2$. The zero lines are marked by an arrow.

Figure 5.30(continued)



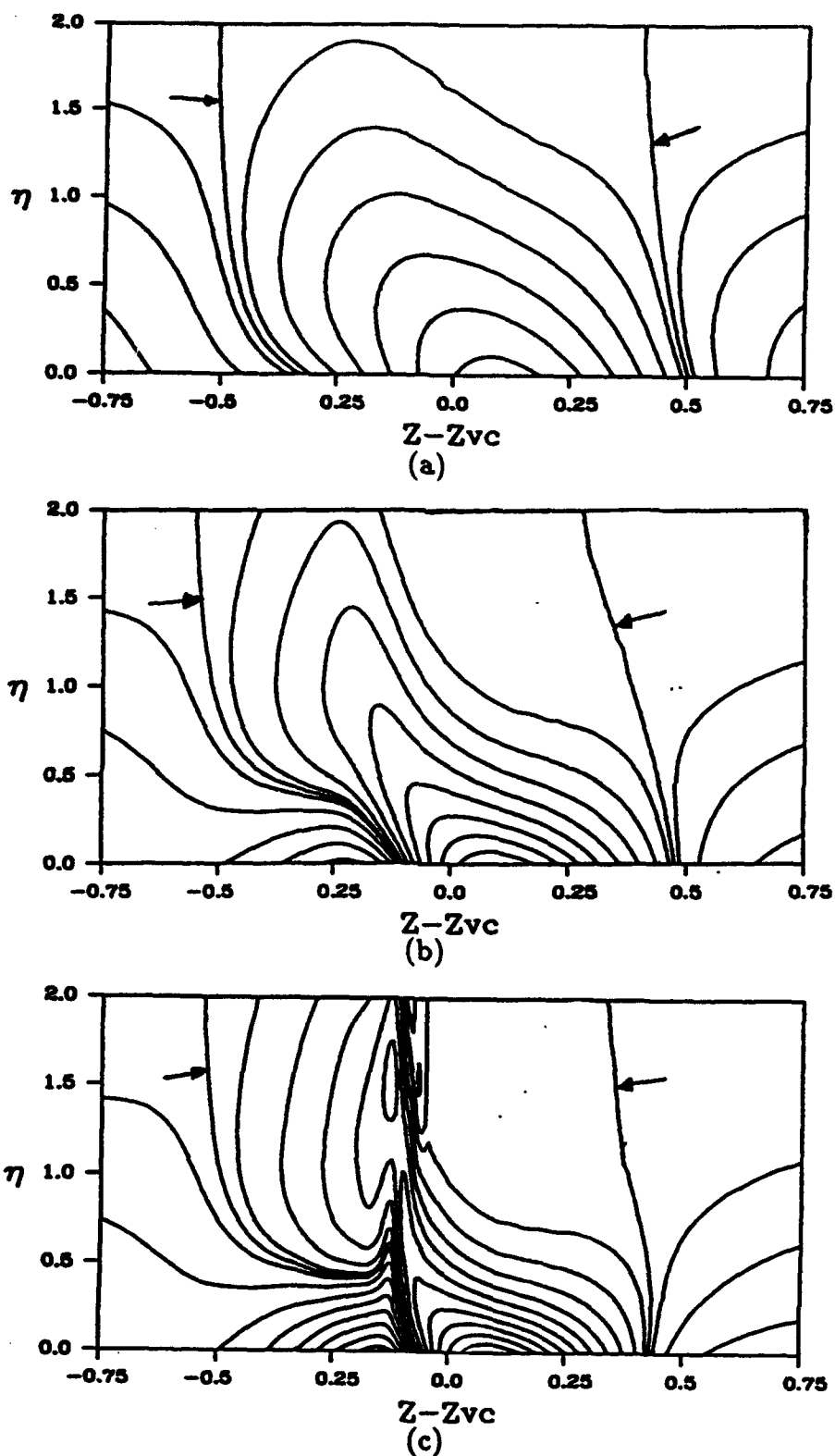


Figure 5.31: Temporal development of the azimuthal vorticity ω_θ in the symmetry plane $\theta = \pi/2$. Here the results are for the symmetric mean flow case and they are shown as lines of constant azimuthal vorticity which are plotted at various times: (a) $t=0.1$, (b) $t=0.3$, (c) $t=0.4$. The zero lines are marked by an arrow.

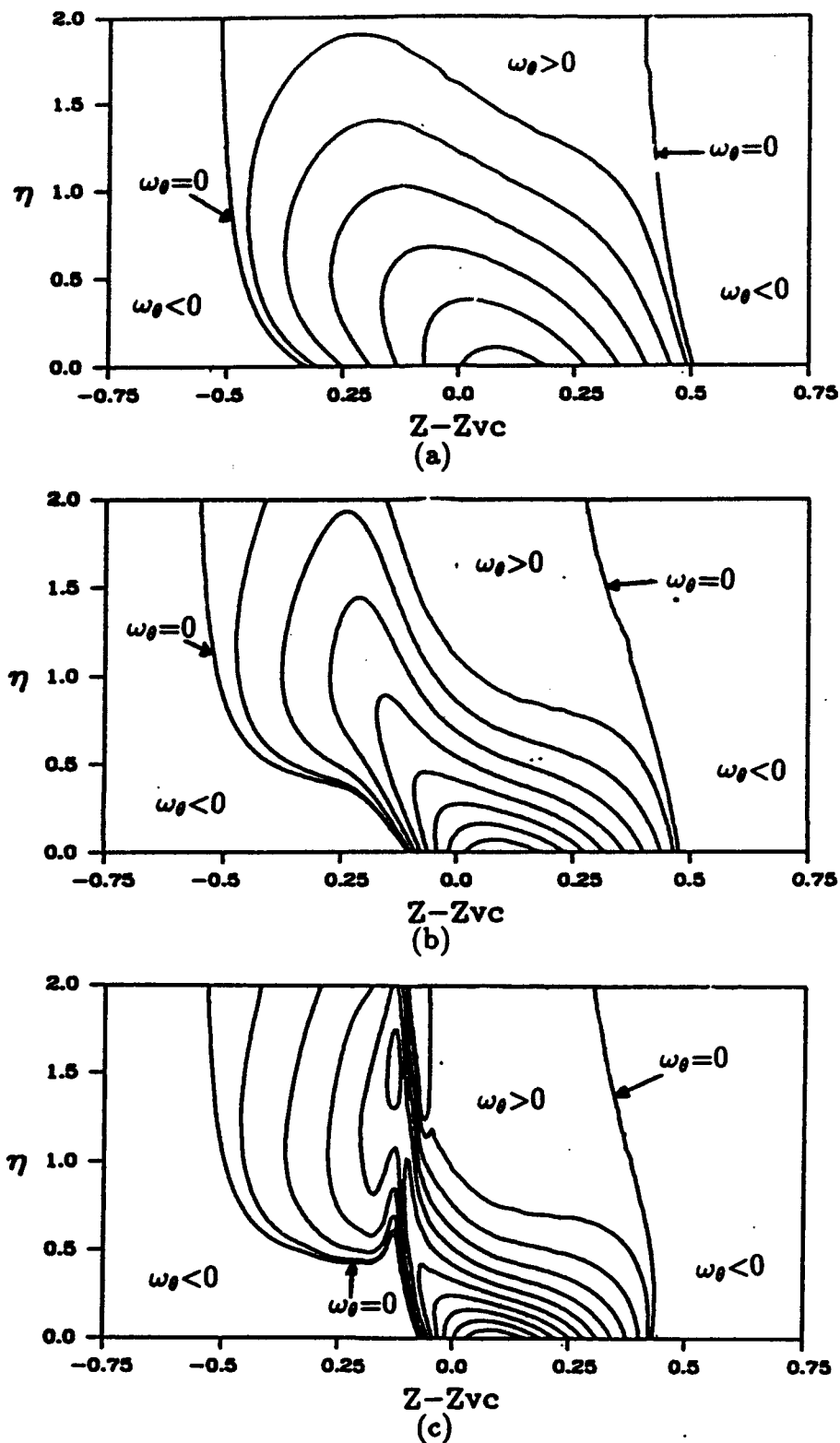


Figure 5.32: Evolution of the zero azimuthal vorticity line in the symmetry plane $\theta = \pi/2$. Here the results correspond exactly to the those shown in previous figure except for the fact that negative vorticity lines are not plotted. The zero lines are marked by an arrow and are shown for times (a) $t=0.1$, (b) $t=0.3$, (c) $t=0.4$.

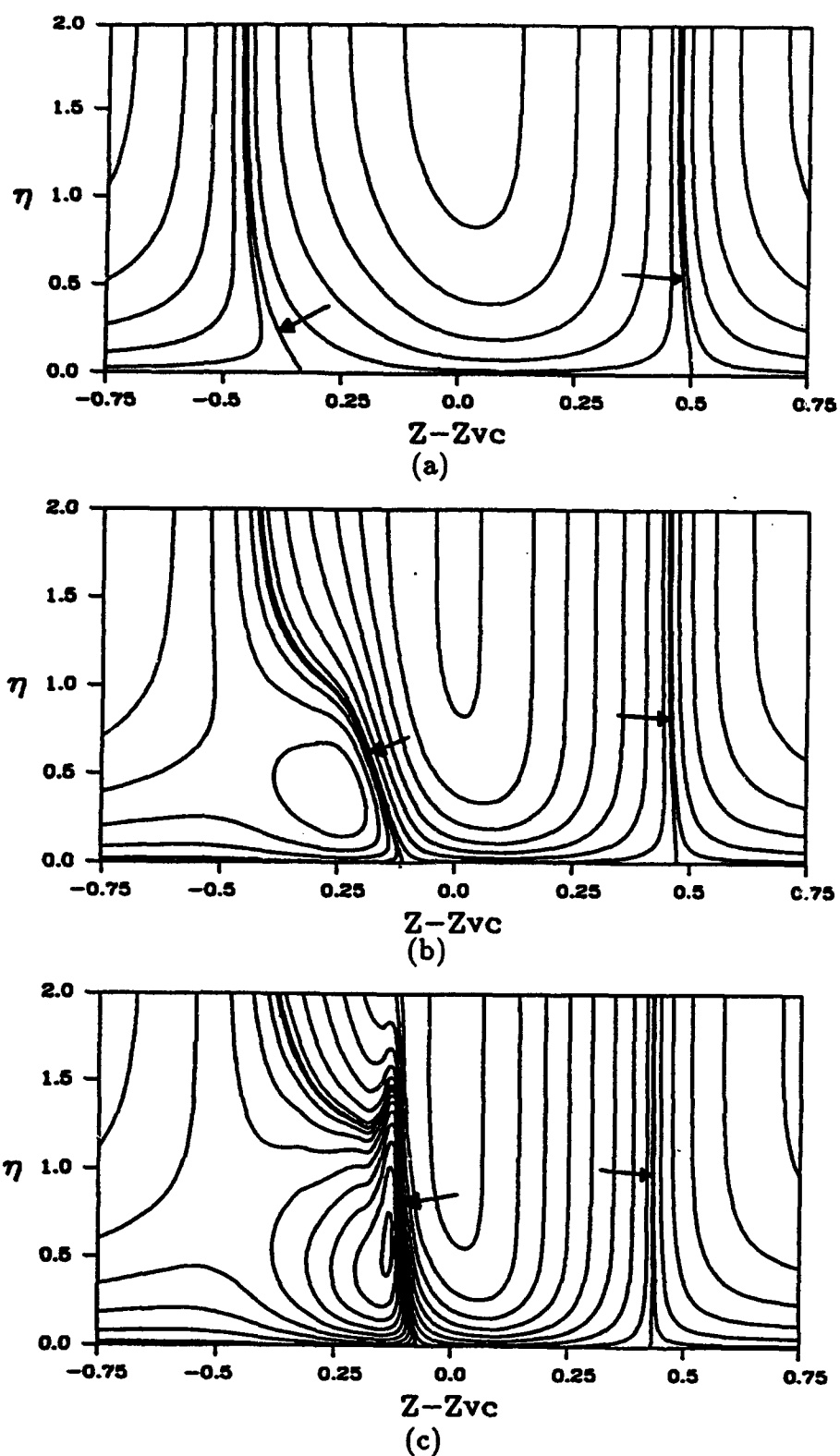


Figure 5.33: Lines of constant velocity u_z plotted across the boundary-layer in the symmetry plane $\theta = \pi/2$. Here the results are for the symmetric mean flow case and are shown at various times: (a) $t=0.1$, (b) $t=0.3$, (c) $t=0.4$. The zero velocity line is marked by an arrow.

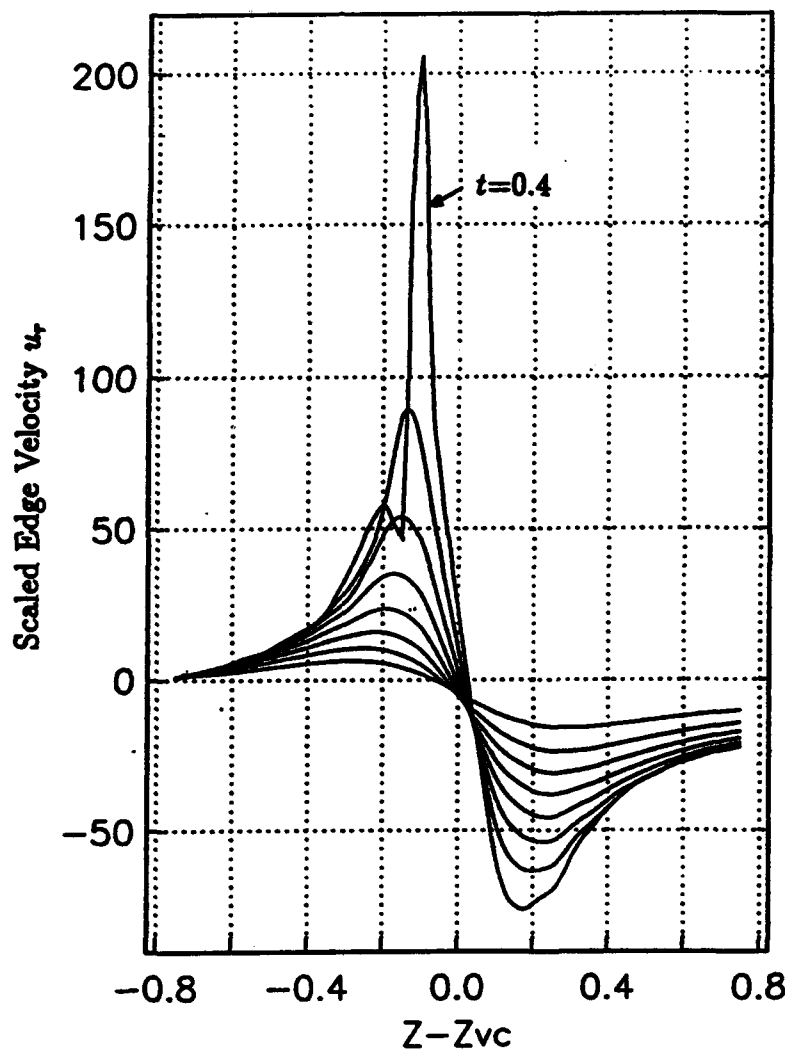


Figure 5.34: Temporal development of the radial velocity at the edge of the boundary-layer evaluated in the symmetry plane $\theta = \pi/2$. Here the results are for the symmetric mean flow case and they are plotted at several times $t=0.05, 0.1, 0.15, \dots, 0.4$.

the cylinder centerline. Note the rapid growth of the velocity as time increases; the result at time $t = .4$ should be viewed as qualitative near $z=0$. As noted previously, the results depicted on this figure provide the temporal limits on the application of boundary-layer theory to problems involving finite Reynolds numbers since $Re^{-1/2}u_r \ll 1$ for boundary-layer theory to apply.

Another view of the development of the edge velocity distribution is presented on Figure 5.35 where lines of constant radial velocity at the edge of the boundary-layer are plotted for times $t = .1$, $t = .2$, $t = .3$ and $t = .4$. Note that at points significantly removed from $\theta = \pi/2$, the edge velocity is varying somewhat more slowly than it is on the symmetry plane. The time evolution of the flow clearly shows rapid growth of the local magnitude of the edge velocity in a region extending off the symmetry plane and in which the location of very high radial velocity is continually contracting in the z -direction just upstream of $Z - Z_{Vc} = 0$. This behavior suggests the physical picture of a wall of a three-dimensional non-circular jet of fluid which will be subsequently squeezed into the inviscid flow at a later time. This situation is similar to the two dimensional case and as was noted in the previous section it may be expected that a local eruption of boundary-layer fluid into the main stream will take place in the form of what van Dommelen and Cowley (1990) refer to as a spreading ridge and a tongue of fluid.

Surface streamlines are shown on Figure 5.36; as with the stagnant medium case there is a nodal point of separation at a position roughly coinciding with the front end of the eddy as shown on Figure 5.28 at $t = 0.4$. There is also a saddle point of attachment corresponding to the streamline which hits the wall just upstream of $z = Z - Z_{Vc} = 0.5$ on Figure 5.28(a-d). This pattern satisfies rule two of Tobak and Peake(1982) which indicates that the number of nodes and the number of saddles on the surface are the same. It is important to reiterate that the three-dimensional streamlines which are depicted on Figures 5.28(e-h) and which begin at locations off the symmetry plane are far above the surface streamlines depicted on Figure 5.36.

The vorticity components ω_θ and ω_z , evaluated at the wall at $t=0.4$ are shown on Figures 5.37 and 5.38. Note that the zero azimuthal vorticity line indicated by the letter "E" on Figure 5.37 is a closed line which results for earlier times(not shown) indicate that this line is present for all times and only changes in shape as time increases. In particular, the major changes occur near the symmetry plane $\pi/2$ where the effects of the secondary flow become dominant especially at the latter times. On the other hand, the lines of constant axial (streamwise) vorticity component ω_z , depicted on Figure 5.38 show the emergence of the zero line off the symmetry plane which is not present at $t=0.1$ (not shown) and is denoted by the label "D". There is also a line of $\omega_z=0$ which spans the whole cylinder in the symmetry plane at $\theta = \pi/2$. This line exists at all times and is a result of the zero azimuthal velocity in the symmetry plane. Note that the region enclosed by the

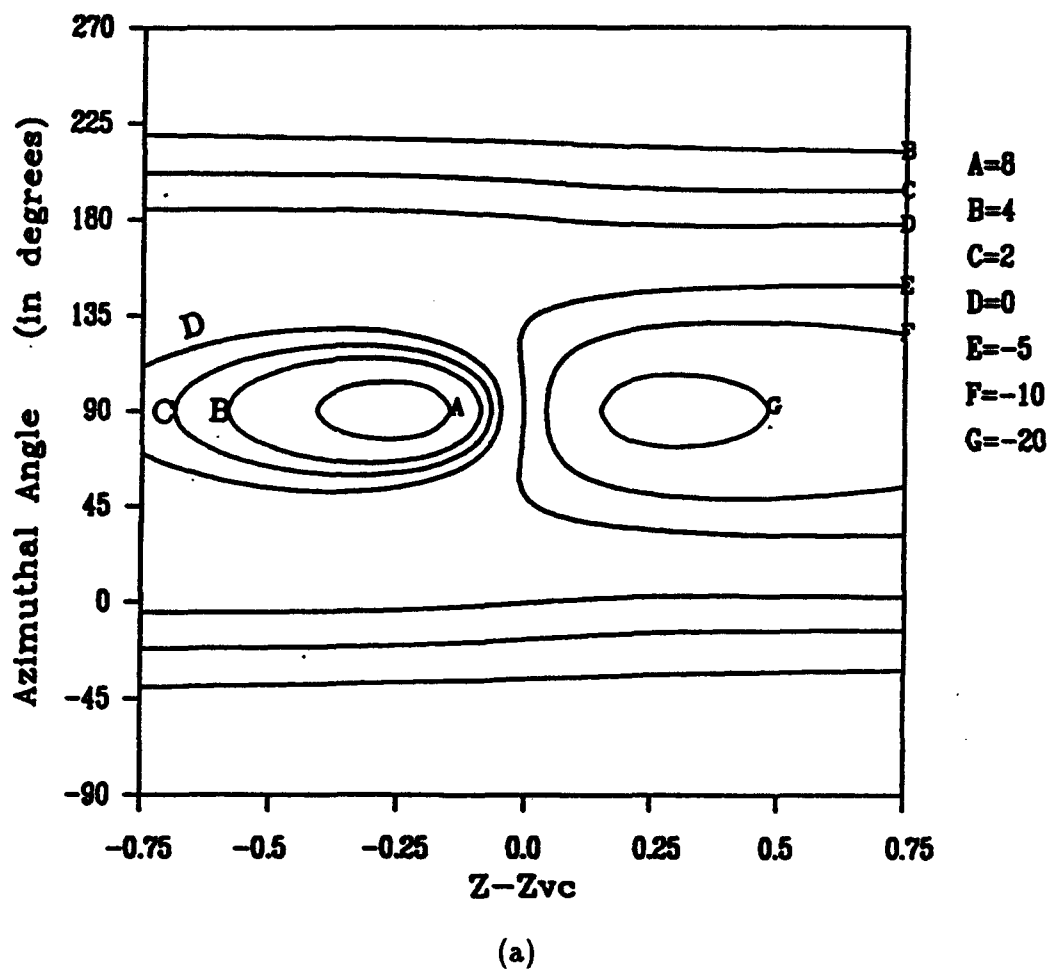


Figure 5.35: Lines of constant radial velocity u_r at the edge of the boundary-layer for the symmetric mean flow case plotted around the cylinder for various times. (a) $t = 0.1$, (b) $t = 0.2$, (c) $t = 0.3$, (d) $t = 0.4$. The values of u_r are shown.

Figure 5.35(continued)

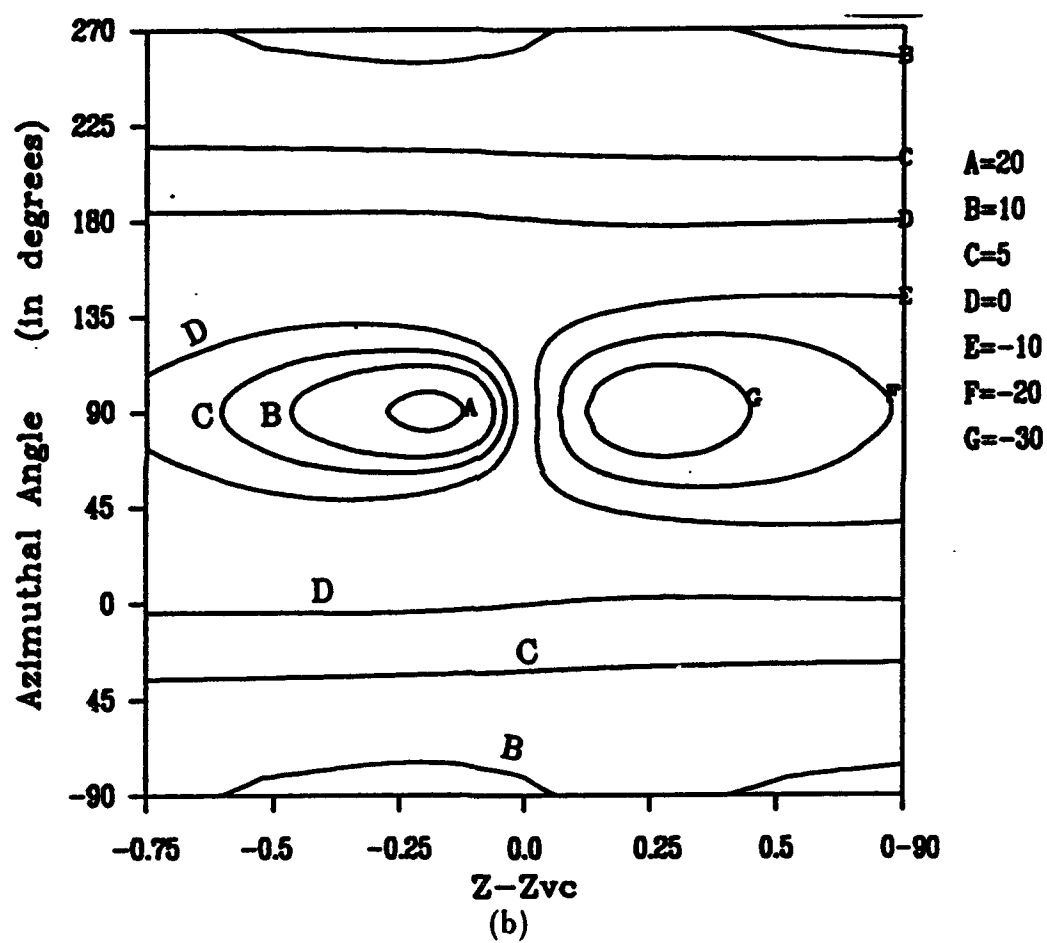


Figure 5.35 (continued)

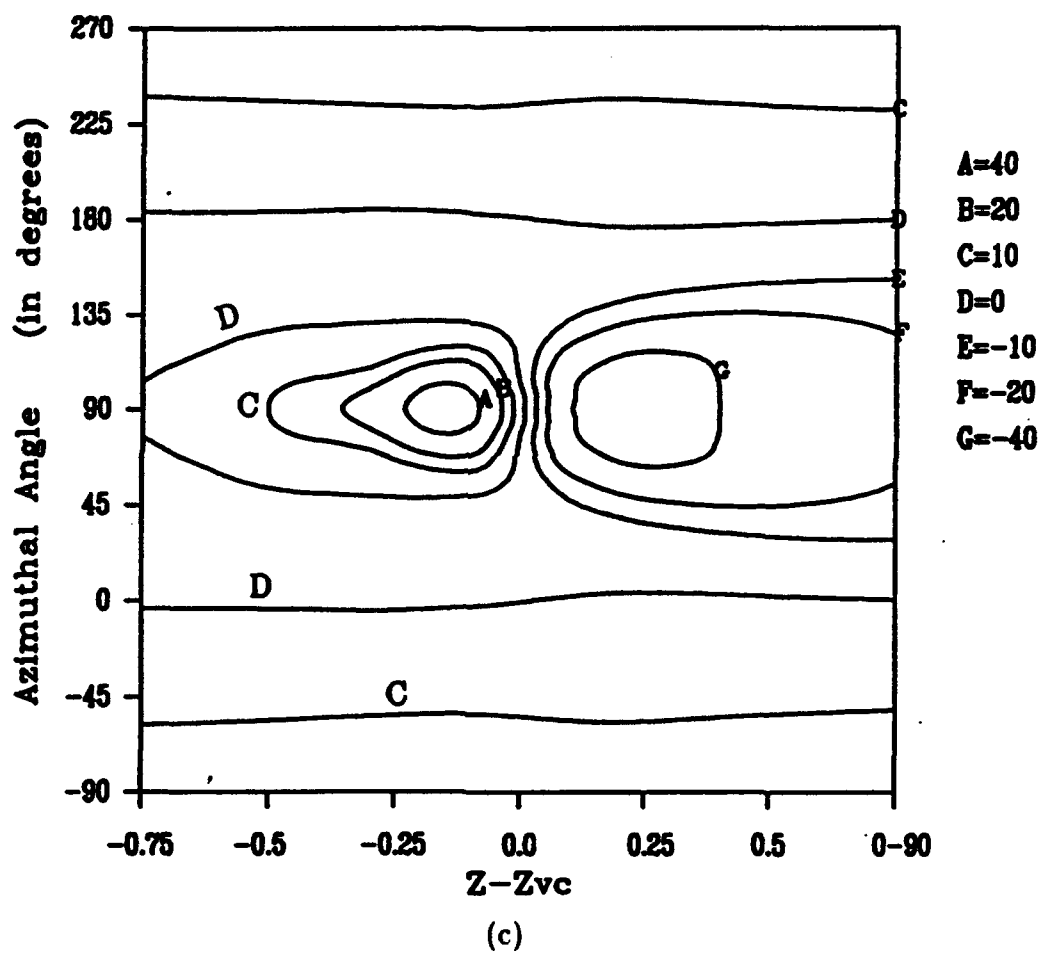
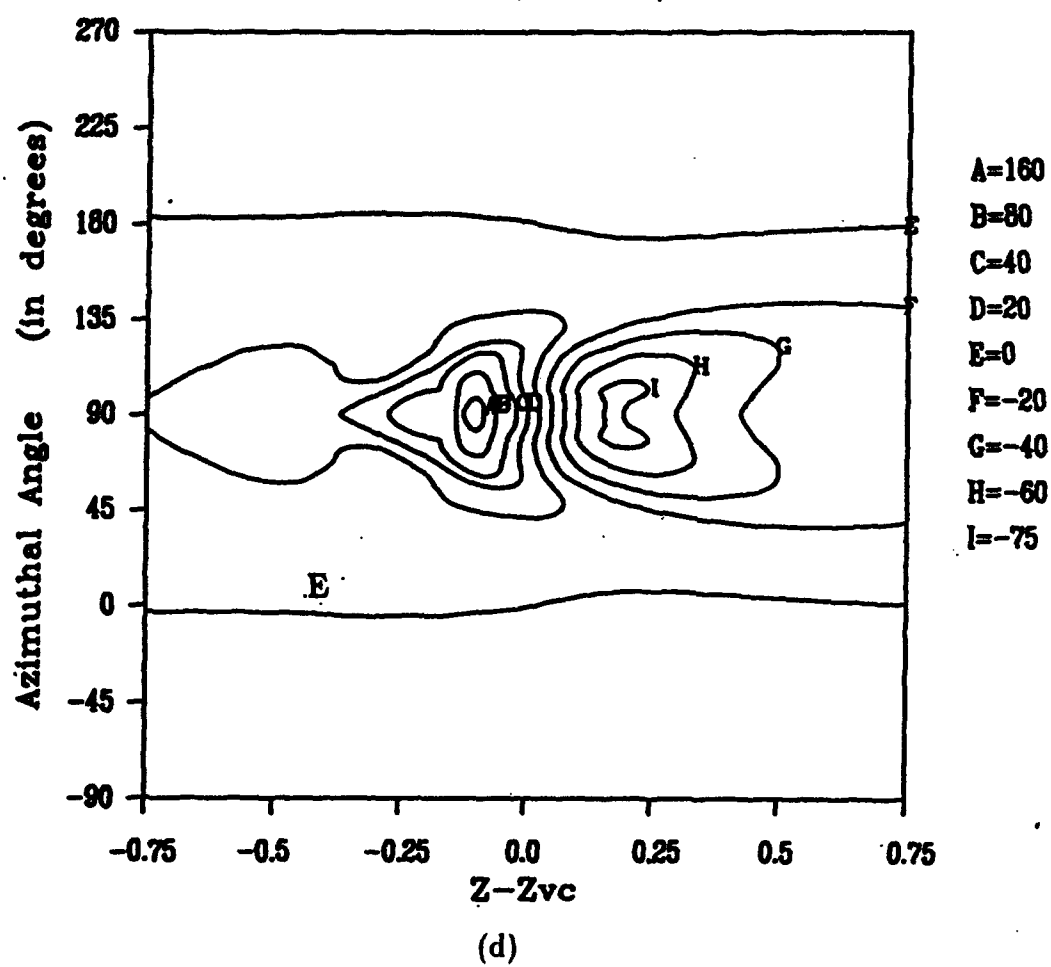


Figure 5.35 (continued)



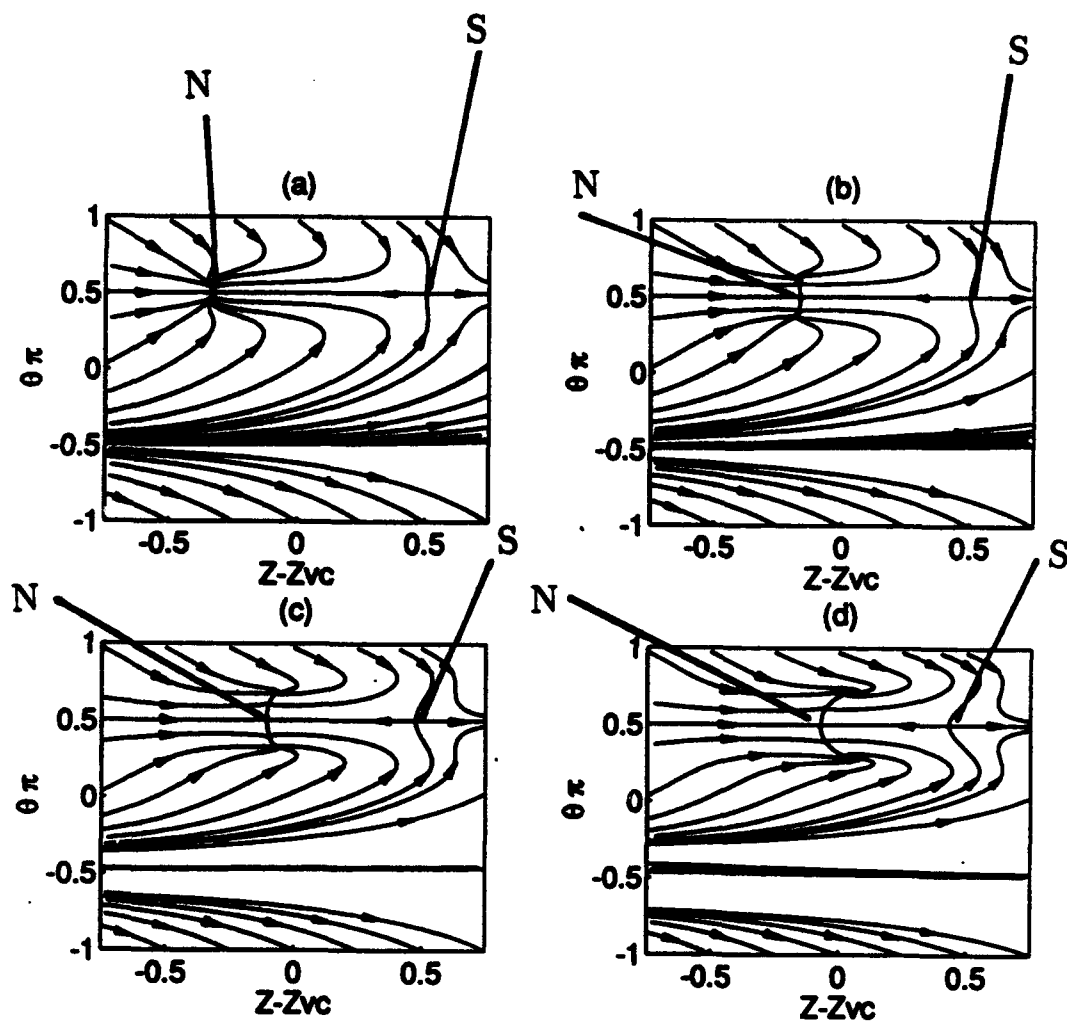


Figure 5.36: Surface streamlines for the symmetric mean flow at various times showing the development of a saddle point of attachment(S) and a nodal point of separation(N). (a) $t = 0.1$, (b) $t = 0.2$, (c) $t = 0.3$, (d) $t = 0.4$.

line $\omega_z=0$ evolves to a horseshoe-like shape as depicted by Figure 5.38.

On Figures 5.39 and 5.40 are lines of constant axial vorticity component ω_z plotted in cross-section on a $z=\text{constant}$ plane; on Figures 5.39(a-c) are the lines of constant ω_z plotted at various times $t=0.1, .2$ and $.3$ at a fixed location $z = -0.2$. Here the vorticity ω_z is also symmetric about $\theta = \pi/2$ where it is identically zero. Note that in addition to the zero line which extends vertically across the boundary layer at $\theta = \pi/2$, the results also show the development of another zero line which, in general, indicates the presence of a reversed flow region. The behavior of ω_z around the cylinder and at different z locations is shown on Figure 5.40(a-c). Here the lines of constant ω_z are plotted across the boundary-layer at different z locations $z=-0.4$ $z=-0.1$ and $z=0.3$ at a fixed time $t=0.35$. Note that the zero axial vorticity line deep within the boundary-layer(indicated by an arrow) exists only in a finite range of z off the symmetry plane, in particular, around $z=-0.1$ as shown on Figure 5.40(b).

It is evident from the foregoing that the axial vorticity is zero in the symmetry plane $\pi/2$ and so the azimuthal vorticity in this plane represents the total vorticity; thus as discussed previously in the stagnant medium case, it can be argued that the development of inverted "V" shape of the vorticity lines in the symmetry plane $\pi/2$ as shown on Figure 5.31 is an indication of an approaching singularity in the boundary-layer equations. Similarly, the singular point is expected at the first occurrence of a stationary point (defined in three-dimensions by van Dommelen and Cowley 1990 as the location of vanishing gradient of an oblique Lagrangian coordinate) and along the line of vanishing vorticity. It should be noted that, unlike the stagnant medium case, there are other locations where both components of vorticity vanish. Figures 5.36, and 5.39 and 5.40 indicate the presence of both zero axial and azimuthal vorticity surfaces and this suggests that the locations of zero vorticity vector occur on a line which results from the intersection of the zero azimuthal vorticity and the zero axial vorticity surfaces. One possibility is that the singularity occurs on the symmetry plane as in the stagnant medium case; this is the most likely scenario. Indeed, initial calculations of the behavior of the maximum displacement velocity in the latter stages of the calculations indicate a behavior $u_{r,max} \sim (t_s - t)^{-7/4}$ which is consistent with the predictions of Elliott, Cowley, and Smith(1983). Efforts to compute the zero vorticity vector line off the symmetry plane $\pi/2$ are ongoing.

On Figure 5.41 the temporal development of the profiles of the velocity component u_z is shown. The axial velocity profiles are plotted at various times $t=0.1, 0.15, 0.2, 0.25$, and 0.3 . For each time level the profiles are plotted at 9 z locations which are equally spaced and centered around the point $z = Z - Z_{Vc}=-0.25$. Similar to the zero mean flow, the symmetric mean flow results also show the development of a forward flow region near the wall as time increases.

On Figure 5.42 are results for the enstrophy. On Figure 5.42(a) and 5.42(b) are

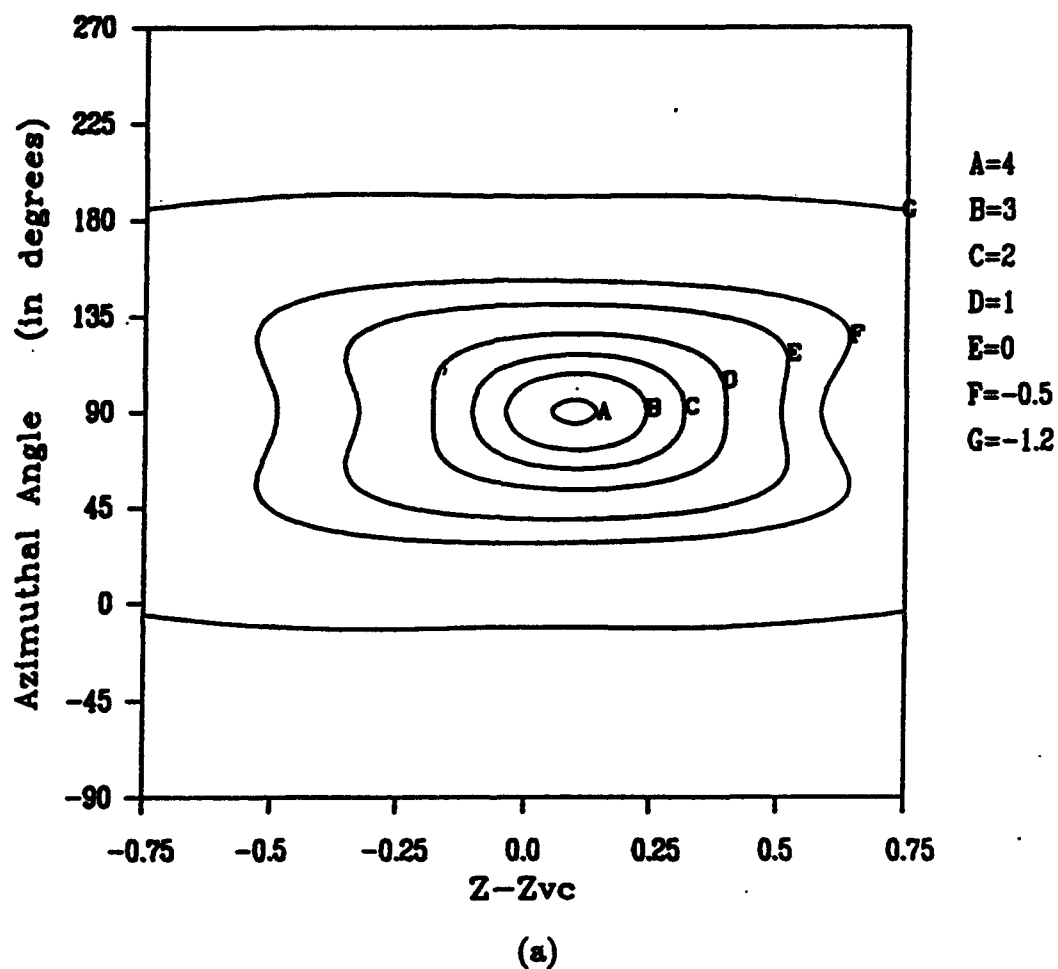


Figure 5.37: Lines of constant azimuthal vorticity ω_θ evaluated at the wall of the cylinder and plotted around the cylinder for various times. (a) $t = 0.1$, (b) $t = 0.2$, (c) $t = 0.3$, (d) $t = 0.4$. Here the results are for the symmetric mean flow case where the flow is symmetric about $\theta = \pi/2$ (or 90°). The values of ω_θ are shown.

Figure 5.37 (continued)

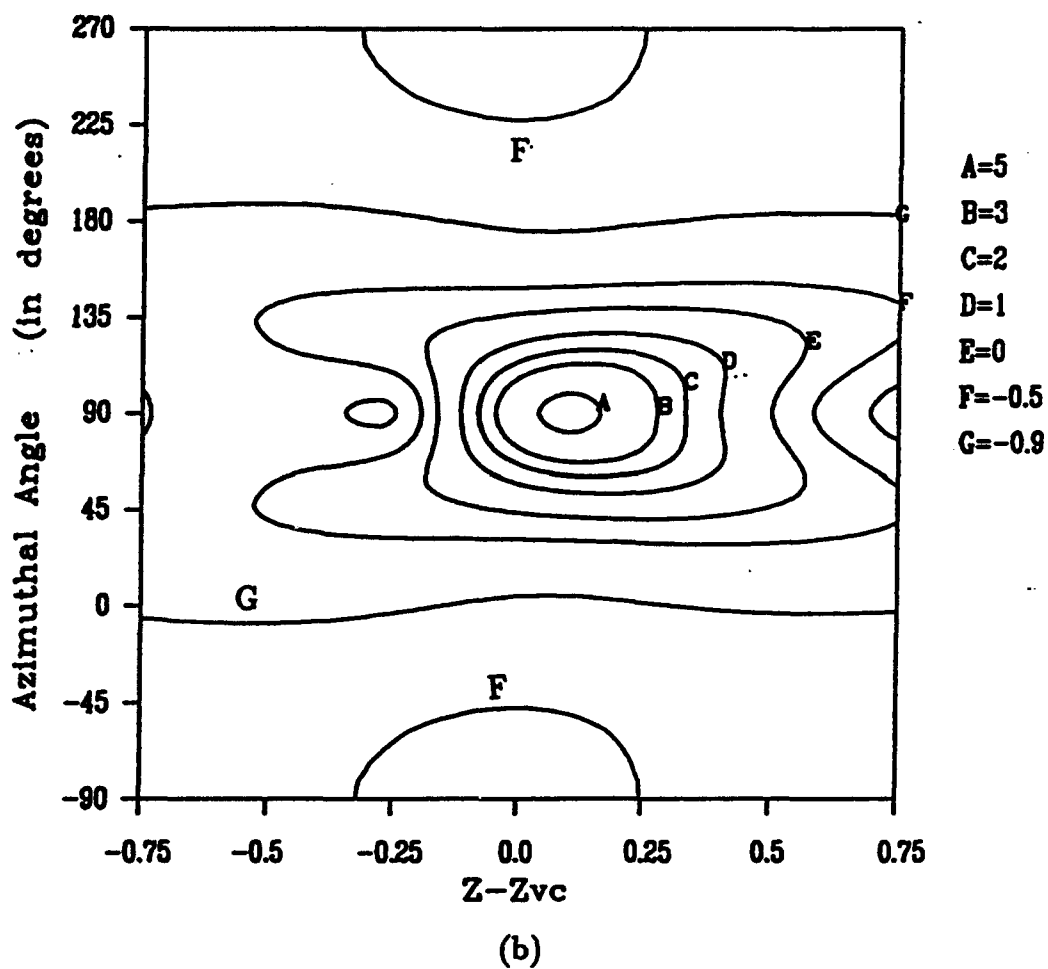


Figure 5.37 (continued)

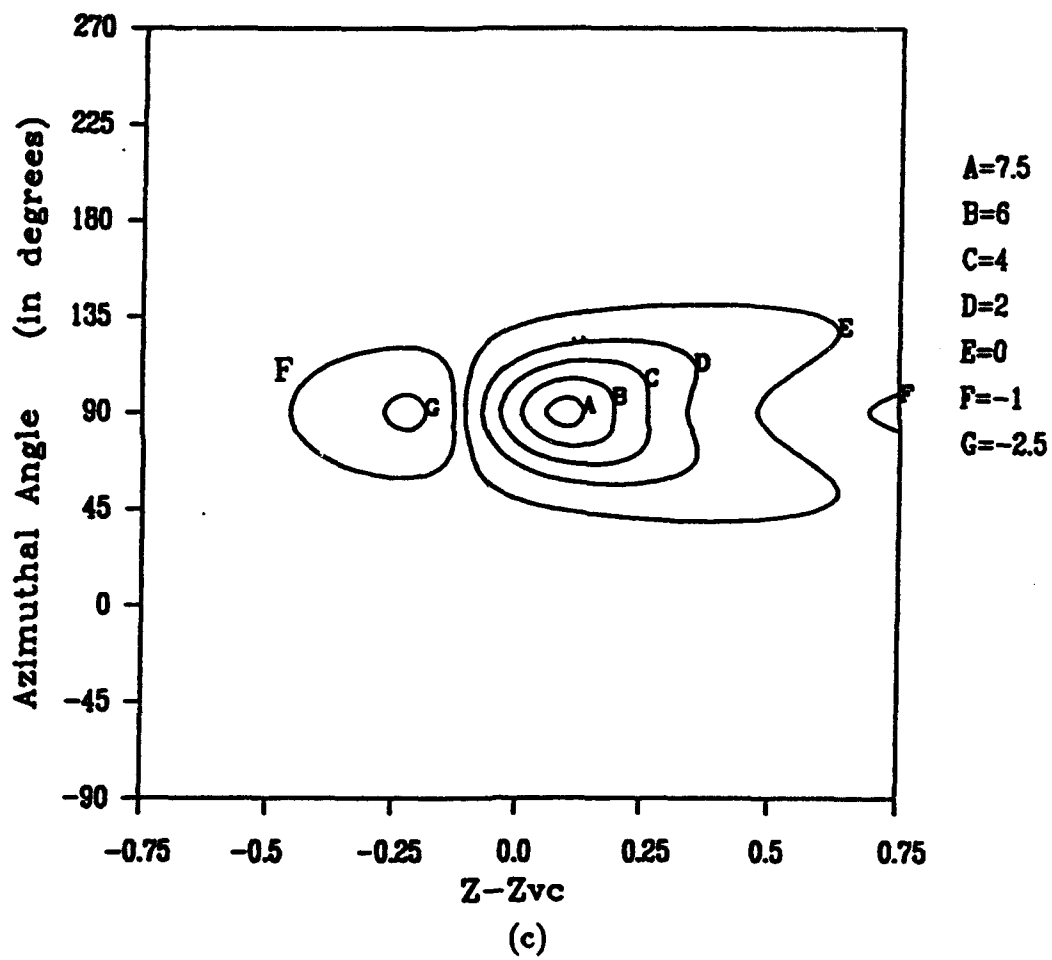
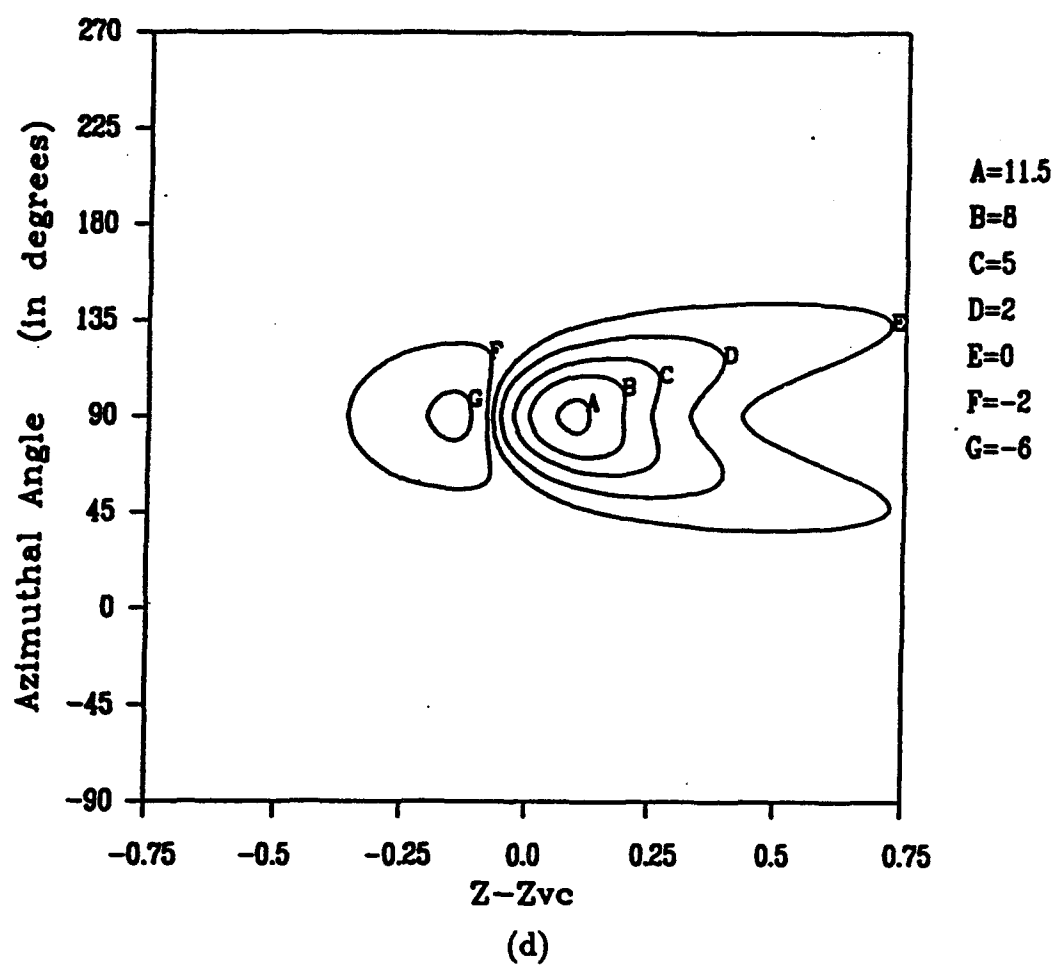


Figure 5.37 (continued)



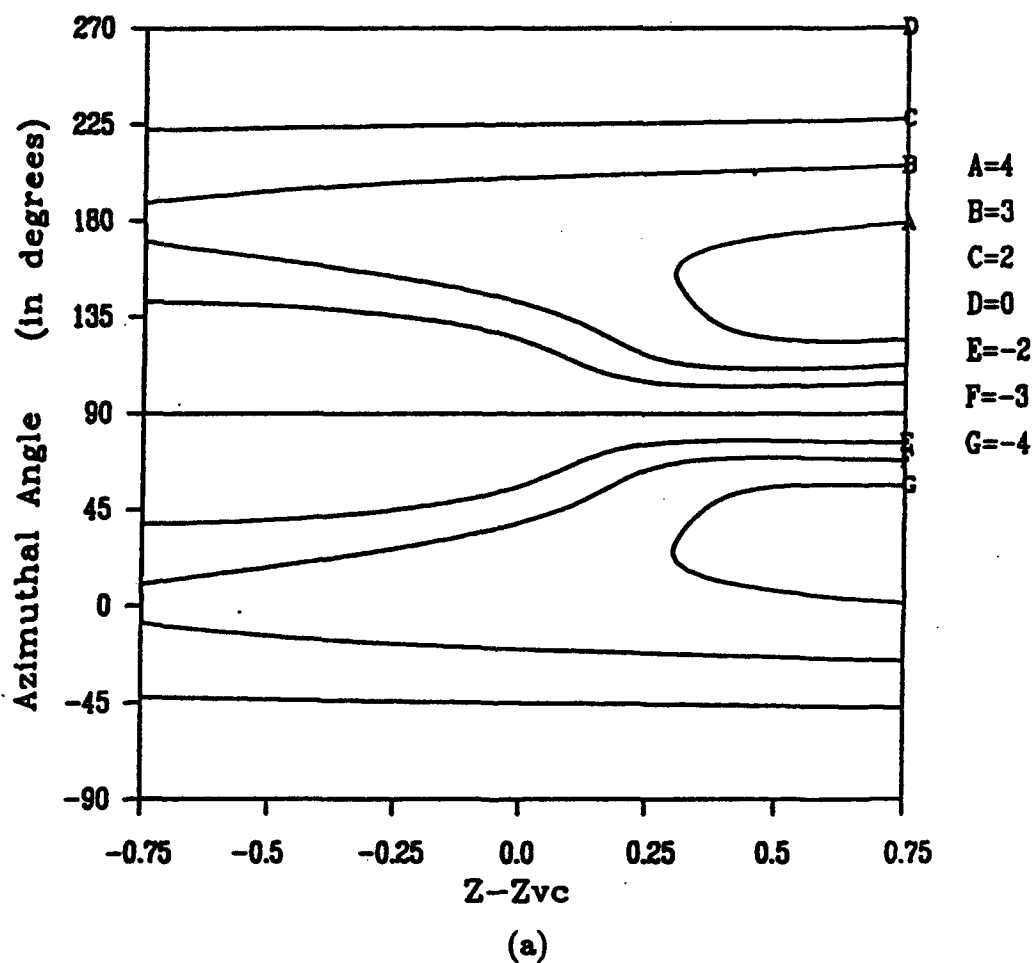


Figure 5.38: Lines of constant axial vorticity ω_z evaluated at the wall of the cylinder and plotted around the cylinder for various times. (a) $t = 0.1$, (b) $t = 0.2$, (c) $t = 0.3$, (d) $t = 0.4$. Here the results are for the symmetric mean flow case where the flow is symmetric about $\theta = \pi/2$ (or 90°). The values of ω_z are shown.

Figure 5.38 (continued)

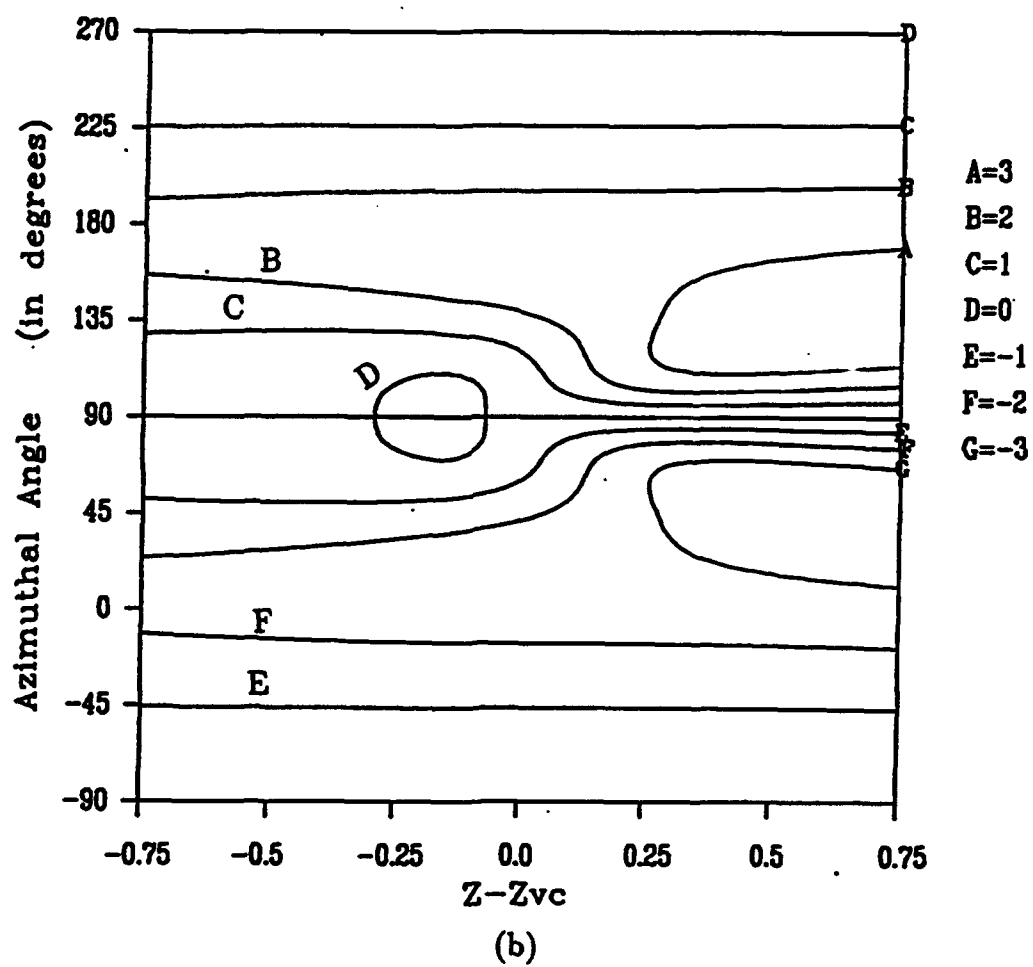


Figure 5.38 (continued)

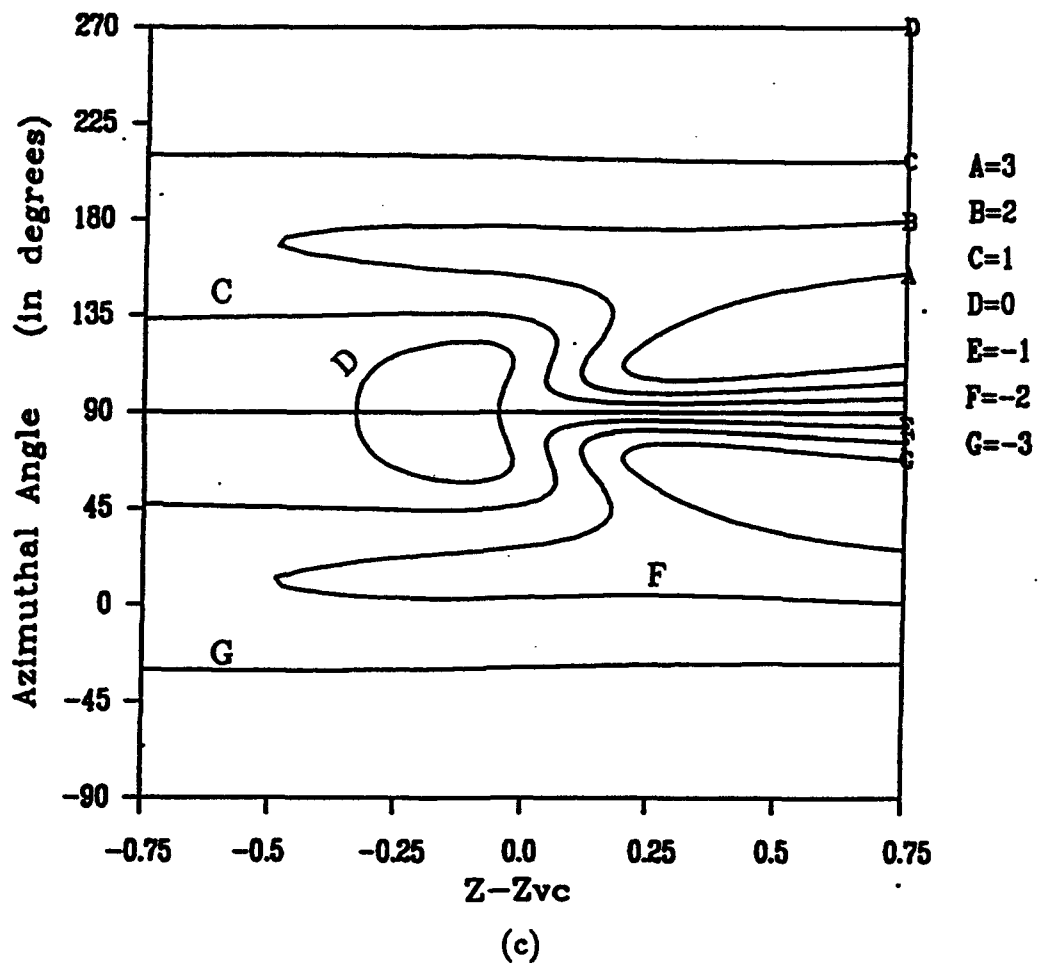
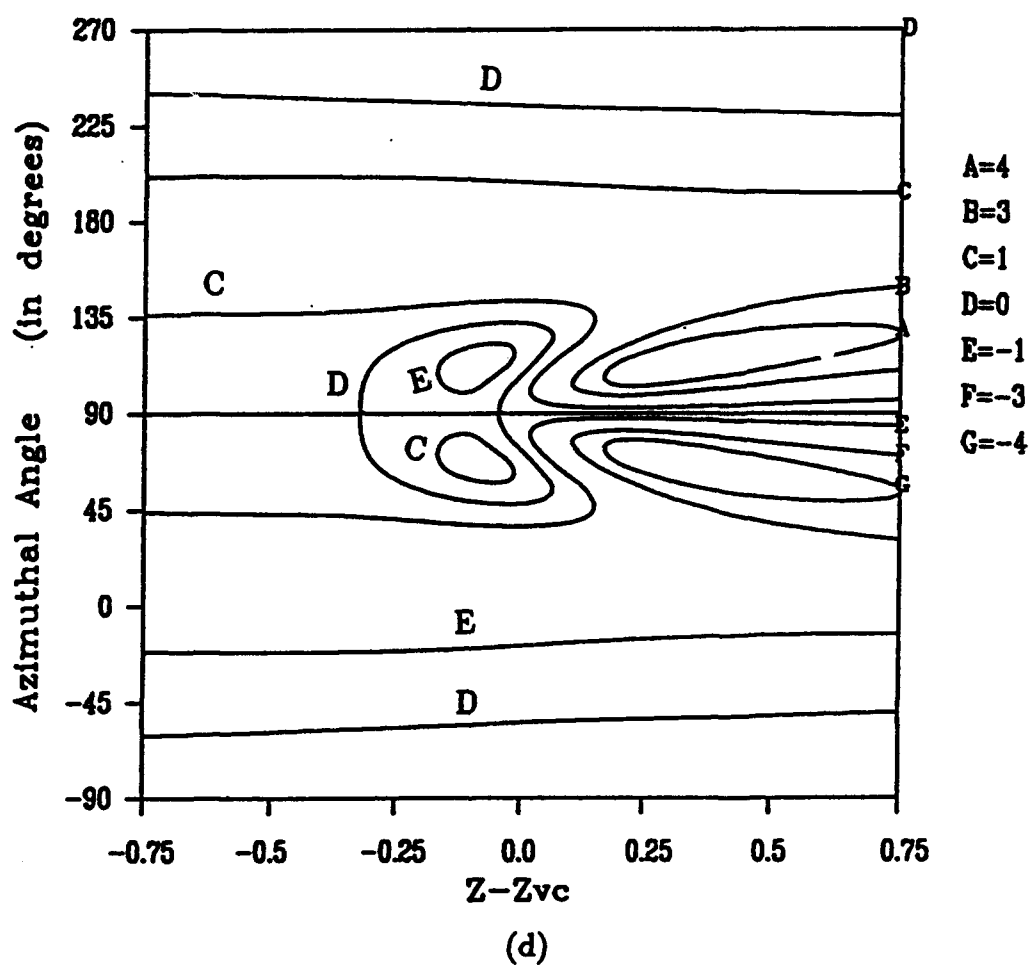


Figure 5.38 (continued)



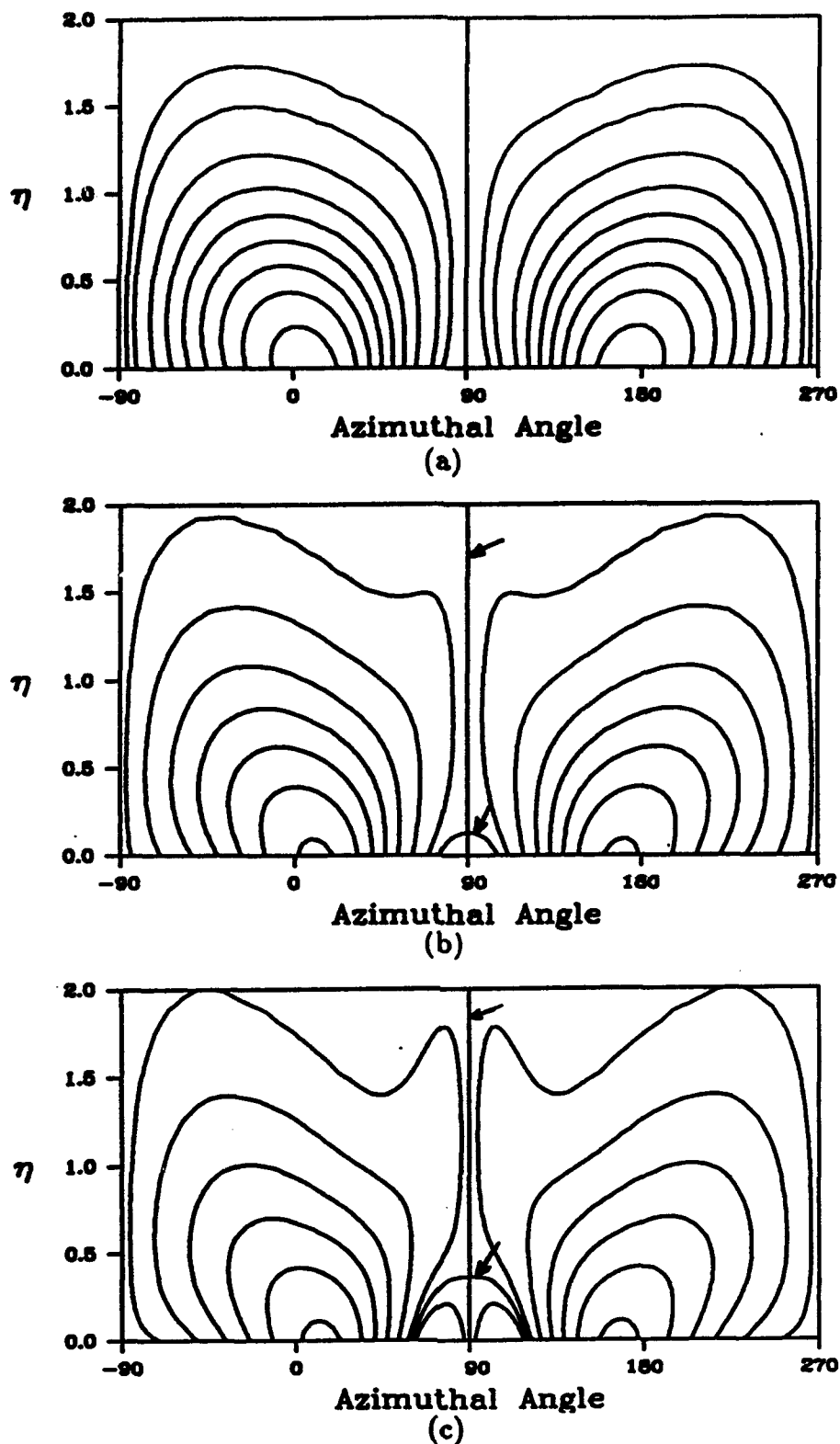


Figure 5.39: Lines of constant axial vorticity ω_z plotted across the boundary-layer around the cylinder in the z plane $z = -0.2$. Here the results are for the symmetric mean flow case and are shown at various times: (a) $t=0.1$, (b) $t=0.3$, (c) $t=0.4$. The zero axial vorticity line is marked by an arrow.

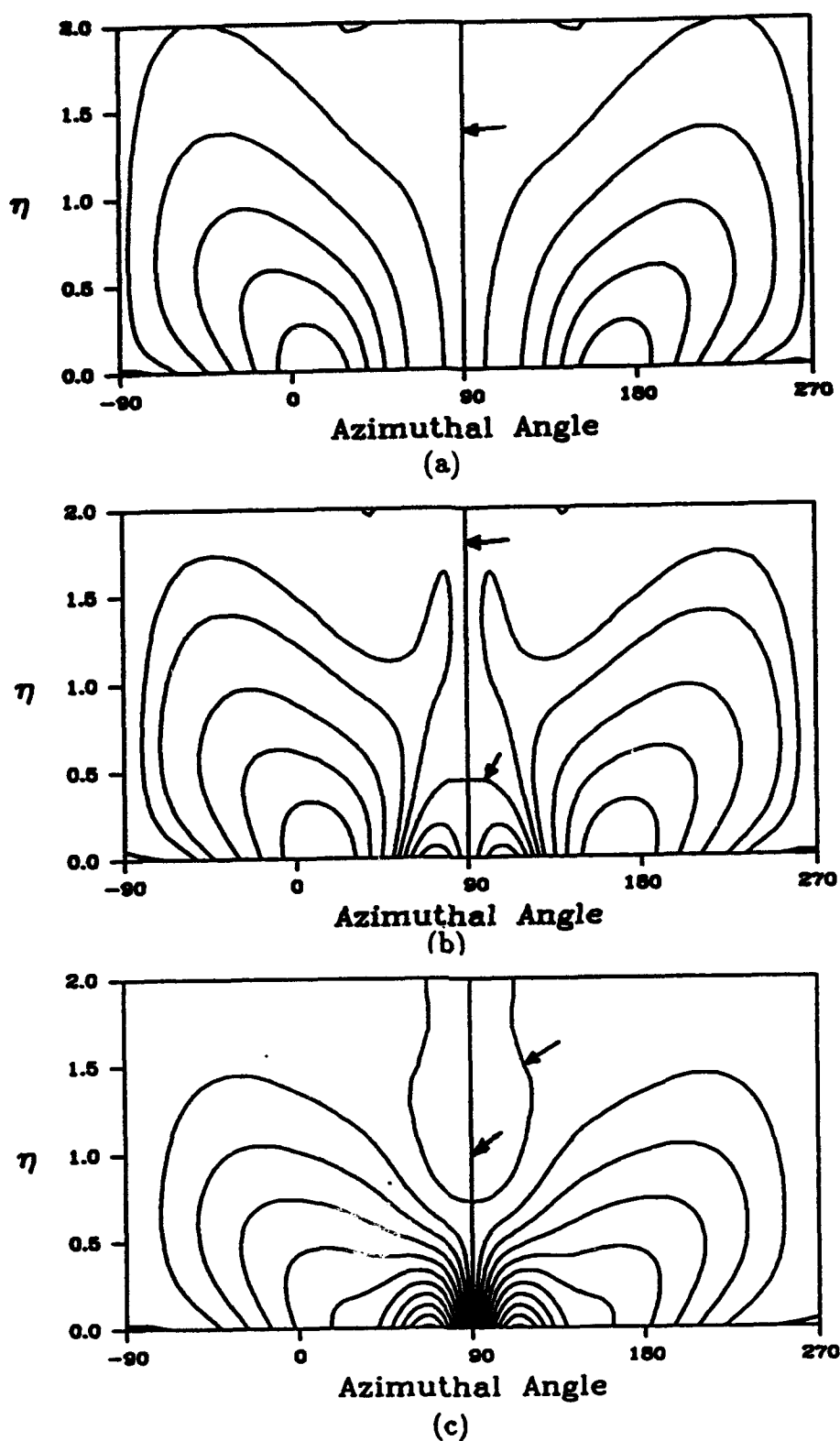


Figure 5.40: Lines of constant axial vorticity ω_z plotted across the boundary-layer around the cylinder at a fixed time $t=0.35$. Here the results are for the symmetric mean flow case and are shown at various z locations: (a) $z=-0.4$, (b) $z=-0.1$, (c) $z=0.3$. The zero axial vorticity line is marked by an arrow.

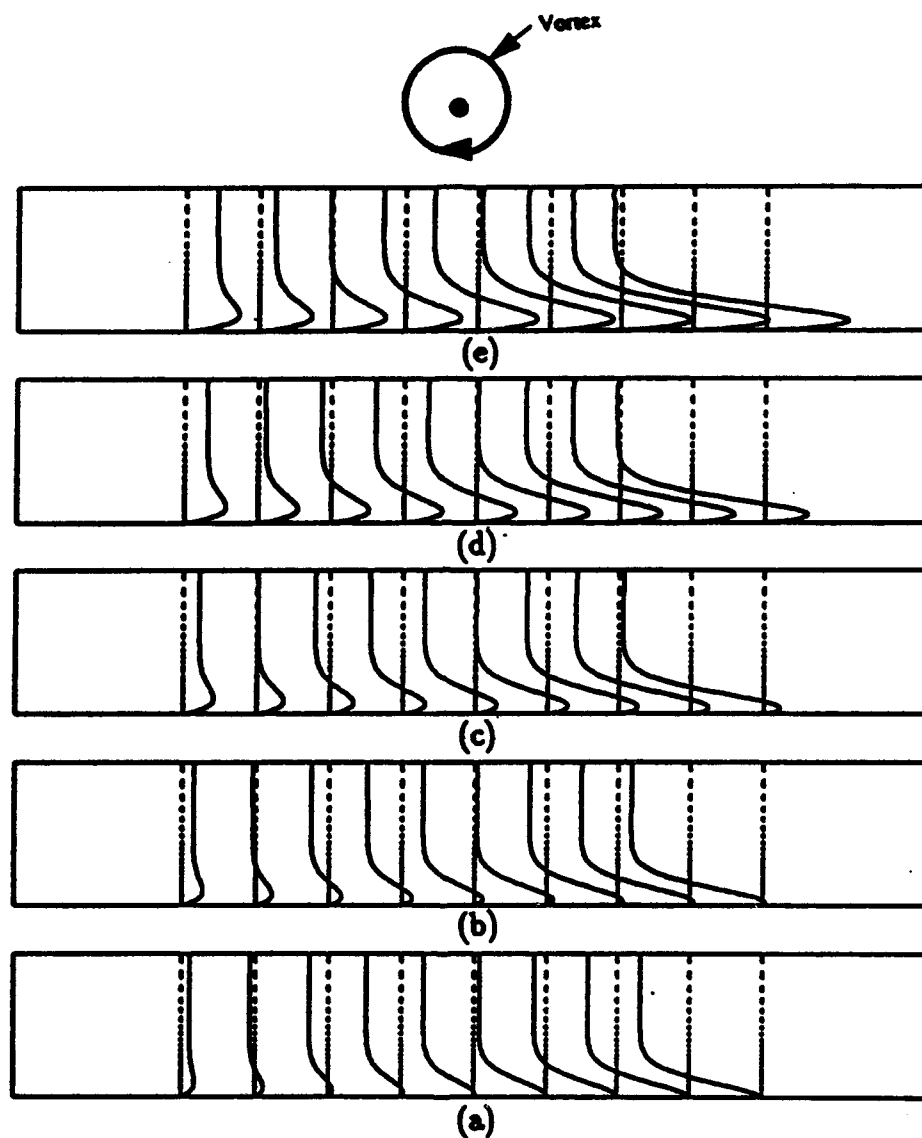


Figure 5.41: Temporal development of the velocity profiles of u_z plotted across the boundary-layer ($0 \leq \eta \leq 6$) at various times: (a) $t=0.1$, (b) $t=0.15$, (c) $t=0.2$, (d) $t=0.25$, (e) $t=0.3$. The profiles are shown at 9 equally spaced locations which are centered around $z = Z - Z_{Vc} = -0.375$ and separated by $\Delta z = 0.025$. The results are for the symmetric mean flow case.

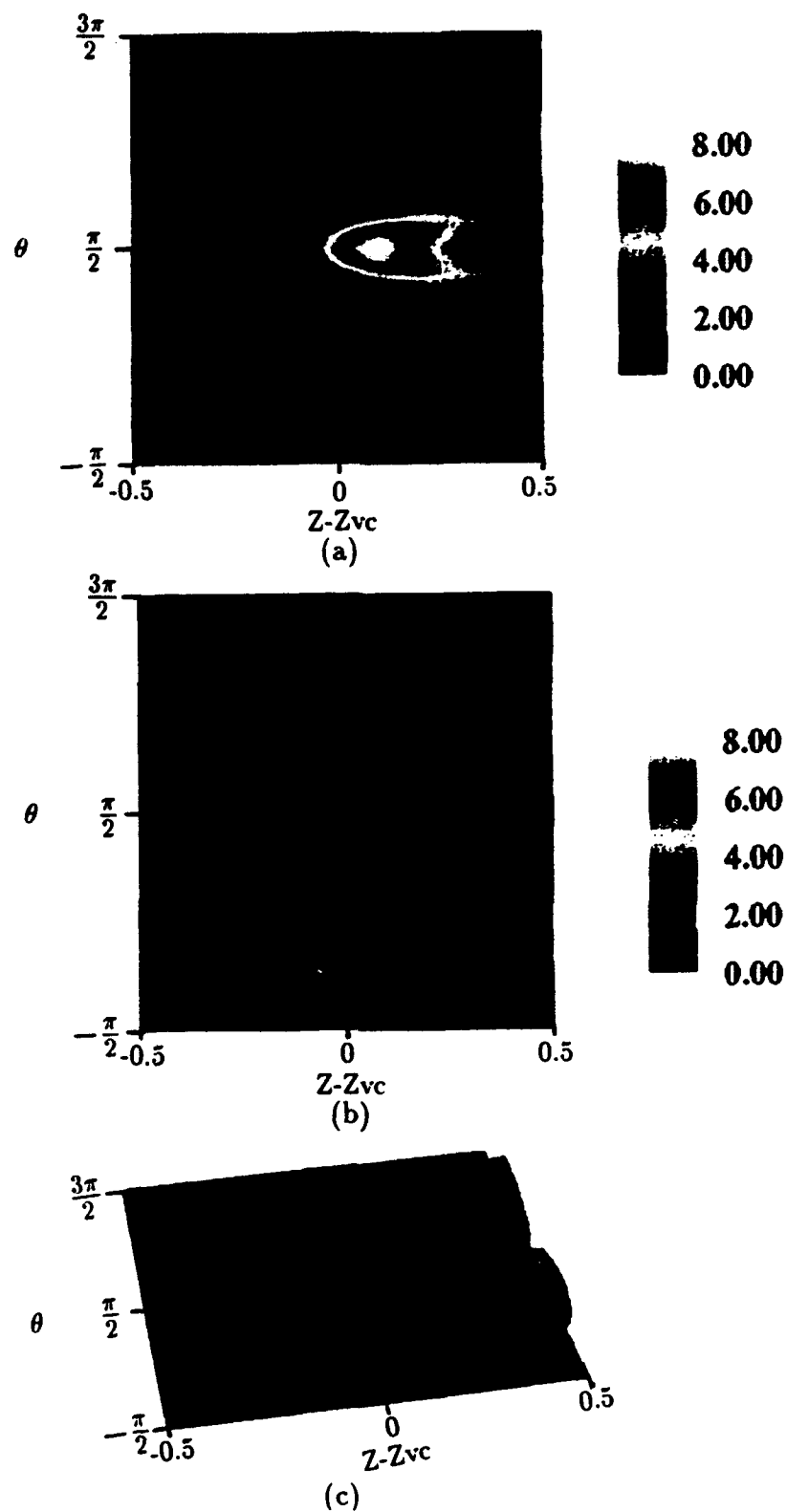


Figure 5.42: Contours of constant entropy plotted in the planes (a) $\eta=0$, (b) $\eta=.268$ and (c) along the surface of the constant value equal to 1.47. Here the results are for the symmetric mean flow case at $t=.3$.

contours of enstrophy at the surface $\eta=0$ and at $\eta=.286$ respectively. As with the stagnant medium case, the maximum value of the enstrophy occurs in the center of the oval-shaped region just downstream of the vortex head. Note that the values of the enstrophy are much larger than that of the stagnant medium case. The two strips denoting the enstrophy $E \sim 2$ are a result of the two-dimensional mean flow past a circular cylinder; the presence of the secondary eddy is indicated by the U-shaped region just upstream of the vortex head. The effect of the secondary eddy is not evident above the wall at $\eta = .286$; the foregoing results indicate that both components of vorticity contribute to the value of the enstrophy. Again, however, outside the immediate vicinity of the shoulders of the cylinder and away from the intense activity under the vortex, the enstrophy rapidly decreases. On Figure 5.42(c), the surface of constant enstrophy $E = 1.47$ is plotted. Unlike the stagnant medium case, the shape of this surface is more complex due to the fact that both azimuthal and axial vorticity components are of equal size and exist in different regions. The enstrophy, which combines both components of vorticity ω_θ and ω_z , gives rise to an "U" shape high vorticity region whose middle is dominated by the azimuthal vorticity component (vortex effect) and whose ends are dominated by the axial vorticity component (due to two-dimensional flow past a circular cylinder). The presence of the secondary eddy is indicated by the bubble-like surface which exists inside the "U" structure to the left.

Asymmetric Mean Flow: The Rotor Tip Vortex

The results to be presented here are for the asymmetric inviscid mean flow case discussed in Chapter 3 and correspond to the experimental parameters of Professor Komerath and his colleagues at Georgia Tech (Affes, et al 1993). Here, the boundary layer variables have been made dimensionless according to equation (5.68) for the symmetric mean flow case. All the relevant inviscid flow parameters are for the case where the advance ratio $\mu = .1$; the values of these parameters are given in Chapter 3. The time step employed in these calculations is $\Delta t = .00444$ which corresponds to $\Delta\psi = .375^\circ$. As has been noted previously, the computation of the pressure gradients in the inviscid flow problem is inconsistent with the boundary-layer flow calculations; in the present case the flow is highly asymmetric and this fact leads to difficulties in the velocity patterns near the edge of the boundary-layer. These difficulties were manifest in an unrealistically rapid adjustment of the axial velocity to its free-stream value. This does not appear to be a problem when computing the boundary-layer flow in the symmetric cases. To remedy this problem, the third-order upwind differencing scheme, which is used to treat the nonlinear terms in the boundary-layer equations, is also employed to compute the nonlinear terms appearing in Euler's equations for the pressure gradients instead of using the numerical scheme discussed in Chapter 3 (i.e Fast Fourier Transform in both θ and z directions). In some of the results to follow, the origin of the z -axis is shifted to the position of the vortex on the top of the airframe at time $\psi = 0$, and then held fixed. The three-dimensional streamline patterns are plotted both in a frame of reference travelling with the vortex point originally at the top of the airframe and in the laboratory frame as defined just above.

On Figure 5.43 are streamline patterns for several times indicating the inception of a secondary eddy. Here the eddy inception is captured by a single series of streamlines beginning at $\eta = 0.4$ for the range of θ from about 80° to 100° . The initial stages of reversed flow are seen to develop near the wall on the top of the airframe. The streamlines begin to kink at about $t = .2843 (\psi = 24^\circ)$ and by time $t = .3554 (\psi = 30^\circ)$, the eddy is well developed. As time goes on, the eddy expands in the azimuthal direction and at time $t = .3953 (\psi \sim 33.3^\circ)$ it encompasses about 10° from the vertical on each side. This is indicated by a second view of the streamline patterns for $t = .3953$ depicted on Figure 5.43(d). These streamline patterns are plotted in a reference frame traveling with the speed of the tip vortex at a point initially on the vertical plane of symmetry of the airframe ($\theta = \pi/2$).

The streamline patterns plotted in the fixed frame of reference are depicted on Figure 5.44 at $\psi = 30^\circ$. Here we note that there is no evidence of a secondary

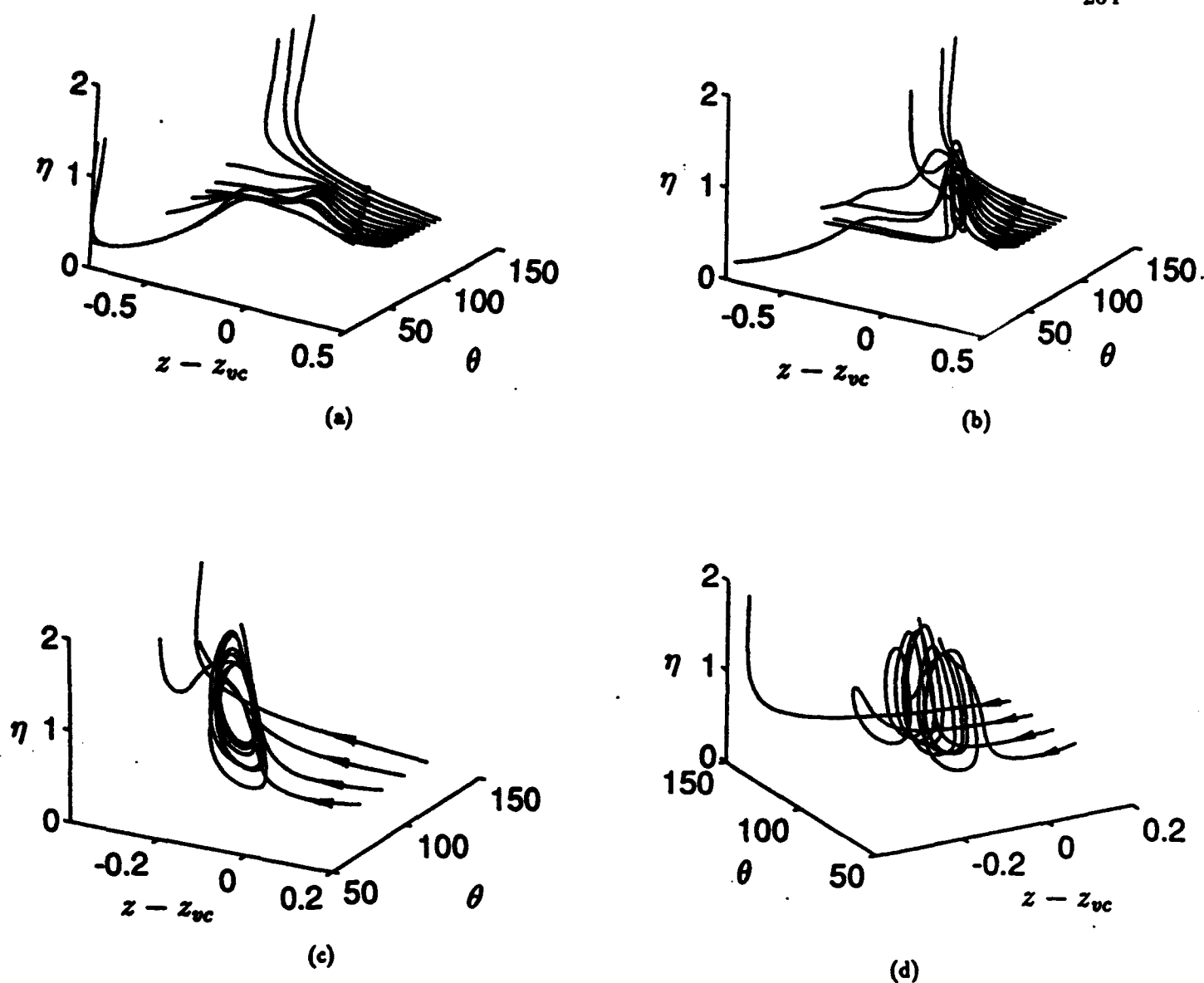


Figure 5.43: Three dimensional streamline patterns for several times in a frame of reference moving with a point on the vortex. (a) $t = .2843(\psi = 24^\circ)$; (b) $t = .3554(\psi = 30^\circ)$; (c) $t = .3953(\psi = 33.3^\circ)$; (d) another view at $t = .3953$ indicating azimuthal extent of the secondary eddy.

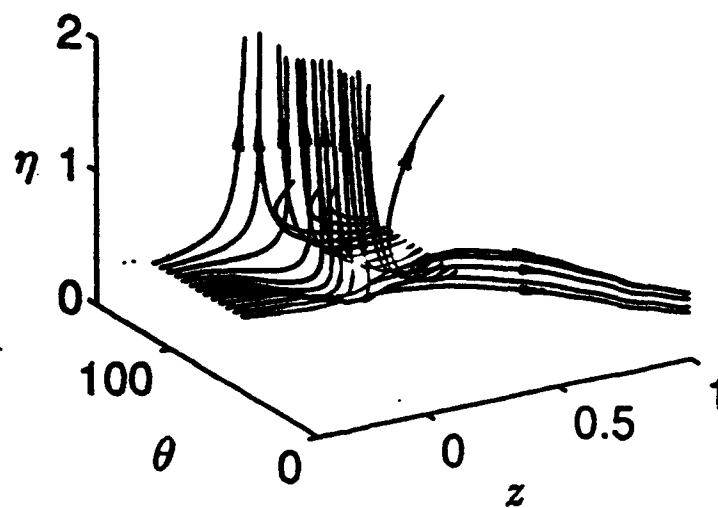


Figure 5.44: Three dimensional streamline patterns at $\psi = 30^\circ$ in the fixed frame of reference with origin in z directly under the vortex at time $\psi = 0$.

eddy pattern and the region of interest is characterized by two sets of colliding streamlines. Note that the pairs of colliding streamlines bound a triangular region near the wall and the evolution of such a region may be clearly seen in the experiments as described below. On Figure 5.45 are lines of constant azimuthal vorticity ω_θ plotted at various azimuthal locations around the cylinder at the time $t=0.3554$. The constant vorticity lines are plotted for values from -1.0 to 2.5. Figures 5.45(a-c) correspond respectively to distributions of azimuthal vorticity across the boundary-layer in the planes $\theta=90^\circ$, 101.25° , and 112.5° . Inside the zero azimuthal vorticity line, which is marked by an arrow, the vorticity is positive; outside this region the vorticity ω_θ is negative. The vorticity patterns show that the region associated with positive vorticity (i.e. opposite to that of the tip vortex) diminishes in size at locations removed from the vertical plane of symmetry. At this time, the maximum value of the vorticity is not large (~ 2.5); the maximum azimuthal vorticity occurs around $\theta = 90^\circ$ and decreases for $\theta > 90^\circ$. On the other hand, at time $t = .3953$ (not shown) the vorticity has increased substantially to $\omega_\theta \sim 10$ near $\theta = 100^\circ$ indicating the emergence of a high vorticity region off $\theta = 90^\circ$ in a very short time period.

Concurrent with the rapid increase in magnitude of the vorticity field is again a rapid increase in the radial velocity. On Figure 5.46 is a three-dimensional plot of the radial velocity u_r at the edge of the boundary-layer plotted around the cylinder for the time $t=0.3554$ ($\psi=30^\circ$). As for the symmetric flow case, the results show that large variations of the radial velocity occur at locations close to the main vortex. At points removed from the vicinity of $\theta \sim 90^\circ$, the edge velocity is small. This behavior is again symptomatic of a subsequent eruption of fluid from the boundary layer.

As with the inviscid flow associated with the tip-vortex described in Chapter 3, collaboration with Professor Komerath and his colleagues at Georgia Tech with regard to investigation of viscous flow phenomena has been ongoing. The most recent experiments at Georgia Tech on the vortex-surface interaction have focused on the near-impact phase in the region just upstream of the vortex and it is useful to describe the methods and results of that experimental work. A pulsed copper vapor laser beam, expanded into a sheet, was used to illuminate desired vertical planes above the surface of the cylinder. Smoke from decomposing wax, generated by heating several vertical wax-coated wires upstream, was used as seeding in the flow. An intensified video camera was used to view the scattered light. Another video camera mounted above the wind tunnel was used to observe a protractor disk attached to the rotor shaft. This video image was superposed in a window on the flow image. The passage of the leading edge of the rotor blades through the light sheet provided the information to calibrate and correct for the phase shift between the two video systems. Thus the rotor position corresponding to each flow image was obtained. However, under the extremely low-light conditions

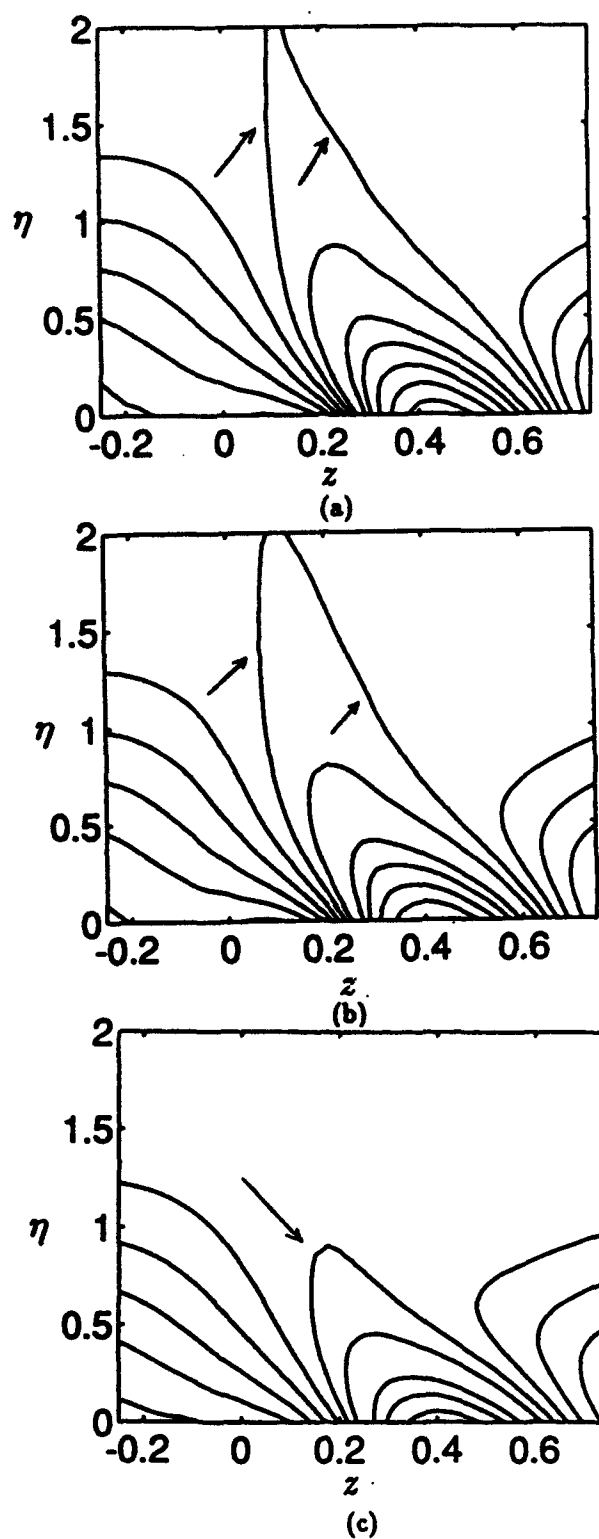


Figure 5.45: Azimuthal component of vorticity at time $t = .3554$ at several locations around the cylinder. (a) $\theta = 90^\circ$; (b) $\theta = 101.25^\circ$; (c) $\theta = 112.5^\circ$.

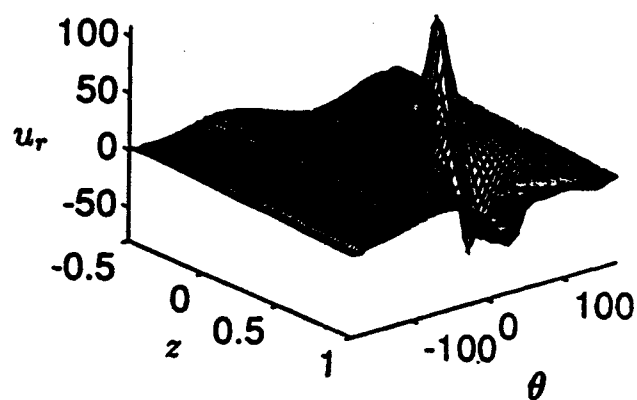
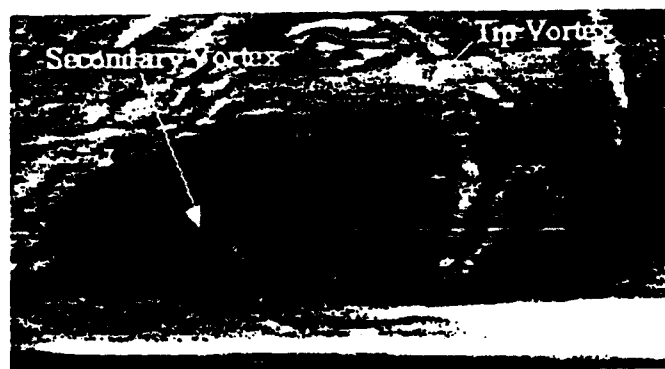


Figure 5.46: Three-dimensional plot of the radial velocity around the cylinder at $\psi = 30^\circ$. Note the large spike around where the tip vortex will eventually impact the airframe.

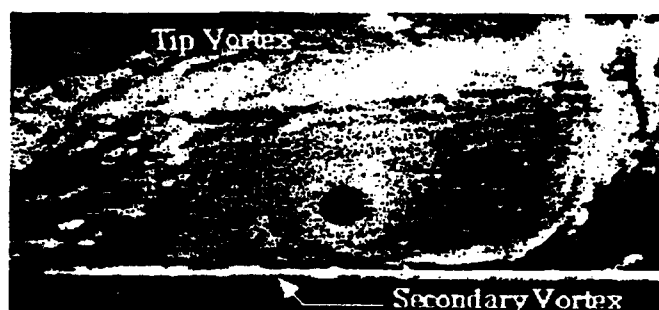
of this experiment, good images were obtained only at a few values of the rotor azimuth.

Figure 5.47 shows a vortex cross-section image captured at $\psi = 72^\circ$ with the laser sheet in the plane 30° from the vertical on the retreating side of the rotor ($\theta = 120^\circ$). This image was captured from one frame of a video tape taken with a camera shutter exposure of $1/10000$ seconds, with the copper vapor laser pulsing at 6000 pulses per second. Each pulse is approximately 25 nanoseconds long. Thus, the image contains information from only one pulse of the laser, "freezing" the flow field with an effective 25 nanosecond exposure. The tip vortex (arrow is pointing to its outer edge; the dark region is its core) is seen, distorting as the impact phase begins. Just upstream, there is a smaller particle void (denoted by the dark region in the image near the end of the other arrow on Figure 5.47(a)) near the wall. The dark regions on Figure 5.47(a) are regions of high vorticity and the emergence of such a region near the wall is suggestive of the development of a secondary vortex structure at an earlier time as indicated by the computations (Figures 5.43, 5.44 and 5.45). On this figure, the vortex core radius is about 5mm and the vertical scale of the secondary flow is about 10mm . At this time, the boundary layer thickness estimated from the Reynolds number based on forward flight speed and the airframe radius is about $1 - 5\text{mm}$ so that the vertical scale of the eruptive region is nominally larger than the associated boundary layer thickness indicating a mechanism whereby boundary layer fluid may erupt into the main stream (see the previous section and Doligalski and Walker 1984, Walker 1978, Chuang and Conlisk 1989, and Walker, et al 1987). It should be noted that the rotor tip speed used to produce the results of Figure 5.47 is half of that used to produce the other results described here (1050 rpm); this was done to facilitate visualization of the boundary layer evolution. On Figure 5.47(b) are the visualization results with the laser sheet in the vertical plane of symmetry ($\theta = 90^\circ$) and note that the size of the secondary eddy is much smaller there.

Figure 5.48(a) shows the surface pressure distribution on the top of the airframe for a rotor tip speed of 2100rpm and an advance ratio of 0.1 in the vertical plane through $\theta = 120^\circ$ on the retreating side of the rotor; see Figure 3.1. Here the influence of the development of the secondary vortex structure on the pressure distribution is characterized by the development of a second spike in the pressure signature; this phenomenon has been present in calculations of the two-dimensional interacting boundary layer problem (Conlisk 1989, Peridier and Walker 1989) and in Chapter 8 it is demonstrated that a second spike does, indeed emerge in the present three-dimensional situation. On Figure 5.48, Xb is a coordinate which measures distance from the nose of the airframe and $R = .457\text{m}$ is the rotor blade radius. C_{pINS} is the instantaneous pressure coefficient defined by $C_{pINS} = \frac{p^* - p_\infty}{\frac{1}{2}\rho W_\infty^2}$ where W_∞ is the freestream speed. These results were reassembled from the data taken with a microphone sensor moved in succession to several stations along the

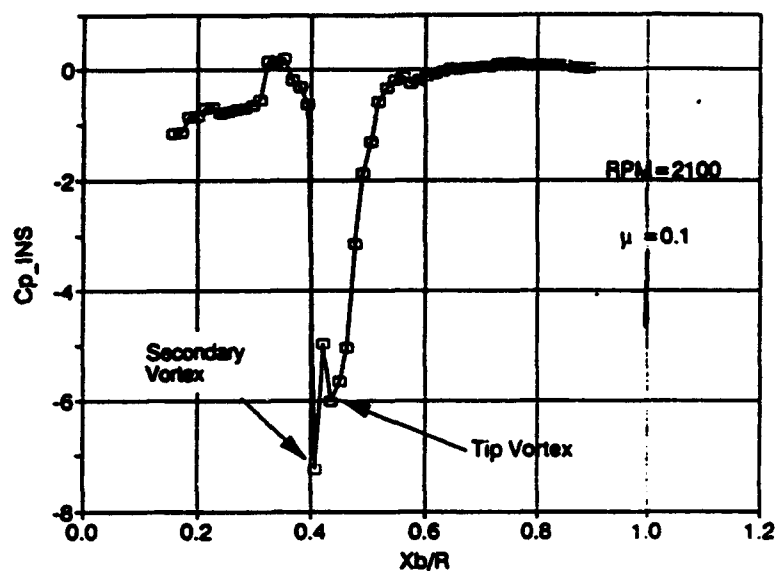


(a)

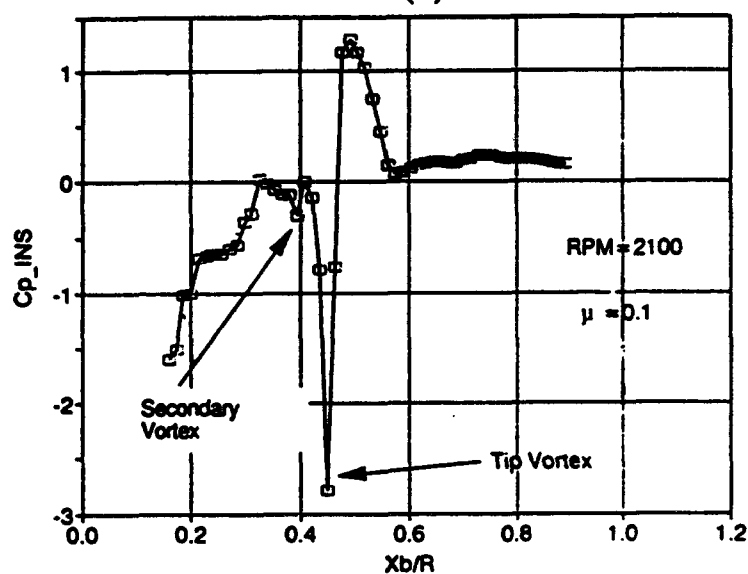


(b)

Figure 5.47: (a) Vortex cross-section image at $\psi = 72^\circ$ in the plane 30° from the vertical on the retreating side of the rotor ($\theta = 120^\circ$). (b) In the vertical plane of symmetry.



(a)



(b)

Figure 5.48: Pressure distribution along the airframe under the tip vortex on the wall at rotor phase angle $\psi = 72^\circ$. (a) In the plane 30° from the vertical; (b) on the top of the airframe. The second spike is believed to be due to the development of the reversed flow eddy in the boundary layer.

surface, with the azimuth-resolved pressure measured at each station. The pressure value in the 6-degree(0.48 millisecond) interval around $\psi = 72^\circ$ was extracted from the data at each station and represented by a square symbol. Note that the effect of the secondary vortex on the pressure distribution is much more visible at $\theta = 120^\circ$ than at $\theta = 90^\circ$ (Figure 5.48(b)). Two possible reasons can be advanced for this. The axial flow present in the core of the tip vortex in the experimental case(zero in the computations) stagnates near the top of the cylinder, perhaps modifying the secondary separation. On the side of the cylinder, this effect is not present. Another reason, and probably more important, becomes evident from the computed results. The secondary separation is three-dimensional and starts at the top of the cylinder, then spreads down the side as time goes on. Since the vortex is farther from the airframe on the retreating side($\theta \geq 90^\circ$), the separation zone has more time to develop, and it is likely to be larger in extent normal to the airframe than it is at the top. While these are plausible explanations for this effect, additional work is required to further clarify this phenomenon.

To further elucidate the development of the reversed flow associated with the secondary eddy, on Figure 5.49 the temporal development of the profiles of the velocity u_z is shown. The velocity profiles are plotted at various times $t=0.0711$, 0.1421, 0.2133, 0.2843 and 0.3554. Similar to the previous cases, the profiles are plotted at 9 z locations which are equally spaced. Here the spacing corresponds to $\Delta z=0.025$ and the points are centered around $z=0.75$. Note the reversed flow region at the latter stage Figure 5.49(e) where the velocity changes sign near the wall.

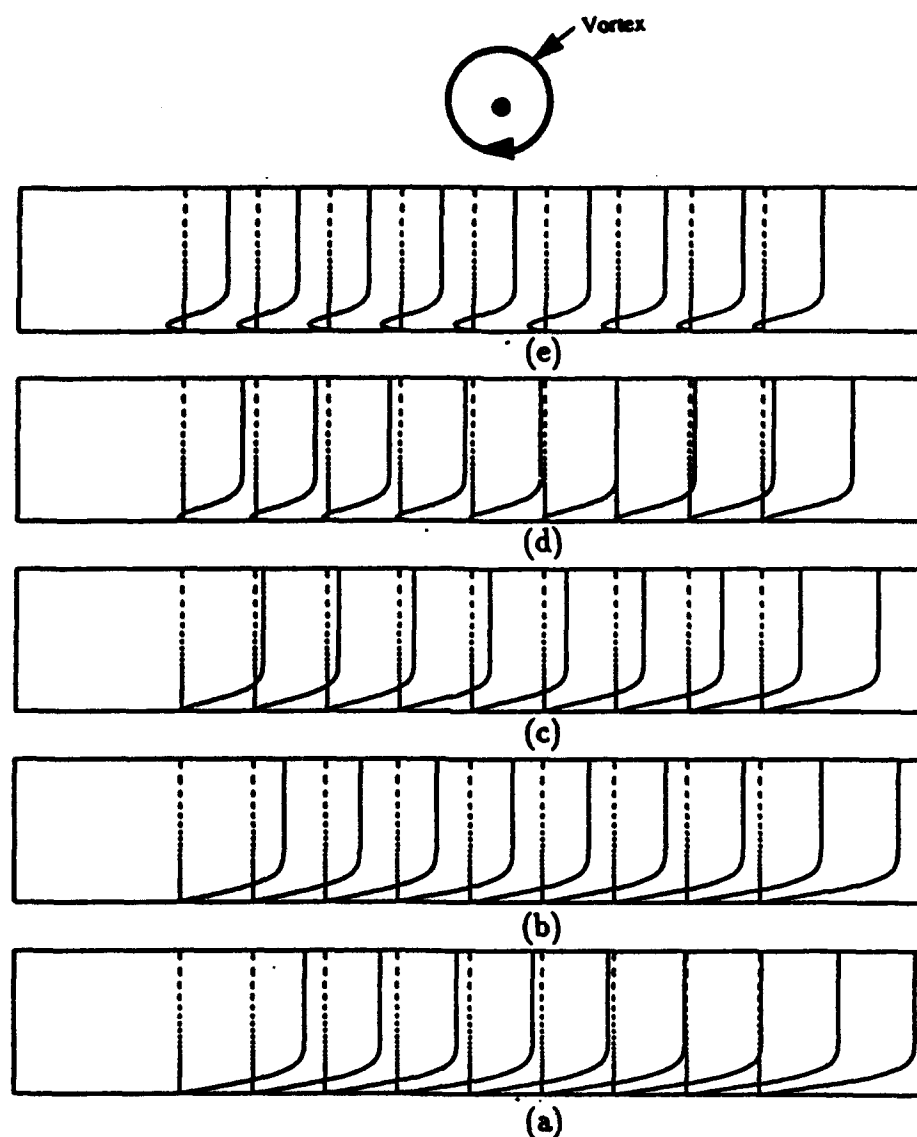


Figure 5.49: Temporal development of the velocity profiles of u_z plotted across the boundary-layer $0 \leq \eta \leq 6$ at various times: (a) $t=0.0711$ ($\psi = 6^\circ$), (b) $t=0.1421$ ($\psi = 12^\circ$), (c) $t=0.2133$ ($\psi = 18^\circ$), (d) $t=0.2843$ ($\psi = 24^\circ$), (e) $t=0.3554$ ($\psi = 30^\circ$). The profiles are shown at 9 equally spaced locations which are centered around $z=0.75$ and separated by $\Delta z=0.025$. The results are for the asymmetric mean flow case.

5.6 Discussion

The boundary-layer flow results discussed above show that, in all three mean flow cases (i.e. the stagnant medium, the symmetric mean flow and the asymmetric mean flow case), a reversed flow region develops when the vortex filament is well above the cylinder. This secondary eddy grows in size with time and eventually it is expected that the boundary-layer fluid comprising the eddy will be ejected into the main stream. In addition, the primary vortex leaves a strong imprint on the surface of the cylinder as indicated by the results for the enstrophy. For the stagnant medium and for the symmetric mean flow case, the secondary eddy leaves a U-shaped enstrophy scar on the wall of the cylinder.

The present computational results for the asymmetric mean flow case are consistent with the recent experiments of Komerath et al and are also consistent with the overall picture of the vortex-surface interaction as described earlier by Liou, Komerath and McMahon (1990). Their inferences based on those measurements show that the interaction process involves the creation of a secondary vortical structure prior to the impingement of the vortex on the airframe. The various stages of the interaction process as described by Liou, Komerath and McMahon (1990) are depicted on Figure 5.50. First, the approach of the primary vortex causes flow reversal near the surface. Secondly, a region of vorticity, which is opposite in sign to the vorticity associated with the main vortex, develops inside the boundary-layer underneath the tip-vortex when it is still well above the cylinder. Finally, as the tip-vortex approaches the cylinder the secondary structure moves above the tip-vortex and rolls over it. After impingement of the primary vortex on the cylinder the secondary vortex moves rapidly downstream under the effect of its image as well as the free stream, but rapidly dissipates. The present work supports this view although we are able to model only the initial stages of the development of a reversed flow region and secondary vortex deep inside the boundary-layer; despite the fact that the convection of the vortex can be continued until the vortex is within about one vortex core radius (Chapter 3), the viscous flow calculations cannot be continued accurately beyond about $\psi \sim 33.3^\circ$. Sometime after this the eruptive process is expected to begin and the recent flow visualization results suggests that the eruption process begins at about $\psi \sim 60^\circ$. The modelling of this eruptive process is extremely difficult and cannot be performed within the boundary-layer approximation; the modelling of the subsequent stages of the flow development and collision of the vortex with the cylinder is ongoing and the general characteristics of the entire vortex-body collision problem are described in the next Chapter.

Nevertheless, the boundary-layer results exhibit the development of a local short-length scale and a short-time scale separated region containing vorticity of a sign opposite to that in the main vortex with a subsequent eruption of the

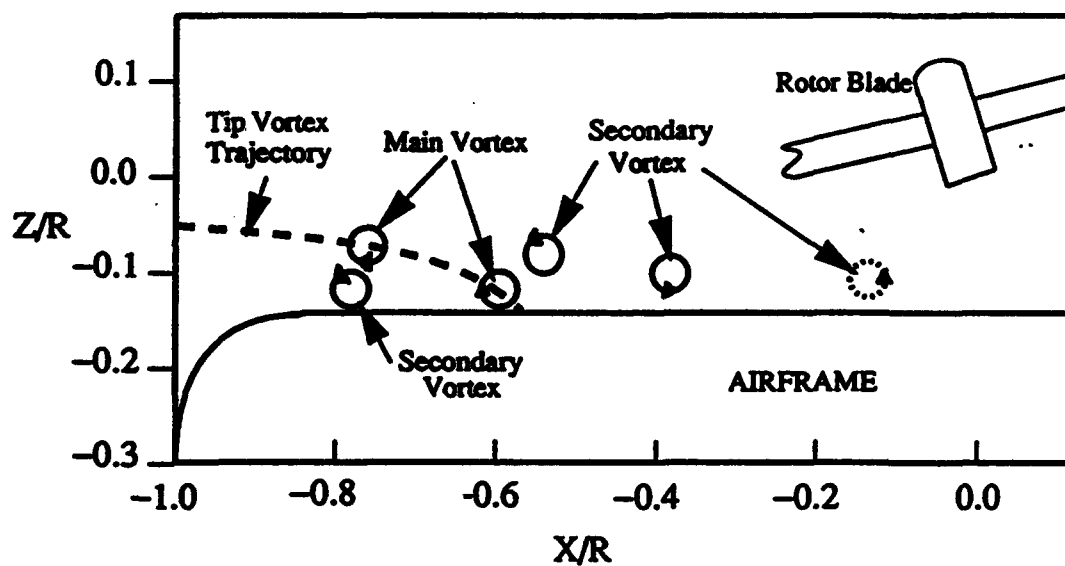


Figure 5.50: Different stages of the interaction of the tip-vortex with the airframe as observed experimentally by Liou, Komerath and McMahon (1990). The coordinate system on this figure is in the notation of the LKM paper.

boundary-layer fluid into the free stream likely.

The eruptive phenomena described here have also been observed in the water-channel experiments of C. R. Smith and his colleagues at Lehigh University. On Figure 5.51 are results taken from the interaction of a three-dimensional vortex system and a cylinder (Smith et al 1991). The induced surface eruptions are visualized using hydrogen bubbles and light-sheet illumination. On Figure 5.51(c-f) are photographs of the temporal development of the vortex-induced surface layer that abruptly focuses into the sharply eruptive spire. Here the eruptive phenomena is clearly seen in the development of a strong shear layer upstream of the main primary vortex which is denoted by the white circular blob of fluid.

It is clear from this discussion of two separate sets of experiments, one set in water and one set in air, that the boundary-layer eruption phenomena which occur when a vortex passes near a surface are generic and will occur in all cases where the vortex is sufficiently strong. However, within the context of classical boundary layer theory, the viscous correction to the normal surface load during the time period when the vortex is sufficiently far from the body is zero, since the pressure is impressed by the inviscid flow on the boundary layer. In this situation, the normal load may be calculated based on a purely inviscid approach. A viscous correction to the normal load on the body will occur on collision and just prior to collision when the outer inviscid flow is permitted to vary as the viscous flow develops. This problem is addressed in Chapter 8.

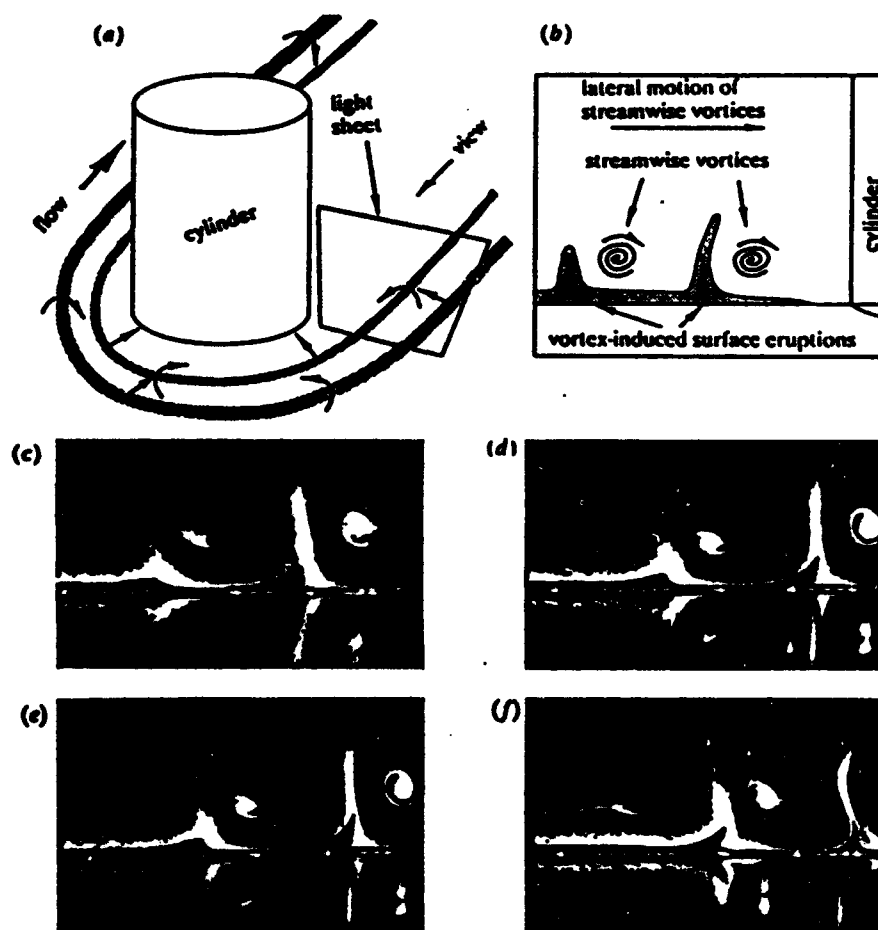


Figure 5.51: End view of necklace vortex legs and induced surface eruptions (from Smith et al. 1991).

CHAPTER VI

The Vortex-Body Collision Problem

6.1 Introduction

In the previous chapters, the motion of the tip-vortex shed from a helicopter rotor blade has been calculated and compared quantitatively with experimental data. In addition, the evolution of the viscous flow so generated under the tip vortex has also been calculated and compared qualitatively with experiment. In both cases, the flow field has been examined during the time interval prior to the collision of the vortex with the airframe. The previous results indicate that when the vortex is far from the airframe, a simple Rankine core is sufficient to predict both the vortex position and the pressure on the top of the airframe with good accuracy (See figures 3.6 and 3.8, for example.). The purpose of the present chapter is to provide a framework to develop a comprehensive model of the vortex-airframe impingement including the collision and subsequent convection of the vortex down the sides of the airframe. In what follows, we discuss qualitatively the picture of the entire impingement and collision process based on the analytical/numerical work discussed previously and the experimental results produced at the Rotorcraft Center of Excellence at Georgia Institute of Technology so far.

The previous experimental and computational work has suggested that one view of the general vortex impingement problem may include three relatively distinct phases; the first phase corresponds to pre-collision described in the previous chapters in this report (Phase 1); the second phase is the actual collision process (Phase 2); the third phase corresponds to the post-collision phase in which the end of the vortex filament and the boundary layer on the airframe coincide (Phase 3). Furthermore, the collision phase may be subdivided into three sub-phases which we term Phases 2.1, 2.2, and 2.3. Phase 2.1 is characterized by the commencement of the deformation of the vortex core, during which a non-zero fluid velocity develops in coordinates moving with the vortex core in a direction normal to the boundary of the vortex core (i.e. a local radial velocity). During this phase the

vortex core begins to deform as the local radial velocity approaches the magnitude of the azimuthal velocity. At some point, however, as the vortex further approaches the airframe, mass flux requirements suggest that the axial velocity, if it is not initially large, must reach the order of magnitude of the other two velocity components (Phase 2.2). It is postulated that fluid in the vortex core must then be expelled from the region adjacent to the airframe in a direction along the centerline of the vortex. The local flow fields described above in Phases 2.1 and 2.2 are inviscid in character. In Phase 2.3, the portion of the vortex impacting the airframe must merge with the boundary layer flow; this process must include a reduction in the local magnitude of the swirl velocity within the vortex and this point is discussed more fully below.

In what follows we consider the characteristics of Phases 2.1 and 2.2 in some detail. The governing equations for Phases 2.1 and 2.2 are derived based on the equations of Callegari and Ting (1978) dropping the assumption of an axisymmetric outer flow field. Chapter 7, following, considers detailed computations of a model for the local vortex flow field during Phase 2.1. The present Chapter concludes with a short discussion of Phases 2.3 and 3.

Of necessity, much of the content of the discussion of Phases 2 and 3 of the present Chapter must be somewhat speculative because the work is ongoing. The present unified description of the vortex impingement problem is only one view and many of the details of what is said here must await further computational and experimental verification. Lastly, the present view of vortex-body collisions applies to the situation where the ratio of the vortex core radius to the characteristic body length scale is small but finite and to the case of a strong vortex in the sense that the dimensionless circulation $\Gamma = \frac{\Gamma^*}{W_{\infty} a}$ is $O(1)$.

6.2 Phase 2.1: Initial Deformation of the Vortex Core

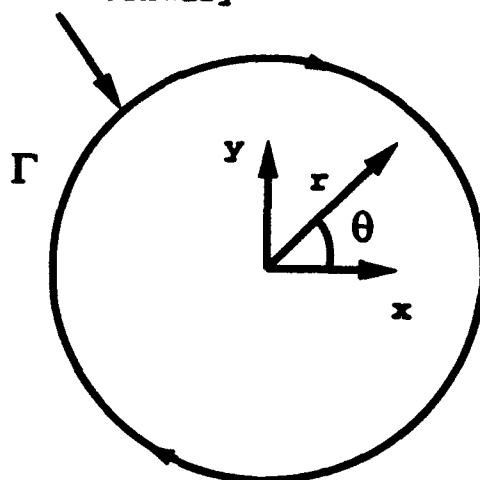
As mentioned earlier, the value of μ in equation (2.20) is obtained assuming that the vortex core structure is locally axisymmetric. To investigate the possible modification of this structure as the tip-vortex approaches the cylinder, the velocity field around the core has been investigated and those results are discussed in Chapter 2 (see Figure 2.15). As shown there, a finite radial velocity at the assumed vortex core boundary begins to develop just prior to the collision of the vortex with the airframe. Based on the results of Figure 2.15, the flow in the core of the vortex must subsequently be permitted to vary with time and location along the vortex if the local radial velocity at the vortex boundary becomes of the order of the local azimuthal velocity, leading to a new value for μ at each point along the vortex and at each time. Dhanak (1981) has described an approach in which the value of μ varies with time according to an overall vortex volume conservation rule; the vortex core flow remains axisymmetric and locally steady. However the experimental

results of Liou, et al(1990) suggest a significant deformation of the vortex core from a circle so it is unlikely that an approach incorporating only changes in the value of μ with space and time would be sufficient unless the shape of the vortex were permitted to change as well. The calculation of an appropriate value of μ for a non-circular core has not been attempted and it is unclear how the value of μ would be defined. Recall that μ is calculated to fit the result for the vortex ring. Consequently, we have developed a model for vortex-core deformation based on a multiple vortex model and this is discussed in the next chapter. The motivation for an essentially inviscid approach to this phase of the motion of the vortex is elucidated by investigation of the governing equations in the core of the vortex and these equations are discussed below.

The equations of motion relative to the motion of the space curve defining the centerline of the vortex have been derived by Callegari and Ting (1978). In that work, the image-induced component of the local velocity field around the vortex is zero and the azimuthal velocity just outside the vortex is the free vortex axisymmetric solution; therefore the core flow will remain axisymmetric if it had originally been axisymmetric. In the present problem, however, as the vortex approaches the cylinder, the image-induced velocity gets progressively larger until it eventually influences the azimuthal velocity field in the vortex core; since the image induced azimuthal velocity is not axisymmetric with respect to the vortex core, the velocity within the core of the vortex must deviate from the simple Rankine vortex model assumed when the distance of the vortex from the surface becomes of the same order as the vortex core radius. This loss of symmetry will result, by local continuity, in the emergence of finite radial and axial velocities within the vortex core (even if such an axial velocity did not exist prior to the strong interaction); the numerical results suggest that this process begins when the vortex is still outside the boundary layer. It is important to note that the substantive loss of axisymmetry of the vortex core flow will not occur until the radial velocity within the core becomes of the same order as the azimuthal velocity; see below. For this reason the calculations performed in Chapter 2 are still approximately valid even for the last time shown on Figure 2.15. In addition, it is necessary to reiterate that the present equations hold only within the vortex core; simultaneously, the boundary layer is erupting around the core and this phase of the development of a new vortex-core flow is thought to occur long after the boundary layer computations presented in the previous Chapter have failed.

It is useful first to consider the case where the axial velocity in the vortex core is not large and in the situation where the local radial velocity is of the same order of magnitude as the azimuthal velocity; again the occurrence of this situation at later times is suggested by the results of Figure 2.15. The governing equations relative to the motion of the vortex core were first derived without the azimuthal variation by Callegari and Ting(1978). In a local coordinate system traveling with

Vortex Core Boundary



(a)

Vortex



Airframe

(b)

Figure 6.1: The local coordinate system around the vortex which is used in the present chapter. (a) View of the vortex core boundary; this is from a side view of the airframe. (b) End view showing airframe.

the vortex(Figure 6.1; $\bar{r} = r\epsilon^{-1/2}$) the equations are

$$u_0 \frac{\partial u_0}{\partial \bar{r}} + \frac{1}{\bar{r}} v_0 \frac{\partial u_0}{\partial \theta} - \frac{v_0^2}{\bar{r}} = -\frac{\partial p_0}{\partial \bar{r}}, \quad (6.1)$$

$$u_0 \frac{\partial v_0}{\partial \bar{r}} + \frac{1}{\bar{r}} v_0 \left(\frac{\partial v_0}{\partial \theta} + u_0 \right) = -\frac{1}{\bar{r}} \frac{\partial p_0}{\partial \theta}, \quad (6.2)$$

$$u_0 \frac{\partial w_0}{\partial \bar{r}} + \frac{1}{\bar{r}} v_0 \frac{\partial w_0}{\partial \theta} = 0, \quad (6.3)$$

where the expansions of the velocity vector and the pressure are(Callegari and Ting 1978)

$$\vec{V} = \frac{1}{\epsilon} \vec{V}_0 + \dots, \vec{V}_0 = (u_0, v_0, \epsilon w_0),$$

$$p = \frac{1}{\epsilon^2} p_0 + \dots$$

Here ϵ may be identified with a local Reynolds number based on the vortex circulation: $\epsilon = Re_v^{-1/2}$ where $Re_v = \Gamma/\nu$. Note that the axial velocity within the vortex core is effectively decoupled from the rest of the velocity field. The viscous terms in the equations are negligible, thus indicating that an inviscid model of the initial stages of vortex deformation is appropriate. The experimental data taken by Professor Komerath and his colleagues at Georgia Tech indicate that the vortex Reynolds number is of the same order of magnitude as the Reynolds number based on free stream speed and the cylinder radius: $Re = \frac{W_\infty a}{\nu}$ say. This means that the vortex core size is nominally of the same size as the boundary layer on the airframe. The continuity equation is given by

$$\frac{\partial \bar{r} h_3 u_0}{\partial \bar{r}} + \frac{\partial h_3 v_0}{\partial \theta} = 0, \quad (6.4)$$

where h_3 is the scale factor in the s-direction and is defined in Callegari and Ting(1978).

We can deduce some properties of the flow field by integration of equation (6.4) around the vortex, and

$$\frac{\partial}{\partial \bar{r}} (h_3 \bar{r} \int_0^{2\pi} u_0 d\theta) = 0. \quad (6.5)$$

For the axisymmetric case, this equation is identically satisfied since $u_0 = 0$. For ϵ small, the quantity under the integral sign is the radial flux of fluid across a line \bar{r} within the vortex. Integrating in \bar{r} we have

$$h_3 F(\bar{r}, \theta, s) = h_3 \int_0^{2\pi} \bar{r} u_0 d\theta = h_3 F_0(\theta, s), \quad (6.6)$$

where F_0 may be identified with the total flux at the boundary of the vortex and s is a variable measuring distance along the vortex centerline (Figure 6.1). This should not be confused with the parametric variable s used to define the vortex in Chapters 2 and 3. Although the term "boundary of the vortex" is, strictly speaking, a somewhat fictitious concept, based on the cut-off procedure used to model the flow in the vortex core, it seems natural to view the results of Figure 2.15 as indicating the development of a "flux" of fluid into the core. Indeed, Figure 2.15 suggests that the radial velocity at the boundary of the vortex does become negative at points closest to the cylinder ($\theta \sim 315^\circ$) as the vortex approaches although the magnitude of the velocity at the time depicted on Figure 2.15 is not large. Shortly after this time the vortex core boundary deformation must be taken into account.

In scaled vortex coordinates, the vorticity component along the axis of the vortex is the largest and of $O(\epsilon^{-2})$; the component is given by

$$\zeta = \frac{1}{\bar{r}h_3} \frac{\partial}{\partial \bar{r}}(\bar{r}v_0) - \frac{\partial u_0}{\partial \theta}. \quad (6.7)$$

Note that by assumption of a Rankine vortex core, the vorticity within the core of the vortex is constant during Phase 1; during Phase 2.1, however, equation (6.7) indicates that the vorticity varies with time; note too that the local velocity field induced by the vortex is quasi-two dimensional, involving only relatively slight bending of the vortex. Also the vorticity is larger than the maximum vorticity in the boundary layer which is $\zeta_{BL} \sim \epsilon^{-1}$.

As the above analysis and the results of Chapter 5 indicate, the vortex flow during Phase 2.1 is still predominantly inviscid and the viscous flow on the airframe is in the process of erupting. As the vortex core begins to deform, the boundary layer continues to evolve and locally, it can be shown that the eruption process becomes essentially inviscid as well (van Dommelen and Cowley 1990; Elliott, Cowley, and Smith 1983). A possible picture of the combined viscous-inviscid interaction on the airframe is depicted on Figure 6.2 based on the experimental visualization results depicted in Figure 5.47. Here the tip-vortex has partially penetrated the boundary layer and the viscous flow on the airframe is dominated locally by the evolution of an eruptive region of fluid as sketched on Figure 6.2. At this point in time both the flow inside the core of the vortex and the flow in the eruptive region are dominated by inviscid dynamics since the velocities are locally large in both the vortex and the boundary layer; in addition, the streamwise length scale of the eruptive region is progressively shortening. As noted just above, this time regime is far beyond the time frame for which the boundary layer solutions of Chapter 5 are valid. The time at which this phase commences depends on the relative magnitudes of the boundary layer and vortex Reynolds numbers. At this stage, the pressure suction peak due to the tip vortex is *decreasing* in amplitude, perhaps due to the change

in the vortex core flow (see Chapter 7 following) and the presence of the eruptive region. The streamwise length scale of the eruptive region in the experiments is about 10 mm while the nominal boundary layer thickness is about 2 mm.

This structure applies for the vortex and mean flow Reynolds numbers of the same order of magnitude. Clearly, the physical situation is much different if the vortex is sufficiently weak so that the boundary layer does not erupt before collision of the vortex with the airframe.

It is interesting to note that the inclusion of a large axial velocity within the vortex core does not change any of the analysis described. This means that the initial deformation of the vortex core is solely an adjustment of the azimuthal and radial velocity fields.

6.3 Phase 2.2: Vortex Core Jet Development

As much of the vortex core comes within a boundary layer thickness of the airframe, rapid variations in the flow field around the impact point are expected. In this regime the derivatives along the vortex centerline become important and the Navier-Stokes equations reduce to

$$u_0 \frac{\partial u_0}{\partial \bar{r}} + \frac{1}{\bar{r}} v_0 \frac{\partial u_0}{\partial \theta} - \frac{1}{\bar{r}} v_0^2 + \frac{w_0}{h_0} \frac{\partial u_0}{\partial \bar{s}} = - \frac{\partial p_0}{\partial \bar{r}} \quad (6.8)$$

$$v_0 \frac{\partial u_0}{\partial \bar{r}} + \frac{1}{\bar{r}} v_0 \left(\frac{\partial v_0}{\partial \theta} + u_0 \right) + \frac{w_0}{h_0} \frac{\partial u_0}{\partial \bar{s}} = - \frac{1}{\bar{r}} \frac{\partial p_0}{\partial \theta} \quad (6.9)$$

$$u_0 \frac{\partial w_0}{\partial \bar{r}} + \frac{1}{\bar{r}} v_0 \frac{\partial w_0}{\partial \theta} + \frac{w_0}{h_0} \frac{\partial w_0}{\partial \bar{s}} = - \frac{\partial p_0}{\partial \bar{s}}. \quad (6.10)$$

where the expansions of the velocity vector and the pressure are the same as in the previous subsection except that the axial velocity is $O(\epsilon^{-1})$; here $\bar{s} = s/\epsilon$. The continuity equation is given by

$$\frac{\partial \bar{r} h_3 u_0}{\partial \bar{r}} + \frac{\partial h_3 v_0}{\partial \theta} + \frac{\bar{r}}{h_0} \frac{\partial w_0}{\partial \bar{s}} + \epsilon \bar{r} \frac{\partial \vec{X}}{\partial \bar{s}} \cdot \hat{\tau} = 0, \quad (6.11)$$

where h_0 is defined by $h_3 = h_0 + \epsilon h_1 + \dots$ and $\hat{\tau}$ is a unit vector in the direction along the axis of the vortex core. Note that we have included a term in the continuity equation which is multiplied by ϵ ; the term $\frac{\partial \vec{X}}{\partial \bar{s}}$ reflects the fact that the acceleration of the vortex centerline varies along the vortex. It is unclear from the present work whether this term will be important in the solution process. However if the time scale during this phase of the motion is fast and of $O(\epsilon)$ then the term will be important.

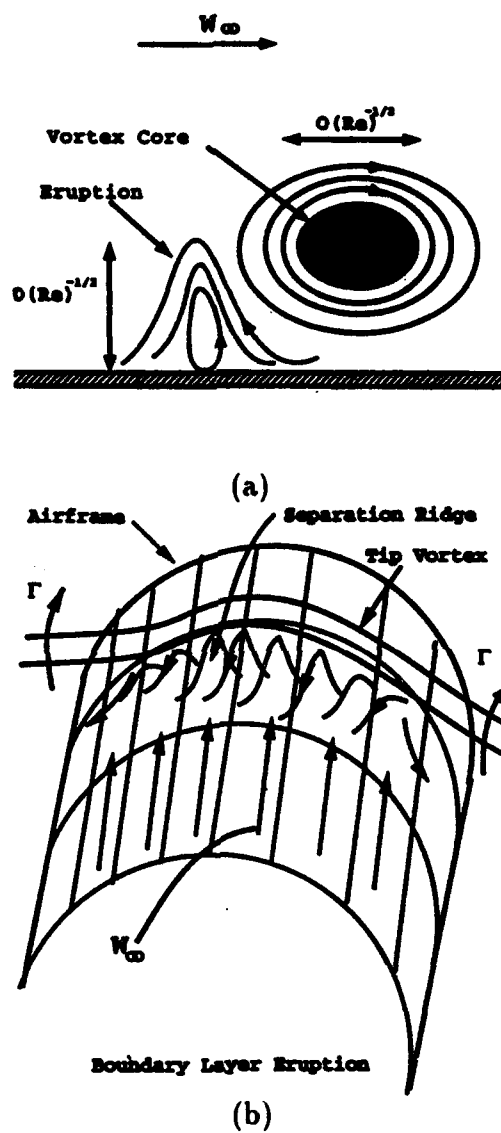


Figure 6.2: The physical picture of a three-dimensional erupting boundary layer flow under a rotor tip vortex during Phase 2.1. (a) Side view of the vortex and fluid erupting from the boundary layer. (b) Perspective view showing approximate spanwise extent of secondary separation.

Some information may be obtained by integration of the continuity equation around the core in θ and along the filament is \bar{s} . The result is

$$\begin{aligned} \frac{\partial}{\partial \bar{r}} \left\{ \bar{r} h_0 \int_{-\infty}^{\infty} \bar{u} ds \right\} + \bar{r} \{ w_0(\bar{r}, \infty) - \bar{w}_0(\bar{r}, -\infty) \} \\ + 2\pi \epsilon \bar{r} \int_{-\infty}^{\infty} \frac{\partial \bar{X}}{\partial \bar{s}} \bullet \bar{\tau} ds = 0 \end{aligned} \quad (6.12)$$

where the overbar on the velocities indicate their azimuthal (with respect to the vortex core) averages. Equation (6.12) clearly indicates that the development of a finite radial velocity in a local region around the impact point results in the generation of an axial flow component as well as the possible axial stretching of the vortex filament. Note however that the response of the vortex in this stage of the impact process is still inviscid. During this stage, the viscous terms are still $O(\epsilon^{-1})$ whereas the leading order terms in equations (6.8) to (6.11) are of $O(\epsilon^{-3})$.

As pointed out by Batchelor (1967, p. 553), the axial flow in the core of a rotor-tip vortex is wake-like rather than jet-like. This means that the axial flow in the core region is in a direction back toward the rotor blade. Thus on the advancing side of the rotor, on collision, the axial velocity in the vortex core must change sign; on the retreating side, the original flow is in the same direction as the subsequent jet flow. Consequently, in the case of the actual rotorcraft problem, the collision process is likely to appear quite different depending on which side of the airframe the interaction is being observed.

6.4 Phase 2.3: Final Merger With the Boundary Layer

In Phase 2.2 the velocities within the core of the vortex are still very large, with the leading order terms being of $O(\epsilon^{-1})$. Thus, these velocities are much larger than the boundary layer velocities which are $O(1)$. It is for this reason that the vortex-body collision process is violent and it is the incorporation of the viscous terms which must reduce the leading order velocities in the vortex core locally to the order of the velocities in the boundary layer. During this phase of the motion the fluid within the boundary layer on the airframe and the fluid which is located within the core of the vortex become indistinguishable; in this regard, it is often stated that a vortex is "chopped" by a body on impingement. The interpretation of this statement must be that an identifiable vortex structure no longer is present locally subsequent to impact and from the point of view of inviscid flow theory, the original single vortex appears to be "split" into two. As noted earlier, the vorticity component in the tip-vortex which is largest is associated with the swirl component within the vortex and this vorticity component is $O(Re_v)$. The vorticity associated with the boundary-layer flow is $O(Re_v^{1/2})$ and so the swirl within the

vortex must locally be reduced to the same order as the velocities in the boundary layer. Note that as the swirl velocity is reduced, the area of the vortex core must increase to keep the circulation constant until viscous forces act to alter the circulation (Batchelor 1967). In addition any large axial flow along the vortex centerline must also be reduced to the same order as in the boundary layer and we can thus speak, in an asymptotic sense of the development of local stagnation points in all three velocity components. It is clear that viscosity must be the physical agent whereby the swirl velocity is reduced within the vortex core and this problem is now under investigation.

6.5 Phase 3: Convection of the Vortex Along the Airframe

In this phase of the process, the end of the vortex coincides with the viscous layer on the airframe boundary. Consequently, the inviscid flow is much different from that described earlier because one vortex point lies essentially on the airframe. The boundary layer flow is considerably different from that discussed in Chapter 5. Analysis of this problem is ongoing and the results will be reported subsequently.

6.6 Summary

Based on the previous calculations described in Chapters 2 to 5 of this work, and on fundamental experiments, a unified picture of the vortex-body collision problem has been formulated. The process has nominally been viewed to consist of three distinct phases. The first phase corresponds to the pre-collision phase in which the flow due to the vortex may be effectively modelled using inviscid flow methods. Phase 2 has nominally been viewed to consist of three separate subphases. The first two subphases are characterized by the deformation of the vortex core, the development of a time-varying velocity field within the vortex core and the emergence of a jet-type flow along the axis of the vortex. The third subphase corresponds to the physical process whereby fluid within the vortex core and boundary layer fluid become indistinguishable; in this situation the viscous terms must be included to reduce the velocity field in the vortex from $O(Re_v^{1/2})$ to the magnitude of the velocity field in the boundary layer. Phase 3 of the process is characterized by the fact that the end of the vortex and the airframe coincide.

Having formulated a picture of the vortex-body collision process, we now consider the development of a multiple vortex model to simulate the initial stages of Phase 2.1.

CHAPTER VII

A Model for the Deformation of the Vortex Core

7.1 Introduction

In this chapter we present detailed results of the modelling of the initial stages of Phase 2.1 in which the vortex core deforms from a circle to a roughly elliptical shape. The present model has been developed for the case of a symmetric mean flow as discussed in Chapter 2. It had been postulated that the decrease in amplitude of the pressure spike seen in the experiments at about $\psi = 54^\circ$ (Figure 3.6g) may be due to vortex-core deformation effects. The results of the current model indicate that the deformation of the vortex core does indeed reduce the amplitude of the pressure suction peak prior to impact of the vortex with the airframe. These results are thus consistent with experimental observation even though results have not been produced for the specific case of an asymmetric mean flow. We begin with a discussion of the corresponding two-dimensional problem for which similar results are evident.

7.2 The Two Dimensional Point-Vortex Model

Formulation

To test the hypothesis that the deformation of the vortex core is the cause of the initial modulation of the suction peak in the experiments around $\psi = 54^\circ$, the interaction of four two-dimensional point vortices with a flat plate was studied first. As noted previously, the inviscid results generated in Chapters 2 and 3 fail to predict such phenomenon due to the fact that the vortex core flow is assumed to be steady and the vortex core boundary rigid and in the shape of a circle.

To model the core deformation of actual vortex, we first consider four point vortices embedded in a two-dimensional mean flow to approximate the finite core of an actual vortex. In this model, four point vortices are placed above an infinite flat wall with clockwise circulation; the mean flow assumed corresponds to the superposition of a potential stagnation point flow and a uniform flow (U_∞) to the right of the wall, as shown in Fig 7.1. The uniform flow is used to prevent the point vortices from moving away from $x = 0$ too rapidly. The flow outside the point vortices is assumed to be potential.

The complex potential due to the superposition of two-dimensional stagnation flow and the uniform flow to the right is given by

$$F_m(z) = z^2 + z, \quad (7.1)$$

where z is the complex variable $z = x + iy$ and x and y are defined on Figure 7.1. The complex potential due to point vortices and their images is given by

$$F_v(z) = \phi + i\psi = \sum_{j=1}^4 \frac{k_j}{2\pi} [\ln(z - \bar{z}_{v_j}) - \ln(z - z_{v_j})], \quad (7.2)$$

where z_{v_j} denotes the position of the j th point vortex and z is a field point. \bar{z}_{v_j} is the complex conjugate of z_{v_j} . The variable k_j is the strength of point vortex j . Differentiating (1) and (2) with respect to z , we obtain the complex velocity, $W = u - iv$, due to the mean flow and the point vortices according to

$$W_m(z) = 2z + 1, \quad (7.3)$$

$$W_v(z) = \sum_{j=1}^4 \frac{ik_j}{2\pi} \left(\frac{1}{z - \bar{z}_{v_j}} - \frac{1}{z - z_{v_j}} \right), \quad (7.4)$$

with the total velocity being given by

$$W(z) = W_m(z) + W_v(z). \quad (7.5)$$

Given the initial position of the point vortices, the trajectories of the four point vortices are computed by integrating the equation

$$\frac{dz_v}{dt} = W(z_v). \quad (7.6)$$

The numerical method employed to integrate equation (7.6) is the Adams-Moulton method with a fourth-order Runge Kutta method as a starting scheme. It is important to note that there are two time scales involved in this problem. One is the short time scale due to the rotation of point vortices around each other. The other time scale is due to the convection of the point vortices with the mean

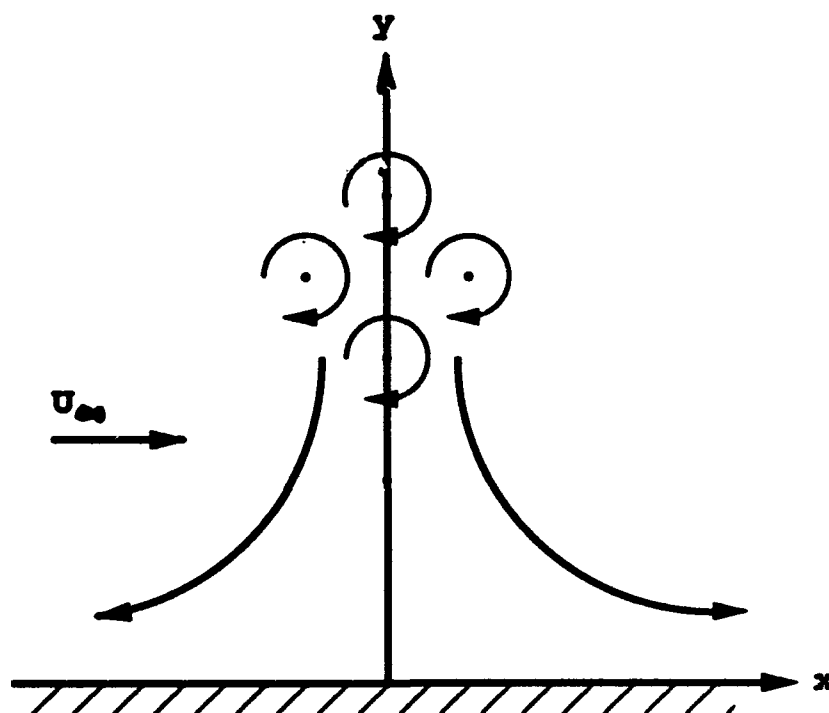


Figure 7.1: Two-dimensional point vortex model for the vortex core deformation.

flow and the velocity induced by the image vortices below the surface. To insure numerical accuracy, the time step used to integrate equation (7.6) should be much less than the short time scale. A time step of 0.001 was found to be accurate enough to ensure three digit accuracy when the strength of each of the four vortices is taken to be 1.

Similar to the previous work in Chapters 2 and 3, the pressure distribution on the wall is computed from the Bernoulli equation

$$\frac{\partial \phi}{\partial t} + \frac{|\vec{U}|^2}{2} + p = f_0(t), \quad (7.7)$$

where f_0 is the Bernoulli constant, here obtained by evaluating the left hand side of equation (7.7) at $x = \infty$; in the present numerical scheme we evaluate the Bernoulli constant at $x = 6.0$ on the wall. The dimensionless pressure is defined as $p = (p^* - p_\infty) / \rho U_\infty^2$, where p^* is dimensional and p_∞ is a constant reference pressure evaluated at $x = 6.0$. Note that in the calculation, velocities are normalized by U_∞ and length is normalized by characteristic distance a of the vortex cluster from the wall at time $t = 0$. The strength of point vortices k_j and the complex potential F are normalized by $U_\infty a$.

Numerical Results

We consider the case where the four point vortices are initially placed at (0.0,1.4), (-0.1,1.5), (0.0,1.6) and (0.1,1.5) respectively. The pressure variation on the wall at time 10.55, 10.65 and 10.70 respectively are depicted on Figure 7(a). From this figure we can see that the pressure suction peak for the four-vortex case increases as time increases from 10.55 to 10.65, then decreases from 10.65 to 10.70. As a comparison, Fig. 7.2(b) shows the results for a single point vortex convecting in the same mean flow as in the multiple point vortex model with its strength of the single point vortex equal to the total strength of the four point vortices. From this figure it is evident that the pressure distribution on the wall monotonically increases as the single point vortex approaches the wall. The corresponding positions of the four point vortices are plotted on Figure 7.3 for the same times as on Figure 7.2. This figure indicates that in a short period of time the orientation of the four point vortices changes dramatically; this results in a pressure oscillation at times greater than those shown on Figure 7.2. The frequency of oscillation corresponds to the frequency of rotation of the vortices around themselves; this oscillation will continue indefinitely because the vortices will never directly collide with the wall. Clearly this is not the situation in practice; however, the results of this relatively simple model of a vortical structure does indicate a mechanism by which the pressure suction peak may be modulated as a cluster of vortices

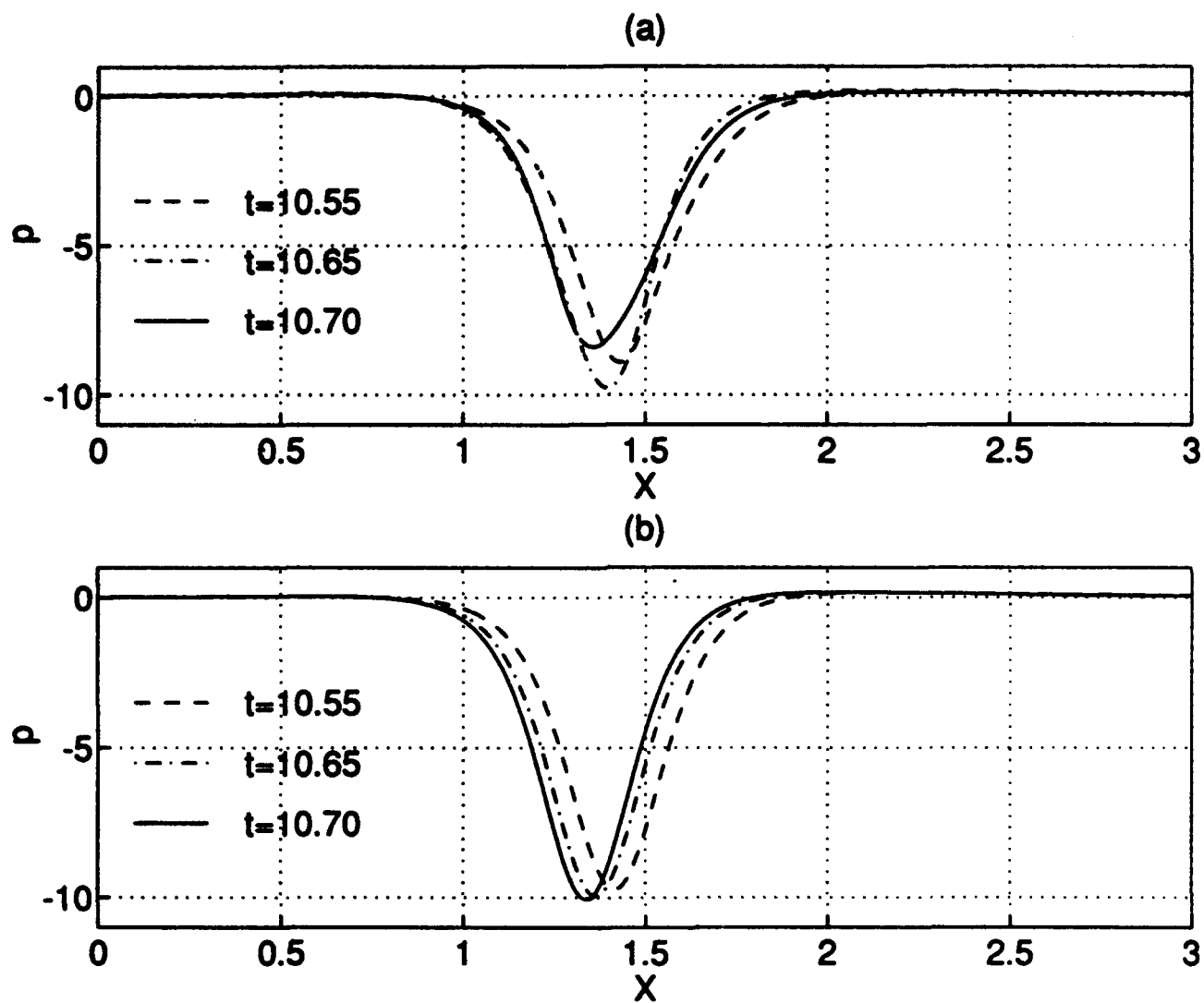


Figure 7.2: Pressure on the wall for the indicated times. (a) four vortices; (b) single vortex.

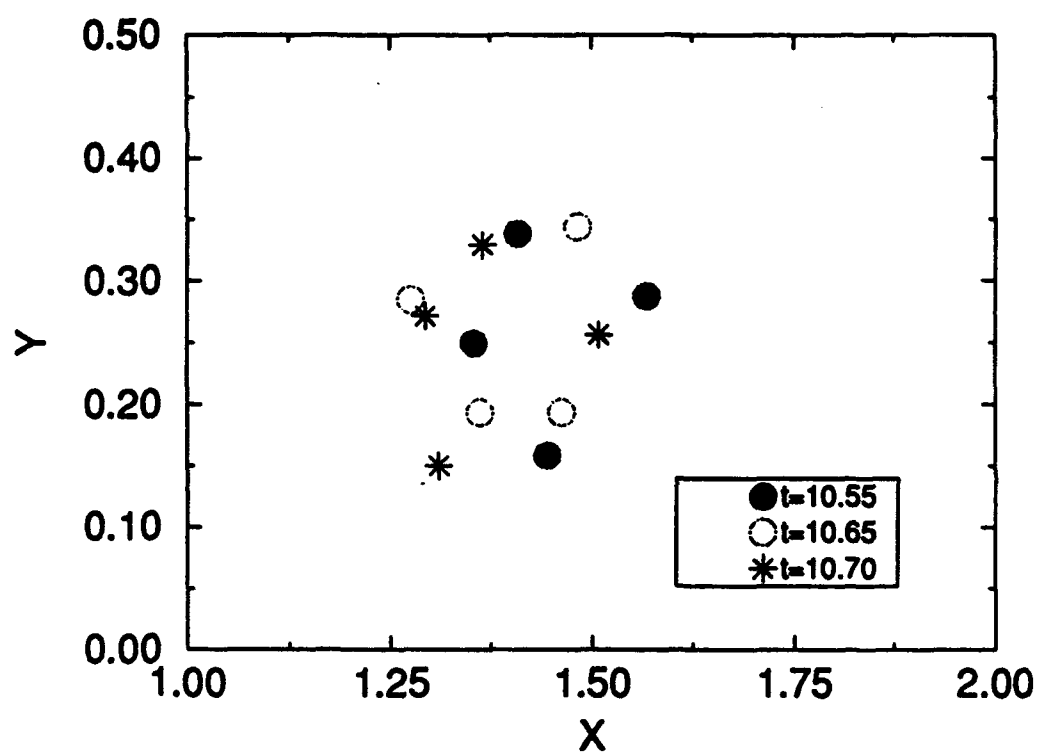


Figure 7.3: The position of four point vortices at several times.

approaches a solid surface. We now consider the corresponding three-dimensional problem of interest.

7.3 The Three Dimensional Multiple Vortex Model

Panel Method

The semi-analytical technique for the evolution of the three-dimensional tip vortex presented in Chapters 2 and 3 is sufficient to describe the motion of the tip-vortex as modelled by a single, finite-core vortex prior to collision; however, the form of the velocity potential makes it difficult to describe the actual collision phase of the motion and so it was decided that an alternative method is required to describe the motion of the vortex into the collision phase. For this reason, all of the results of this section were computed using a panel method.

To describe the panel method (Hess and Smith 1967), the infinitely long circular cylinder is first approximated by $M \times N$ rectangular source panels, where M is the number of panels along the cylinder and N is the number of panels around the cylinder. Figure 7.4 shows a three-dimensional oblique view of the cylinder panels; on this figure the panels are of equal size although a variable panel geometry is employed in the calculations. The vortex is similarly discretized and a typical set of constant-length vortex segments are also shown on Figure 7.4. Here \underline{X} , \underline{Y} and \underline{Z} are the global cartesian coordinates.

Let X, Y and Z denote the *local coordinates* of a single panel, as shown on Figure 7.5. Note that these coordinates are separate and distinct from those used in all the previous Chapters. Then the velocity components at (X, Y, Z) due to source element $q dX' dZ'$ at $(X', 0, Z')$ are given by

$$dU = \frac{dq}{4\pi} \frac{X - X'}{[(X - X')^2 + Y^2 + (Z - Z')^2]^{3/2}}, \quad (7.8)$$

$$dV = \frac{dq}{4\pi} \frac{Y}{[(X - X')^2 + Y^2 + (Z - Z')^2]^{3/2}}, \quad (7.9)$$

and

$$dW = \frac{dq}{4\pi} \frac{Z - Z'}{[(X - X')^2 + Y^2 + (Z - Z')^2]^{3/2}}. \quad (7.10)$$

To determine the velocity induced by the panel on other, neighboring panels, we integrate the local velocity field given by equations (7.8)-(7.10) over the rectangular panel and the result is

$$U = \frac{q}{4\pi} \ln \left(\frac{b - Z + \sqrt{(a - X)^2 + Y^2 + (b - Z)^2}}{b + Z - \sqrt{(a - X)^2 + Y^2 + (b + Z)^2}} \right)$$

$$+ \frac{q}{4\pi} \ln \left(\frac{b+Z - \sqrt{(a+X)^2 + Y^2 + (b+Z)^2}}{b-Z + \sqrt{(a+X)^2 + Y^2 + (b-Z)^2}} \right), \quad (7.11)$$

$$\begin{aligned} V = & \frac{q}{4\pi} \tan^{-1} \left[\frac{(a-X)(b-Z)}{Y \sqrt{(a-X)^2 + Y^2 + (b-Z)^2}} \right] \\ & + \frac{q}{4\pi} \tan^{-1} \left[\frac{(a-X)(b+Z)}{Y \sqrt{(a-X)^2 + Y^2 + (b+Z)^2}} \right] \\ & + \frac{q}{4\pi} \tan^{-1} \left[\frac{(a+X)(b-Z)}{Y \sqrt{(a+X)^2 + Y^2 + (b-Z)^2}} \right] \\ & + \frac{q}{4\pi} \tan^{-1} \left[\frac{(a+X)(b+Z)}{Y \sqrt{(a+X)^2 + Y^2 + (b+Z)^2}} \right], \end{aligned} \quad (7.12)$$

and

$$\begin{aligned} W = & \frac{q}{4\pi} \ln \left(\frac{a-X + \sqrt{(a-X)^2 + Y^2 + (b-Z)^2}}{a+X - \sqrt{(a+X)^2 + Y^2 + (b-Z)^2}} \right) \\ & + \frac{q}{4\pi} \ln \left(\frac{a+X - \sqrt{(a+X)^2 + Y^2 + (b+Z)^2}}{a-X + \sqrt{(a-X)^2 + Y^2 + (b+Z)^2}} \right), \end{aligned} \quad (7.13)$$

Here U, V, W are the velocity components in the local X, Y, Z coordinate system respectively, q is the uniform source density of a panel, a is the half length of a panel (and not the cylinder radius as used previously), b is the half width of a panel. Let q_k denote the source density of panel k , v_j denote the velocity due to external sources normal to the true cylinder surface lying directly above panel j . Then the source strengths q_k are obtained by solving the matrix equation

$$AQ = B, \quad (7.14)$$

where A is an MN by MN matrix of influence coefficients; the element A_{jk} is the normal velocity at point j on the surface due to the source panel k of unit density. Also Q is the column vector of source densities q_k , B is the column vector of normal velocities $-v_j$. From the above equation the source density vector Q is given by

$$Q = A^{-1}B \quad (7.15)$$

where A^{-1} is the inverse of A ; it is important to note that the matrix of influence coefficients A is independent of time and only needs to be calculated once. A

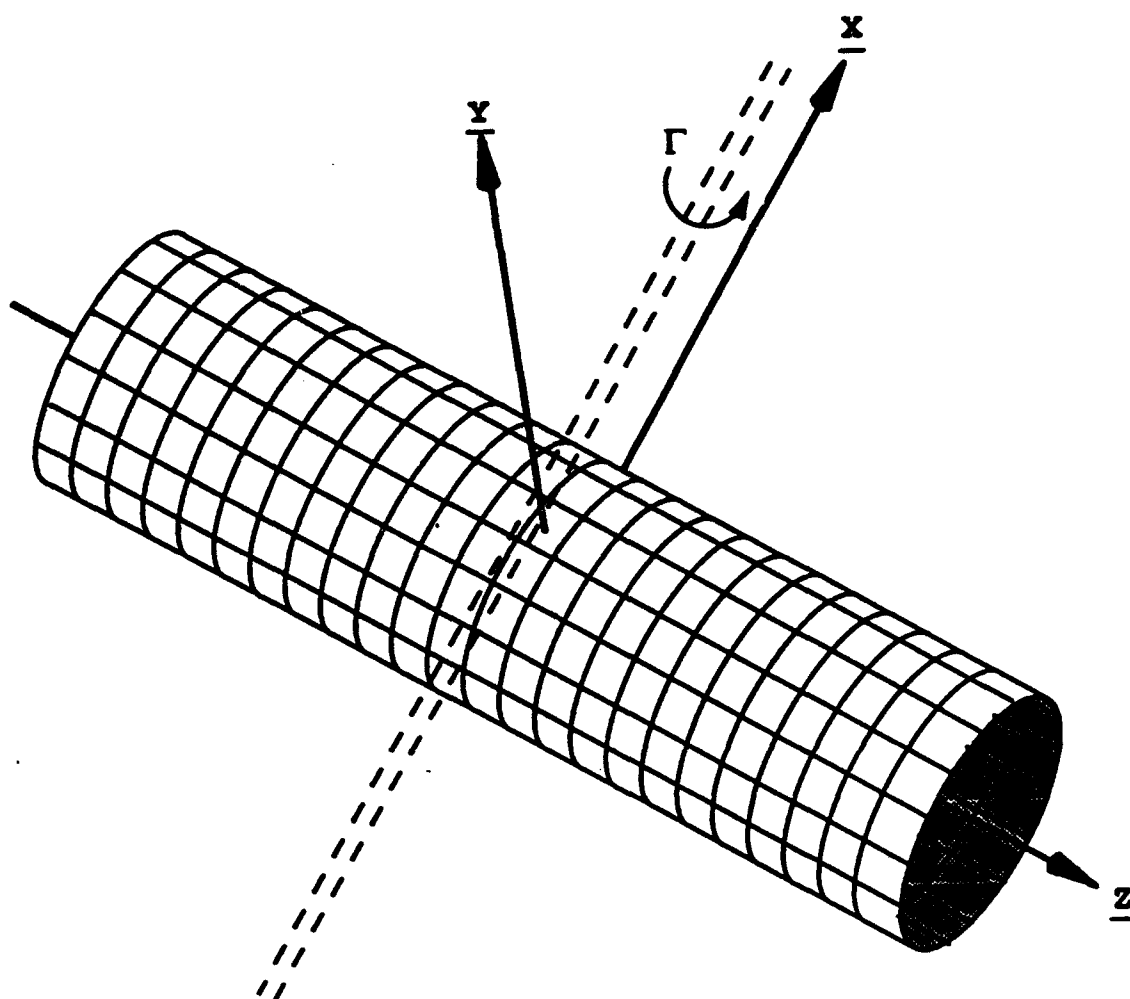


Figure 7.4: Three-dimensional oblique view of a typical set of cylinder panels and vortex segments for each being of constant size.

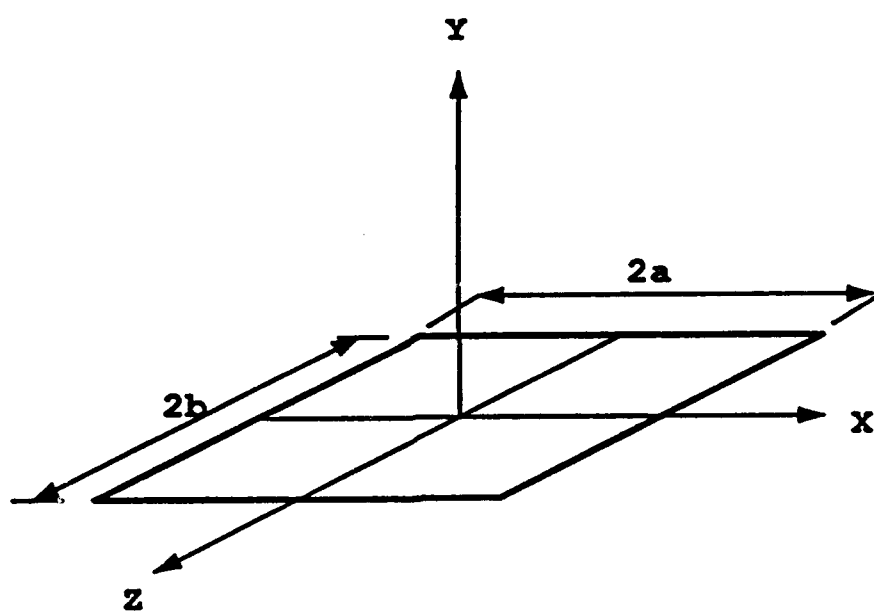


Figure 7.5: A single source panel and local panel coordinates.

LINPACK routine is employed to solve the system of equations defined by equation (7.14). In the present calculation, the mean flow is assumed to correspond to that described in Chapter 2.

Vortex Motion

As in the previous Chapters, the tip vortex is broken into M segments. Figure 7.6 shows a vortex line segment AB and field point C . The self-induced velocity field at the field point C by the vortex line segment AB is calculated by the modified Biot-Savart law as

$$d\vec{v} = \frac{\vec{\Gamma} \times \vec{r}}{4\pi(r^2 + \mu^2)^{3/2}} ds, \quad (7.16)$$

where μ is defined as in Chapter 2. In the calculation, μ is taken to be 0.11. Integrating over the length of the vortex-line segment, and taking local vortex coordinates $(\bar{X}, \bar{Y}, \bar{Z})$ such that the triangle ABC lies in the \bar{X} - \bar{Y} plane (i.e. \bar{Z} is fixed) with AB along the \bar{X} -axis, then the velocity induced by the vortex segment is in the \bar{Z} -direction and can be written as

$$w = \frac{\Gamma h}{4\pi} \int_{\bar{X}_A}^{\bar{X}_B} \frac{d\bar{X}}{[(\bar{X} - \bar{X}_C)^2 + h^2 + \mu^2]^{3/2}} = \frac{\Gamma h}{4\pi(h^2 + \mu^2)} (\cos \bar{\alpha} + \cos \bar{\beta}), \quad (7.17)$$

where

$$\cos \bar{\alpha} = \frac{\bar{X}_C - \bar{X}_A}{\sqrt{(\bar{X}_C^2 - \bar{X}_A^2) + h^2 + \mu^2}}, \quad (7.18)$$

and

$$\cos \bar{\beta} = \frac{\bar{X}_B - \bar{X}_C}{\sqrt{(\bar{X}_B^2 - \bar{X}_C^2) + h^2 + \mu^2}}, \quad (7.19)$$

This procedure is different from and simpler than that described in Chapter 2 because only local coordinates are used. However, the present formulation assumes that each vortex segment is straight; this assumption is not made in the procedure described in Chapter 2 where Simpson's rule is applied to the differential form of the Biot-Savart Law. The influence of this assumption does not appear to be significant if the length of the vortex segment is sufficiently small. Note that for $\mu \rightarrow 0$, both $\bar{\alpha} \rightarrow \alpha$ and $\bar{\beta} \rightarrow \beta$. In this Chapter α and β refer to the angles indicated on Figure 7.6. Note also that equation 7.17 reduces to the infinite line-vortex limit for both $\bar{\alpha}$ and $\bar{\beta} \rightarrow 0$.

The motion of a vortex above the circular cylinder is governed by equation (2.45) in the global vortex coordinates. The vortex is advanced using the Adams-Moulton multistep method. If the equation is given in generic form by

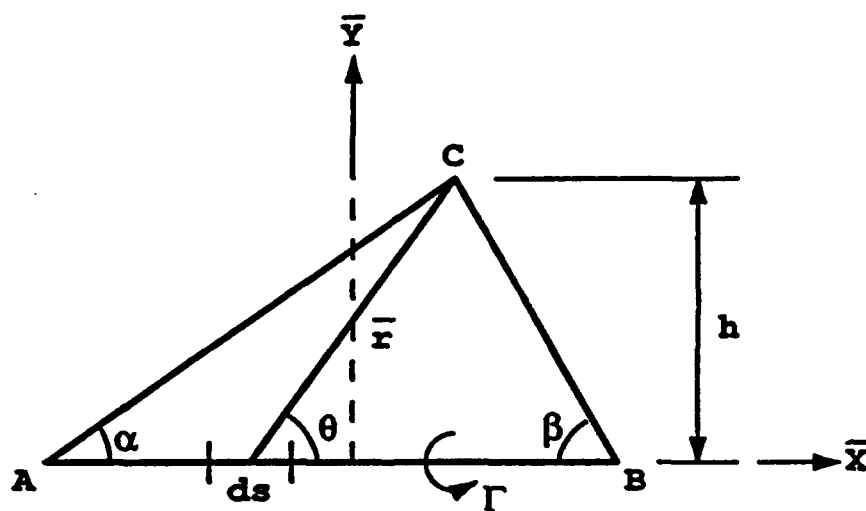


Figure 7.6: Vortex line segment AB and field point C .

$$\frac{d\vec{x}}{dt} = \vec{u}, \quad (7.20)$$

then the Adams-Moulton predictor-corrector method is defined by

$$\vec{x}_{i+1} = \vec{x}_i + \frac{h}{24}[55\vec{u}_i - 59\vec{u}_{i-1} + 37\vec{u}_{i-2} - 9\vec{u}_{i-3}], \quad (7.21)$$

for the predictor and

$$\vec{x}_{i+1} = \vec{x}_i + \frac{h}{24}[9\vec{u}_{i+1} + 19\vec{u}_i - 5\vec{u}_{i-1} + \vec{u}_{i-2}], \quad (7.22)$$

for the corrector, where the subscript i refers to discrete time values. The values of the solution vector \vec{x} at the first four time steps are computed by the explicit fourth-order Runge-Kutta method.

Since bending of the vortex occurs mainly at the locations directly above the cylinder, the length of a vortex segment varies along the vortex, with the finest segments taken directly under the vortex and near the top of the airframe. The length of a panel also varies in a way similar to the size of the vortex segments. The size of the vortex segment k and the length of the panel k are the same and the length is described by

$$\Delta_k = \Delta_{min} + Bk^2, \text{ for } k = 1 \text{ to } M/2, \quad (7.23)$$

where

$$B = 6 \frac{Z_{max} - \frac{M}{2}\Delta_{min}}{\frac{M}{2}(\frac{M}{2} + 1)}, \quad (7.24)$$

and where M is the number of panels along the z axis. Δ_{min} is the minimum size of the panel or vortex line segment. z_{max} is the assumed half-length of the (infinite) circular cylinder and of the vortex. The panel width in the θ direction varies according to the formula

$$\Delta\theta_j = \frac{2\pi}{N} - (\frac{2\pi}{N} - \Delta\theta_{min})\cos(\theta_j), \text{ for } j = 1 \text{ to } N/2, \quad (7.25)$$

where N is the number of panels in θ direction. $\Delta\theta_j$ is the width of the j th panel. $\Delta\theta_{min}$ is the minimum panel width in θ direction. The results of the panel method code have been compared with the results computed for the stagnant medium in Chapter 2 with agreement to two significant digits while using 81 panels on the cylinder in the streamwise direction and 32 panels in the θ direction; the previous results were computed using 101 points in the same direction.

Computational Results

The tip vortex is modeled using four infinitely long, initially straight vortices which are placed above the circular cylinder. Two sets of results will be discussed corresponding to a four vortex bundle and a nine vortex bundle. The four vortices are oriented along the spanwise direction in the global coordinate system (\bar{X} in the notation of this chapter), as shown on Figure 7.7. The global coordinates ($\bar{X}, \bar{Y}, \bar{Z}$) of the vortices in the symmetry plane are (0.0, 1.25, 0.0), (0.0, 1.30, -0.05), (0.0, 1.35, 0.0) and (0.0, 1.30, 0.05) respectively; thus the nominal radius of the bundle is 0.1, which is the core radius assumed in the calculations in Chapter 2, and close to the radius of 0.11 in the experiments. The minimum vortex segment (the same for all the individual vortices), the minimum length of a panel and the minimum width of a panel are taken to be 0.05. The maximum half length of the cylinder is taken to be 5.0.

The symmetric mean flow used in Chapter 2 is employed to convect the vortex filaments toward the circular cylinder. The strength of the vortex bundle is taken to be 2.2 which is the same as in the Georgia Tech experiments; the individual vortices have strength $2.2/4$. As in the two-dimensional multiple point-vortex case, there are two time scales involved in this problem. The shorter time scale is due to the rotation of the filaments around each other, and the longer time scale is related to the convection of the filaments due to the uniform mean flow and the image effect. Time steps corresponding to 0.01, 0.005 and 0.001 have been tested and a time step of 0.005 was found to be small enough to ensure three digit accuracy in the computed results. The dimensionless time is defined as in Chapter 5.

Figure 7.8 illustrates the bending of the vortex as it approaches the airframe; this behavior is similar to that of the single-vortex results. At this time the bottom of the vortex is less than one core radius from the airframe, as shown on Figure 7.9. Note that far from the airframe, the bundle is still circular whereas near the cylinder the bundle changes shape. Away from the airframe, the vortices are seen to roll about each other while remaining about the same distance apart. Figure 7.9 shows the vortex positions when viewed in the symmetry plane. Here we note the changing shape of the vortex core caused by the relative motion of the vortex bundle as it approaches the airframe. In addition, the nominal radius of the bundle has decreased indicating the presence of stretching in the spanwise or x -direction. The presence of the time scale where the vortices rotate about each other is shown in Figure 7.10. Here the vortex positions at three separate times in the later stages of the calculation are shown.

The time evolution of the nine-vortex bundle is shown in cross-section on Figure 7.11. Here the nominal radius of each individual vortex is $a_v = 0.033$ with the total area over which the vorticity is non-zero equal to that of the four-vortex case. Note again the deformation of the nominal vortex core and the rotation of the vortices about each other. From Figure 7.9, the nominal period of the four-vortex case is

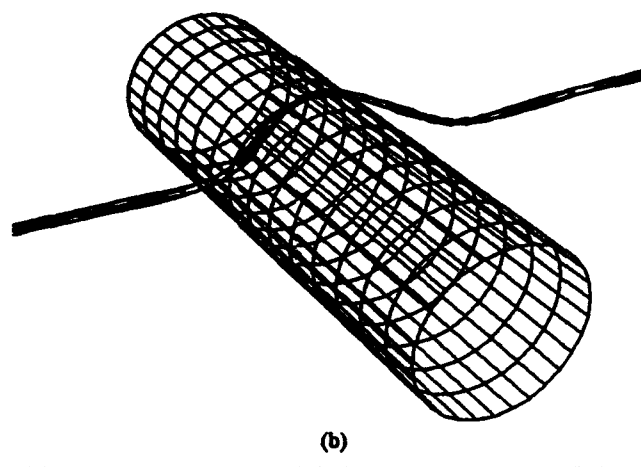
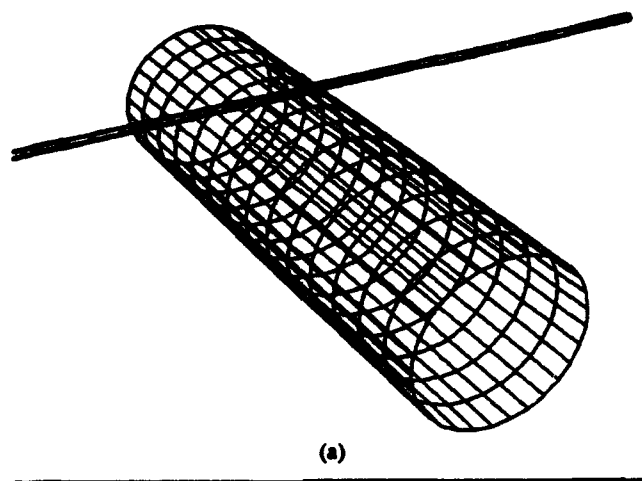


Figure 7.7: Three dimensional view of the four-vortex bundle showing local nature of the core deformation at two different times. The results are computed with a variable panel geometry even though a constant panel grid is shown. (a) $t = 0.0$, (b) $t = 0.6$.

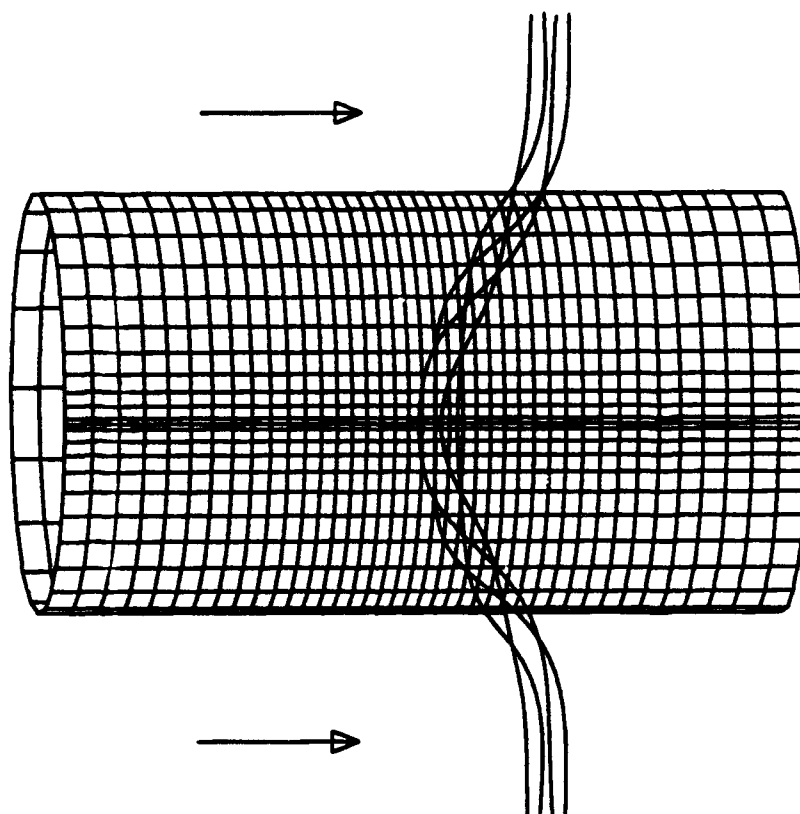


Figure 7.8: Top view of the position of the four-vortex bundle at $t = 0.5$ showing the variable panel distribution.

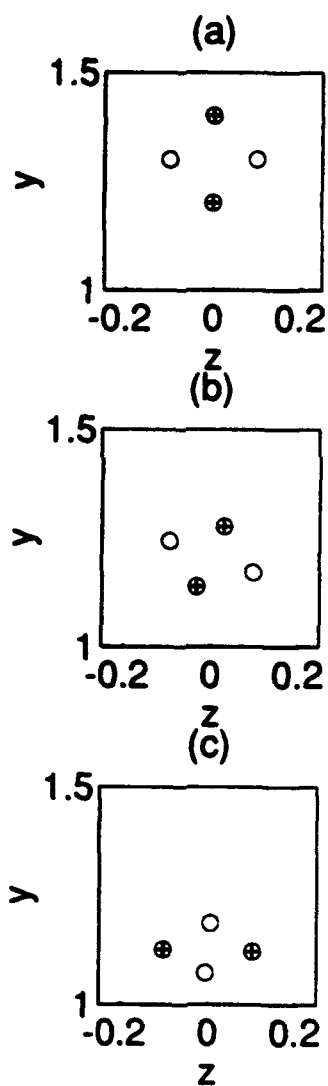


Figure 7.9: View of the four-vortex bundle motion on the symmetry plane for three times. (a) $t = 0.0$, (b) $t = 0.25$. (c) $t = 0.5$.

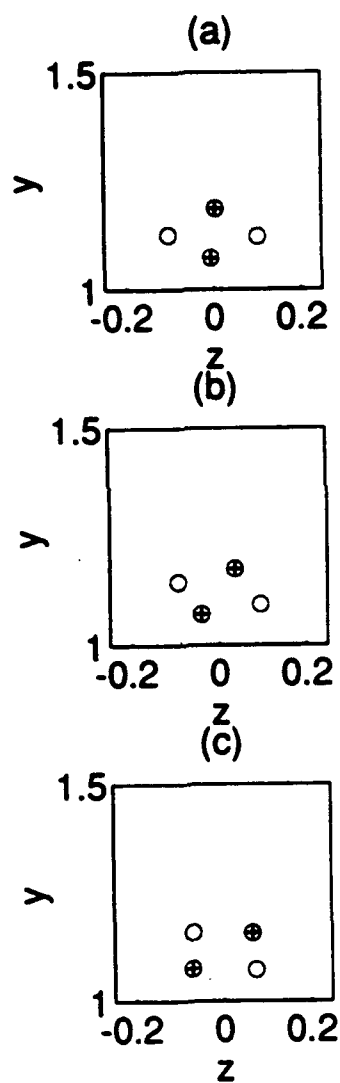


Figure 7.10: View of the four-vortex bundle motion on the symmetry plane at three different times showing the rotation of the vortices about themselves. (a) $t = 0.50$, (b) $t = 0.52$, (c) $t = 0.54$.

slightly less than about 0.25 whereas the period for the nine-vortex case is about 0.25 from Figure 7.11. The continued deformation of the vortex core after $t = 0.5$ is shown on Figure 7.12. The shape of the vortex bundle is approximately elliptical and similar to the results for the four-vortex case depicted on Figure 7.10.

Figure 7.13(a) shows the pressure gradient on the symmetry plane of the circular cylinder at times 0.50, 0.52 and 0.54 respectively for four vortices in the bundle. From this figure we can see that the overall amplitude of the pressure spike is decreased and the extent of the influence of the vortex on the pressure gradient has widened. Note that the amplitude of the pressure gradient increases until $t = .5$ when it begins to modulate as a result of the proximity of the vortex core from the airframe. On the other hand, the pressure gradient on the same plane due to a single vortex continually increases in amplitude monotonically (Figure 7.13b). Here the single vortex has its starting position at $(x, 1.3, 0)$ where x varies from $-\infty$ to ∞ with its strength equal to the total strength of the four vortex filaments, i.e., 2.2. Beyond this time the pressure gradient begins to oscillate and shortly after this the calculations become inaccurate.

Figure 7.14 shows the pressure on the airframe. Here we see a significant decrease in the amplitude of the suction peak for the four-vortex bundle. The amplitude of the suction peak for the corresponding single vortex result increases, although slowly at the same times.

On Figures 7.15 and 7.16 are the corresponding results for the pressure gradient and the pressure for the nine vortex case. Here it is noted that significant differences from that of the four-vortex bundle occur. In particular there is not much difference between the single and nine-vortex bundle in the pressure although there does appear to be a definite trend toward reduction of amplitude in the suction peak as can be seen in the $t = 0.54$ result on Figure 7.16. However, it is clear that additional calculations are required to support this contention fully.

7.4 Summary

In this Chapter, a multiple vortex model for the tip-vortex has been developed in an attempt to explain the initial stages of pressure modulation which occurs around $\psi = 54^\circ$ in the experiments. The symmetric mean flow discussed in Chapter 5 has been employed to produce the results. It has been found that for the parameters of interest in the experiments, there is a pressure modulation corresponding to the rotation of the vortex bundle, which seems to occur when the vortex is less than a core diameter from the airframe. This corresponds to the time frame when the outer edges of the vortex core rest on the airframe. Although the present results are promising, it is apparent that additional results for other bundle sizes and for the asymmetric, rotorcraft mean flow are necessary.

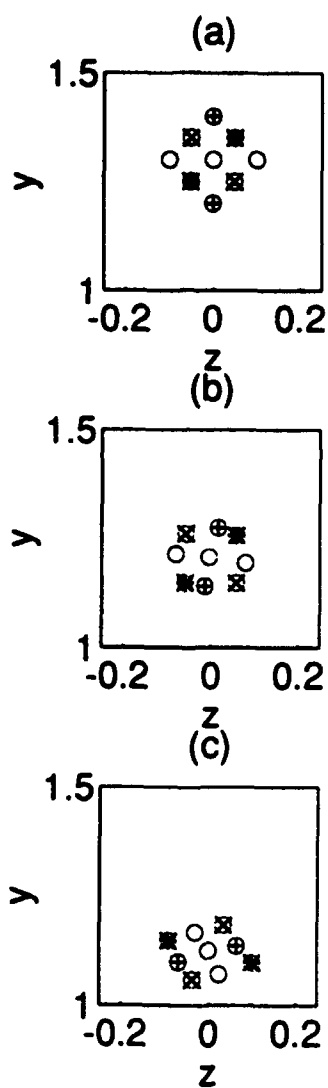


Figure 7.11: View of the nine-vortex bundle motion on the symmetry plane for three times. (a) $t = 0.0$, (b) $t = 0.25$. (c) $t = 0.5$.

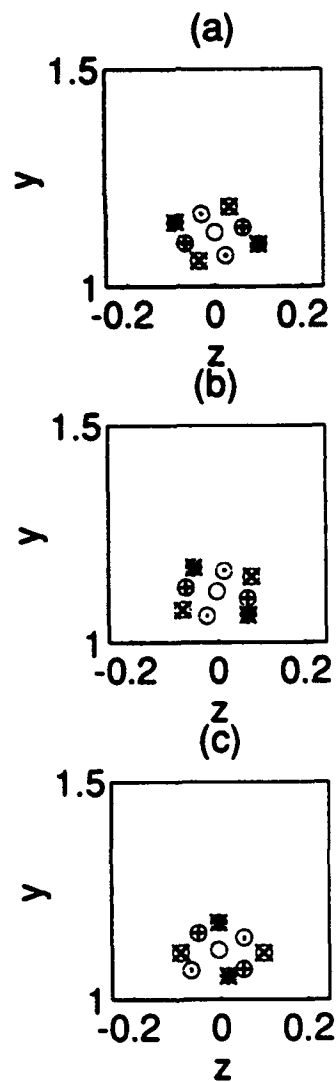


Figure 7.12: View of the nine-vortex bundle motion on the symmetry plane at three different times showing the rotation of the vortices about themselves. (a) $t = 0.50$, (b) $t = 0.52$, (c) $t = 0.54$.

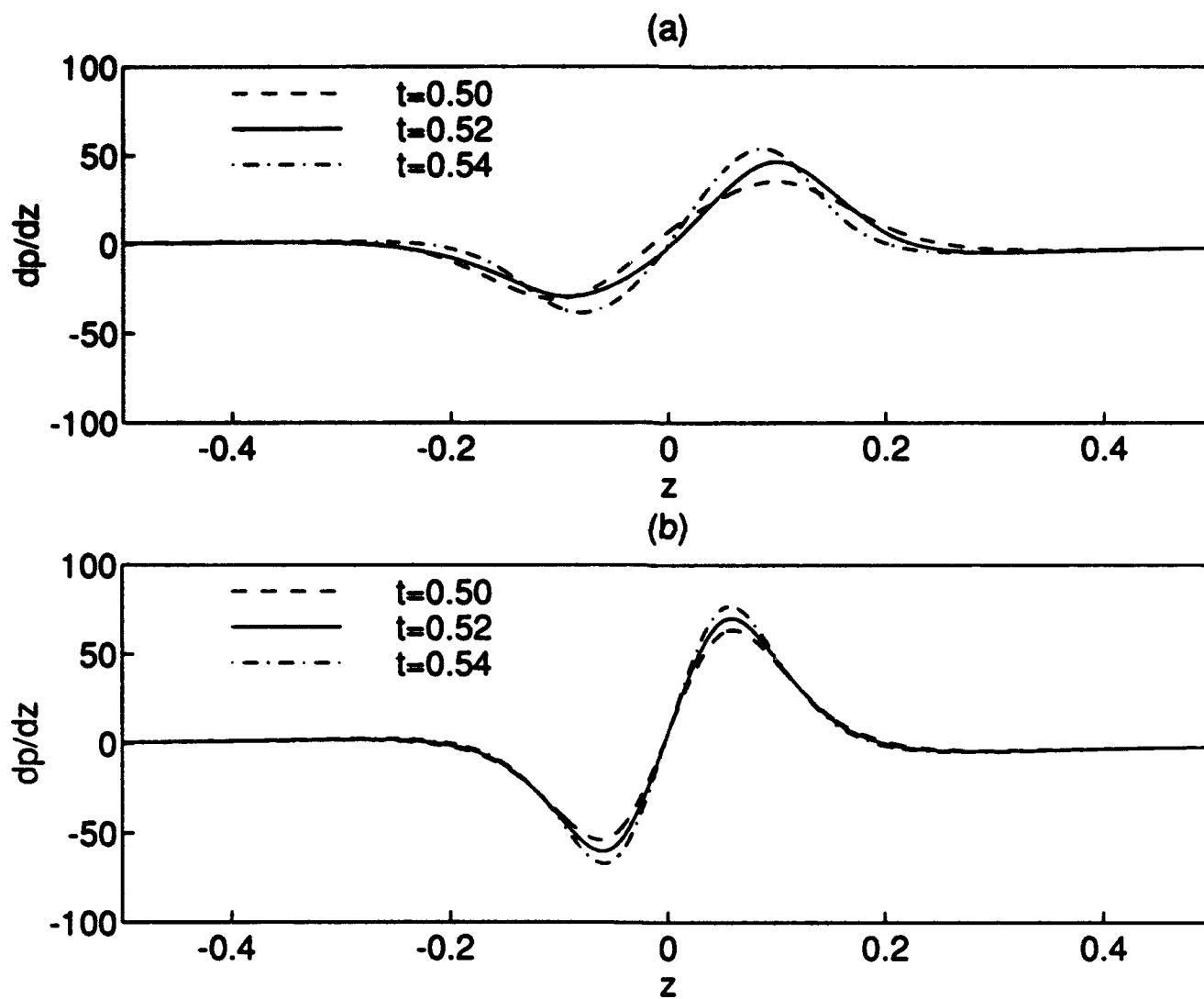


Figure 7.13: Pressure gradient on the top of the cylinder for the four-vortex bundle. (a) Vortex bundle; (b) single vortex.

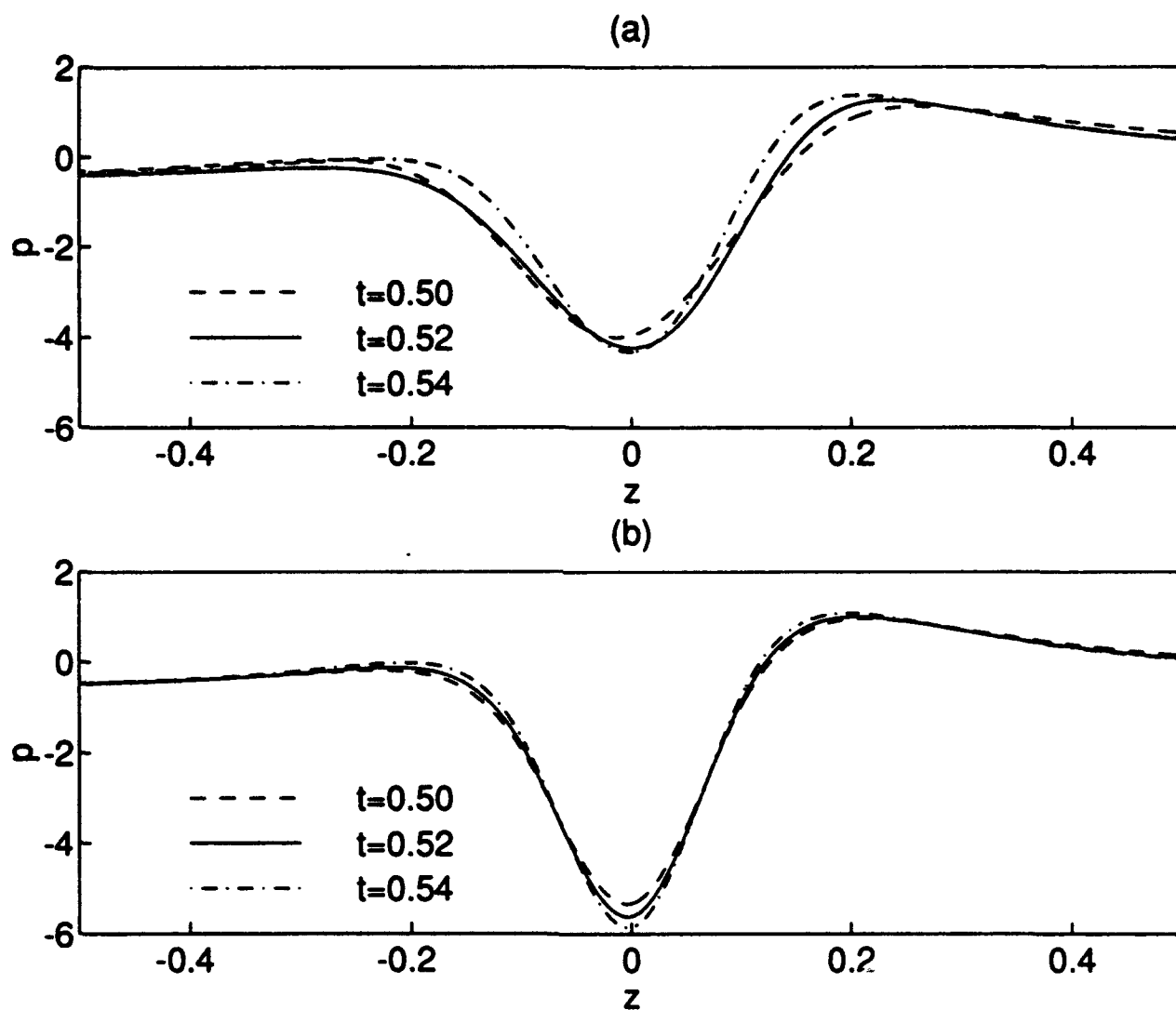


Figure 7.14: Pressure on the top of the cylinder for the four-vortex bundle. (a) Vortex bundle; (b) single vortex.

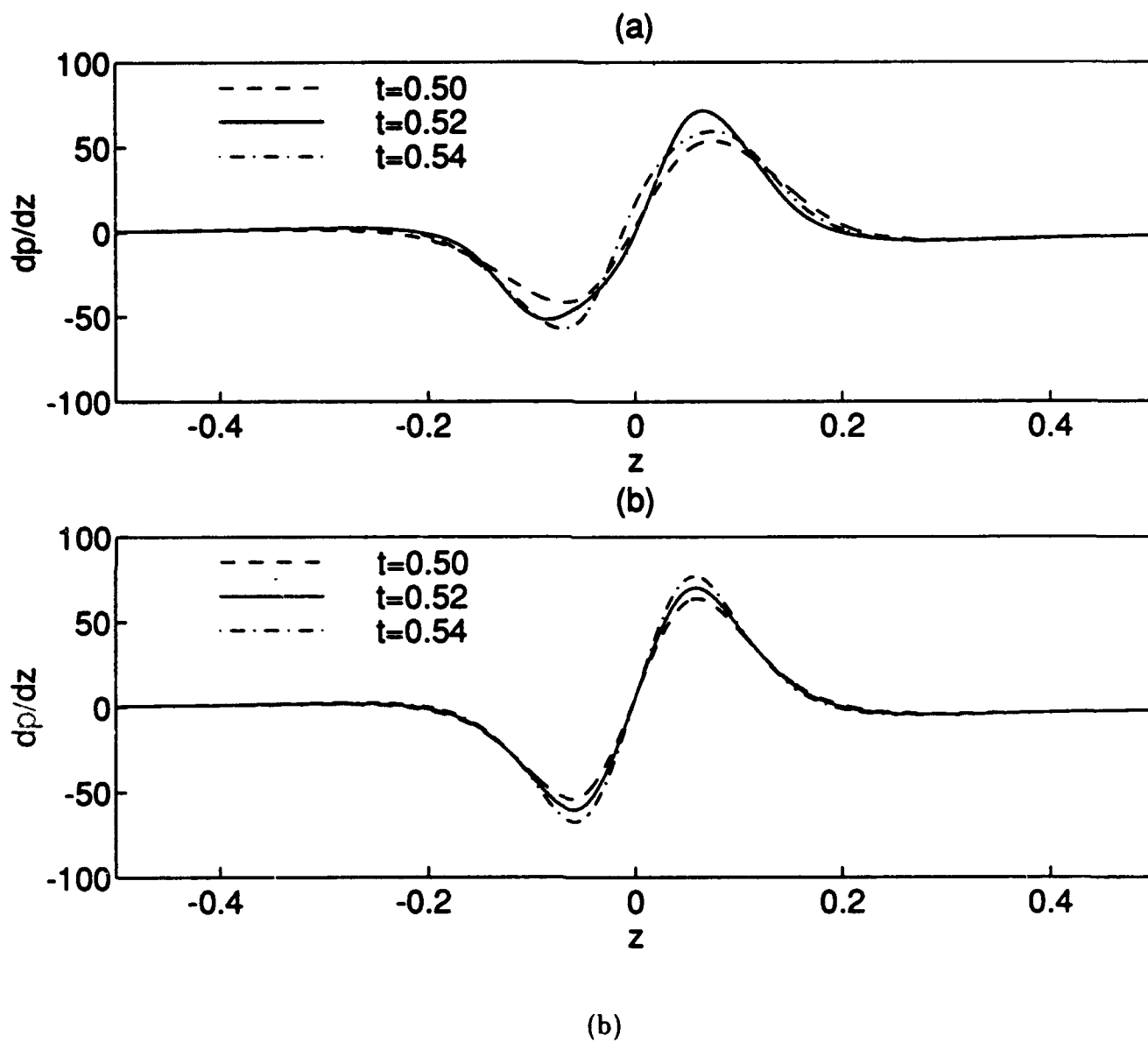


Figure 7.15: Pressure gradient on the top of the cylinder for the nine-vortex bundle. (a) Vortex bundle; (b) single vortex.

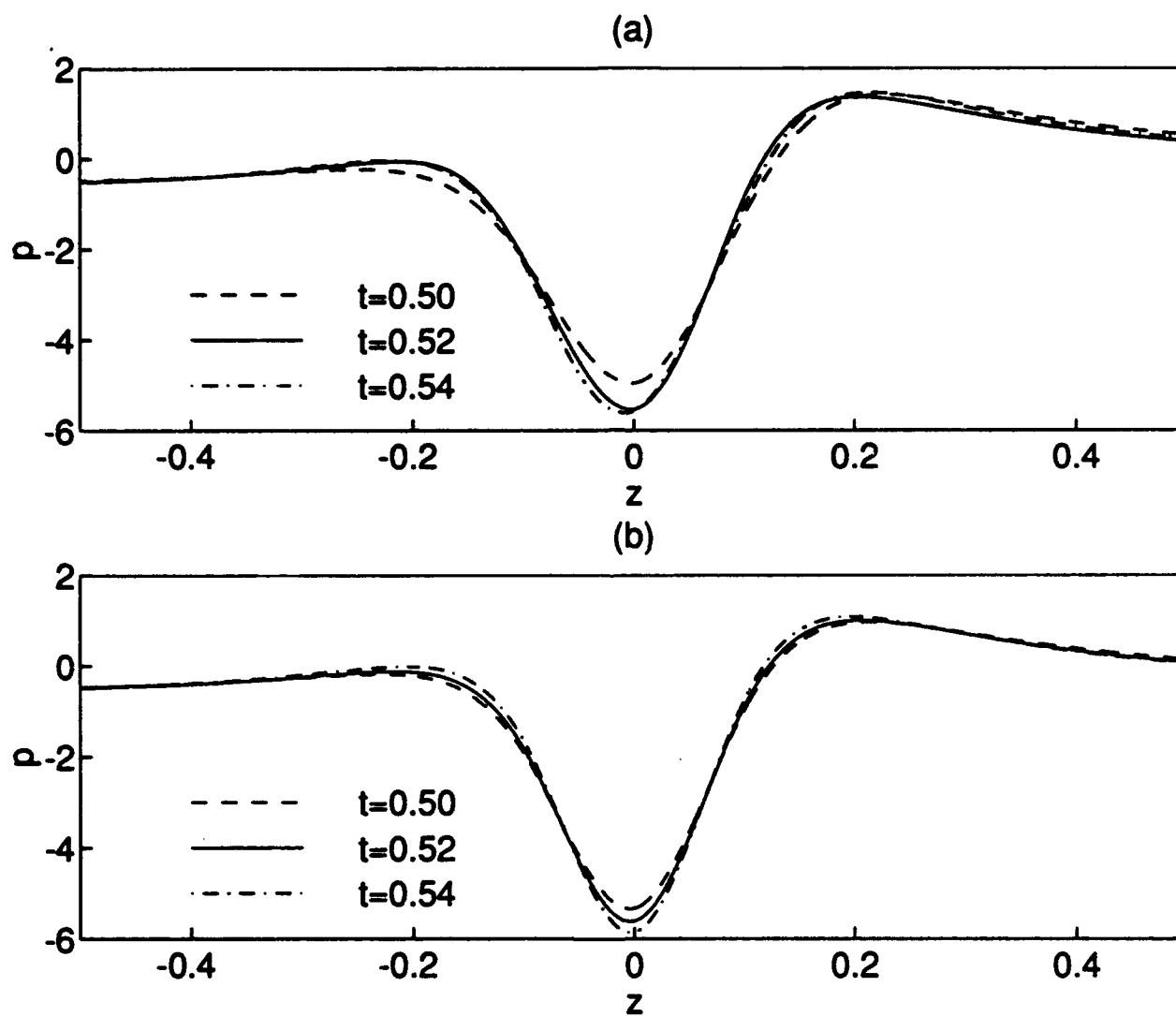


Figure 7.16: Pressure on the top of the cylinder for the nine-vortex bundle. (a) Vortex bundle; (b) single vortex.



CHAPTER VIII

The Three-Dimensional Interacting Boundary Layer

8.1 Introduction

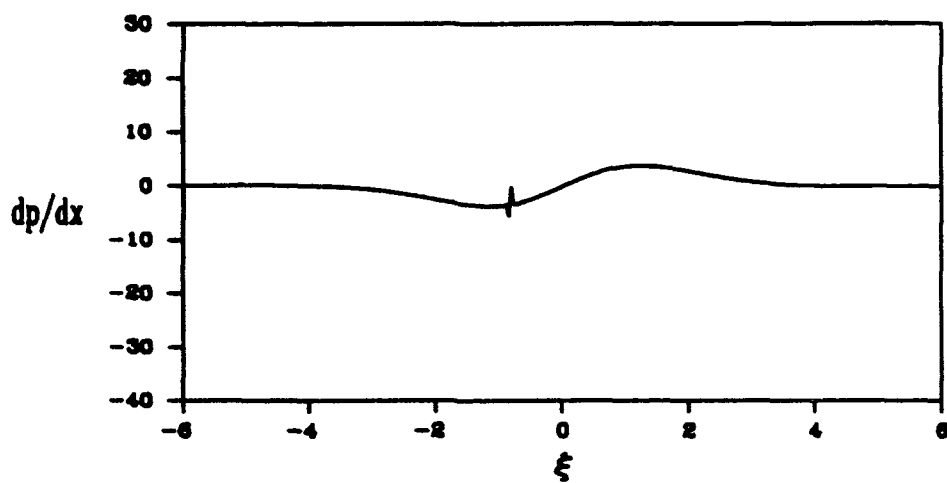
In Chapter 5 the three-dimensional unsteady boundary-layer flow on an infinitely long circular cylinder due to a vortex is considered in the limit case ($Re \rightarrow \infty$). The results suggest that, similar to the flow in a two dimensional unsteady boundary layer near a solid surface, the flow locally reverses direction and a closed eddy develops which grows in time and which is eventually expected to be ejected from the boundary layer into the main stream flow. The calculations described in Chapter 5 correspond to classical boundary-layer solutions because the pressure gradient from the inviscid flow is impressed on the viscous flow underneath. As in the two-dimensional case the displacement velocity exhibits extreme growth in a narrow region under the vortex indicating the possible formation of a singularity of the type suggested by van Dommelen and Cowley(1990).

The prime motivation for this work is the discovery of a second pressure spike in the pressure on the top of the airframe in the experimental results of Figure 5.48. This feature of the pressure distribution can not be modelled in the context of inviscid fluid dynamics or classical boundary-layer theory. The two dimensional results for the interacting boundary layer due to a vortex moving above a wall(Conlisk 1989; also unpublished) and Peridier, Smith and Walker(1992) for a vortex- driven boundary layer in an otherwise stagnant medium suggest that this influence may be simulated by allowing interaction between the inviscid outer flow and the viscous boundary-layer flow. In both the above studies, there is a second pressure spike in the pressure field in the later stages of the calculations. This has been attributed to the formation of the secondary eddy, the influence of which permeates the inviscid surface speed and the streamwise pressure gradient. The second spike in the pressure arises from the influence of the displacement velocity on the pressure gradient which develops a local spikey structure; an example of

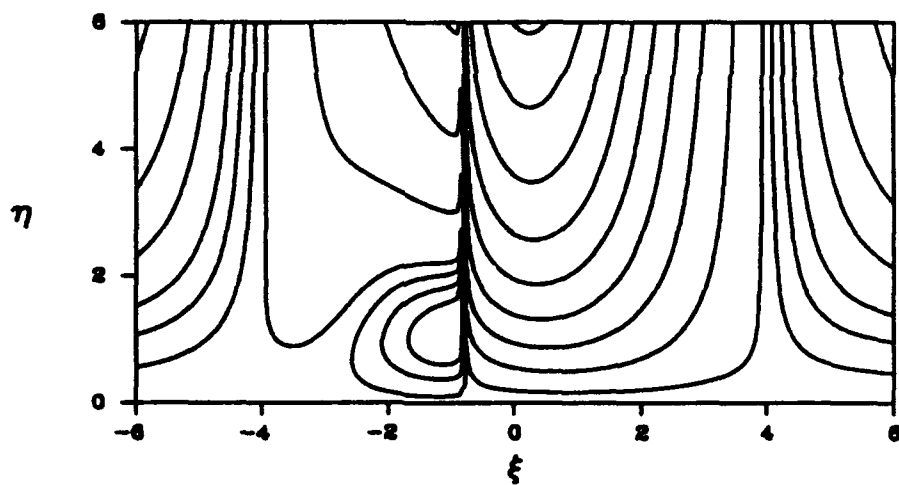
this in a two-dimensional flow is shown on Figure 8.1. These are results for a boundary layer driven by a vortex placed in a uniform flow. Here the strength of the vortex is taken to be that used by Chuang and Conlisk(1989) and other parameters are similar. The Reynolds number is 8×10^8 . The classical boundary-layer computations become numerically unstable at a time of about $t = 0.9$ and the interacting boundary-layer results become numerically unstable slightly sooner at this Reynolds number. Note on Figure 8.1 the extremely localized effect of interaction which is prominent even for the relatively large Reynolds number chosen. At lower Reynolds numbers the amplitude of the pressure gradient spike increases and occurs sooner; thus interaction hastens the flow development and this is contrary to the results of Henkes and Veldman(1987), and Riley and Vasantha(1989) who conclude that the singular behavior of the solutions could be postponed substantially. Riley and Vasantha(1989) suggest that the singularity could be removed altogether in the impulsively started cylinder problem. The results of Chuang and Conlisk(1989) suggest that the singularity could be slightly postponed by the incorporation of interaction. The difficulties with the Chuang and Conlisk(1989) work appear to be due to the time lagging of the effect of interaction and this has been corrected in the results depicted on Figure 8.1. The work of Peridier et al(1992) was the first to suggest that interaction could hasten the flow development and breakdown in their Lagrangian computation of the boundary layer caused by a vortex in a stagnant medium. Complicating the situation is the assertion by Tutty and Cowley(1986) that a Rayleigh instability is present in interacting boundary layer equations.

The difficulty with the foregoing calculations may lie in the treatment of the Hilbert integral and in the precise form of the coupling between the inviscid and viscous flow. In the calculations of Chuang and Conlisk(1989) the calculation of the Hilbert integral was time-lagged one time step and this appears to have permitted the calculation to proceed further in time. An additional difficulty may lie in the use of only a first-order scheme to evaluate the Hilbert Integral as discussed by Conlisk(1989). In any case, interacting boundary-layer calculations are delicate and the results need to be interpreted carefully. In the present calculations, the flow appears to develop faster than the classical case, a fact which is consistent with now conventional wisdom(Peridier et al 1992).

The extension of the interacting boundary layer procedure to three dimensional flows has received only limited attention in recent years. Cebeci, Chen, and Chang(1986) used the approach to solve the problem of steady transonic flow around a wing. In their study, two separate approaches are adopted to compute the viscous-inviscid interaction. The first one is the displacement-thickness approach, in which the displacement thickness is added to the inviscid geometry in the normal direction before carry out the inviscid calculation. The second approach is the transpiration, or blowing approach; in this approach the no-flux surface boundary



(a)



(b)

Figure 8.1: Pressure gradient and streamlines for the two-dimensional boundary layer induced by a vortex. ξ is the streamwise variable and the results are for $t = 0.88$.

condition in the inviscid calculation is modified to allow a prescribed surface blowing condition, accounting for the addition or subtraction of mass flux through the displacement surface to maintain the growth or decay of displacement thickness. Chen and Wu(1984) have developed an interacting boundary layer procedure which uses an integral inverse boundary-layer method and an integral representation of the incompressible inviscid flow to investigate the separated flow over a flat plate with a protuberance. Edwards(1986) employs a quasi-simultaneous technique to couple a finite difference representation of the viscous boundary layer flow to an integral representation of the inviscid outer flow for the same geometry studied by Chen and Wu(1984). Duck and Burggraf(1986) have considered the steady three-dimensional flow past a finite surface-mounted obstacle within the context of Triple-Deck Theory.

In the work mentioned above, the focus is on the three-dimensional steady boundary-layer flow problem. Indeed, the authors are aware of no fully nonlinear computational results on the unsteady three-dimensional interacting boundary layer problem in any geometry. This is in part due to the extensive computer power required to compute accurate solutions to the three-dimensional unsteady problem. Triple-Deck solutions involving the flow past an unsteady surface-mounted obstacle have recently been obtained by Duck(1990) and a discussion of the progress to date in unsteady interactive flows is given in that paper.

The objective of the present Chapter is to apply the interacting boundary-layer procedure to the unsteady three-dimensional problem considered in Chapter 5. The presence of the second spike should be independent of the precise inviscid mean flow chosen and only a vortex passing above a cylinder should be necessary to demonstrate the fundamental effect. Thus, for the purposes of this presentation, the surrounding medium is assumed to be stagnant. Additional results for the other two cases of interest will be forthcoming. In this study, the computational approach taken in Chapter 5 is employed for the boundary layer and the inviscid flow is calculated using the panel method discussed in Chapter 7.

8.2 Numerical Methods

The viscous boundary-layer flow is computed by the procedure described in Chapter 5. In the Eulerian formulation, the boundary layer is governed by (5.11), (5.12) and (5.13) subject to the boundary conditions (5.14). Rayleigh variables are employed and the solution procedure is otherwise similar to that discussed in Chapter 5.

8.3 Inviscid Flow Solution

The panel method employed in Chapter 7 is used here to carry out the external flow calculation outside the viscous boundary layer. The surface of the circular cylinder is approximated by $M \times N$ rectangular source panels. The size of the panels in each of the z and θ directions is not uniform; the size in the z -direction varies as equation (7.23), while the panel size in the θ direction varies according to equation (7.25). The number of panels used in all the subsequent calculations are taken to be 101 panels along the cylinder and 32 panels around the cylinder. The pressure gradients on the cylinder surface are calculated using the Euler equations (5.4) and (5.5) with the modification that the edge velocities are corrected each time step for the effect of the displacement velocity (see below). In the present case of the stagnant medium outer solution, Euler's equations are solved using finite differences with second-order central differences in both space and time.

In contrast to the previous computations of the motion of the vortex, we use a simple first order Euler solver to advance the vortex; the results were compared with those of Chapter 5 with very little difference in the computed positions of the vortex since a time step about ten times smaller than in Chapters 2 and 5 has been used here. It should be noted that interaction is not expected to influence the position of the vortex greatly.

8.4 Viscous-Inviscid Flow Interaction

There are two approaches which can be used to incorporate the viscous and inviscid flow interaction. The first approach which has been employed in past work is the displacement-thickness approach in which the displacement thickness due to the viscous boundary layer is added to the original inviscid geometry; the potential-flow solution is thus updated at each time step. The disadvantage of this approach is that in three dimensions, the displacement thickness is not defined in a closed form. Moore (1953) shows that for incompressible flow the displacement thickness in three dimensions is governed by a partial differential equation which in boundary-layer coordinates is written as

$$\frac{\partial}{\partial z}(U_z \delta^* - U_z \delta_z) + \frac{\partial}{\partial \theta}(U_\theta \delta^* - U_\theta \delta_\theta) = 0, \quad (8.1)$$

where δ^* denotes the three dimensional boundary layer thickness and the integral thicknesses δ_z and δ_θ are defined by

$$\delta_z = \int_0^\infty \left(1 - \frac{u_z}{U_z}\right) dy, \quad (8.2)$$

$$\delta_\theta = \int_0^\infty \left(1 - \frac{u_\theta}{U_\theta}\right) dy, \quad (8.3)$$

where U_z and U_θ are the inviscid flow speeds. To incorporate interaction, the above partial differential equation must be solved to obtain the displacement thickness δ^* . The disadvantage of this approach is that the equation for δ^* must be solved at each time step adding another equation to the system. Moreover, the initial conditions in z and θ associated with equation (8.2) are not obvious. According to the derivation of Moore(1953), equation (8.2) is valid for steady or unsteady flow.

In the blowing approach, the influence of the viscous boundary-layer flow on the external potential flow is imposed by the introduction of the $O(Re^{-1/2})$ correction to the inviscid surface speeds. From the point of view of the inviscid flow the presence of the boundary layer induces a velocity normal to the surface of magnitude

$$V_{blow} = \frac{u_{r,edge}}{\sqrt{Re}} \quad (8.4)$$

where $u_{r,edge}$ is the normal component of velocity at the edge of the boundary layer calculated from the boundary-layer equations. The presence of the blowing velocity adds an additional component to the right side of the matrix equation for the source densities given by equation 7.14.

The individual components of the vector $B_j = -v_j - V_{blow,j}$ of equation (7.14) where v_j is the velocity normal to the cylinder induced by the vortex. Using this expression for B_j the panel-source densities are updated at each iteration during each time step. The interacting boundary-layer procedure is described as follows. First, we assume that the boundary-layer and potential-flow solutions are known at the previous time step; from this solution we can calculate the blowing velocity V_{blow} on the cylinder surface. This blowing velocity is added to the source panel as a boundary condition for the inviscid flow. After solving the matrix equation of the source panel density given by equation (7.15), the velocity on the vortex is then calculated and the position of the vortex at the next time level is advanced by the first-order Euler method described above. Note that the matrix inversion for the source-panel densities need not be re-computed at each time step. After obtaining the new position of the vortex, the surface speeds and the pressure gradients are predicted at the new time level. The boundary-layer equations are then solved to obtain a predicted distribution of the blowing velocity. This blowing velocity is again added to the surface of the cylinder to obtain a corrected surface speed and pressure gradient. A corrected boundary-layer solution is then obtained. This iteration process continues until convergence. In the actual calculation, the boundary layer converges to four decimal places in about 20 to 30 iterations. The pressure normally converges in about 15 iterations although this varies with grid size.

The minimum panel size used is 0.01 in the z -direction and 0.05 in the θ direction. The minimum size of the vortex segment is 0.01. The half length of the cylinder is taken to be 5.0 for the potential-flow calculation and 1.5 for the viscous boundary-layer flow calculation. Experience with the classical boundary-layer flow has suggested that these two parameters are sufficiently large because of the rapid decay of the inviscid flow upstream and downstream of the vortex. Since the grid size used in the boundary-layer calculation differs from the panel size used in the potential flow calculation, cubic-spline interpolation is used to transfer data between these two systems. Three grid sizes in (η, θ, z) have been tested corresponding to (61, 32, 61), (61, 32, 121) and (61, 32, 241). The solutions are most sensitive to the grid size in the z direction; the time step for both the inviscid and viscous flows is $\Delta t = .00625$. $\eta_{max} = 6$ in all of the calculations to be presented here.

8.5 Numerical Results and Discussion

The results presented here have been obtained for $Re = 10^6$. We mainly discuss here results for the finest grid corresponding to (61, 32, 241); it should be noted that there is some grid dependence in the solutions, especially for the pressure gradient. In particular, as the grid size is reduced, the amplitude of the pressure spike increases and focuses in the z direction. However, the spikey structure of the pressure gradient which causes the second pressure spike in the pressure distribution is present in the solutions for all the grids tested. On Figure 8.2 is the result for the streamwise pressure gradient at several times. Note the spikey structure in the solution as time increases. The corresponding classical result given on Figure 5.2 varies much more slowly with time, and no spike appears. Figure 8.3 shows the three-dimensional streamline patterns in a frame traveling with the center point of the vortex for several values of time. The major difference between the interacting result and the classical result depicted on Figure 5.18 is that the eddy is somewhat larger at the same time. It is interesting to note that the classical calculation converges until about $t = 0.9$ while the present interacting case breaks down numerically just after $t = 0.7$. Figure 8.4 shows the pressure corresponding to the results of Figure 8.2. At about $t = 0.7$ the second spike is beginning to form and is growing although its amplitude is still small.

Figure 8.5 shows the axial shear stress along the cylinder on the symmetry plane for several values of time. Note that around times $t = 0.4$ and 0.5 the shear stress appears to be constant with time; at about $t = 0.6$ however, the profile begins to develop a spike. This is consistent with the situation in two dimensions where a spike also occurs in the wall shear (Conlisk 1989, Peridier et al 1992). Figure 8.6 shows the surface streamlines at several times. The surface streamlines are defined

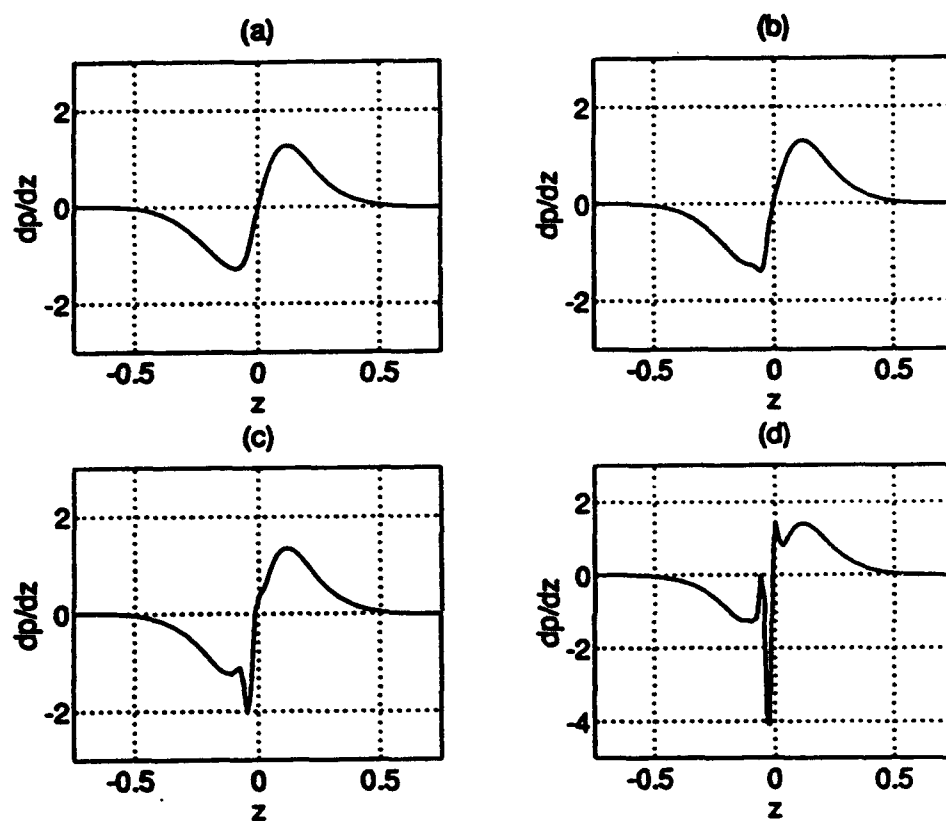


Figure 8.2: Streamwise pressure gradient on the symmetry plane for $Re = 10^6$; (a) $t = 0.4$, (b) $t = 0.5$, (c) $t = 0.6$, (d) $t = 0.7$.

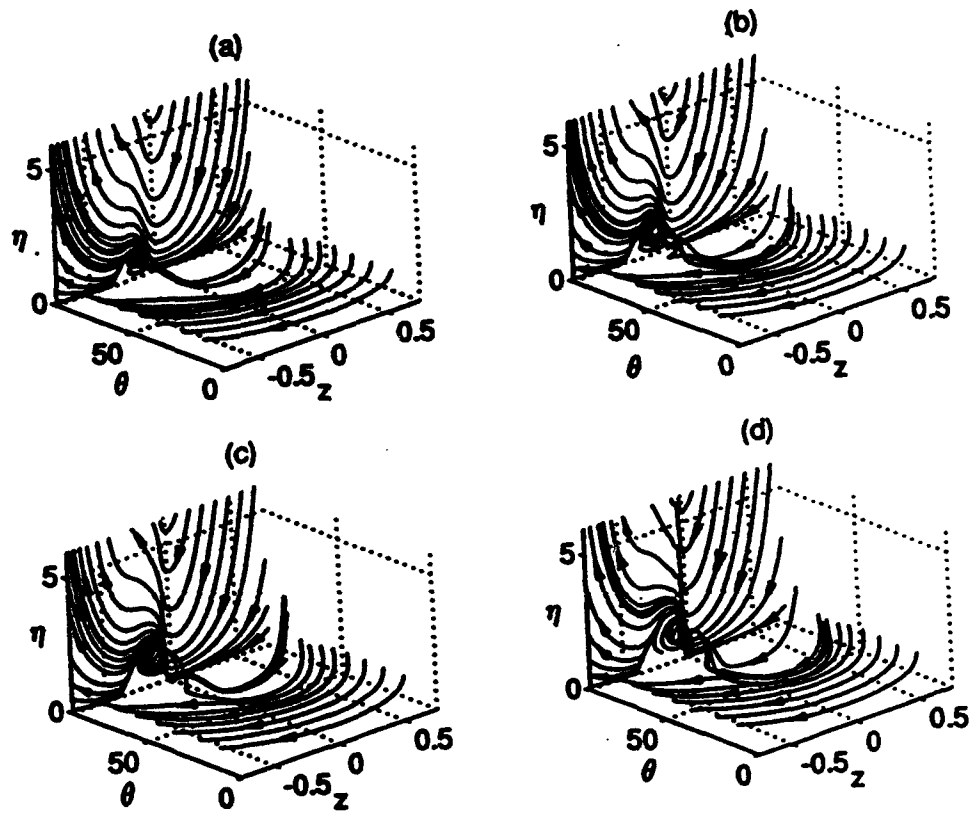


Figure 8.3: Three dimensional streamline patterns for $Re = 10^6$; (a) $t = 0.4$, (b) $t = 0.5$, (c) $t = 0.6$, (d) $t = 0.7$.

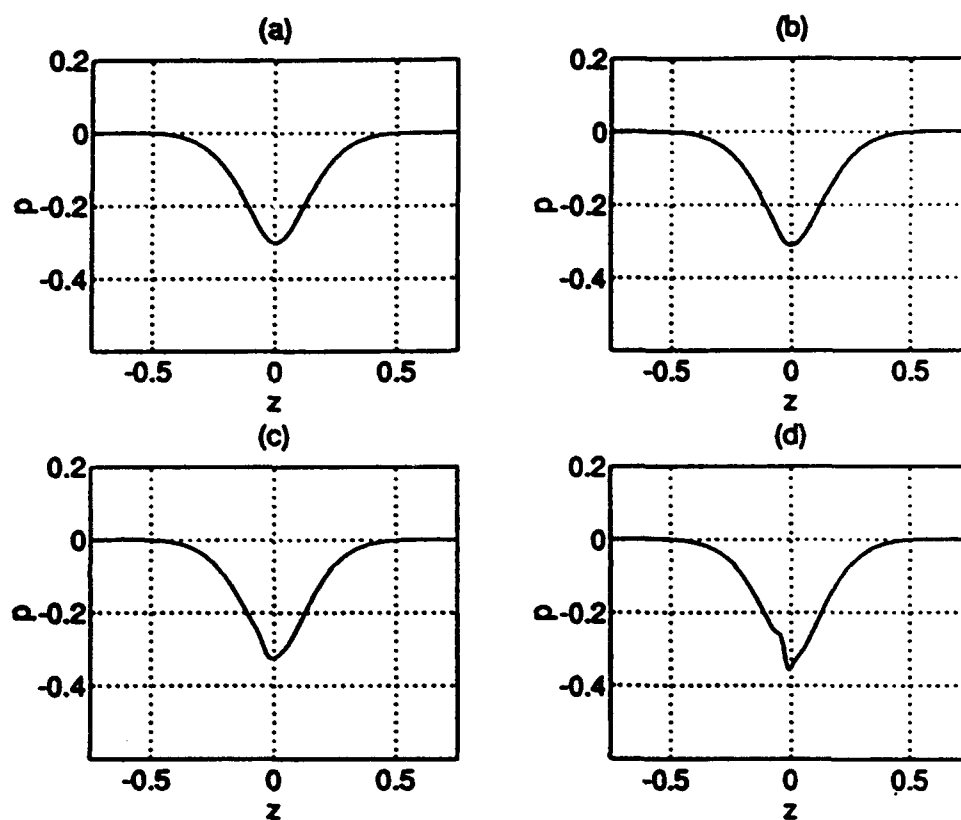


Figure 8.4: Pressure on the symmetry plane for $Re = 10^6$; (a) $t = 0.4$, (b) $t = 0.5$, (c) $t = 0.6$, (d) $t = 0.7$.

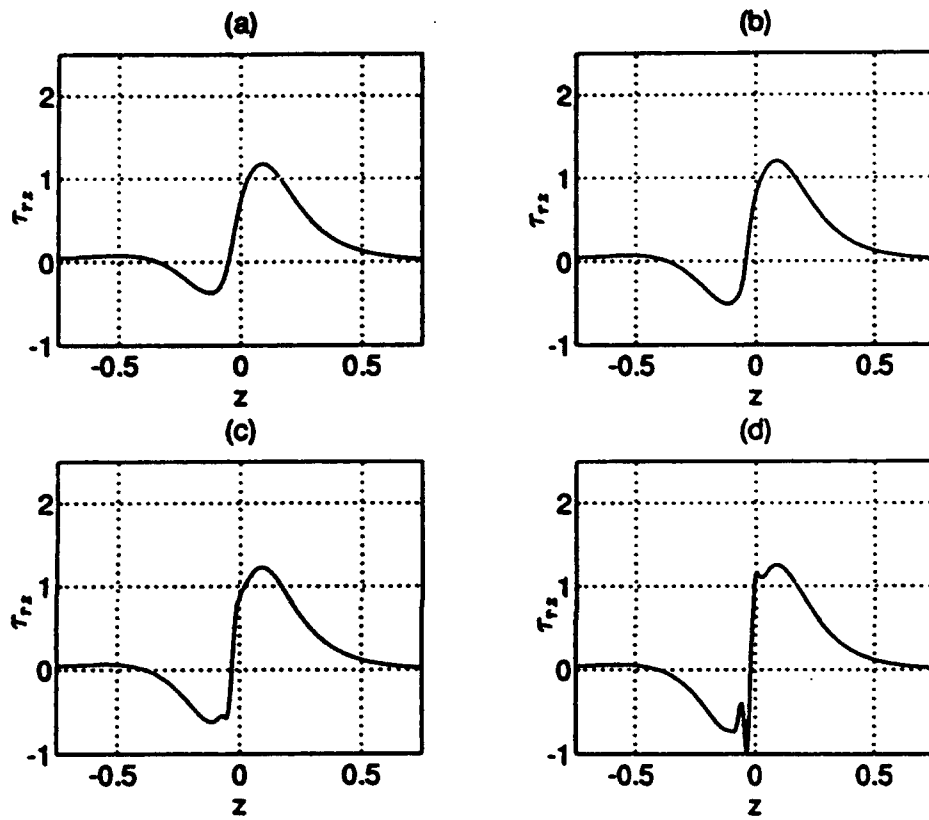


Figure 8.5: Axial shear stress τ_{rz} on the symmetry plane for $Re = 10^6$; (a) $t = 0.4$, (b) $t = 0.5$, (c) $t = 0.6$, (d) $t = 0.7$.

spike also occurs in the wall shear (Conlisk 1989, Peridier et al 1992). Figure 8.6 shows the surface streamlines at several times. The surface streamlines are defined by

$$\frac{\tau_z}{\tau_\theta} = \frac{dz}{d\theta} \quad (8.5)$$

where τ_z and τ_θ denote the shear stress components on the wall. At time $t = 0.1$ the flow tends to be attached. However, at time $t = 0.3$ the flow is just beginning to separate, following which, the surface streamlines develop a nodal point of attachment and a saddle point of separation. The left singular point is a nodal point of attachment and the right singular point is the saddle point of separation. Between these two singular points, there is a small region of reversed flow. The lines adjacent to the symmetry line do not intersect the dividing surface streamline normally and the situation here is very similar to that depicted on Figure 5.24. Note that in the classical solutions, the singular points do not develop until after $t = 0.3$. The reason that the skin friction lines are affected by the interaction at such an early stage is the deviation of the pressure gradient from the classical result at this stage. Additional results not shown here indicate a slight but finite deviation from the classical result which is suggestive of the emergence of the singular points before their occurrence in the classical case.

On Figure 8.7 is the streamwise edge velocity for several times. As with the pressure, there is a small blip which begins to emerge at $t = 0.6$.

It should be noted that the effect of grid size is most evident in the pressure gradients and wall shear. Other results such as stream line patterns and pressure are not overly sensitive to the grid used. Note that for all grids used the pressure gradient develops a spikey structure and this is expected to lead to the development of the large-amplitude, second suction peak of Figure 5.48.

Results have also been produced for $Re = 10^5$. In general the emergence of the spikey structure in the pressure gradient occurs sooner and the amplitude of the spike in the streamwise pressure gradient is considerably larger than for $Re = 10^6$. The pressure distribution and the streamwise shear are thus also affected by the decrease in Reynolds number with the amplitude of the spikes in those quantities larger for the lower Reynolds number. However, the streamlines and the edge velocity are similar to the results for the higher Reynolds number.

8.6 Summary

In this Chapter an unsteady three-dimensional interactive boundary-layer procedure is developed which couples the solution of the viscous boundary layer region with that of the potential flow region. The finite-difference method combined with the Fourier transform technique is used to solve the boundary-layer equation and a source panel method is employed to calculate the potential-flow solution.

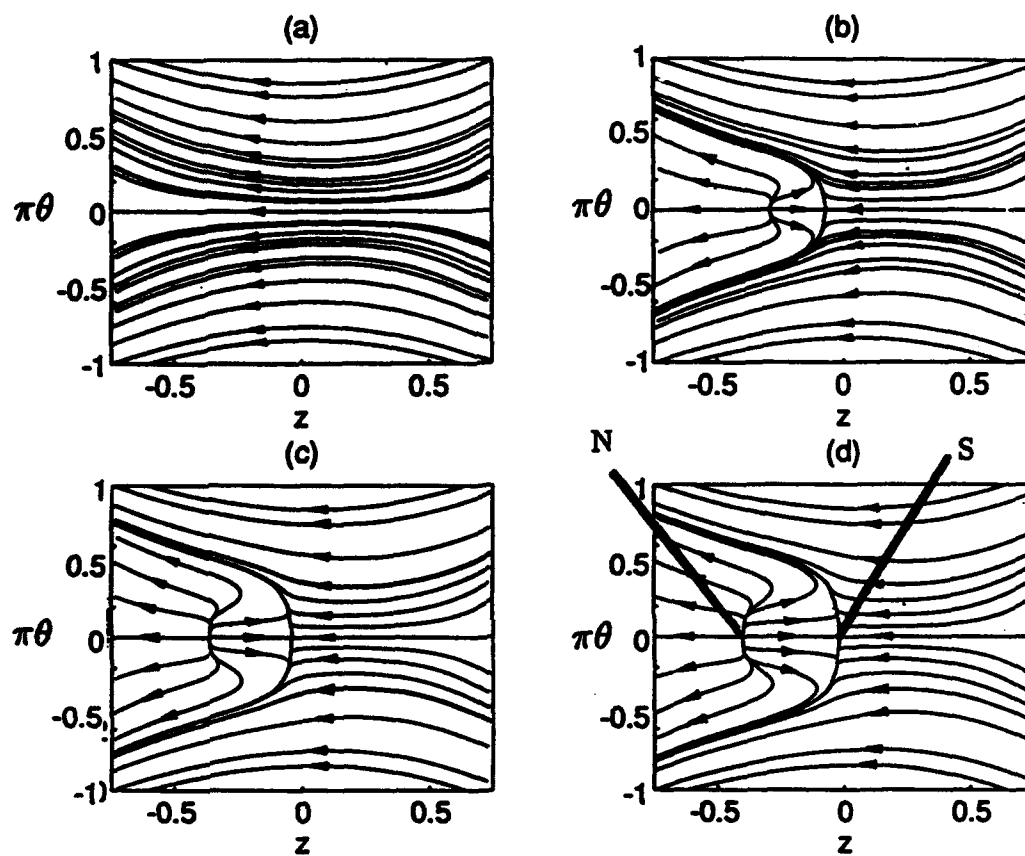


Figure 8.6: Surface streamlines for $Re = 10^6$; (a) $t=0.1$, (b) $t=0.3$, (c) $t=0.5$, (d) $t=0.7$.

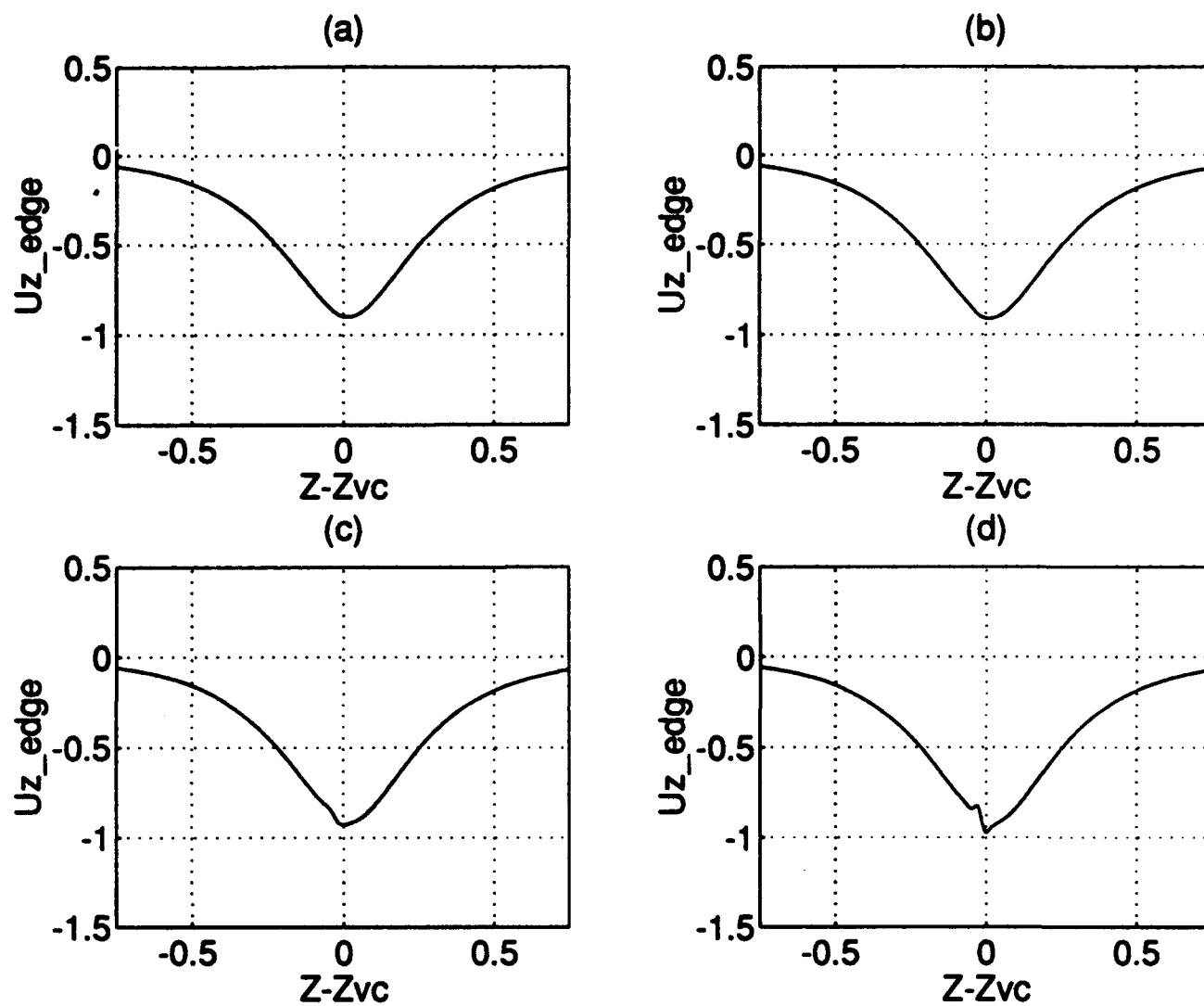


Figure 8.7: Edge velocity on the symmetry plane for $Re = 10^6$ at several times. (a) $t = 0.4$, (b) $t = 0.5$, (c) $t = 0.6$, (d) $t = 0.7$.

placement velocity calculated from the boundary layer solution is imposed as a boundary condition for the potential flow.

Three conclusions can be drawn from this study. First, numerical solutions suggest that the interacting boundary-layer procedure cannot remove the singular behaviour of the classical boundary-layer flow. Second, the value of the Reynolds number plays an important role in the flow development with smaller Reynolds number tending to speed the emergence of eruptive behavior within the boundary layer flow. Third, the presence of interaction between the boundary layer and potential flow causes the pressure gradient to spike and also causes a second spike in the suction peak on the airframe. However, the numerical solutions cannot be continued far enough into the interactive regime for the second pressure spike to develop to large amplitude.

In two dimensions, it has been shown that a singularity can arise in a generic interacting boundary-layer flow (Smith 1988) and it is expected that a similar singularity will occur in this fully three-dimensional flow. However, a much finer mesh is required to determine the temporal and spatial characteristics of the flow near the singular time.

CHAPTER IX

Summary and Conclusions

9.1 Summary

In the present work, the unsteady interaction of a rotor tip vortex with a helicopter airframe has been investigated using a combined analytical/computational model. The results have been compared with the experimental results produced by Professor Komerath and his colleagues at Georgia Tech; those results indicate that a tip-vortex in close proximity to the airframe has a major influence on the unsteady airloads on the surface. In particular, they show that unsteady effects can often have considerably larger magnitudes than the time averaged effects. The motivation for the present work has been the fact that until recently there has been no attempt to quantitatively predict the unsteady effect of the tip-vortex on the airframe.

In Chapter 2, a simplified model for the interaction of a rotor tip-vortex with a cylindrical airframe is developed using potential flow analysis. The tip-vortex is idealized as a single three-dimensional vortex filament and the airframe is modeled by an infinitely long circular cylinder. The flow is assumed to be inviscid and irrotational outside the vortex core. A parametric study has been conducted to investigate the effects of the mean flow and the size of the vortex core. The results indicate that the effect of vortex core size is negligible until the vortex approaches within about one core radius from the airframe. Subsequent to this, significant differences in the position of the vortex and the induced pressure distribution are observed. Of particular note is that a large adverse pressure gradient develops under the vortex causing a rapid drop in the pressure there; large variations of the curvature of the vortex are not observed.

In Chapter 3, the methods for computing the vortex trajectory and the pressure field on the cylinder developed in Chapter 2 are used to compare with the experimental results of Professor Komerath and his colleagues at Georgia Tech. Despite the relative physical simplicity of the model(i. e. a potential flow model),

it has been demonstrated that the experimental and analytical/numerical results for both the vortex trajectory and the pressure distribution on the airframe are in substantial agreement prior to impact of the vortex with the airframe. While some of the experimental data itself has been employed to determine the mean flow speed far from the airframe, the present analytical/computational effort is substantially free of fit parameters and may thus be termed a predictive effort. Estimates for the initial position of the vortex filament, the circulation of the vortex, and the vortex core radius have been determined directly from the experiments. In particular, it has been shown that the position and magnitude of the suction peak induced on the airframe can be adequately predicted using the aforementioned three-dimensional potential flow analysis.

The large adverse pressure gradients induced on the airframe increase in magnitude as the vortex approaches the airframe. Since it is well known that large adverse pressure gradients may induce boundary-layer separation, attention has also been focused on understanding the nature of the viscous flow response to the motion of the vortex. To motivate the study of the fully three-dimensional boundary layer flow, in Chapter 4, the two-dimensional boundary-layer flow about an impulsively started circular cylinder is computed. Previous results computed by other numerical techniques are reproduced using the methodology of the present work.

In Chapter 5, the methodology described in Chapter 4 is applied to the analysis of the three-dimensional boundary layer induced by a vortex. Three types of external flow in which the vortex is embedded are considered to investigate the effect of the vortex on the boundary layer. In the first case, the vortex is embedded in a stagnant environment; the boundary layer results indicate that the flow separates in the sense that a reversed-flow eddy forms early in the calculation and grows in time. The region of reversed flow develops just upstream of the vortex and is oriented in the spanwise direction. The spanwise extent of the vortex at the latest time computed is about 10° on either side of the top of the airframe. The influence of the tip vortex decreases rapidly away from the top of the airframe and there is no evidence of a substantially separated flow away from this location. The boundary layer solutions near the top of the airframe ultimately show the development of a spike in the displacement velocity indicating the possible occurrence of a singularity of the type discussed by van Dommelen and Cowley(1990). The present results are consistent with the development of a singularity along the symmetry plane where both the axial and azimuthal components of vorticity vanish. Subsequent to this period of time it is expected that boundary-layer fluid will be ejected into the main stream.

In the case where the vortex is embedded in a mean flow which is symmetric about the vertical plane ($y=0$), the boundary layer flow results also show the development of a detached secondary eddy that grows in time. Because the vortex is

now convected toward the airframe faster, the development of the secondary flow is faster than in the case of the stagnant medium. The secondary vortex structure is illuminated by the calculation of the three-dimensional streamline patterns which, similar to the stagnant medium case, indicate the presence of a complicated three-dimensional eddy pattern. Velocity vector plots indicate that the fluid velocity is toward the symmetry plane under the secondary eddy, and away from the symmetry plane in and above the secondary eddy. The influence of the vortex on the boundary layer is extremely local; nevertheless, the flow is expected to separate two-dimensionally near the shoulder of the airframe as is the case in the results of Chapter 4. However, the locally separated flow which is initiated near the shoulder appears to develop independently from the boundary layer flow near the top of the airframe. As with the stagnant medium, a spike develops in the displacement velocity suggesting again the presence of a singularity subsequently in time.

It is important to note that the secondary eddy which forms in the boundary layer flows described above has its genesis deep within the boundary layer. For the physical parameters of the experiments conducted at Georgia Tech the origin of the eddy begins on a length scale less than one millimeter. Consequently, the initial stages of development of the secondary structure are extremely difficult to capture experimentally. Thus the approach taken in the last portion of Chapter 5 where the actual asymmetric, tip-vortex/airframe interaction is considered is to demonstrate the initiation of the secondary eddy computationally; parallel experimental measurements were conducted at Georgia Tech and they confirm the existence of a high-vorticity region which, we believe is associated with the reversed flow region seen in the computations. The computations indicate a reversed flow region developing under the main vortex just prior to the rotor phase angle $\psi = 30^\circ$; the vorticity in the reversed flow region is of a sign opposite to that of the main vortex and begins to increase rapidly just after $\psi = 30^\circ$. Experimentally, a high-vorticity region under the tip vortex is observed at rotor phase angle $\psi = 72^\circ$. Moreover, the position of the secondary vortex in the early times is consistent with the results of the experiments at the relatively later times indicated (Figure 5.47). From the plots themselves, the axial location of the center of the secondary flow in the computations is about 10mm upstream of the center of the main tip vortex position while the experiments indicate about 25mm. The secondary flow regime is much more visible on the retreating side of the rotor in the experiments. This is consistent with the computations which show that by $\psi = 30^\circ$ the eddy has spread significantly beyond $\theta = 90^\circ$ although the local vorticity values are not large at the last time at which the computations are valid; the experiments show a significant high-vorticity region as far as $\theta = 120^\circ$ at $\psi = 72^\circ$.

The scale of the secondary flow on Figure 5.47 suggests that boundary layer fluid may be erupting into the main stream. Moreover, the experiments show that the secondary flow affects the pressure field on the airframe through the

development of a second spike(Figure 5.48). This effect is believed to be due to interaction between the boundary layer and the inviscid flow and this phenomenon is discussed just below.

When the vortex is far from the airframe, a simple Rankine core is sufficient to predict both the vortex position and the pressure on the top of the airframe with good accuracy(See Figures 3.6 and 3.8, for example.). However, as the vortex approaches the airframe, experiments indicate that the core of the vortex undergoes significant changes. Because, from a rotorcraft perspective, the entire vortex-airframe collision process contributes to the induced loading on the airframe, an attempt has been made to formulate a unified picture of this vortex-body collision process. Thus in Chapter 6 we suggest that a comprehensive model of the vortex-airframe impingement problem including the collision and subsequent convection of the vortex down the sides of the airframe can be developed based on the previous computational and experimental results. One view of the general vortex impingement problem may include three relatively distinct phases; the first phase corresponds to pre-collision described in Chapters 1-5 in this report(Phase 1); the second phase is the actual collision process(Phase 2); the third phase corresponds to the post-collision phase in which the end of the vortex filament and the boundary layer on the airframe coincide(Phase 3). Furthermore, the collision phase may be subdivided into three sub-phases which we term Phases 2.1, 2.2, and 2.3. Phase 2.1 is characterized by the commencement of the deformation of the vortex core, during which a non-zero fluid velocity in a direction normal to the boundary of the vortex core(i.e. a local radial velocity) develops. This phase has been observed to commence in the experiments just prior to $\psi = 54^\circ$ for an advance ratio of 0.1(Figure 3.6g). During this phase the vortex begins to entrain a significant amount of fluid. At some point, as the vortex moves closer to the airframe, mass flux requirements suggest that the axial velocity, if it is not initially large, must reach the order of magnitude of the other two velocity components(Phase 2.2). The experimental flow visualization of the boundary layer flow depicted on Figure 5.47 indicates that this phase of the process perhaps begins near $\psi = 72^\circ$. It is postulated that as the vortex core deforms under the action of the image vortex in the airframe, fluid must then be expelled from the region adjacent to the airframe in a direction along the centerline of the vortex. The local flow fields described above in Phases 2.1 and 2.2 are shown to be inviscid in character. In Phase 2.3, the portion of the vortex impacting the airframe must merge with the boundary layer flow; this process must include a reduction in the local magnitude of the swirl velocity within the vortex and, it is suggested, must include viscous effects.

Chapters 1-3 and 5 focus on the flow induced by the tip vortex in Phase 1. In Chapter 7, a model for the initial stages of Phase 2.1 has been developed for the case of the symmetric mean inviscid flow discussed in Chapter 2. In this model the tip vortex is assumed to consist of a number of finite core vortices of total

strength equal to that of the corresponding single vortex. The initial deformation of the vortex core is believed to be the cause of the pressure spike modulation in the experiments which is present in the results at $\psi = 54^\circ$. The results of the model do, indeed indicate that the pressure spike amplitude is modulated when compared with the single-vortex model. However, the results do depend on the number of vortices employed to model the core and additional work is required. The present results are, however, suggestive that the pressure modulation seen in experiments is due to vortex core modifications.

It has been suggested that the second pressure spike on Figure 5.48 is due to the presence of the secondary eddy depicted on Figure 5.47. This feature of the pressure distribution can not be modelled in the context of inviscid fluid dynamics or classical boundary layer theory and so an interacting boundary layer procedure has been developed to couple the outer potential flow with the boundary layer calculation. The presence of the second spike should be independent of the precise inviscid mean flow chosen and only a vortex passing above a cylinder should be necessary to demonstrate the fundamental effect. Thus, for the purposes of the results of Chapter 8, the surrounding medium is assumed to be stagnant.

Three conclusions can be drawn from the results of the interacting boundary layer study. First, numerical solutions suggest that the interacting boundary layer procedure cannot remove the singular behaviour of the classic boundary layer flow. Second, the value of Reynolds number plays an important role in the flow development with smaller Reynolds number tending to speed the explosive process of the boundary layer flow. Third, the presence of interaction between the boundary layer and potential flows causes the pressure gradient to spike and causes a second spike in the pressure suction peak on the airframe. However, the numerical solutions cannot be continued far enough into the interactive regime so that the second pressure spike reaches large amplitude.

In summary, the major conclusions of this study may be identified as follows:

- (1) The motion of the tip vortex and the pressure distribution on the top of the airframe may be adequately predicted using a three-dimensional potential flow analysis in the time regime when the vortex is nominally more than one core radius from the airframe. This time regime corresponds to Phase 1 identified earlier. During this period, the results are independent of the size of the vortex core and a large adverse axial pressure gradient develops. When compared with experimental data, this period extends to perhaps sometime just prior to $\psi = 54^\circ$.
- (2) As the vortex approaches the airframe, the strong adverse pressure gradient induced by the vortex initiates a reversed flow leading to the development of a complicated three-dimensional secondary flow. The existence of the secondary

flow is confirmed by experiments which indicate the presence of a high vorticity region subsequent to the time frame covered by the computations.

(3) Experiments show that just prior to impact of the vortex with the airframe, the vortex core begins to deform and initiate a pressure modulation (i.e. a decrease in the pressure spike amplitude). This effect has been modelled using several vortices to describe the tip-vortex. The computational results do show a modulation of the pressure suction peak seen in experiments although additional computations are required to delineate the influence of the number of vortices required to model the vortex core. Additional results to confirm the actual time of initiation of the vortex core deformation and computations for the parameters of the experiments are also required.

(4) Evidence exists to support the view that the secondary spike in the pressure distribution seen in experiments may be modelled by incorporating interaction between the inviscid and viscous flows near the airframe. Additional calculations for the experimental flow conditions are required.

The first two conclusions of this work have already been communicated to the scientific community at large; two papers on the inviscid flow problem, one co-authored by Professor Komerath will be published in the AIAA J. before the end of this calendar year and two more papers on the viscous flow problem will be submitted for archival publication within the next few months. A list of publications and presentations supported on this grant appears in Appendix D.

9.2 Future Work

From this work, it is evident that the present inviscid flow results are limited in validity to the time period prior to the actual collision of the vortex with the airframe. Moreover, it has been shown that the boundary-layer calculations fail at a much earlier time when the vortex is still about two core radii from the airframe. Indeed, the experimental results of Professor Komerath and his colleagues at Georgia Tech suggest that the tip-vortex will nominally "break" into two seemingly separate vortices upon impact with the airframe. Since a vortex cannot end in an inviscid fluid (Batchelor 1967), viscosity must play a role in the local vortex core destruction process. The term "break" as used above should be interpreted as meaning that a portion of vortex core fluid which lies within the boundary-layer on the airframe, becomes indistinguishable from boundary-layer fluid on collision.

In the present work only the problem of the interaction of a tip-vortex with an airframe during the pre-collision stage has been addressed. Although we have been able to quantitatively predict the effects of the vortex on the airframe during the pre-collision stage, it is very difficult to extend the present model through the

collision process because of emerging new length scales and time scales as indicated in the discussion in Chapters 3, 5 and 6. In particular, the present results show that the vortex core structure may become affected when the vortex is approximately one core radius from the cylinder. This fact is supported by the experimental flow visualization studies (Komerath 1991,1992) which show that the vortex core flattens as it approaches the airframe.

Analysis of the second phase of the vortex-body collision process has only partially been completed. The actual vortex collision process requires additional analysis and computation along with input from the experiments being performed at Georgia Tech. This phase of the process is presently under investigation. A mechanism by which the vortex will disconnect at the point of impact is presently being developed based on the investigation of the aforementioned inviscid flow model as well as the investigation of the interacting boundary-layer problem. It should be noted that the interacting boundary-layer problem is crucial to the understanding of the first response of the boundary-layer to the vortex collision and will suggest additional modifications of the vortex structure and the local pressure distribution.

The third phase focuses on the post-collision stage where the vortex ends are oriented approximately normal to the airframe and interact with the boundary-layer as they convect along the sides of the airframe. The development of a model by which it is possible to reconnect both vortex ends must also be considered. Work on Phases 2 and 3 is ongoing.

In order to extend the solution for the boundary layer accurately further in time, an adaptive gridding procedure must be employed to cluster grid points into the region just under the vortex. This is presently being done for the two-dimensional problem (Adams et al 1994) and it is desirable to extend those results to the present problem.





Appendices



Appendix A

The Calculation of the Self-Induced Velocity Field

A.1 Evaluation of $\int \vec{Q}_{V\infty} ds'$

The procedure to obtain analytical solutions to the the integrals along the straight portions of the vortex filament appearing in equation (2.26) is outlined here. The integrals in question are namely $\int_{-\infty}^{-l} \vec{Q}_{V\infty}(s, s', t) ds'$ and $\int_l^{\infty} \vec{Q}_{V\infty}(s, s', t) ds'$ where $\vec{Q}_{V\infty}$ is given by equation (2.28) and denote the integrand which is a function of vortex position and time. Here \vec{X} is the field point and \vec{X}' is the integration variable along the vortex. Decomposing the vectors appearing in equation (2.28) into their Cartesian components we get

$$\frac{\partial \vec{X}'}{\partial s'} = \frac{\partial x'}{\partial s'} \hat{i} + \frac{\partial y'}{\partial s'} \hat{j} + \frac{\partial z'}{\partial s'} \hat{k} \quad (\text{A.1})$$

and

$$\vec{X} - \vec{X}' = (x - x')\hat{i} + (y - y')\hat{j} + (z - z')\hat{k}. \quad (\text{A.2})$$

Note that since y' and z' are not functions of s' in these straight portions of the filament and since x' can be chosen to be a linear function of s' , further simplifications of the expression for $\vec{Q}_{V\infty}$ can be made. By taking advantage of the fact that

$$\frac{\partial x'}{\partial s'} = 1 \quad (\text{A.3})$$

$$\frac{\partial y'}{\partial s'} = 0 \quad (\text{A.4})$$

$$\frac{\partial z'}{\partial s'} = 0, \quad (\text{A.5})$$

equation (2.28) may be written as

$$\bar{Q}_{V\infty} = \frac{-(z-z')\hat{j} + (y-y')\hat{k}}{[(x-x')^2 + (y-y')^2 + (z-z')^2 + \mu^2]^{3/2}}. \quad (\text{A.6})$$

After some simple algebraic manipulations the integrals along the infinite straight portions of the filament, analytical solutions are obtained and they are given by

$$\int_{-\infty}^{-l} \bar{Q}_{V\infty} ds' = - \left[\frac{z-z_l}{c_{0l}} \left(1 - \frac{x-x_l}{c_{1l}} \right) \right] \hat{j} + \left[\frac{y-y_l}{c_{0l}} \left(1 - \frac{x-x_l}{c_{1l}} \right) \right] \hat{k}, \quad (\text{A.7})$$

and

$$\int_l^{\infty} \bar{Q}_{V\infty} ds' = - \left[\frac{z-z_r}{c_{0r}} \left(1 - \frac{x-x_r}{c_{1r}} \right) \right] \hat{j} + \left[\frac{y-y_r}{c_{0r}} \left(1 - \frac{x-x_r}{c_{1r}} \right) \right] \hat{k}, \quad (\text{A.8})$$

where (x_l, y_l, z_l) and (x_r, y_r, z_r) correspond respectively to the vortex points $\vec{X}(-l, t)$ and $\vec{X}(l, t)$. Here c_{0l} , c_{1l} , c_{0r} and c_{1r} are coefficients which are given by

$$c_{0l} = (y-y_l)^2 + (z-z_l)^2 + \mu^2, \quad (\text{A.9})$$

$$c_{1l} = [(x-x_l)^2 + (y-y_l)^2 + (z-z_l)^2 + \mu^2]^{1/2}, \quad (\text{A.10})$$

$$c_{0r} = (y-y_r)^2 + (z-z_r)^2 + \mu^2, \quad (\text{A.11})$$

$$c_{1r} = [(x-x_r)^2 + (y-y_r)^2 + (z-z_r)^2 + \mu^2]^{1/2}. \quad (\text{A.12})$$

A.2 Evaluation of the integral $\int_{-l}^l P ds'$

The integral $\int_{-l}^l P(s, s') ds'$ appearing in equation (2.26) is also computed analytically (Hon and Walker 1987) and the solution is given by

$$\begin{aligned} \int_{-l}^l P(s, s') ds' &= \frac{1}{2B_0} \left\{ \frac{l-s}{[B_0(l-s)^2 + \mu^2]^{1/2}} - \frac{l+s}{[B_0(l+s)^2 + \mu^2]^{1/2}} \right. \\ &\quad \left. + \frac{1}{B_0^{1/2}} \log \left| \frac{B_0^{1/2}(l-s) + [B_0(l-s)^2 + \mu^2]^{1/2}}{B_0^{1/2}(l+s) + [B_0(l+s)^2 + \mu^2]^{1/2}} \right| \right\}, \end{aligned} \quad (\text{A.13})$$

where

$$B_0 = \left| \frac{\partial \vec{X}}{\partial s} \right|^2. \quad (\text{A.14})$$

A.3 Approximation of \vec{R}_V

The approximation of \vec{Q}_V (see equation 2.27) when the field point approaches a filament point is given by equation (2.30). We rewrite this equation here for clarity; thus we have

$$\vec{R}_V(s', s) = \vec{D}(s' - s)^3 + \vec{E}(s' - s)^4 + \dots \quad (\text{A.15})$$

where

$$\begin{aligned} \vec{D} = & \frac{1}{3\alpha^{3/2}} \left(\frac{\partial \vec{X}}{\partial s} \times \frac{\partial^2 \vec{X}}{\partial s^2} \right) \\ & - \frac{3}{4\alpha^{5/2}} \left(\frac{\partial \vec{X}}{\partial s} \cdot \frac{\partial^2 \vec{X}}{\partial s^2} \right) \left(\frac{\partial \vec{X}}{\partial s} \times \frac{\partial^2 \vec{X}}{\partial s^2} \right) (s' - s)^2 + \dots \end{aligned} \quad (\text{A.16})$$

$$\begin{aligned} \vec{E} = & \frac{1}{24\alpha^{3/2}} \left(3 \frac{\partial \vec{X}}{\partial s} \times \frac{\partial^4 \vec{X}}{\partial s^4} + 2 \frac{\partial^2 \vec{X}}{\partial s^2} \times \frac{\partial^3 \vec{X}}{\partial s^3} \right) \\ & - \frac{2}{4\alpha^{5/2}} \left(\frac{\partial \vec{X}}{\partial s} \cdot \frac{\partial^2 \vec{X}}{\partial s^2} \right) \left(\frac{\partial \vec{X}}{\partial s} \times \frac{\partial^3 \vec{X}}{\partial s^3} \right) (s' - s)^2 \\ & - \frac{1}{16\alpha^{5/2}} \left(3 \frac{\partial^2 \vec{X}}{\partial s^2} \cdot \frac{\partial^2 \vec{X}}{\partial s^2} + 4 \frac{\partial \vec{X}}{\partial s} \cdot \frac{\partial^3 \vec{X}}{\partial s^3} \right) \left(\frac{\partial \vec{X}}{\partial s} \times \frac{\partial^2 \vec{X}}{\partial s^2} \right) (s' - s)^2 + \dots \end{aligned} \quad (\text{A.17})$$

where

$$\alpha = \left| \frac{\partial \vec{X}}{\partial s} \right| (s' - s)^2 + \mu^2. \quad (\text{A.18})$$

A.4 Evaluation of the integral \vec{I}_V

The integral \vec{I}_V shown by equation (2.31) is obtained analytically. First, the integrand \vec{R}_V is obtained in terms of the new variable $\tau = s' - s$. By using equations (A.15-A.18), it can be shown that

$$\begin{aligned} \vec{R}_V = & \frac{\tau^3}{(b^2\tau^2 + \mu^2)^{3/2}} \vec{A}_0 + \frac{\tau^5}{(b^2\tau^2 + \mu^2)^{5/2}} \vec{A}_1 \\ & + \frac{\tau^4}{(b^2\tau^2 + \mu^2)^{3/2}} \vec{A}_2 + \frac{\tau^6}{(b^2\tau^2 + \mu^2)^{5/2}} \vec{A}_3, \end{aligned} \quad (\text{A.19})$$

where

$$b = \left| \frac{\partial \vec{X}}{\partial s} \right|, \quad (\text{A.20})$$

and

$$\bar{A}_0 = \frac{1}{3} \frac{\partial \bar{X}}{\partial s} \times \frac{\partial^2 \bar{X}}{\partial s^2}, \quad (\text{A.21})$$

$$\bar{A}_1 = -\frac{3}{4} \left(\frac{\partial \bar{X}}{\partial s} \cdot \frac{\partial^2 \bar{X}}{\partial s^2} \right) \left(\frac{\partial \bar{X}}{\partial s} \times \frac{\partial^2 \bar{X}}{\partial s^2} \right), \quad (\text{A.22})$$

$$\bar{A}_2 = \frac{1}{24} \left(3 \frac{\partial \bar{X}}{\partial s} \times \frac{\partial^4 \bar{X}}{\partial s^4} + 2 \frac{\partial^2 \bar{X}}{\partial s^2} \times \frac{\partial^3 \bar{X}}{\partial s^3} \right), \quad (\text{A.23})$$

$$\begin{aligned} \bar{A}_3 = & -\frac{1}{2} \left(\frac{\partial \bar{X}}{\partial s} \cdot \frac{\partial^2 \bar{X}}{\partial s^2} \right) \left(\frac{\partial \bar{X}}{\partial s} \times \frac{\partial^2 \bar{X}}{\partial s^2} \right) \\ & - \frac{1}{16} \left(3 \frac{\partial^2 \bar{X}}{\partial s^2} \cdot \frac{\partial^2 \bar{X}}{\partial s^2} + 4 \frac{\partial \bar{X}}{\partial s} \cdot \frac{\partial^3 \bar{X}}{\partial s^3} \right) \left(\frac{\partial \bar{X}}{\partial s} \times \frac{\partial^2 \bar{X}}{\partial s^2} \right). \end{aligned} \quad (\text{A.24})$$

Thus the integral \bar{I}_V can be obtained by integrating analytically in s , the final solution is given by

$$\bar{I}_V = \left\{ \frac{3h}{b^2} \alpha^{1/2} - 2h^3 \alpha^{-1/2} - \frac{3\mu^2}{2b^2} \log \left| \frac{\alpha^{1/2} + bh}{\alpha^{1/2} - bh} \right| \right\} \left(\frac{1}{b^2} \bar{A}_2 + \frac{5}{3b^4} \bar{A}_3 \right) - \frac{2h^5}{3b^2} \alpha^{-3/2} \bar{A}_3, \quad (\text{A.25})$$

where $h = \Delta s$ denotes the size of the upper and lower limits of the integral \bar{I}_V .

Appendix B

Evaluation of the integrals H and G

Here we show how the integrals H and G given by equations (2.33) and (2.34) are computed analytically. Consider the integral

$$I(k) = \int_{-\infty}^{\infty} \frac{az + b}{(c^2 + z^2)^{3/2}} e^{-ikz} dz \quad (\text{B.1})$$

which has the form of H and G ; this integral may be evaluated as follows. Integrate by parts the first term of $I(k)$:

$$dv = \frac{az + b}{(c^2 + z^2)^{3/2}} \cdot v = \frac{a}{(c^2 + z^2)^{1/2}},$$

$$u = e^{-ikz}, \quad du = -ike^{-ikz}$$

then

$$I(k) = -ika \int_{-\infty}^{\infty} \frac{e^{-ikz}}{(c^2 + z^2)^{1/2}} dz + b \int_{-\infty}^{\infty} \frac{e^{-ikz}}{(c^2 + z^2)^{3/2}} dz. \quad (\text{B.2})$$

Using the tables of Campbell and Foster (1948), we get

$$\left. \begin{aligned} \int_{-\infty}^{\infty} F(f) e^{2\pi i f g} df &= E(g) \\ \int_{-\infty}^{\infty} E(g) e^{-2\pi i f g} dg &= F(f) \end{aligned} \right\} \quad (\text{B.3})$$

Let $f' = 2\pi f$ then

$$\left. \begin{aligned} E(g) &= \int_{-\infty}^{\infty} F(f') e^{i f' g} df' \\ F(f') &= \int_{-\infty}^{\infty} E(g) e^{-i f' g} dg \end{aligned} \right\} \quad (\text{B.4})$$

where E is the inverse transform with F being the direct transform. The two transforms of $I(k)$ are given on pages 125 and 126 of Campbell and Foster (1948) by

$$E(g) = \frac{1}{2(g^2 + \sigma^2)^{1/2}} \longleftrightarrow F = K_0(\sigma |p|)$$

$p = if'$, and similarly

$$E(g) = \frac{\alpha}{2(g^2 + \alpha^2)^{3/2}} \longleftrightarrow F = |p| K_1(\alpha |p|)$$

where K_0 , K_1 are the modified Bessel functions of order 0 and 1 respectively.

The integrals I_3 to I_8 appearing in equations (2.41) and (2.43) are defined by

$$I_3 = 2 \int_0^\infty Ak K_1(c_1 k) \frac{K'_m(kr)}{K'_m(k)} \cos k(z - z') dk,$$

$$I_4 = -2 \int_0^\infty Bk K_0(c_1 k) \frac{K'_m(kr)}{K'_m(k)} \sin k(z - z') dk,$$

$$I_5 = -2 \int_0^\infty Ak K_1(c_1 k) \frac{K_m(kr)}{K'_m(k)} \cos k(z - z') dk,$$

$$I_6 = 2 \int_0^\infty Bk K_0(c_1 k) \frac{K_m(kr)}{K'_m(k)} \sin k(z - z') dk,$$

$$I_7 = -2 \int_0^\infty Ak K_1(c_1 k) \frac{K_m(kr)}{K'_m(k)} \sin k(z - z') dk,$$

$$I_8 = -2 \int_0^\infty Bk K_0(c_1 k) \frac{K_m(kr)}{K'_m(k)} \cos k(z - z') dk.$$

Appendix C

Calculation of the Pressure Gradients on the Cylinder

In the calculations of the pressure gradients, the θ and z derivatives of $U_{V\theta}$ and U_{Vz} can be obtained analytically and they are given by

$$\begin{aligned} \frac{\partial U_{V\theta}}{\partial \theta} = & \frac{\Gamma}{4\pi} \int_C \left\{ \frac{\partial z'}{\partial s'} (x' \sin \theta - y' \cos \theta) + (z - z') \left(\frac{\partial x'}{\partial s'} \sin \theta - \frac{\partial y'}{\partial s'} \cos \theta \right) \right\} \frac{ds'}{\rho^3} \\ & - 3 \frac{\Gamma}{4\pi} \int_C \left\{ \frac{\partial z'}{\partial s'} (1 - x' \cos \theta - y' \sin \theta) - (z - z') \left(\frac{\partial x'}{\partial s'} \cos \theta + \frac{\partial y'}{\partial s'} \sin \theta \right) \right\} \\ & (x' \sin \theta - y' \cos \theta) \frac{ds'}{\rho^5}, \end{aligned} \quad (C.1)$$

$$\begin{aligned} \frac{\partial U_{V\theta}}{\partial z} = & -\frac{\Gamma}{4\pi} \int_C \left\{ \frac{\partial x'}{\partial s'} \cos \theta + \frac{\partial y'}{\partial s'} \sin \theta \right\} \frac{ds'}{\rho^3} \\ & - 3 \frac{\Gamma}{4\pi} \int_C \left\{ \frac{\partial z'}{\partial s'} (\sin \theta - y') - \frac{\partial y'}{\partial s'} (z - z') \right\} (z - z') \sin \theta \frac{ds'}{\rho^5} \\ & - 3 \frac{\Gamma}{4\pi} \int_C \left\{ \frac{\partial z'}{\partial s'} (\cos \theta - x') - \frac{\partial x'}{\partial s'} (z - z') \right\} (z - z') \cos \theta \frac{ds'}{\rho^5}, \end{aligned} \quad (C.2)$$

$$\begin{aligned} \frac{\partial U_{Vz}}{\partial \theta} = & \frac{\Gamma}{4\pi} \int_C \left\{ \frac{\partial x'}{\partial s'} \cos \theta + \frac{\partial y'}{\partial s'} \sin \theta \right\} \frac{ds'}{\rho^3} \\ & - 3 \frac{\Gamma}{4\pi} \int_C \left\{ \frac{\partial x'}{\partial s'} (\sin \theta - y') - \frac{\partial y'}{\partial s'} (\cos \theta - x') \right\} (x' \sin \theta - y' \cos \theta) \frac{ds'}{\rho^5}, \end{aligned} \quad (C.3)$$

$$\frac{\partial U_{Vz}}{\partial z} = -3 \frac{\Gamma}{4\pi} \int_C \left\{ \frac{\partial x'}{\partial s'} (\sin \theta - y') - \frac{\partial y'}{\partial s'} (\cos \theta - x') \right\} (z - z') \frac{ds'}{\rho^5}. \quad (C.4)$$

Appendix D

Papers and Presentations and Degrees Awarded

PAPERS

Affes, H. and Conlisk, A.T., "The Unsteady Interaction of a Three-Dimensional Vortex Filament With a Cylinder", Proceedings of the International Specialists' Meeting on Rotorcraft Basic Research, Georgia Institute of Technology, March 25-27, 1991, pp. 37-1-37-11.

Affes, H. and Conlisk, A.T., "A Model For Rotor Tip Vortex-Airframe Interaction Part 1: Theory", *AIAA J.*, vol. 31, no. 12, 1993. Also AIAA 92-0320.

Affes, H., Conlisk, A.T., Kim, J.M., and Komerath, N.M., "A Model For Rotor Tip Vortex-Airframe Interaction Part 2 : Comparison with Experiment", *AIAA J.*, vol. 31, no. 12. Also AIAA 92-0319.

Affes, H. and Conlisk, A.T., "The Three-Dimensional Boundary Layer Flow Due to a Vortex Filament Outside a Circular Cylinder, AIAA 93-0212, January, 1993. Also in preparation for submission to a journal.

Affes, H., Xiao, Z., A. T. Conlisk, Kim, J. M., and Komerath , N. M., "The Three-Dimensional Boundary Layer Flow Due to a Rotor Tip Vortex", AIAA 93-3081, AIAA Fluid Dynamics Meeting, Orlando, Florida, July, 1993. Also in preparation for submission to a journal.

Xiao, Z., Burggraf, O. R., and Conlisk, A. T., "The Three-Dimensional Interacting Boundary Layer Flow Due to a Vortex Outside a Circular Cylinder", submitted for the 25th AIAA Fluid Dynamics Meeting, June 1994, Colorado Springs.

PRESENTATIONS

Affes, H. and Conlisk, A.T., "The Unsteady Interaction of a Three-Dimensional Vortex Filament with a Cylinder", APS, 1989.

Affes, H. and Conlisk, A.T. "The Unsteady Interaction of a Three-Dimensional Vortex Filament With a Cylinder", Proceedings of the International Specialists' Meeting on Rotorcraft Basic Research, Georgia Institute of Technology, March 25-27, 1991, pp. 37-1-37-11.

Affes, H. and Conlisk, A.T., "The Pressure Distribution Due to a Three-Dimensional Vortex Filament above a Cylinder", APS, 1991.

Affes, H., Conlisk, A.T., Kim, J.M., and Komerath, N.M., "An Analytical and Experimental Study Of The Interaction Of A Vortex With An Airframe", AIAA 92-0319.

Affes, H. and Conlisk, A.T., "A Simplified Model For The Interaction Of A Rotor Tip Vortex with an Airframe", AIAA 92-0320.

Affes, H., Xiao, Z., and Conlisk, A. T., "The Three-Dimensional Boundary Layer Flow Due to a Vortex Filament Outside a Circular Cylinder", APS, 1992.

Affes, H. and Conlisk, A.T., "The Three-Dimensional Boundary Layer Flow Due to a Vortex Filament Outside a Circular Cylinder", AIAA 93-0212.

Affes, H., Xiao, Z., Kim, J. M., and Komerath, N. M., "The Three-Dimensional Boundary Layer Flow Due to a Rotor Tip Vortex", AIAA 93-3081, AIAA Fluid Dynamics Meeting, Orlando, Florida, July, 1993.

DEGREES AWARDED

Habib Affes, Phd, August, 1993.

Bibliography

- [1] Abramowitz, M. and Stegun, I. (1965), *Handbook of Mathematical Functions*, Dover, New York.
- [2] Adams, E. C., Smith, F. T., and Conlisk, A. T. (1994) "An Adaptive Grid Scheme for the Unsteady Boundary Layer Induced by a Vortex", submitted to the 25th AIAA Fluid Dynamics Meeting, June 1994, Colorado Springs.
- [3] Affes, H. and Conlisk, A.T. (1991), "The Unsteady Interaction of a Three-Dimensional Vortex Filament With a Cylinder", Proceedings of the International Specialists' Meeting on Rotorcraft Basic Research, Georgia Institute of Technology, March 25-27, 1991, pp. 37-1 to 37-11.
- [4] Affes, H. and Conlisk, A.T. (1992), "A Simplified Model for the Interaction of a Rotor Tip Vortex With an Airframe", AIAA paper 92-0320, AIAA Aerospace Sciences Meeting, Reno, Nev., January 1992.
- [5] Affes, H. and Conlisk, A. T. (1993) "The Three-Dimensional Boundary Layer Flow Due to a Vortex Filament Outside a Circular Cylinder", AIAA paper 93-0212, AIAA Aerospace Sciences Meeting, Reno, Nev., January, 1993.
- [6] Affes, H., Conlisk, A.T., Kim, J.M., and Komerath, N.M. (1992), "An Experimental and Analytical Study of the Interaction of a Vortex With an Airframe", AIAA paper 92-0319, AIAA Aerospace Sciences Meeting, Reno, Nev., January 1992.
- [7] Affes, H., Xiao, Z., Conlisk, A.T., Kim, J.M., and Komerath, N.M. (1993), "The three-Dimensional Boundary Layer Flow Due to a Rotor Tip Vortex", AIAA paper 93-3081, AIAA 24th Fluid Dynamics Conference, Orlando, Florida, July 1993.
- [8] Baskin, V. Ye., Vil'dgrube, L.S., Vozhdayey, Ye.S., and Maykapar, G.I. (1975), *Theory of Lifting Airscrews*, NASA TTF-823.
- [9] Batchelor, G.K. (1967), *Introduction to Fluid Dynamics*, Cambridge University Press, Cambridge.
- [10] Betz, A. (1915), "Die Wichtigsten Grundlagen fur den Entwurf von Luftschrauben", *Zeitschrift fur Mathematik*, 6 97.

- [11] Betz, A. (1958), "Screw Propellers with Minimum Energy Loss", Technical Translation 736, National Research Council of Canada, Ottawa, Canada.
- [12] Betzina, M.D. and Smith, C.A. (1983), "Rotor/Body Aerodynamic Interactions", NASA TM 85844, October 1983.
- [13] Bi, Nai-pei and Leishman, J.G. (1990), "Experimental Study of Rotor/Body Aerodynamic Interactions", *J. Aircraft*, Vol. 27, pp.779-788.
- [14] Bi, Nai-pei and Leishman, J.G. (1991), "Analysis of Unsteady Pressure Induced on a Body in the vicinity of a Rotor", Proceedings of the International Specialists' Meeting on Rotorcraft Basic Research, Georgia Institute of Technology, March 25-27, 1991.
- [15] Bouard, R. and Coutenceau, M. (1980), "Early Stage Development of the Wake behind an Impulsively Started Cylinder of $40 < Re < 10,000$ ", *J. Fluid Mech.*, Vol. 101, pp. 583-607.
- [16] Bramwell, A.R.S. (1976), *Helicopter Dynamics*, Edward Arnold.
- [17] Brand, A.G., McMahon, H.M., and Komerath, N.M. (1989), "Surface Pressure Measurements on a Body Subject to Vortex Wake Interaction", *AIAA J.*, Vol. 27, May 1989, pp. 569-574.
- [18] Brand, A.G., McMahon, H.M., and Komerath, N.M. (1990), "Correlations of Rotor Wake/Airframe Interaction Measurements and Flow Visualization Data", *J. Am. Hel. Soc.*, Vol. 10, pp. 4-15.
- [19] Brand, A.G. (1989), "An Experimental Investigation of the Interaction Between a Model Rotor and Airframe in Forward Flight", Ph.D. Thesis, Georgia Institute of Technology, March 1989.
- [20] Callegari, A.J. and Ting, L. (1978), "Motion of a Curved Vortex Filament with Decaying Vortical Core and Axial Velocity", *SIAM J. Appl. Math.*, Vol. 35, No. 1, pp. 148-174.
- [21] Campbell, G.A and Foster, R.M. (1948), *Fourier Integrals for Practical Applications*, D. van Nostrand Co. Inc., Princeton, N.J.
- [22] Cebeci, T. (1979), "The Laminar Boundary Layer on a Circular Cylinder Started Impulsively from Rest", *J. Comp. Phys.*, Vol. 31, pp. 153-172.
- [23] Cebeci, T., Chen, L. T. and Chang, K. C. (1986) "An Interactive Scheme for Three-Dimensional Transonic Flows", in *Numerical and Physical Aspects of Aerodynamic Flows*, ed. T. Cebeci, pp. 412-431.
- [24] Chen, Ching-Shung (1987), "Axisymmetric Incompressible Navier-Stokes Calculations of the Vortex Wake of a Hovering Rotor", Ph.D. Dissertation, The Ohio State University.

- [25] Chen, Z.L. and Wu, J.M. (1984) "Approximate Viscous/Inviscid Interacting Method for Laminar and Turbulent Flows", AIAA Paper 84-0267.
- [26] Chuang, F.S. and Conlisk, A.T. (1989), "The Effect of Interaction on the Boundary Layer Induced by a Convected Rectilinear Vortex", *J. Fluid Mech.*, Vol. 200, pp. 337-365.
- [27] Churchill, R.V. (1972), *Operational Mathematics*, Third Ed., McGraw-Hill, New York.
- [28] Clark, D.R., Maskew, B. (1991), "A Re-examination of the Aerodynamics of Hovering Rotors Including the Presence of the Fuselage", Proceedings of the International Specialists' Meeting on Rotorcraft Basic Research, Georgia Institute of Technology, March 25-27, 1991.
- [29] Conlisk, A.T. (1989), "The Pressure Field in Intense Vortex-Boundary Interaction", 27th Aerospace Sciences Meeting, Reno, Nev, AIAA paper 89-0293.
- [30] Cooley, J. W. and Tukey, J. W. (1965), "An Algorithm for the Machine Calculation of Complex Fourier Series", *Maths. Comp.*, Vol. 19, pp. 297-300.
- [31] Cowley, S.J. (1983), "Computer Extension and Analytic Continuation of Blasius Expansion for Impulsive Flow past a Circular Cylinder", *J. Fluid Mech.*, Vol. 135, pp. 389-405.
- [32] Crouse, G.L., Leishman, J.G., and Bi, N. (1990), "Theoretical and Experimental Study of Unsteady Rotor/Body Aerodynamic Interactions", presented at the 46th Annual Forum of The American Helicopter Society, Washington D.C., May 21-23, 1990.
- [33] Dhanak, M. R. (1981), "Interaction Between a Vortex Filament and an Approaching Rigid Sphere", *J. Fluid Mech.*, Vol. 109, pp. 129-147.
- [34] Doligalski, T.L. and Walker, J.D.A. (1984), "The Boundary Layer Induced by a Convected Rectilinear Vortex", *J. Fluid Mech.*, Vol. 139, pp. 1-28.
- [35] Drzewicki, S. (1920), "Theorie Generale de 1 Helice", Paris.
- [36] Duck, P. W. "Triple-Deck Flow over Unsteady Surface Disturbances: The Three-Dimensional Development of Tollmein-Schlichting Waves", (1990) *Computers and Fluids*, vol. 18, no. 1, pp. 1-34.
- [37] Duck, P.W. and Burggraf, O.R. (1986), "Spectral Solutions for Three Dimensional Triple Deck Flow over Surface topography", *J. Fluid Mech.*, Vol. 162, pp. 1-22.
- [38] Duncan, W.J., Thom, A.S., and Young, A.D. (1960), *An Elementary Treatise on the Mechanics of Fluids*, pp. 90-91, Edward Arnold Publishers LTD., London.

- [39] Dvorak, F.A, Maskew, B., and Woodward, F.A. (1977), "Investigation of the Three-Dimensional Flow Separation on Fuselage Configurations", Analytical Methods, Inc., USAAMRDL Tech. Rep. 77-4, Eustis Directorate, U.S Army Air Mobility Research and Development Laboratory, Fort Eustis, VA.
- [40] Egolf, T.A and Landgrebe, A.J. (1983), "Helicopter Rotor Wake Geometry and its Influence in Forward Flight, Volume 1- Generalized Wake Geometry and Wake Effect on Rotor Airloads and Performance", NASA CR 3726, October 1983.
- [41] Egolf, T.A and Lorber, P.F., (1987), "An Unsteady Rotor/Fuselage Interaction Method", Proceedings of the International Specialists' Meeting on Aerodynamics and Astroacoustics, Arlington, Texas February 1987.
- [42] Elliott, J.W., Cowley, S.J., and Smith, F.T. (1983), "Breakdown of Boundary Layers: i. On Moving Surfaces, ii., In Semi-Similar Flow, iii., In Fully Unsteady Flow", *Geophys. Astrophys. Fluid Dyn.*, Vol. 25, pp. 77-138.
- [43] Ersoy, S. and Walker, J.D.A. (1985), "The Viscous Flow Near a Wall by Counter-Rotating Vortex Pairs and Vortex Loops", Report FM-8, Department of Mechanical Engineering and Mechanics, Lehigh University.
- [44] Ersoy, S. and Walker, J.D.A. (1987), "The Boundary Layer due to a Three-Dimensional Vortex Loop", *J. Fluid Mech.*, Vol. 185, pp. 569-598.
- [45] Freeman, C.E. (1980), "Development and Validation of a Combined Rotor-Fuselage Induced Flow Field Computational Method", NASA TP 1656.
- [46] Froude, R.E. (1889), "On the Part Played in Propulsion by Differences in Fluid Pressures", *Transaction Institute of Naval Architecture*, Vol. 30., p. 390.
- [47] Froude, R.E. (1878), "On the Elementary Relation Between Pitch, Slip and Propulsion Efficiency", *Transaction Institute of Naval Architecture*, Vol. 19., pp. 47-65.
- [48] Gessow, A. and Myers, G. (1952), *Aerodynamics of Helicopter*, Frederick Ungar, Publishing Co., New York.
- [49] Glauert, H. (1922), "An Aerodynamic Theory of the Airscrew", British ARC R&M 786.
- [50] Glauert, H. (1928), "On Horizontal Flight of a Helicopter", R&M 1157.
- [51] Goldstein, S. (1948), "On Laminar Boundary Layer Flow Near a Position of Separation", *Quart. J. Mech. Appl. Maths.*, Vol. 1, pp. 43-69.
- [52] Goldstein, S. (1929), "On the Vortex Theory of Screw Propellers", *Proceeding of the Royal Society (London)*, Ser. A., Vol. 112, pp. 440-465.

- [53] Gray, R.B (1955), "On the Motion of the Helical Vortex Shed from a Single-Bladed Hovering Helicopter Rotor and its Application to the Calculation of the Spanwise Aerodynamic Loading", Princeton University Aero. Engr. Dept., Report No. 313, Sept 1955.
- [54] Gray, R.B (1956), "An Aerodynamic Analysis of a Single-Bladed Rotor in Hovering and Low-Speed Forward Flight as Determined from Smoke Studies of the Vorticity Distribution in the Wake", Princeton University Aero. Engr. Dept., Report No. 356, Sept 1956.
- [55] Harvey, J.K. and Perry, F.J. (1971), "Flow Field Produced by Trailing Vortices in the Vicinity of the Ground", *AIAA J.*, Vol. 9, pp. 1659-1660.
- [56] Hess, J.L. (1962), "Calculation of Nonlifting Potential Flow About Arbitrary Three-Dimensional Bodies", Report No. ES 40622, McDonnell Douglas Aircraft Company. Long Beach, CA.
- [57] Hess, J.L. and Smith, A.M.O. (1972), "Calculation of Potential Flow About Arbitrary Three-Dimensional Lifting Bodies", Report No. MDC J5679-01, McDonnell Douglas Aircraft Company. Long Beach, CA.
- [58] Hess, J.L. and Smith, A.M.O. (1967), "Calculation of Potential Flow About Arbitrary Bodies, in *Progress in the Aeronautical Sciences*, vol. 8, Pergamon, New York. pp. .
- [59] Hon, L. and Walker, J.D.A. (1987), "An Analysis of the Motion and Effects of Hairpin Vortices", Rept FM-11, Dept. of Mechanical Engineering and Mechanics , Lehigh University.
- [60] Hunt, J.C.R., Abell, C.J., Peterka, J.A., and Woo, H. (1978) "Kinematical Studies of the Flows Around Free or Surface-Mounted Obstacles; Applying Topology to Flow Visualization", *J. Fluid Mech.*, Vol. 86, pp. 179-200.
- [61] Ingham, D.B. (1984), "Unsteady Separation", *J. Comput. Phys.*, Vol. 53, pp. 90-99.
- [62] Johnson, Wayne (1980), *Helicopter Theory*, Princeton University Press.
- [63] Johnson, W. and Yamauchi G.K. (1984), "Applications of an Analysis of Asymmetric Body Effects on Rotor Performance and Loads", Paper N0. 3., Tenth European Rotorcraft Forum, August 1984.
- [64] Kim, J.M. (1992), Private Communication.
- [65] Kim, J.M. and Komerath, N.M. (1993) "Summary of the Interaction of a Rotor Wake with a Circular Cylinder", With an Airframe", AIAA paper 93-3084, AIAA 24th Fluid Dynamics Conference, Orlando, Florida, July.
- [66] Klemin, A. (1945), "Principles of Rotary-Wing Aircraft", AERO Digest, May 1 and June 1, 1945.

- [67] Knight, M. and Hefner, R.A. (1937), "Static Thrust Analysis of the Lifting Airscrew", NACA TN-626.
- [68] Komerath, N.M. (1991), Private Communications.
- [69] Komerath, N.M. (1992), Private Communications.
- [70] Kraus, W. (1978), "Panel Methods in Aerodynamics", *Numerical Methods in Fluid Dynamics*, H.J. Wirz and J.J. Smolderen, Eds., McGraw-Hill Book Company, New York, pp. 237-297.
- [71] Lamb, H., (1932), *Hydrodynamics*, Sixth Edition, Cambridge University Press, Cambridge.
- [72] Landgrebe, A.J. (1971), "An Analytical and Experimental Investigation of Helicopter Rotor Performance and Wake Geometry Characteristics", USAAM-RDL TR 71-24.
- [73] Landgrebe, A.J. and Cheney, M.C.J. (1972), "Rotor Wakes-Key to Performance Predictions", AGARD-CPP 111, Sept. 1972.
- [74] Landgrebe, A.J. (1986), "Overview of Helicopter Wake and Airloads Technology", Proceeding of the *12th European Rotorcraft Forum*, Paper No. 18, Garmisch-Partenkirchen, FRG, Sept. 1986.
- [75] Landgrebe, A.J., Moffitt R.C., and Clark D.R. (1977), "Aerodynamic Technology for Advanced Rotorcraft", *J. Am. Hel. Soc.*, Vol. 22, Nos. 2 and 3, April and July 1977.
- [76] Larmor, J. (1889), "Electromagnetic and other Images in Spheres and Planes", *Quart. J. Pure Appl. Math.*, Vol. 23, pp. 94-101.
- [77] Legendre, R. (1956), "Separation de l'Ecoulement Laminaire Tridimensionnel", *Rech. Aero.*, Vol. 54, pp. 3-8.
- [78] Leishman, J.G. and Bi, Nai-pei (1990), Aerodynamic Interactions Between a Rotor and a Fuselage in Forward Flight", *J. Am. Hel. Soc.*, Vol. 35, pp. 22-31.
- [79] Leonard, B.P. (1984), "Third-Order Upwinding as a Rational Basis for Computational Fluid Dynamics", In *Computational Techniques & Applications: CTAC-83*, (ed. Noye, J. and Fletcher, C.), Elsevier Science Publishers B.V. (North-Holland).
- [80] Lewis, T.C. (1879), "On the Images of Vortices in a Spherical Vessel", *Quart. J. Pure Appl. Math.*, Vol. 16, pp. 338-347.
- [81] Lighthill, M.J. (1963), "Attachment and Separation in Three-dimensional Flow", in *Laminar Boundary Layers*, ed. L. Rosenhead, II, 2.6, Oxford Univ. Press, pp. 72-82.

- [82] Lighthill, M.J. (1940), "The Image System of a Vortex Element in a Rigid Sphere", *Cambridge Phil. Soc.*, Vol. 52, pp. 317-321.
- [83] Liou, S.G., Komerath, N.M., and McMahon, H.M. (1990), "Measurement of the Interaction Between a Rotor Tip Vortex and a Cylinder", *AIAA J.*, Vol. 28, No. 6, pp. 975-981.
- [84] Lock (1924), "Experiments to Verify the Independence of the Elements of an Airscrew Blade", British R & M 853.
- [85] Lock (1931), "The Application of Goldstein's Theory to the Practical Design of Airscrews", Rep. Memo. Aeronaut. Res. Coun. 1377.
- [86] Lorber, P.F. and Egolf, T.A (1990), "An Unsteady Rotor-Fuselage Interaction Analysis", *J. Am. Hel. Soc.*, Vol. 35, No. 7, pp. 32-42; also NASA CR-4178, August 1988.
- [87] Mangler, K.W and Squire, H.B. (1950), "The Induced Velocity Field of a Rotor", R & M 2642, May 1950.
- [88] Mavris, D.N, Komerath, N.M., and McMahon, H.M. (1989), "Prediction of Aerodynamic Rotor-Airframe Interactions in Forward Flight", *J. Am. Hel. Soc.*, Vol. 34, No. 4, October 1989.
- [89] Milne-Thomson, L.M. (1962), *Theoretical Hydrodynamics*, MacMillan, London.
- [90] Moore, D.W. (1972), "Finite Amplitude Waves on Aircraft Trailing Vortices", *Aero. Quart.*, Vol. 23, pp. 307-314.
- [91] Moore, D. W. (1953), "Displacement Effect of a Three-Dimensional Boundary Layer", Report 1124, NACA.
- [92] Morino, L., Kaprielian Z., and Sipic S.R. (1985), "Free Wake Analysis of Helicopter Rotors", *Journal of Aircraft*, Vol. 9, No. 2, pp. 127-140.
- [93] Peridier, V., F.T. Smith, and Walker, J.D.A. (1991) "Vortex-Induced Boundary Layer Separation, Part 1: $Re \rightarrow \infty$; Part 2, Unsteady Interacting Boundary Layer Theory", *J. Fluid Mech.*, Vol. 232, pp. 99-165.
- [94] Press, W.H., Flannery, B.P., Teukolsky, S.A., and Vetterling, W.T. (1986), *Numerical Recipes. The Art of Scientific Computing*, Cambridge University Press, Cambridge.
- [95] Rankine, W.J. (1865), "On the Mechanical Principles of the Action of Ship Propellers", *Transaction Institute of Naval Architecture*, Vol. 6., pp. 13-39.
- [96] Richardson, S.M. and Cornish, A.R.H. (1977), "Solution of Three Dimensional Incompressible Flow Problems", *J. Fluid Mech.*, Vol. 82, pp. 309-319.
- [97] Rosenhead, L. (1963), *Laminar Boundary Layers*, Oxford University Press.

- [98] Sarpkaya, Turgut (1989), "Computational Methods with Vortices-The 1988 Freeman Scholar Lecture", *J. Fluids Engineering*, Vol. 111, No. 3, pp. 5-52.
- [99] Schrage, D.P and Peskar, R.E. (1977), "Helicopter Vibration Requirements", Proceeding of the 35th Annual Forum of the American Helicopter Society, Washington, D.C. May 1977.
- [100] Scully, M.B. (1971), "Computation of Helicopter Rotor Wake Geometry and its Influence on Rotor Harmonic Airloads", MIT ASRL-TR-176-1.
- [101] Seddon, J. (1990), *Basic Helicopter Aerodynamics*, BSP Professional Books.
- [102] Sears, W.R. and Telionis, D.P. (1975), "Boundary Layer Separation in Unsteady Flow", *SIAM J. Appl. Maths.*, Vol. 23, pp. 215-234.
- [103] Sheridan, P.F. and Smith, R.F. (1980), "Interactional Aerodynamics-A New Challenge to Helicopter Technology", *J. Am. Hel. Soc.*, Vol. 25, No. 1, January 1980.
- [104] Simons, I.A., Pacifico, R.R., and Jones, J.P. (1966), "The Movement, Structure, and Breakdown of Trailing Vortices from a Rotor Blade", Proceedings of the CAL/USAA AVLABS Symposium, Buffalo, NY.
- [105] Smith, C.A. (1979), "Some Effects of Wake Distortion Due to Fuselage Flow Field on Rotor Thrust Limits", ARO Workshop on Rotor Wake Technology, Raleigh, NC, April 1979.
- [106] Smith, C.A. and Betzina, M.D. (1986), "Aerodynamic Loads Induced by a Rotor on a Body of Revolution", *J. Am. Hel. Soc.*, Vol. 31, No. 1, pp. 4-15, January 1986.
- [107] Smith, C.R., Walker J.D.A, Haidari, A.H., and Sobrun, U. (1991), "On the Dynamics of Near-Wall Turbulence", *Phil. Trans. R. Soc. Lond. A* 336, pp. 131-175.
- [108] Smith, F.T. (1986), "Steady and Unsteady Boundary Layer Separation", *Ann. Rev. Fluid Mech.*, Vol. 18, pp. 197-220.
- [109] Smith, F.T. (1988), "Finite-time Breakup Can Occur in Any Unsteady Interacting Boundary Layer", *Mathematica*, Vol. 35, pp. 256-273.
- [110] Stepniewski W.Z. and Keys C.N. (1984), *Rotary-Wing Aerodynamics*, Vols 1 and 2, Dover Publications Inc., New York.
- [111] Summa, J.M. (1976), "Potential Flow About Impulsively Started Rotors", *Journal of Aircraft*, Vol. 13, No. 4, pp. 317-319.
- [112] Summa, J.M. and Clark, D.R. (1979), "A Lifting-Surface Method for Hover Climb Airloads", 35th annual Forum of American Helicopter Society, Washington D.C.

- [113] Telionis, D.P. and Tsahalis, D.Th. (1974), "Unsteady Laminar Separation over Impulsively Moved Cylinders", *ACTA Astronaut.* Vol. 1, pp. 1487-1505.
- [114] Theodorsen, T. (1948), *Theory of Screw Propellers*, McGraw Hill Book Co., Inc., New York, N.Y.
- [115] Tobak, M. and Peake, D.J. (1982) "Topology of Three Dimensional Separated Flows", *Ann. Rev. Fluid Mech.*, Vol. 14, pp. 61-85.
- [116] van Dommelen, L.L. (1981), "Unsteady Boundary-Layer Separation", Ph.D. dissertation, Cornell University.
- [117] van Dommelen, Leon and Cowley, Stephen J. (1990), "On the Lagrangian Description of Unsteady Boundary-Layer Separation. Part 1. General Theory", *J. Fluid Mech.*, Vol. 210, pp. 593-626.
- [118] van Dommelen, L.L. and Shen, S.F. (1982), "The Genesis of Separation", In *Numerical and Physical Aspects of Aerodynamic Flows*, ed. T. Cebeci, Springer, pp. 299-311.
- [119] van Dommelen, L.L. and Shen, S.F. (1980), "The Spontaneous Generation of the Singularity in a Separating Laminar Boundary Layer", *J. Comp. Physics*, Vol. 25, pp. 125-140.
- [120] Walker, J.D.A. (1978), "The Boundary Layer Due to a Rectilinear Vortex", *Proc. Roy. Soc. A*, Vol. 359, pp. 167-188.
- [121] Walker, J.D.A., Smith, C.R., Cerra, A.W., and Doligalski, T.L. (1987), "The Impact of a Vortex Ring on a Wall", *J. Fluid Mech.*, Vol. 181, pp. 99-140.
- [122] Weiss, P. (1944), "On Hydrodynamics Images: Arbitrary Irrotational Flow Disturbed by a Sphere", *Proc. Camb. Phil. Soc.*, Vol. 40, pp. 259-261.
- [123] Williams, James C. (1978), "On the Nature of Unsteady Three-Dimensional Boundary-Layer", *J. Fluid Mech.*, Vol. 88, pp. 241-258.
- [124] Wilson, J.C. and Mineck, R.E. (1975), "Wind-Tunnel Investigation of Helicopter Rotor Wake Effects on Three Helicopter Fuselage Models", NASA TM X-3185, March 1975.
- [125] Wu, T. (1985), "Unsteady Incompressible Boundary Layer Separation over a Two Dimensional Impulsively Started Elliptic Cylinder Calculated by Lagrangian Method", MS Thesis, Cornell University.
- [126] Wu, T. and Shen, S. (1991), "Emergence of Three Dimensional Separation over Suddenly-Started Prolate Spheroid at Incidence", AIAA Paper No. 91-0544.
- [127] Xiao, Z.H, Shen, S.F., and Wu T.Y. (1990), "The Calculations of Unsteady Boundary Layer Flows by Non-Iterative Time Marching Scheme", (unpublished), Cornell University.

- [128] Xu, W.C. and Wang, K.C. (1988), "Unsteady Laminar Boundary Layer Along the Symmetry Plane of an Impulsively Started Prolate Spheroid", *J. Fluid Mech.*, Vol. 195, pp. 413-435.